ANTIFOULING, BIOFUNCTIONAL “ROMANTIC” POLYMER COATINGS

SYNTHESIS OF ANTIFOULING, BIOFUNCTIONAL “ROMANTIC” POLYMER COATINGS

By ALEXANDER JESMER, B.Sc.

A Thesis Submitted to the School of Graduate Studies in Partial Fulfilment of the Requirements for the Degree Doctor of Philosophy

DESCRIPTIVE NOTE

McMaster university DOCTOR OF PHILOSOPHY (2022) Hamilton, Ontario (Chemical Biology)

TITLE: Synthesis of antifouling, biofunctional “romantic” polymer coatings

AUTHOR: Alexander Jesmer, B.Sc. (University of Ottawa)

SUPERVISOR: Professor Ryan Wylie

NUMBER OF PAGES: xxi, 217

LAY ABSTRACT

When a material, such as a medical implant or sensor, is placed in contact with tissues and biological fluids, biomolecules stick to the exposed surfaces through nonspecific interactions. It is important to minimize nonspecific interactions because they can lead to bacterial infections, inflammation, implant failure and loss of device performance. Coatings to minimize nonspecific interactions therefore remain an active area of research. In this thesis, we explored new methods to create biomolecule and cell repellent coatings of long, chainlike molecules known as polymers grafted onto surfaces. Specific types of polymers, known as antifouling, were particularly effective at reducing these interactions.

Although it is important to block nonspecific interactions, many devices require bioactive surfaces through selective interactions. For example, sensors for analysis of blood products require the selective binding of the target ligand with minimal binding of non-target agents. To this end, functionalizable antifouling polymers are often modified with a capture or binding agent corresponding to the target ligand. Polymer coatings which are both antifouling and functionalizable for specific interactions, are called "romantic" because of their selective love of a single interaction. To synthesize these romantic polymer coatings, two main methods have been reported: 1) "grafting-from" where the polymer is grown from the surface, producing a very dense coating, and 2) "grafting-to" where the polymer is synthesized in solution, and then immobilized onto the material surface, which produces coatings of lower density. For antifouling polymer coatings to be as effective as possible, polymers should be tethered densely on the material surface, but to maximize the loading of capture agents, polymer density must be lower to allow for grafting within the layer. Further, the grafting-from method is typically more synthetically challenging hindering commercialization.

To improve the selective bioactivity of graft-to and graft-from coatings as well as antifouling properties of graft-to coatings, we present two methods to improve the specific bioactivity of anti-fouling polymer coatings and the first description of Graft-then-Shrink, a method to enhance the antifouling properties of graft-to coatings for medical implants and label-free *in vitro* sensors. For graft-from coatings, we produced a hierarchical romantic surface that consists of two polymer layers, the lower of which is dense and antifouling, and the upper of which is low-density and can accommodate high-levels of bioactive agents, resulting in a best of both worlds; the density of the layers is controlled by a novel pH controlled polymerization procedure. A method to improve the less labor intensive "grafting-to" strategy was then devised, called "Graft-then-Shrink" where the antifouling polymers are grafted onto a shrinkable material, and then the material is shrunk, leading to an increase in grafted polymer content over grafting-to alone. This method was successfully applied to a heat shrinkable material and an elastomeric silicone material, a common material for medical devices, for improved antifouling properties. Finally, a method for combining the Graft-then-Shrink technique

with a novel localized surface plasmon resonance (LSPR) biosensor was found, that provides a simple route to access romantic surfaces on high-sensitivity, easy to fabricate LSPR biosensors. Together, these fabrication methods will simplify and expedite the translation of antifouling and romantic surfaces for medical devices and sensors.

ABSTRACT

Materials in contact with the biological milieu (biomaterials) spontaneously and nonspecifically adsorb constituent proteins which may lead to unwanted cell adhesion and responses or hinder device performance. These interactions and their related phenomena lead to complications in ~3% of implant surgeries. Thus, resistance to these nonspecific interactions is critical to the performance of many implanted biomaterials and biosensing surfaces. Further, these interactions have widespread importance to industrial materials in contact with biological environments such as food packaging, and agricultural and nautical surfaces.

Thin film coatings of antifouling polymers are one of the leading methods for reducing nonspecific interactions. Both polymer composition (chemical composition and molecular weight) and polymer grafting density are the principal determinants of coating performance. For applications requiring specific bioactivity, such as selective ligand-analyte interactions for sensors, the polymer coating must remain antifouling and be amenable to functionalization with capture ligands. Tethered polymer coatings can be made by surface initiated polymerization ("graft-from") which results in higher density coatings, but complex fabrication limits commercialization and capacity of functionalization with capture ligands. Simpler "graft-to" procedures, where pre synthesized polymers are immobilized to a surface, are more amenable to translation but suffer from inferior antifouling properties due to lower density coatings. New fabrication methods are therefore required to improve both graft-to and graft-from coatings.

Herein, the effects of polymer density on material performance are explored and leveraged to produce novel functional surfaces using two classes of polymers, namely amphiphilic and thermoresponsive poly(oligo(ethylene glycol)) methyl ether methacrylate, and zwitterionic, functionalizable poly(carboxybetaine methacrylamide) (pCB), as well as copolymers thereof. Specifically, polymer grafting techniques which exploit grafting density effects on surfaces were developed, leading to surfaces: 1) that are both high-loading and antifouling due to two different grafting densities within bimodal architectures, and (2) with enhanced anti-fouling properties despite being prepared via a "grafting-to" method using shrinkable or expandable substrates. Interestingly, shrinking substrates with antifouling polymers resulted in a novel LSPR biosensor with high translation potential.

Chapter 2 describes the pH controlled, one-pot production of two-layer brushes composed of an antifouling dense layer and a high-loading lower density layer where capture ligand immobilization was improved by 6 times compared to a single high density layer. Towards improving fouling and bioactivity of graft-to surfaces, *Chapter 3* describes the first demonstration of Graft-then-Shrink where a stretched polystyrene (PS) substrate coated in a thin gold layer modified with thiol-terminated pCB was thermo-shrunk to one sixth in footprint to increase polymer surface coating content for enhanced antifouling properties and the production of micro/nano gold wrinkles to generate a localized surface plasmon resonance (LSPR) active surface. The low-cost sensors can

detect biomolecular interactions by tracking changes in absorbance in the visible spectrum using ubiquitous plate readers. In *Chapter 4*, Graft-then-Shrink was extended to elastomeric materials, where thiol terminated polymers were grafted onto solvent swollen silicone via thiol-maleimide click chemistry, producing strongly antifouling materials.

Taken together, these developments represent significant advances in the preparation and application of antifouling polymer coatings towards the improvement of antifouling surface properties of medical devices and resulted in the development of a novel, low-cost LSPR sensor without the need for specialized equipment.

ACKNOWLEDGEMENTS

Many people who have helped me to this point are not named in this acknowledgements section as it could not possibly fit all of you. Nevertheless, I would like to thank you. Even though these thanks are insufficient for all you have done, they are here, in any case. Primary, middle, and high school teachers, undergraduate professors, friends, colleagues, past supervisors, and acquaintances that encouraged me all along the way, thank you.

Having a fantastic supervisory committee has greatly enriched my experience at McMaster. Thank you to my supervisor Dr Ryan Wylie, for supporting my scientific curiosity, allowing me to pursue new and unknown challenges, and for your constant feedback, critique, advice, patience, and trust. Professors on my committee, Dr David Latulippe and Dr Anthony Rullo, thank you for lending your expertise to this project and for asking me the tough things, I always have your voices echoing when planning an experiment or analyzing data.

Thank you to members of McMaster Chemistry and Chemical Biology, and Chemical Engineering for all of the support and access to instrumentation. A huge thank you to all of the members of the Wylie group for the unending companionship. Specifically thank you to Dr Vince Huynh for teaching me so much, your leadership in the group, and for preparing such a strong foundation for the lab, thank you to Muneeb Shoaib for showing me the importance of the fundamentals, thank you to Devang Nijsure for introducing me to Everton Football Club, and thank you to April Marple for looking

at every new graph, and for being a fantastic lab mate, friend, and a month filled entirely with Wednesdays.

To my family for supporting me all the way, thank you. Thank you to my parents for providing me with the tools to take on this challenge, and for always wanting the best for me. Thank you to my sister for encouragement and reading so many things. Thank you to Tracy and Scott for welcoming me so warmly into your family, despite moving so far away with your daughter, and supporting us every step of the way. Thank you to Danielle for your trust, your unrelenting belief in my abilities, and for really believing me when I say things are going to be okay, even when I don't believe myself.

TABLE OF CONTENTS

LAY ABSTRACT ..... **iii**
ABSTRACT ..... **v**
ACKNOWLEDGEMENTS ..... **vii**
LIST OF FIGURES ..... **xiii**
LIST OF SUPPLEMENTARY FIGURES ..... **xv**
LIST OF SCHEMES ..... **xvi**
LIST OF TABLES ..... **xvii**
LIST OF SUPPLEMENTARY TABLES ..... **xviii**
LIST OF ABBREVIATIONS ..... **xix**
CHAPTER 1. LOW-FOULING POLYMER COATINGS FOR BIOMEDICAL APPLICATIONS **1**
1.1. Abstract **2**
1.2. Polymer coatings **3**
1.3. Synthetic strategies **6**
1.3.1. Grafting-to 6
1.3.2. Grafting-from 7
1.3.2.1. Surface initiated - atom transfer radical polymerization *8*
1.3.2.2. Surface – reversible addition fragmentation transfer *9*
1.3.2.3. Architectures *10*
1.3.3. Grafting-through 11
1.3.4. Non-tethered methods 11
1.3.4.1. Bulk-bloom *11*
1.4. Antifouling surfaces **12**
1.4.1. Classes of antifouling polymers 13
1.4.1.1. Uncharged hydrophilic monomers *13*
1.4.1.2. Betaine monomers *15*
1.4.1.3. Polyampholytes *16*
1.4.1.4. Hydrophobic materials *17*
1.4.2. Other factors determining fouling 18
1.5. Surface functionalization **18**
1.5.1. Chain end functionalization 18
1.5.2. Side chain functionalization 19
1.6. Surface characterization **20**
1.6.1. Thickness and grafting density 20
1.6.2. Surface sensitive techniques 22
1.6.3. Fouling characterization techniques 23
1.6.3.1. Nonspecific protein adsorption *23*
1.6.3.2. SPR and QCM-D *25*
1.6.3.3. Ellipsometry *26*
1.6.3.4. AFM *26*
1.6.3.5. Methods for characterizing unlabeled proteins *27*

1.6.3.5.1. Extraction of adsorbed protein for quantification 27
1.6.3.5.2. ELISA: Detecting adsorbed proteins..... 28
1.6.3.5.3. LC-MS: Determining adsorbed protein content after extraction 29
1.6.3.5.4. Surface sensitive techniques: XPS and ToF-SIMS 30
1.6.3.6. Methods for quantifying adsorbed proteins modified with detection labels 31
1.6.3.6.1. Fluorescent labels 31
1.6.3.6.2. Radioactive labels 33
1.6.3.6.3. Coated AFM: Modified tips for selective protein detection 33
1.6.3.7. Cell-adhesion 34
1.6.3.7.1. Quantifying mammalian cell fouling 35
1.6.3.7.2. High throughput methods to measure macrophage adhesion and activation 36
1.6.3.8. Bacterial fouling related to medical implants 37
1.7. Conclusion and outlook 40
1.8. Thesis Objectives 41
1.9. References 42
CHAPTER 2. FABRICATION OF LOW-FOULING, HIGH-LOADING POLYMERIC SURFACES THROUGH PH-CONTROLLED RAFT 62
2.1. ABSTRACT 63
2.2. Introduction 64
2.3. Materials and methods 67
2.3.1. Materials 67
2.3.2. Modification of silica surfaces 69
2.3.2.1. *Modification of silica surfaces and APTES deposition 69*
2.3.3. Immobilization of RAFT chain transfer agent 70
2.3.4. Solution and graft-from polymerizations 70
2.3.4.1. *Synthesis of pDMAPMA 70*
2.3.4.2. *Synthesis of bimodal solution and graft-from pCB 71*
2.3.4.3. *GPC characterization of solution polymers 72*
2.3.5. Surface characterization 72
2.3.5.1. *Ellipsometry 72*
2.3.5.2. *X-ray Photoelectron Spectroscopy 73*
2.3.5.3. *Water contact angle 73*
2.3.6. Modification of pCB surfaces with capture agents 73
2.3.6.1. *Bevacizumab-647 immobilization 73*
2.3.6.2. *Avidin immobilization and biotin fluorescein capture 74*
2.3.7. Characterization of protein and macrophage fouling on pCB coated surfaces 75
2.3.7.1. *Nonspecific protein fouling 75*
2.3.7.2. *Nonspecific macrophage adhesion 76*
2.3.8. Statistical methods 76
2.4. Results and Discussion 77

2.4.1. Demonstration of pH-controlled RAFT polymerization in solution: synthesis of multimodal pDMAPMA and pCB 77
2.4.2. Graft-from pCB synthesis on silicon wafer surfaces was confirmed by XPS 83
2.4.3. Graft-from synthesis of bimodal pCB through pH-controlled S-RAFT . 84
2.4.4. Avidin modified bimodal pCB surfaces enhanced biotin capture 87
2.4.5. pCB surfaces prepared by pH-controlled RAFT are low-fouling 88
2.5. Further discussion 91
2.6. Conclusions 92
2.7. Supporting information 93
2.8. References 96
CHAPTER 3. GRAFT-THEN-SHRINK: SIMULTANEOUS GENERATION OF ANTIFOULING POLYMERIC SURFACES AND LSPR BIOSENSORS 101
3.1. Abstract 102
3.2. Introduction 103
3.3. Results and discussion 106
3.3.1. Graft-then-Shrink increases pCB content within a defined footprint ... 109
3.3.2. Influence of grafted polymers and shrinking conditions on Au wrinkled structures 112
3.3.3. Graft-then-Shrink enhances pCB coated surface resistance to macrophage adhesion 115
3.3.4. Characterization and sensitivity of Graft-then-Shrink LSPR sensors ... 119
3.3.5. Capture ligand immobilization and analyte sensing with Graft-then-Shrink sensors 122
3.4. Conclusion 127
3.5. Experimental Section/Methods 128
3.5.1. Materials 128
3.5.2. Substrate preparation 129
3.5.3. Carboxybetaine methacrylamide monomer synthesis 129
3.5.4. Synthesis of thiol terminated polycarboxybetaine methacrylamide 130
3.5.5. Synthesis of thiol terminated polycarboxybetaine methacrylamide – co – N-(3-aminopropyl)methacrylamide 130
3.5.6. Synthesis of thiol terminated poly (oligo ethylene glycol) methyl ether methacrylate 131
3.5.7. Preparation of Graft-then-Shrink PS-Au-pCB 132
3.5.8. Preparation of Shrink-then-Graft PS-Au-pCB 132
3.5.9. Polymer characterization by GPC 132
3.5.10. Characterization of surface hydrophilicity 133
3.5.11. Scanning electron microscopy 133
3.5.12. Determination of relative polymer content 133
3.5.13. XPS 134
3.5.14. Determination of grafting density by fluorescent polymer microscopy 134

3.5.15. Macrophage adhesion 135
3.5.16. Pseudomonas aeruginosa adhesion 135
3.5.17. LSPR sensitivity measurements 136
3.5.18. Protein sensing with LSPR surfaces 136
3.5.19. Covalent protein immobilization 136
3.5.20. Fluidic device fabrication 137
3.5.21. Non-covalent protein sensing 137
3.5.22. Statistical analysis 137
3.6. Supporting information 138
3.7. References 150
CHAPTER 4. GRAFTING POLYMERS TO SOLVENT SWELLED PDMS ELASTOMERS INCREASES THIN FILM DENSITY AND ANTIFOULING PERFORMANCE 160
4.1. Abstract: 161
4.2. Introduction 163
4.3. Results and discussion 167
4.3.1. Graft-then-Shrink with substrate swelling increases polymer content on PDMS 168
4.3.2. Characterization of biological fouling properties 174
4.3.2.1. Nonspecific bacterial adhesion 176
4.3.3. Physical characterization of modified elastomers 178
4.3.4. Further Discussion 180
4.4. Conclusions 182
4.5. Materials and methods 183
4.5.1. Materials 183
4.5.2. PDMS elastomer preparation and swelling 183
4.5.3. *Tert*-butyl protected Carboxybetaine methacrylamide monomer synthesis 184
4.5.4. General polymerization protocol 184
4.5.5. Polymer characterization by GPC 185
4.5.6. Polymer grafting procedure 185
4.5.7. Excess maleimide assay 186
4.5.8. Fluorescent polymer content characterization 186
4.5.9. Characterization of surface hydrophilicity 186
4.5.10. Bacterial adhesion assay 187
4.5.11. Macrophage adhesion 187
4.5.12. Statistical analysis 188
4.6. Supporting information 188
4.7. References 201
CHAPTER 5. CONCLUSIONS 212
5.1. Major Contributions 212
5.2. Concluding Remarks 215
5.3. References 216

LIST OF FIGURES

Figure 1.1: Schematic representation of surface-tethered polymer grafting density regimes, and thickness proportionalities. 4
Figure 1.2: Schematic representation of commonly used grafting protocols. 7
Figure 1.3: Hydration shell associations with uncharged hydrophilic, ampholyte and betaine monomers. 17
Figure 1.4: Schematic representation of functionalizable polymer structures. 20
Figure 2.1: Schematic for the synthesis of bimodal pCB layers via pH-controlled S-RAFT for enhanced capture agent immobilization on low-fouling surfaces. 67
Figure 2.2. GPC analysis of multimodal distributions from solution polymerization of pDMAPMA using pH-controlled RAFT. pH time courses during polymerizations are plotted on the right. 79
Figure 2.3: Dependence of pH 11 time interval on pCB's bimodal Mw distributions in the presence of butylamine. 82
Figure 2.4: Surface characterization of functionalized silicon wafers by WCA and ellipsometry 85
Figure 2.5: Immobilization of bevacizumab confirmed the greater loading capacity of bimodal pCB wafers. 86
Figure 2.6. Bimodal, two layer, pCB wafers modified with avidin have greater biotin capturing efficiency. 88
Figure 2.7: One and two layer pCB surfaces were equally low-fouling when exposed to serum. 91
Figure 3.1: Graft-then-shrink: Simultaneous improvement of polymer surface coverage for improved antifouling properties and generation of LSPR active Au surfaces. 108
Figure 3.2: pCB content is greater on Graft-then-Shrink Au surfaces. 110
Figure 3.3: SEM micrographs of wrinkled Au surfaces from Shrink-then-Graft and Graft-then-Shrink (dry and wet) with immobilized pCB of various MWs. 113
Figure 3.4: Graft-then-Shrink improved resistance to nonspecific macrophage adhesion. 117
Figure 3.5: Sensitivity characterization of bare (no pCB) and pCB coated wrinkled Au LSPR sensors. 121
Figure 3.6: Sensing avidin binding/unbinding with polymer coated LSPR sensors. 123
Figure 3.7: Graft-then-Shrink LSPR sensors are concentration sensitive. 127
Figure 4.1. Graft-then-Shrink via thiol maleimide click chemistry for increasing grafted polymer content on PDMS. 167
Figure 4.2. Grafting polymers onto swelled PDMS increases graft polymer content. 170
Figure 4.3: PDMS swelling solvent modulates polymer grafting content. Fluorescence intensity of (A) 10:1 and (B) 30:1 PDMS swelled in EtAc or toluene functionalized with pCB-COOH and pCB-TBu fluorescent copolymers and (B) 8mer pOEGMA fluorescence copolymers (mean ± SD, n = 3). 171
Figure 4.4. Grafting salt choice and concentration modifies grafted pCB-COOH content. 174

Figure 4.5. Graft the shrink with high M_w pOEGMA onto swelled elastomers improves antifouling properties. 176
Figure 4.6. Resistance of pOEGMA and pCB-COOH modified elastomers towards *E. coli* bacterial attachment. 177
Figure 4.7. Graft-then-Shrink on elastomers decreases hydrophilicity, except with 2mer pOEGMA. 180

LIST OF SUPPLEMENTARY FIGURES

Figure S2.1: ^{1}H NMR (600 MHz) spectra of (A) monomodal and bimodal pCB and (B) pDMAPMA in D_2O. 93
Figure S2.2: Degradation of CTA solutions at pH 4.5. 94
Figure S2.3: GPC chromatograms of pCB distributions as a function of polymerization time at pH 11 without butylamine. 95
Figure S2.4: Thick 1 layer monomodal pCB surface. 96
Figure S3.1: BCA activity with pCB. 138
Figure S3.2: High-resolution XPS of wrinkled Au surfaces. 139
Figure S3.3: Determination of chain density of fluorescently labeled pCB-*co*-APMA. 140
Figure S3.4: Low magnification SEM of surfaces. 141
Figure S3.5: Hydrophilicity of pCB coated surfaces. 143
Figure S3.6: Nonspecific adhesion of *P. aeruginosa* to bare and pCB coated wrinkled gold. 144
Figure S3.7: Confocal microscopy for quantification of nonspecific BSA-Cy5 adsorption to wrinkled pCB-Au surfaces. 145
Figure S3.8: HABA – Avidin displacement assay of pCB-*co*-APMA modified with biotin and desthiobiotin. 146
Figure S3.9: LSPR response of biotin modified pCB-*co*-APMA sensor exposed to BSA in HEPES buffer. 147
Figure S3.10: Removal of haze from PS following Graft-then-Shrink wet.. 148
Figure S3.11: Gel permeation chromatographs of polymers used. 149
Figure S3.12: Construction of fluidic channel in a 96 well plate for placement of a Graft-then-Shrink sensor. 150
Figure S4.1. Surface fluorescence of pOEGMA on PDMS. 189
Figure S4.2. Maleimide content of elastomers after polymer grafting. 190
Figure S4.3. pCB-TBu ester deprotection in pH 1.3 HCl. 191
Figure S4.4. Quantification of fluorescence of pCB copolymers grafted in MES and GHCl on PDMS. 192
Figure S4.5. Apparent molecular weight of pCB changes with GHCl concentration. ... 193
Figure S4.6. Macrophage adhesion to PDMS modified with non-antifouling polymers. 194
Figure S4.7. Representative fluorescence micrographs of RAW 264.7 macrophage adhesion on polymer modified PDMS. 196
Figure S4.8. Water contact angle measurements of polymer modified PDMS. 198
Figure S4.9. H NMR spectroscopy of CB-TBu monomer. 198
Figure S4.10. NMR spectroscopic characterization of pCB-TBu synthesis from pDMAPMA. 199

LIST OF SCHEMES

Scheme 1: Mechanisms of popular SI-CRP methods used to produce low-fouling polymer coatings. 9
Scheme 2: Mechanism of thiocarbonylthio aminolysis. RAFT chain end modification via pH dependent aminolysis. 78

LIST OF TABLES

Table 1.1: Example low and antifouling polymers and their associated traits for application in romantic surfaces. Adapted from Chen *et al* with permission.[52] 14
Table 1.2: Primary bacterial infections and conditions by implant site..... 37
Table 1.3: Advantages and limitations of commonly employed techniques to characterize protein adsorption and cell adhesion..... 38
Table 1.4: Techniques for the characterization of biological responses to biomaterial surfaces. 40
Table 2.1: Characterization of low and high M_W populations in bimodal solution polymerizations. M_W = weight average molecular weight, M_n = number average molecular weight..... 80
Table 2.2: XPS derived elemental composition of pristine and modified silicon wafers. 83

LIST OF SUPPLEMENTARY TABLES

Table S4.1: Polymerization conditions used for the preparation of RAFT polymer library. 200
Table S4.2: Calculated molecular weights, dispersities and degrees of polymerization of polymers used. 201

LIST OF ABBREVIATIONS

Abbreviation	Definition
ANOVA	Analysis of variance
APMA	N-(3-aminopropyl)methacrylamide)
APMA-HCl	Aminopropyl methacrylamide - hydrochloride
APTES	Aminopropyl triethoxy silane
ARGET-ATRP	Activators regenerated by electron transfer - atom transfer radical polymerization
ATR-FTIR	Attenuated total reflection - Fourier-transform infrared spectroscopy
BCA	Bicinchoninic acid
biotin-fluorescein	Biotin (5-fluorescein) conjugate
BSA	Bovine serum albumin
BSA-Cy5	Bovine serum albumin - Cy5 conjugate
BuOH	n-Butanol
CB	Carboxybetaine
CBS	Calf bovine serum
CB-Tbu	Carboxybetaine tert-butyl ester
CFI-JELF	Canada Foundation for Innovation: John R. Evans Leaders Fund
cLogP	Calculated partition coefficient
CRP	Controlled radical polymerization
CSL	Carbon spacer length
CTA	Chain transfer agent
Đ	Dispersity
DCM	Dichloromethane
DI	Deionized
DIC	N,N'-Diisopropylcarbodiimide
DMEM	Dulbecco's modified Eagle medium
DMF	Dimethylformamide
DOL	Degree of labeling
EDC	1-Ethyl-3-(3-dimethylaminopropyl)carbodiimide
EtAc	Ethyl acetate
EtOH	Ethanol
FBR	Foreign body response
FBS	Fetal bovine serum
FTIR	Fourier-transform infrared spectroscopy
FWHM	Full width at half-maximum
GHCl	Guanidine hydrochloride
GPC	Gel permeation chromatography
HABA	4'-Hydroxyazobenzene-2-carboxylic acid
HCl	Hydrochloric acid

HEPES	4-(2-hydroxyethyl)-1-piperazineethanesulfonic acid
IPA	Isopropanol
kDa	Kilodalton
LCST	Lower critical solution temperature
LOD	Limit of detection
LogP	Partition coefficient
LPS	lipopolysaccharide
LSPR	Localized surface plasmon resonance
M	Molarity
MES	2-(N-morpholino)ethanesulfonic acid
Mn	Number average molecular weight
Mw	Weight average molecular weight
MWCO	Molecular weight cut off
N	degree of polymerization
NaOH	Sodium hydroxide
NHS	N-hydroxysuccinimide
NMR	Nuclear magnetic resonance
NSERC	Natural Sciences and Engineering Research Council
OD600	Optical density at 600 nm
ORF-RI	Ontario Research Fund - Research Infrastructure
PBS	Phosphate buffered saline
PBS-T	PBS with 0.05% TWEEN
PC	Phosphorylcholine
pCB	Poly(carboxybetaine methacrylamide)
pDMAPMA	poly(Dimethyl aminopropyl methacrylamide)
PDMS	poly(dimethyl siloxane)
PEG	polyethylene glycol
pHEMA	poly(2-hydroxyethyl methacrylate)
PIMP	Photoiniferter-mediated polymerization
pIPAAM	poly(N-isopropylacrylamide)
pMEDSAH	poly(2-(methacryloxy)ethyl)dimethyl-3-sulphopropyl ammonium hydroxide)
pMPC	poly(methacryloyloxylethyl phosphorylcholine)
pOEGMA	poly(oligoethylene glycol methylether methacrylate)
PS	Polystyrene
pSMBA	poly(sulfobetaine methacrylate
PVMS	poly(vinyl methyl siloxane)
QCM	Quartz crystal microbalance
RAFT	Reversible addition-fragmentation chain-transfer
Rg	Radius of gyration
RSA	Random sequential adsorption
S	Swelling ratio
SB	Sulfobetaine
SDS	Sodium dodecyl sulfate

SI-ATRP	Surface initiated - atom transfer radical polymerization
SI-CRP	Surface initiated - controlled radical polymerization
SMCC	Succinimidyl-4-(N-maleimidomethyl)cyclohexane-1-carboxylate
SPR	Surface plasmon resonance
S-RAFT	Surface initiated - reversible addition-fragmentation chain-transfer
TCP	Tissue culture plastic
TFA	Trifluoro acetic acid
ToF-SIMS	Time of flight - secondary ion mass spectrometry
WCA	Water contact angle
XPS	X-ray photoelectron spectroscopy
δ	Solubility parameter
δRIU	Difference in refractive index units
δλ	Shift in localized surface plasmon resonance wavelength

CHAPTER 1. ANTIFOULING POLYMER COATINGS FOR BIOMEDICAL APPLICATIONS

Author's Preface:

A portion of the following chapter has been reprinted with permission from *Frontiers Media SA* under a CC-BY license, and was published in *Frontiers in Chemistry – Chemical Biology* under the citation:

Jesmer, A.H., and Wylie, R.G., 2020. Controlling Experimental Parameters to Improve Characterization of Biomaterial Fouling. Frontiers in Chemistry, 8, p.604236.

A.H. Jesmer conceived of the manuscript, conducted the literature review, and wrote the manuscript. R.G. Wylie conceived of and revised the manuscript.

1.1. Abstract

Over the past 40 years, advances in coating technology have led to the discovery of surface modifications for resistance towards nonspecific protein adsorption (fouling) while in contact with biological media, which is critical for the improvement of common medical implants and biosensors. Of potential surface modifications, the surface grafting of antifouling polymers has proven useful for numerous biomedical applications. These polymer mediated improvements in antifouling performance have been achieved not only upon the discovery of antifouling monomers and polymer compositions, but also through investigation of polymer grafting techniques that control the grafting density of end-tethered polymers. Further to fouling resistance, the functionalization of these polymer coatings with biological capture agents for filtration and sensing purposes is also of great interest to the biomedical community. The fabrication of antifouling, functionalizable "romantic surfaces" remains complex and expensive, limiting translation potential. Successful production and adoption of romantic surfaces as in-line medical devices or biosensors rests on the development of simple methods that also improve upon antifouling and sensing properties.

1.2. Polymer coatings

Polymeric surface coatings for antifouling and functionalizable biointerfaces are being developed for medical implants, biomolecule sensing in complex fluids, and blood purification[1–6]. For example, zwitterionic coatings applied to continuous glucose monitors allow for reduced noise and calibrations, improving patient quality of life, by reducing nonspecific protein interactions with the sensor surface. To mitigate fouling and immunogenicity, the parameters of the interface between the device and the biological environments must be carefully controlled by modulating properties such as hydrophobicity and roughness[7]. A common method to alter the interface is to create a polymer layer on the surface of the device or sensor. Polymer coatings are prepared through a variety of methods based on the required coating properties such as thickness, uniformity, stimuli responsiveness and grafting density[8]. Choice of material and synthetic method requires careful consideration as both prescribe final coating fouling performance and functionalizability[5,7,8].

End tethered polymer coatings, commonly referred to as "polymer brushes," can be produced through several synthetic strategies. Polymers can be synthesized in solution and functionalized for immobilization to a functional surface, known as "grafting-to" which produces low grafting density coatings in the "mushroom" regime[9] (**Figure 1.1**). To access high grafting density "brush" regimes, polymer chains (**Figure 1.2**) can be synthesized via surface-initiated polymerizations, known as "grafting-from[8]." Though both techniques produce ultrathin polymer coatings, between 1 and 100 nm, the

properties attainable through each such as thickness, density and surface architecture are more thoroughly controlled via grafting-from[8].

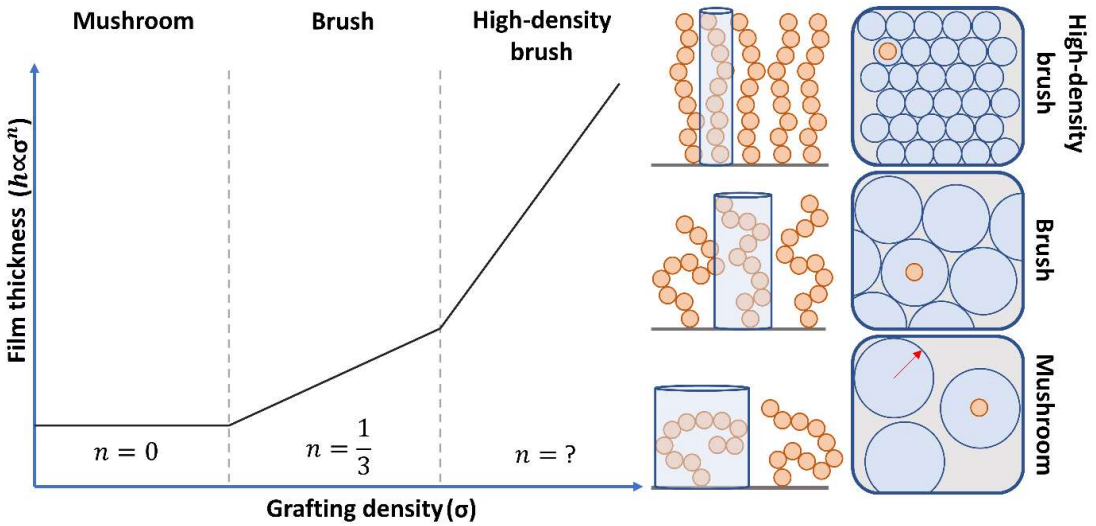

Figure 1.1: Schematic representation of surface-tethered polymer grafting density regimes, and thickness proportionalities. The thickness of polymer films in the mushroom regime does not increase with increasing grafting density because of the absence of polymer-polymer interactions, while films in the brush and high-density brush regimes increase in thickness because the polymer chains repel adjacent tethered chains, forcing them to extend away from the substrate.

The characterization of grafted polymer coating properties remains a difficult task, with several open challenges[10]. Chain grafting density and coating thickness both determine the functional properties of tethered polymer coatings, and as a result, their accurate characterization has garnered widespread attention[10]. Despite the importance of these parameters, current characterization methods require several assumptions which introduce significant error into calculated values. Surface characterization techniques for romantic surfaces comprise two classes 1) physical and chemical characterization and 2) functional characterization. Developed techniques for the physical and chemical characterization of these surfaces come directly from standard materials science and are

concerned with characteristics of the polymer films directly[10]. Functional characterization of romantic surfaces is specific to the application of the coatings and comprise the use of biological matter to determine the interactions of the interface with the biological environment, as well as the function of the capture agents, if any are present for sensing or filtration applications.

A premier focus of polymer applications is the production of antifouling surfaces that do not elicit negative biological responses[11]. The fouling of surfaces can lead to several unwanted consequences including the degradation of device performance as well as immune responses from implanted biomaterials[7], polymer coatings are therefore used to minimize nonspecific interactions. Reduction of nonspecific protein adsorption and cell adhesion at surfaces is achieved generally though the production of high grafting density polymer coatings with strong hydration via labour intensive grafting-from methods[8,12,13]. Other surface properties such as micro and nano-structure also impact nonspecific adhesion at biointerfaces[14].

Polymer coatings with reactive groups that are amenable to modification with bioactive molecules or capture agents are referred to as functionalizable. Coatings which are both antifouling, that is they reduce nonspecific interactions with a biological environment, and functionalizable with molecules that have strong biospecific interactions such as antibodies and enzymes have been dubbed “romantic surfaces” [5,15,16]. For example, functionalization of antifouling surfaces with peptides can be used to selectively direct the adhesion of cells[17,18] or with biomolecules for improved biosensors[19]. Achieving both high-density functionalization of polymer surfaces while

maintaining a antifouling nature is a desired outcome for the production of highly sensitive biosensors[20–22] and for immobilized enzyme bioreactors[23].

Here, an overview of the current methods of synthesis and materials available for production of romantic surfaces will be presented. Recent discoveries in improved biocompatible controlled radical polymerizations and antifouling monomers are discussed. Methods of functionalization of these materials and their impacts on the fouling properties of the polymer coatings, following functionalization, are shown. Finally, methods of characterization of romantic surfaces are examined.

1.3. Synthetic strategies

1.3.1. Grafting-to

In the grafting-to methodology, pre-synthesized polymers are immobilized to a suitably functionalized surface through end-functionalization such as thiol-gold[24], silane chemistry[9], DOPA functionalization[13,25], click reactions (thiol – ene[26], azide – alkyne[27]) or through physical interactions in co-polymers[28], known as physisorption. Polymer coatings produced through the grafting-to method have a limited grafting density due to the steric interactions of large globular macromolecules diffusing to the surface. The grafting density is theoretically limited to twice the radius of gyration (R_g) of the polymer, but practically limited by random sequential adsorption (RSA) to be ~50% coverage (jamming limit)[29]. Grafting-to is synthetically simple as polymers are produced in solution and can be characterized by well-established techniques prior to immobilization on a surface. Further, polymer coatings produced via grafting-to allow for all converted monomer to by immobilized onto the surface of interest in contrast to

grafting-from as will be discussed (Section 1.3.2). The limited film thickness and density achievable by grafting-to due to the lack of penetration through the already grafted polymers can be somewhat ameliorated by using conditions which minimize the conformational size of the polymer during grafting or the size of the substrate after grafting such as grafting using theta solvents, cloud point grafting[30,31], aggregation and charge screening by chaotropic salts[32], and shrinking the substrate following the grafting-to procedure[33,34].

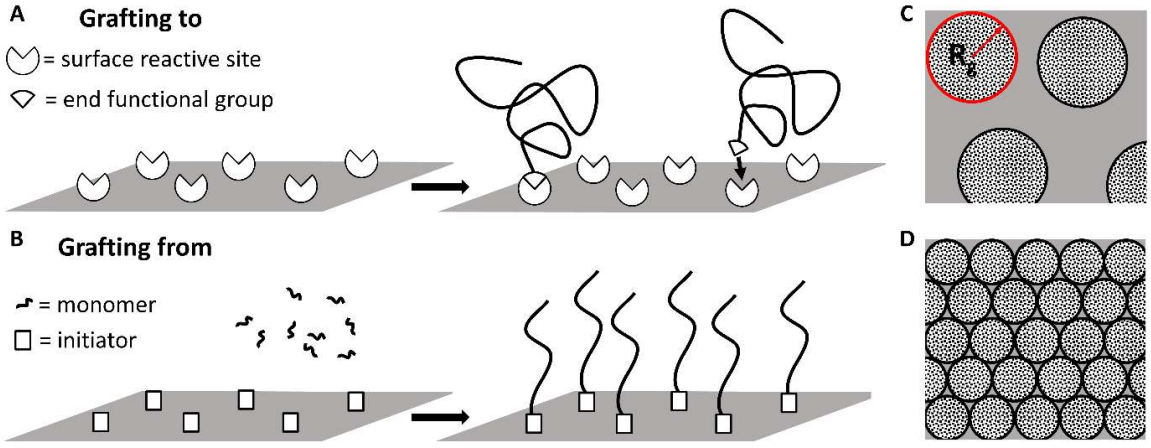

Figure 1.2: Schematic representation of commonly used grafting protocols. A) Grafting-to immobilizes end-functionalized pre-synthesized polymers to functionalized surfaces yielding relatively lower grafting density, limited by the radius of gyration of the polymer in solution. B) A polymer coating synthesized via grafting-from where polymer chains are polymerized from a functionalized surface, producing a grafting density not limited by the of radius of gyration limit. C) Top view of surface coverage of mushroom polymers from grafting-to, grafting density limited by RSA in the jamming limit. D) Top view of densely packed polymer chains synthesized by grafting-from.

1.3.2. Grafting-from

Grafting-from surface coatings are limited in density only by the size of the monomer, with larger monomers having lower theoretical grafting density maximums[10]. Due to the steric repulsion between adjacent grafted chains, coatings produced via the

grafting-from method can have tunable thickness by controlling the degree of polymerization. These coatings can be made thicker than grafting-to coatings with many architectures available through surface initiated-controlled radical polymerization (SI-CRP) methods. Surfaces functionalized for SI-CRP can be prepared with either the initiation species or the transfer agent (ligand or chain transfer agent) on the surface[8].

1.3.2.1. Surface initiated - atom transfer radical polymerization

Surface initiated - atom transfer radical polymerization (SI-ATRP) is mediated by a reversible equilibrium of halogen transfer between a dormant alkyl halide polymer and a transition metal / ligand complex which allows for the propagation of a radical polymerization when activated (**Scheme 1**)[35]. The most commonly used transition metal halogen pair is CuBr[8]. Extensions of standard ATRP have been developed to regenerate transition activators, providing, in the case of CuBr based ATRP, a regenerating source of Cu^{I}, which is depleted through conversion to Cu^{II} over the course of a conventional ATRP due to loss of chain end functionality. Among these extensions is Activators regenerated by electron transfer - atom transfer radical polymerization (ARGET-ATRP) which is tolerant to air and simplifies the synthesis of polymer coatings reducing the need for stringent degassing and air sensitive techniques[36]. ARGET-ATRP has been used to produce antifouling coatings on air exposed poly(dimethyl siloxane) (PDMS) and cellulose substrates[37,38]. Standard ATRP is limited in its application to biomedical materials due to the presence of toxic transition metal catalysts[39], because of this, ATRP protocols have been extended to regenerate low oxidation state copper, reducing total

copper required to the parts per billion range[36], and recently completely metal-free photoinduced ATRP has been shown[40,41].

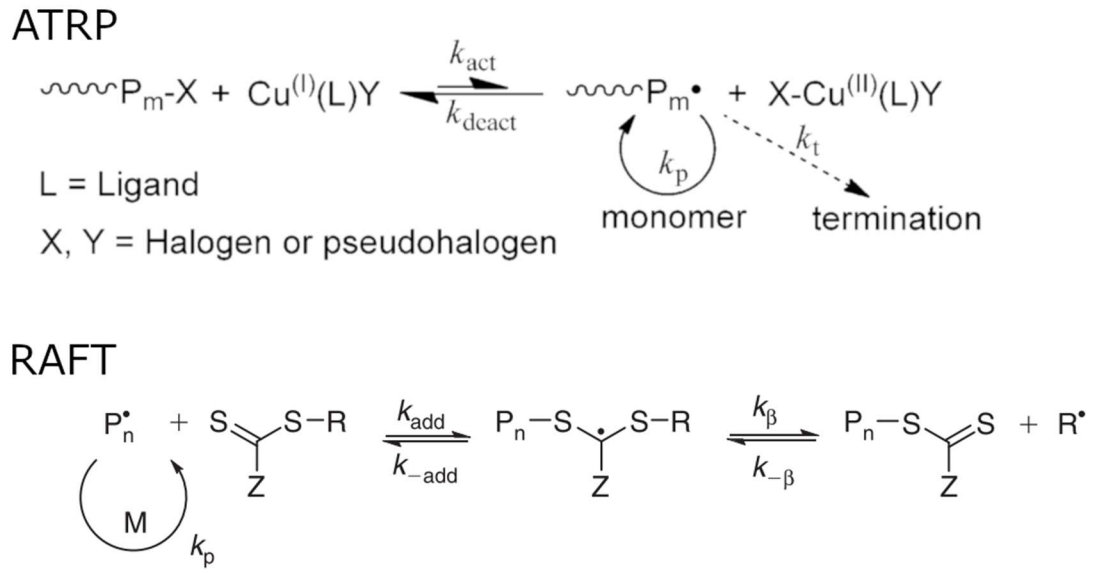

Scheme 1: Mechanisms of popular SI-CRP methods used to produce antifouling polymer coatings. ATRP is controlled through the reversible exchange of a halogen ligand between a dormant chain and a transition metal-ligand complex which activated the chain to propagate. RAFT is controlled via the reversible addition and transfer of a thiocarbonylthio chain transfer agent from a dormant chain onto a propagating chain to begin propagation of the dormant chain. Adapted from Peng *et al.*[35] and Moad *et al.*[42]

1.3.2.2. Surface – reversible addition fragmentation transfer

The synthesis of coatings with surface – reversible addition fragmentation transfer polymerization (S-RAFT) does not require transition metal catalysts, providing a biocompatible surface without extensive washing steps for catalyst removal. RAFT polymerizations are carried out similarly to standard free radical polymerization, with the addition of a thiocarbonylthio containing chain transfer agent (CTA), which bonds reversibly to the propagating chain end providing control and the living nature to the

resulting polymer chain[42]. S-RAFT can be conducted from surfaces with CTAs immobilized through the Z or R group of the CTA (**Scheme 1**), providing different functional groups for further surface modification following polymerization. For example, CTAs immobilized through the Z group result in an accessible free thiol following CTA lysis which can be used for further immobilization[8] or modification[43]. Further, polymer coatings produced through S-RAFT provide multiple avenues for post-synthesis modification such as hetero Diels-Alder, thiol-ene, thiol-maleimide and disulfide among others due to the function rich CTA cap[43].

1.3.2.3. Architectures

The control over polymer molecular weight, dispersity and composition during coating that is afforded by the grafting-from method, gives access to a multitude of useful surface architectures not accessible via the grafting-to technique. For example, photolithographic patterning of surfaces produced by photo-mediated polymerizations provide methods for spatially specific, aligned cell adhesion[44]. Polymer coatings of gradient thickness have been produced for numerous biological applications as controlling thickness yields gradients in wettability, adhesion and fouling; these varying surface properties provide ideal experimental platforms for the testing of many conditions[45]. Romantic surfaces with enhanced biomolecule loading and sensing properties have been produced through two-layer or hierarchical surface architectures of thin dense brush layers with a sparse layer polymer to facilitate high density biomolecule immobilization[20–22]. A list of currently available coating architectures has been exhaustively compiled recently in *Chemical Reviews*[8].

1.3.3. Grafting-through

For initiators or chain transfer agents that are not amenable to immobilization, the grafting-through technique can be used. Polymer films synthesized via grafting-though are tethered to the surface through side chains rather than chain ends, where some number of side chains are first immobilized to the surface and by their incorporation into polymerizing chains, the polymer is bound to the surface. This leads to a grafting process which is limited in density similar to grafting-to films, but can achieve higher densities than strict grafting-to as at the start of the reaction very small macroradicals can penetrate the growing polymer layer[46]. Polymerizable monomer units are immobilized to the surface to be modified, and then polymerization is carried out above the material. Rather than polymerizing from one group on the surface, as in grafting-from, the polymer chain is tethered to the surface where surface bound monomers are added to the polymer. This places the technique somewhere between those in section 1.3.1 and 1.3.2 as the surface bound monomer can be added directly to an initiating species, a single monomer radical unit or a macroradical (an already polymerizing chain). This leads to a grafting process which is limited in density similar to grafting-to films, but can achieve higher densities than strict grafting-to as at the start of the reaction very small macroradicals can penetrate the growing polymer layer[46].

1.3.4. Non-tethered methods

1.3.4.1. Bulk-bloom

The bulk-bloom method takes advantage of the dynamic nature of polymeric materials, allowing for a simple route to create a self-healing surface. A polymer blend can be prepared containing the base material polymer as well as a polymer for coating, which will bloom to the surface of the polymeric material substrate. Block copolymers have been used with a long chain solubilizer and a antifouling end-block[47], such as polystyrene-*block*-polyisoprene with fluorinated side chains, or linear polyurethanes with fluorinated end caps[48], which are combined with a bulk polymer, and subsequently bloom to the interface[49]. Bulk mixtures of poly(hydroxymethyl methacrylate) (pHEMA) and zwitterionic poly(methacryloyloxylethyl phosphorylcholine) (pMPC) were used to produce antifouling surfaces on contact lenses to extend wear time[50], wear the zwitterion migrates to the interface in hydrated conditions. This method is exceptionally simple from a manufacturing standpoint, and materials amenable to this technique are of particular importance to medical applications[51].

1.4. Antifouling surfaces

The reduction of nonspecific interactions with biological media is of utmost importance for controlling biointerfaces[52]. Polymer coatings are used to resist the nonspecific adsorption of biological material (i.e., proteins and cells) collectively known as "fouling." The resistance of fouling is of interest in implanted biomaterials, extracorporeal filtration devices and biosensors, for the mitigation of the foreign body response (FBR) and the improvement of signal quality. Adsorption of < 10 ng cm^{-2} of fibrinogen can cause the adhesion of macrophages[52]. Nonspecific protein adsorption is measured to determine surface fouling resistance, with < 5 ng cm^{-2} of protein adsorbed

after exposure to non-diluted blood serum being generally considered a "antifouling" surface[53]. It should be noted that improvements in resistance to cell adhesion at surfaces can be achieved by other methods than material and coating choice, notably the surface topology can be used to modulate cell adhesion[14].

General rules for the selection of antifouling materials were devised in the early 2000s, known as "Whitesides' Rules" which are: 1) hydrophilicity, 2) no overall charge, 3) hydrogen bond acceptors and 4) no hydrogen bond donors[54,55]. Some materials have since been shown to be antifouling despite the presence of hydrogen bond donors such as HPMA and mannitol[56]. Beyond hydrophilicity, the mechanism of water molecule attraction, and thereby hydration strength, is important to fouling mitigation. Hydration shells formed by hydrogen bonds are easily disrupted while those formed through electrostatic interactions with charged groups are much stronger with hydration free energies of zwitterionic pCB and uncharged, hydrophilic oligo ethylene glycol of -404 kJ mol^{-1} and -182 kJ mol^{-1} [57] respectively (Figure 1.3).

1.4.1. Classes of antifouling polymers

1.4.1.1. Uncharged hydrophilic monomers

Uncharged, hydrophilic, hydrogen bond forming, fouling resistant materials are found in nature in the form of saccharides and peptides and in the lab from synthetically derived materials[52]. Among non-charged, hydrophilic materials, poly ethylene glycol (PEG) is the most commonly used in biomedical applications[58]. Fouling resistance of uncharged hydrophilic polymers is primarily dependent on hydration and chain

flexibility. Uncharged hydrophilic materials attract hydration shells solely though hydrogen bonding, limiting the total number of associated water molecules, and the strength of their association with the material, compared to those formed around charged groups[59]. Fouling resistance is also contributed to by the flexibility of the polymer coating, with flexible polymers such as PEG performing exceptionally well in this regard. Because chain flexibility contributes to the fouling resistance of PEG coated surfaces, very high grafting density (>0.16 and 0.19 chains nm^{-2} for 5000 and 2000 Dalton (Da) PEG respectively) can actually increase fouling[52,60]. The density above which fouling increases is dependent on the protein adsorbed, the molecular weight of the polymer, and the PEG end group (hydroxy or methoxy), with critical values for hydroxy terminated PEG up to 0.27 – 0.5 chains nm^{-2} but no reported critical upper density limit for hydroxy terminated PEG[61,62]. Despite its popularity, there is a search for alternatives to PEG due to the discovery of anti-PEG antibodies in 42% of the population[58] and oxidative instability in biological environments[52,63]. Among alternative uncharged hydrophilic materials are PEG derivative poly(oligoethylene glycol methylether methacrylate) (pOEGMA)s, HEMA, peptide-based materials, and sugars such as mannitol (Table 1.1).

Table 1.1: Example low and antifouling polymers and their associated traits for application in romantic surfaces. From Chen *et al* with permission.[52]

Materials	Protein adsorption	Cell adhesion	Materials	Protein adsorption	Cell adhesion
Hydrophilic materials			*Polybetaine*		
PEG-based materials			Poly(CBAA)	Yes	Yes
PS-g-PEGMA and PMMA-g-PEGMA	Yes	No	Poly(SBMA)	Yes	Yes
PEG-poly(phosphonate) terpolymer	Yes	No	Poly(CBMA)	Yes	Yes
PLL-g-PEG	Yes	Yes	Poly(MPC)	Yes	Yes
PEGMA	Yes	No	PC-SAM	Yes	Yes
$PPEG_xLys$	Yes	No	OPC-SAM	Yes	Yes
POEGMA	Yes	Yes	*Polyampholyte*		
PEO-PU-PEO	Yes	No	SA/TMA-SAM	Yes	Yes
PEO-PPO-PEO	Yes	No	CA/TMA-SAM	Yes	Yes
PEO	Yes	No	PM/TMA-SAM	Yes	No
PEG	Yes	Yes	Poly(TM-SA)	Yes	No
Py-g-PEG	Yes	No	Poly(METMA-MES)	Yes	No
mPEG-DOPA	Yes	No	PDDA/PSS	Yes	No
mPEG-MAPD	Yes	No			
OEG-SAM	Yes	Yes			
PMOXA	Yes	No			
Dendron					
Glycerol dendron	Yes	No			
HPG	Yes	No			
Tetraglyme	Yes	Yes			
Dextran	Yes	No			
Polysaccharide	Yes	No			
Poly (HEMA)	No	Yes			
PVA	Yes	No			
Mannitol-SAM	Yes	Yes			
Peptide-based SAM	Yes	No			
Peptide-based SAM	Yes	No			

1.4.1.2. Betaine monomers

Zwitterionic betaine monomers, containing positive and negative charges on each monomer unit, provide neutral polymer chains[51]. Zwitterionic materials are associated more strongly to hydration shells than neutral hydrophilic materials, due to electrostatic interactions with water molecules[64] (Figure 1.3). Zwitterions comprise a set of monomers which are antifouling including phosphorylcholine (PC)[51], sulfobetaine (SB)[65], carboxybetaine (CB)[65] and sulfopyridinium betaine[51] among others (**Table 1.1**). Within the zwitterion class, hydration shell strengths and entropic penalties due to increased order in associated water molecules varies[57]. Interestingly, SB and CB have dipole orientations with cationic groups closer to the polymer backbone, while PC has this

orientation reversed. The effect of reversing the dipole orientation of SB has been investigated and shown to have no significant effects on antifouling performance, despite the reverse SB's more "biomimicking" orientation[66]. Other considerations for betaine monomers include the backbone structure and carbon spacer length (CSL) between charged units. Commonly, betaine monomers contain either methyl or hydrogen substituted backbones with acrylamide or acrylate groups adjacent to the backbone. Each combination impacts polymer stability, with methacrylamide backbones providing improved stability in biologically relevant conditions[67]. CSL impacts fouling properties of surfaces as larger CSLs can introduce instability in some betaines[68] leading to a loss of zwitterionic properties. Further, CSLs of 3 reduce the fouling resistance of pCB due to increased intra-chain interactions[69]. Zwitterionic monomers have also been made intrinsically functional by incorporating azide click handles onto quaternary amines in SB and alkynes and vinyl groups onto choline phosphates, whereby the monomers are zwitterionic both before and after functionalization[70,71] to yield antifouling functionalized surfaces.

1.4.1.3. Polyampholytes

Polyampholytes contain positively and negatively charged monomers resulting in a neutral overall charge[72]. These materials can attract water through hydrogen bonds as well as electrostatic forces which increases the strength of association compared with hydrophilic based surfaces (Figure 1.3). During the synthesis of polyampholyte materials, defects can occur of groupings of same charged monomers, leading to a non-neutral polymer sub-section. Although, the sequential incorporation of similarly charged

monomers is unfavoured because of charge-charge repulsion, even with monomers with different reactivity ratios and molar feed ratios[73]. Minor local charge defects have minimal effect on overall fouling with 0.95:1 ratios between positive and negative monomers being able to produce antifouling surfaces[74].

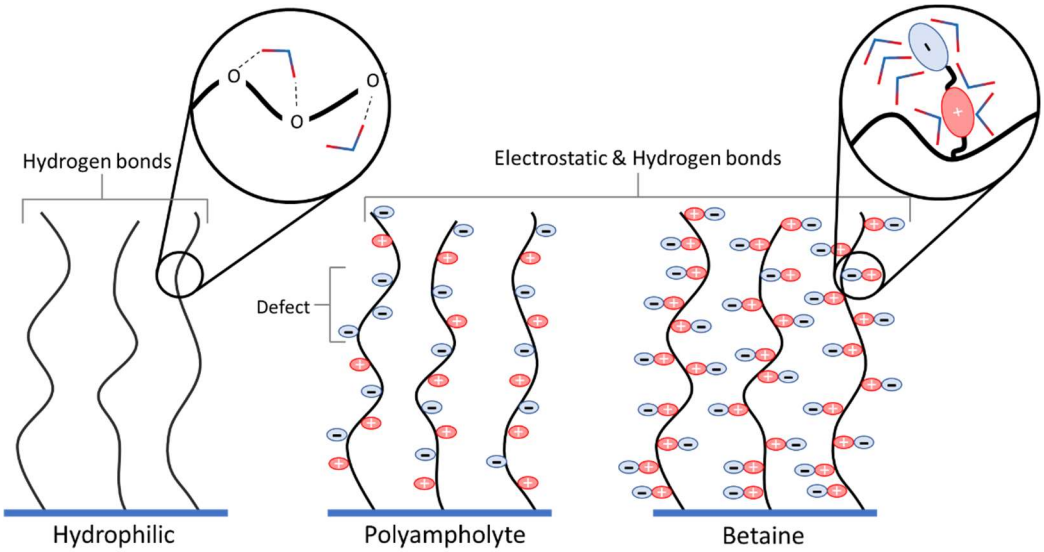

Figure 1.3: Hydration shell associations with uncharged hydrophilic, ampholyte and betaine monomers.

1.4.1.4. Hydrophobic materials

Hydrophobic surfaces with a low surface energy can also reduce fouling by self-cleaning and release mechanisms[75]. These hydrophobic surfaces can be prepared with polymer coatings of fluorinated molecules such as semi fluorinated block polymers[76], or fluorinated polymer coatings that are then infused with liquid fluorocarbons[77,78]. Polycarbonate polyurethane with fluorinated surface modifying macromolecules showed reduced macrophage retention after 7 days of incubation, with addition of a cell adhesive RGD peptide leading to selective surface cell adhesion over 7 days[79] These hydrophobic

coatings have been synergistically combined with hydrophilic PEG based coatings to produce antifouling and foulant release surfaces, combining the properties of both materials[80–82].

1.4.2. Other factors determining fouling

Cell adhesion to surfaces is also driven by material properties independent of protein adsorption[83]. Surface stiffness can control the adhesion of cells *in vitro*[84] and influence cell signaling and differentiation *in vivo*[85]. Surface structure, roughness, and engineered structures can also influence cell adhesion[14], while patterns direct cell alignment[86]. Selective cell adhesion has been demonstrated by controlling feature size on surfaces. For example, surface features smaller than the footprint of mammalian cells can prevent nonspecific adhesion of osteoblasts and promote bacterial adhesion[87].

1.5. Surface functionalization

1.5.1. Chain end functionalization

Chemical handles can be produced at terminal monomers as chemistry is often unique at polymer ends (e.g., containing CRP groups, unreacted polymerization groups etc.) than within monomer units. In coatings produced via grafting-to, these handles can be modified prior to immobilization or following the polymer grafting protocol. If end groups are required for large biomolecule immobilization, immobilization of large biomolecules is preferred following the grafting protocol to minimize polymer size during grafting. Polymers can be modified to contain an end-functionality prior to immobilization via grafting-to or have a functional end-group that can be modified for functionalization already present such as halogens used in SI-ATRP, via nucleophilic

substitutions[88], and thiocarbonylthio bonds in CTAs and iniferters used in S-RAFT and SI-PIMP respectively, via thiol reactive chemistry[43]. RAFT CTAs are also available with a suite of built in functional groups for post polymerization functionalization such as alcohols, N-hydroxysuccinimide (NHS)-esters and azides[89]. Methods developed for chain end functionalization provide monomer independent processes that can be applied to all polymers synthesized via a common technique. Chain end functionalization results in a one-to-one ratio between polymers and immobilized agent, limiting maximum immobilization levels of a single monolayer on surfaces.

1.5.2. Side chain functionalization

To produce additional functionalization capabilities, polymer side chains can be modified for the grafting of bioactive agents or for grafting to surfaces. Polymer chains can be made antifouling and functionalizable through the copolymerization (block or statistical) of functional monomers with antifouling monomers, or using antifouling monomers with functional capabilities. Careful consideration must be made for chemical composition, for example, block copolymers with antifouling poly(2-(methacryloxy)ethyl)dimethyl-3-sulphopropyl ammonium hydroxide) (pMEDSAH) with a functionalizable block of poly (glycidyl methacrylate) lost fouling resistance once functionalized[90]. Whereas, statistical copolymers of functional glycidyl methacrylate and zwitterionic SB[91] and intrinsically reactive, zwitterionic carboxybetaine monomers[92] have been shown to remain antifouling following functionalization with biomolecules. Modified PC and SB monomers have also been synthesized which remain zwitterionic after functionalization, avoiding the overall positive charge resulting from modifying the

carboxylic acid group of CB[70,71]. Dense polymer surfaces are sterically hindered by one another, limiting the immobilization of large biomolecules to surfaces[20], and so, architectures to decrease grafting density, but maintain fouling resistance remains an active area of research[21,22].

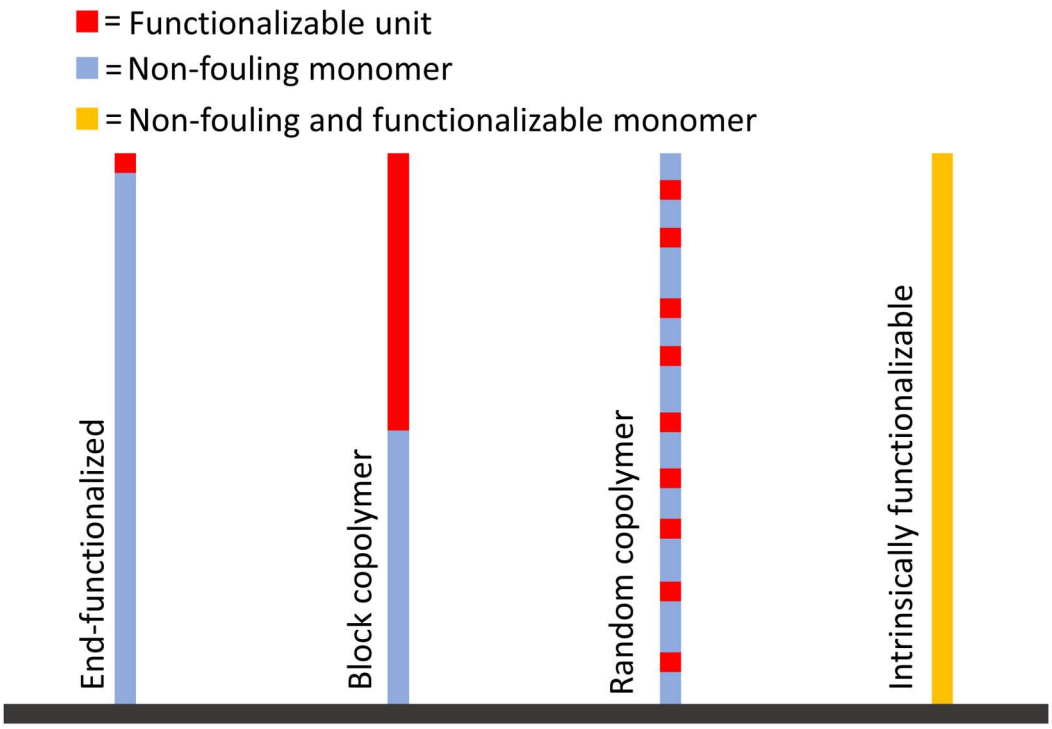

Figure 1.4: Schematic representation of functionalizable polymer structures.

1.6. Surface characterization

1.6.1. Thickness and grafting density

Polymer film thickness and chain grafting density are related film parameters as a film with similar degree of polymerization (N) will increase in thickness as grafting density increases (Equation 1,2). The hydration state of the polymer coating determines the thickness measured (e.g., solvated vs dry). Thicknesses determined in each hydration state can be used to determine degree of polymerization of the polymer chains using

Equation (1) for dried polymer films and Equation (2) for hydrated films, if density is known or vice versa; where h is the thickness of the film, *N* is the degree of polymerization, *a* is the monomer size and σ is the grafting density.

$$\boldsymbol{h_{dry} = Na^3\sigma} \quad (1)$$

$$\boldsymbol{h_{wet} = Na^{4/3}\sigma^{1/3}} \quad (2)$$

Film thickness can be measured and grafting density calculated via a variety of techniques with benefits and drawbacks, with three common techniques, 1) dry thickness measurement, 2) swelling experiments, and 3) thermogravimetric analysis[10]. For dry thickness measurement, polymers in the dry state are collapsed onto the surface, and the density of this collapsed state is assumed to be equal to that of the bulk polymer. This assumption introduces the most significant source of error into the grafting density calculations performed with this technique as dried state polymer coatings can differ from bulk polymer density, especially in cases of low grafting density[10]. Thicknesses are commonly measured via ellipsometry[93], X-ray reflectivity or neutron reflectivity[94]. These techniques are similarly employed in swelling experiments, where dry thickness measurements are conducted, followed by measurements of the coating in the hydrated state. Grafting density is then found as the product of the monomer size and the swelling ratio between hydrated and dry states, raised to a characteristic value of the polymer[10].

Gravimetric analysis can be used to determine the mass of substrate before and after coating to estimate the grafting density[95]. For density estimation, total polymer mass immobilized is measured and total surface is known. From these values, and the known monomer molecular weight, total monomers per unit area can be calculated, if degree of

polymerization is known or estimated. All techniques require knowledge of some input parameters such as degree of polymerization which ultimately require the removal of tethered polymers for precise chromatographic analysis for true grafting density calculations[96]. Degree of polymerization can be estimated from solution phase polymers synthesized concurrently but this has been shown to provide a poor estimate of surface polymer size and dispersity[97].

A variety of microscopy techniques can also be used to determine film thickness and polymer density, such as SEM/TEM, AFM, and fluorescent light microscopy (when coupled with suitable polymer chemistries)[98]. Electron microscopy has been used to determine the cross-sectional thickness of the polymer film itself, following amenable sample preparation[99], and also has been used in tandem with wrinkling substrates to characterize the layer thickness, given known stiffness parameters[100,101]. Electron microscopy can also be coupled with EDS to measure material elemental composition and bonding to verify polymer layer composition. Contact based microscopy techniques such as AFM (and profilometry) can also characterize polymer layer thickness, and thickness gradients, given that substrates have uncoated control regions[99]. Finally, fluorescence-based microscopy, has been used in tandem with fluorescently labeled polymer coatings, and drop cast polymer film calibration curves, to quantify grafted film density[34,102].

1.6.2. Surface sensitive techniques

Chemical composition of polymer overlayers can be determined by spectroscopic methods such and X-ray photoelectron spectroscopy (XPS) and Fourier-transform

infrared spectroscopy (FTIR), and surface energy determined by water contact angle (WCA). XPS with a penetration depth of 5 – 10 nm is able to discriminate between polymer thin films and the underlying material, determining layer thickness, and can determine both elemental composition and chemical binding data of polymers[103,104]. Attenuated total reflection – Fourier-transform infrared spectroscopy (ATR-FTIR) can probe surface depths of up to several microns, providing both chemical binding data and also layer thickness information, if calibrated with other techniques such as AFM[105]. WCA is a measurement of the wettability property of a material and sensitive to the very topmost layer of the material. The WCA can provide important insight into the eventual function of the material as it is an aggregate measure of the composition, functional groups, and topography compared to other methods above[99].

1.6.3. Fouling characterization techniques

1.6.3.1. Nonspecific protein adsorption

Nonspecific protein adhesion is measured by either direct detection of protein on a surface through modification of surface plasmon resonance (SPR)[12] or quartz crystal microbalance (QCM)[19] sensing surfaces, or through modifying proteins to produce a signal such as with radioactive[106] or fluorescent tags[107]. Fluorescently tagged and radiolabeled fouling assays are conducted with simple mixtures of protein which generally produce lower fouling than complex protein mixtures of biological relevance such as whole blood or serum[108]. Non-tagged techniques such as SPR and QCM have been used to determine fouling levels of modified gold and silicon surfaces respectively.

These techniques can directly compare fouling levels between single proteins (such as bovine serum albumin (BSA)) to complex biological media. Unfortunately, these techniques necessitate the modification of specific materials required for these techniques, which while commonly modified materials[8], restricts the application of these methods to a wide variety of surfaces.

Several quantitative methods are commonly employed to measure protein adsorption on antifouling coatings using sensors, planar surfaces or detection labels and reagents. Due to differences in detection, fouling results from different techniques and methods must be carefully examined before comparison. Each technique will introduce deviations in experimental parameters that influence fouling levels such as concentration, flow, temperature, and time. Furthermore, many techniques use sensors or surfaces that are coated with antifouling materials, grafting efficiency will therefore further introduce variability. Additionally, it has recently been shown that minor deviations during sample preparation for characterization techniques can also impact fouling levels [109]. To overcome these differences in sample preparation, as well as reduce variability between samples, several techniques for characterizing antifouling coatings have been extended to high throughput screening (HTS)[110–112]. Finally, even if pooled whole blood sources are used to attempt to minimize variation from protein source and allow comparisons, there still exists significant differences from pool to pool on identical materials, where even relative levels between materials change, leading to different conclusions of which material is best[113].

Several of these methods provide quantitative data without the need for fluorescent or radioactive labels, allowing for biofouling characterization with a wide variety of proteins and complex biofluids (**Table 1.3**). Whereas techniques that require fluorescent or radioactive labels on proteins are generally limited to biofouling experiments with individual proteins.

1.6.3.2. SPR and QCM-D

Surface plasmon resonance (SPR) allows for the characterization of antifouling surface coatings, usually polymeric films, with unmodified protein solutions and complex biofluids; SPR signal increases with protein adsorption allowing real-time measurements. SPR is limited to characterizing films that can be synthesized from or grafted to the sensor's gold surface; the immobilized coating must be compatible with flow conditions of the SPR microfluidics. Generally, SPR's limit of detection is reported around 0.3 ng cm^{-2}, which is above the fouling limit of several reported antifouling surfaces, making comparisons difficult for very lower-fouling materials[114]. Furthermore, the calculation of total protein nonspecifically adsorbed relies on calibration standards that assume saturated monolayers of model proteins[115].

Quartz crystal microbalance with dissipation monitoring (QCM-D) is less sensitive (1.8 ng cm^{-2})[116] than SPR but offers greater variety of sensor surface chemistry, with metallic and polymeric coatings commercially available for functionalization. The added complexity of QCM-D data compared to SPR affords additional capabilities providing insight into the adsorbed protein layer's mechanical properties[117]. Furthermore,

the sensitivity of QCM-D sensors to changes in the viscoelastic properties of overlayers can be used to characterize changes in cellular dynamics once adhered to a surface of interest[118]. Similar to SPR, antifouling coatings must be compatible with QCM-D's microfluidic system, and coating thickness may hinder protein adsorption within the detection volume of the sensor[119]. Unique to QCM-D sensors, the viscosity and thickness of anti-fouling polymer brush layers on QCM-D sensors are known to influence fouling results.

1.6.3.3. Ellipsometry

Ellipsometry is a light-based method used to measure film thickness by variations in reflected polarized light and can detect protein adsorption down to 5 ng cm^{-2} with a large array of available surface chemistries for coatings[120]. Unlike SPR and QCM-D, ellipsometry does not require flow conditions but sensors must be made from reflective materials for sample characterization in liquid or air. The technique is routinely employed to characterize the modification of materials with polymer overlayers. Ellipsometry measurements can determine adsorbed protein film thickness and mass from refractive index and thickness values[121]. Ellipsometry has also been combined with other methods, such as QCM-D to provide richer protein adsorption data. On a nanopillar surface, ellipsometry models in conjunction with QCM-D were used to distinguish between fibronectin adsorbed to the tops or in between nanopillars to elucidate how location of adsorbed protein impacts cell adhesion[122].

1.6.3.4. AFM

Atomic force microscopy (AFM) can image proteins adsorbed on surfaces, providing protein conformation information. On flat surfaces, cell adhesion and spreading has also been characterized by AFM. For example, AFM was used to determine the conformation of nonspecifically adsorbed IgG, and its impact on *S. epidermidis* adhesion[123]. The conformation of BSA adsorbed onto surfaces with physiosorbed or covalently bound RGD peptide was also deduced by AFM to demonstrate that BSA conformation is maintained in "ECM like environments"[124].

Not all antifouling materials are amenable to characterization methods utilizing planar sensor surfaces, as described in section above. For example, the material may not be amenable to surface grafting or important material properties such stiffness and surface structures may not be recapitulated on the sensor surface. The following techniques are routinely employed to quantify protein adsorption without planar sensor surfaces. These techniques offer greater experimental flexibility and detection specificity but also require the careful selection of controls to ensure results can be accurately interpreted (**Table 1.3, Table 1.4**).

1.6.3.5. Methods for characterizing unlabeled proteins

1.6.3.5.1. Extraction of adsorbed protein for quantification

After materials are exposed to protein solutions or biological fluids, unlabeled proteins are removed from the surface of interest with a detergent compatible with total protein detection assay such as sodium dodecyl sulfate[125–127]. For example, the bicinchoninic acid (BCA) assay detects protein peptide bonds and has been used for

adsorbed protein quantification on a variety of biomaterials, with detection levels of ~ μg cm^{-2}. The absorbance signal produced by the BCA assay is amino acid dependent, calibration curves should therefore be prepared with proteins of interest[128].

Methods requiring extraction of adsorbed proteins are limited by the fact that most detergents do not quantitatively remove all proteins from surfaces[129]. Therefore, assays usually report values relative to positive controls; calibrations curves can estimate adsorbed protein amounts, assuming near quantitative removal[130]. The use of detergents prevents the investigation of adsorbed protein conformation, or bioactivity.

1.6.3.5.2. ELISA: Detecting adsorbed proteins

Enzyme-linked immunosorbent assays (ELISA) can be used to measure proteins nonspecifically adsorbed to surfaces, blood complement activation, and proteins produced by adhered cells. ELISAs detect surface adsorbed proteins, which act as the capture layer. Generally, ELISAs are limited to detecting a single adsorbed protein; ELISAs are therefore suitable for fouling experiments using a simple protein solution (i.e., fibronectin solution) or a biofluid to detect a specific protein's adsorption from a complex mixture (i.e., fibrinogen adsorption from blood).

ELISA can provide adsorbed protein conformation and bioactivity information. ELISAs have been used to measure adsorbed fibronectin bioactivity, which is advantageous over total protein measurements that cannot assess bioactivity[131,132]. ELISAs can also be used to detect potential immune responses. To measure complement

activation due to a hydrogel, an ELISA was used to measure C5b-9 complement activation in serum exposed to material surfaces[133].

ELISA measurements are independent of the substrate material, eliminating the need for proxy surfaces like SPR's gold sensors. When measuring fibrinogen adsorption onto antifouling zwitterionic coatings on planar materials, ELISA and SPR were compared[134]. Upon quantifying fibrinogen adsorption, ELISA indicated greater adsorption than SPR due to differences in polymer grafting density between glass and the SPR gold sensor. Therefore, ELISAs may provide more relevant data for non-gold surfaces.

1.6.3.5.3. LC-MS: Determining adsorbed protein content after extraction

Understanding the types and ratios of adsorbed proteins may provide insight into potential downstream *in vivo* effects and immune responses upon implantation[135]. To profile all adsorbed proteins, liquid chromatography with mass spectrometry (LC-MS) may be employed to provide more information than total protein methods such as BCA. For example, protein adsorption from serum onto surfaces of varying hydrophilicity (water contact angle of 49˚ to 92˚) showed similar total protein levels on all surfaces, but LC-MS determined differences in the types of proteins adsorbed. The same surfaces also displayed different bioactivities, which was demonstrated by tracking cytokine release from macrophages seeded on the biomaterial surface; macrophages released more pro-inflammatory cytokines (tumor necrosis factor alpha (TNF-α), interleukin 6 (IL-6), IL-1b,

interferon gamma-induced protein 10) and less anti-inflammatory cytokines (arginase, IL-10) with increasing surface hydrophobicity[136]. Protein profiling provided key information which total protein characterization could not.

LC-MS protein identification has been used to relate adsorbed proteins on hydrogel implants to the potential FBR capsule formation and thickness. On hydrogels that varied in composition and stiffness, total adsorbed protein amounts did not correlate to FBR capsule thickness. LC-MS analysis of adsorbed proteins 30 minutes after implantation demonstrated that the presence of proteins associated with extracellular matrix construction and cell adhesion were strong predictors of FBR capsule thickness[137].

1.6.3.5.4. Surface sensitive techniques: XPS and ToF-SIMS

Surface sensitive techniques to determine material composition can characterize protein overlayers on biomaterials. Both x-ray photoelectron spectroscopy (XPS) and time of flight secondary ion mass spectrometry (ToF-SIMS) only detect the first ~10 and 2 nanometers respectively of a material[138], making them ideal techniques for quantification of adsorbed material without requiring extraction and collection. Although, substrate composition (e.g. elemental composition overlap with protein) and film thickness impact the sensitivity of both techniques[139]. Film thickness impacts each technique differently as the sampling depth of XPS is deeper than ToF-SIMS, for example, on sodium styrenesulfonate coated and bare gold surfaces exposed to various protein solutions, ToF-SIMS signals saturated before XPS signals of protein adsorption, due to the increased sampling depth of the XPS technique as adsorbed protein overlayers

can be thicker than the ToF-SIMS sampling depth[140]. XPS and ToF-SIMS have been used in conjunction to measure surface chemical composition and protein adsorption levels on gradient polyethylene glycol (PEG) surfaces. The high spatial resolution of the techniques, and ability of both to detect protein in situ allowed for correlation between adsorbed protein and surface polymer density without requiring multiple sample surfaces[141].

1.6.3.6. Methods for quantifying adsorbed proteins modified with detection labels

Quantification of fluorescent or radioactive protein is easily achieved using the corresponding instrumentation with standards for calibration; labelled proteins have improved limits of detection when compared to absorbance-based protein quantification methods (**Table 1.3**). Labels may limit fouling studies to individual proteins and alter protein properties such a hydrophobicity and bioactivity. Generally, *in vitro* fouling assays with labeled protein are carried out below physiological concentrations without competing proteins, which may poorly predict *in vivo* performance. Therefore, fluorescent, and radioactive labels offer greater sensitivity but current experimental design for fouling experiments may not always mimic *in vivo* conditions.

1.6.3.6.1. Fluorescent labels

Because of their high sensitivity, fluorescently labeled proteins are commonly used to characterize nonspecific protein adsorption to surfaces. Quantification of

adsorbed fluorescent proteins is regularly performed by fluorescence microscopy or protein extraction for solution fluorescent measurements.

Fluorescent techniques can also provide information about protein folding, orientation, and reversibility of nonspecific adsorption at single molecule binding resolution. Using fibronectin with fluorescence resonance energy transfer (FRET) labels, residence time and folding state of adsorbed protein was determined on different polymeric PEG surfaces. Fibronectin's adsorption rate decreased with higher PEG density but surface residence time increased due to more protein unfolding[142]; greater residence time with higher PEG densities has not been observed with unlabeled proteins. Fluorescein, a commonly used fluorescent label, was shown to change the orientation of adsorbed lysozyme on surfaces in a modeling study[143]. FRET pairs have also been used to confirm conformation of surface adsorbed protein[142]. Single molecule resolution TIRF for Alexa Fluor 647 labeled BSA and fibrinogen fouling on PEG surfaces determined that nonspecific adsorption was reversible. Fouling was also inversely correlated to protein concentration on PEG surfaces, where ~1 μg mL^{-1} BSA and fibrinogen solutions resulted in fouling whereas the use 1 mg mL^{-1} solutions yielded surfaces with no detectable protein[144]. The authors proposed that increased protein concentrations near the material surface could stabilize protein conformation and decrease the likelihood of proteins denaturing on the surface leading to lower fouling levels at the higher concentration.

Fluorescent labels can also alter protein properties that may influence adsorption degrees. For example, fluorescent labeling has been shown to influence the protein's isoelectric point (by ~ 0.1), size, and charge[145]. Characterization via single-labelled

fluorescent proteins does not provide information on protein conformation or orientation and is limited to simple protein solutions, the use of biofluids is difficult due to labelling differences within the large protein population.

1.6.3.6.2. Radioactive labels

In contrast to fluorescent tags, radioactive labels can be introduced during protein expression with a radioactive amino acid or by covalently grafting a small tag. Due to high sensitivity, radio-tagged protein assays have detection limits as low as 0.05 ng cm^{-2}.[146] While grafting small radiolabels has minor impacts on protein properties, oxidizing conditions used in many labelling reactions can result in protein aggregation and degradation, resulting in greater protein adsorption over unlabeled proteins[147]. Radio labels are typical used to measure total adsorption of an individual protein, and do not provide information about protein conformation or orientation.

1.6.3.6.3. Coated AFM: Modified tips for selective protein detection

Protein coated AFM tips can quantify adhesive forces between individual adsorbed proteins and biomaterials, which can impact cell adhesion outcome. Fibronectin coated AFM in concert with fluorescently labelled proteins can be used to correlate total protein adsorption (via fluorescence) and adhesive forces to surfaces; a strong linear relationship between single protein adhesive strength and total protein adsorption is usually observed[148]. In conjunction with ELISA, AFM can be used to measure protein adsorption force to multiple surface chemistries and protein conformation. Fibronectin coated AFM also demonstrated that the strength of protein material interactions

determines cell fate. Stronger interactions between fibronectin and materials led to decreased cell viability by hindering matrix remodelling[149].

1.6.3.7. Cell-adhesion

Cells in biological media can also nonspecifically adhere at interfaces. Most surfaces which resist protein adsorption, also resist cell adhesion, though some counter examples exist, such as pHEMA[150,151]. To determine nonspecific cell adhesion, microscopy of stained cells can be performed following incubation with the material of interest, which provides information on total number of cells adhered as well as their morphology, other methods of include biochemical marker assays and cell removal and subsequent culturing[152]. Also, cell type influences adhesion with size and cell stiffness causing differences in adhesion between eukaryotic and bacterial cell adhesion[14,153].

For biomaterials that will be exposed to cells, quantifying cell adhesion and activity is necessary as protein adsorption does not necessarily correlate with downstream cellular activities; even when protein adsorption is below detection limits, cells have been shown to interact with surfaces.

Antifouling materials are generally designed to prevent or minimize cell adhesion, but cell adhesion can be advantageous for some medical implants. For example, adhesion of cells associated with anti-inflammatory pathways may improve biomaterial outcomes, and cell integration is necessary for dental and joint replacements. Although, cellular interactions with biomaterials should be studied to avoid deleterious immune responses for most medical implants.

1.6.3.7.1. Quantifying mammalian cell fouling

Interactions between mammalian cells and biomaterials are routinely characterized by: 1) detection of the adhered cells through microscopy or metabolic activity; and, 2) detection of signals produced by cells (i.e. adhesins or cytokines; **Table 1.3, Table 1.4**). These methods are complimentary and together can provide detailed information regarding biomaterial fouling and potential immune outcomes. *In vitro* methods to recapitulate the full *in vivo* immune response remain an active area of research[154].

Adhered cells are commonly characterized by microscopy to determine cell number, morphology, elongation and spreading, which can all be related to cell bioactivity. For example cell morphology has been linked to macrophage phenotype, with elongated cells exhibiting anti-inflammatory properties[155]. SEM and fluorescence microscopy have also been used to quantify cell elongation and spreading on grooved surface, which correlated with cytokine profiles[155]. To study interactions between topographical surfaces with cells, a method combining focused ion beam and SEM (FIB-SEM) was developed to determine cell adhesion preferences and morphologies as a function of nanostructures. Cells were found to preferentially bind to protrusions over pores by visualizing adhesion points[156].

Biochemical techniques used in concert with microscopy can find trends between bioactivity and cell number or morphology. ELISA assessment of IL-6 and TNF-α with fluorescent microscopy demonstrated that macrophage adhesion on fibronectin coated

surfaces correlated with a low inflammatory activation state; FRET experiments indicated that cells on surfaces with stabilized fibronectin had low inflammatory cytokine profiles[157]. Interestingly, unfolded adsorbed fibronectin promoted a pro-inflammatory state, indicating the need to study protein stability and not just total amounts.

The treatment and preparation of materials before cell adhesion assays can impact cell adhesion outcomes; pre-exposing biomaterial surfaces to proteins prior to cell assay impacts cell density and spreading[137]. For example, protein choice during pre-exposure impacted the adhesion and spreading of human fibroblasts on polymer coated titanium surfaces; BSA did not significantly influence cell adhesion or spreading unlike fibrinogen, which promoted adhesion and spreading[158].

1.6.3.7.2. High throughput methods to measure macrophage adhesion and activation

To minimize pro-inflammatory polarization of immune cells, implantable biomaterials are now being designed to promote anti-inflammatory polarizations. To this end, a high-throughput method for nonspecific protein adsorption alongside macrophage adhesion and polarization, a component of inflammation[159], was developed using microprinted polymer spot arrays[160]. Polymer spot microarrays were assayed for cell attachment and macrophage polarization by microscopy and calprotectin/mannose receptor staining. High-throughput screening hits were then subjected to more rigorous screens for cytokine profile and phagocytic ability of macrophages as well as mass spectrometry of adsorbed proteins from fetal bovine serum (FBS).

1.6.3.8. Bacterial fouling related to medical implants

Resistance of material surfaces to bacterial colonization is commonly pursued through two main strategies of 1) adhesion resistance and 2) active killing. Adhesion resistance strategies prevent bacteria from adhering and eventually forming biofilms, usually through methods that repel protein and host cell adhesion. In active killing strategies, surfaces may kill settled bacteria on contact through chemical or physical means, or the release antibacterial agents[161]. Methods of testing *in vitro* bacterial fouling have been well reviewed recently[162–165].

When measuring the resistance of a biomaterial to bacterial adhesion and biofilm formation, the environment of the intended implant location should be replicated. The implant site will also guide the selection of bacteria strain to investigate. Implant sites also vary in shear forces from fluid flow, immune environments, and host cell-bacteria interactions[166] (**Table 1.2**). For example, two antifouling surfaces with similar resistance to fibrinogen adsorption showed drastically different biofilm formation when exposed to the *P. aeruginosa* due to differences in flow conditions; under static conditions, no biofilm was observed after 6 months[167], whereas biofilms formed after just 10 days under flow conditions[134].

Table 1.2: Primary bacterial infections and conditions by implant site.

Implant site	Primary bacterial infection	Shear rate (s^{-1})	Fluid type	REF
Ocular surface	*P. aeruginosa* / *S. epidermidis*	0.35	Tears	[168,169]

	Urinary tract	*P. aeruginosa*	15	Urine	[170,171]
	Bone	*S. aureus* / CoNS	---	---	[172]
	Spinal column	Early *S. aureus,* Late *P. acnes*	---	---	[173]
	Peritoneal cavity	*S. epidermidis / S. aureus*	20 - 120	CSF	[174,175]
Vascular	**TIVAP**	< 30 d - *S. aureus* Total - CoNS	10 - 1000[176]	Blood	[177]
	Vascular graft	Early CoNS, Late *S. aureus / E. coli*			[178]
	PICC / CVC	CoNS			[179]

CoNS = Coagulase negative staphylococci, CSF = Cerebrospinal fluid, TIVAP = Totally implantable venous access port, PICC = Peripherally inserted central venous catheter, CVC = Central venous catheter. Early = < 3 months after surgery, Late = >3 months after surgery.

Table 1.3: Advantages and limitations of commonly employed techniques to characterize protein adsorption and cell adhesion.

	Technique	**Advantages**	**Limitations**	**Label required**	**LOD**	**Ref**
Protein adsorption	**SPR**	Good detection limit	Substrate must be planar, thin coatings, limited sensors options	-	**0.3 ng cm^{-2}**	[114]
	QCM-D	Good detection limit, sensitivity to viscoelasticity	Planar, thin materials, stringent substrate materials	-	**1.8 nm cm^{-2}**	[116]
	Ellipsometry	Good detection limit	Specific material requirements	-	**0.1 nm[a] / 5 ng cm^{-2}**	[180]

TIRF	Single molecule, time dynamic	Planar, label required, low concentration limit	+	---	144
XPS	Elemental and bonding information	Qualitative, presence of high background signals in common polymeric materials (e.g., nitrogen)	-	**10 – 200 ng cm^{-2}**	139
ToF-SIMS	Good detection limit, high spatial resolution	Limited sampling depth	-	**0.1 – 49 ng cm^{-2}**	139,181
Total protein assay (BCA)	Affordable	Requires detergents, large surface areas	**-**	**0.5 ug mL^{-1}**	182
ELISA	Protein type specific, orientation information	Expensive, time consuming,	**-/+**	**0.5 – 5 ng cm^{-2}**	183
LC-MS	Protein specific information	High cost	**-**	**1 pg mL^{-2} / 2 – 4 pmol mm^{-2}**	184,185
Coated AFM	Quantitative adhesion force	Tip labeling/modification with proteins is required	**-**	**10 pN**	186
Fluorescent labeling	Affordable, quantitative	Simple protein mixtures	+	**1 ng cm^{-2}**	187
Radio labeling	Quantitative, good detection limit, small label size	Handling, accessibility	+	**0.05 ng cm^{-2}**	146

Cell adhesion	**Visible light microscopy**	Common instrumentation, cell geometry (ex. spreading, elongation)	Rudimentary data provided	**-/+**	**~0.3 µm**	188
	SEM	Direct adhesion visualization	Low throughput, sample prep	**-**	**10 nm**	156

Label required (+), label free (-). LOD = limit of detection, SPR = surface plasmon resonance, QCM-D = quartz crystal microbalance with dissipation monitoring, TIRF = total internal reflection fluorescence microscopy, XPS = x-ray photoelectron spectroscopy, ToF-SIMS = time of flight secondary ion mass spectrometry ELISA = enzyme linked immunosorbent assay, LC-MS = liquid chromatography-mass spectrometry, AFM = atomic force microscopy, SEM = scanning electron microscopy. [a] = thickness of overlayer.

Table 1.4: Techniques for the characterization of biological responses to biomaterial surfaces.

Biological response	Technique	Advantages	Limitations	Ref
Thrombogenesis	ELISA, Optical density	Recapitulates blood response	Impacted by blood source, storage and test set up	189
Platelet activation	ELISA, microscopy	Recapitulates blood response	Impacted by blood source, storage and test set up. Expensive detection.	189
Macrophage activation / polarization	ELISA, microscopy	Relevance to *in vivo* outcomes	M1-M2 classification may be too simplistic	159,190
Biofilm formation	Surface culture, microscopy	Relevant, challenging endpoint	Variable with strain and environment	162

1.7. Conclusion and outlook

Nonspecific interactions at the interface of materials and biological systems still lead to poor outcomes. Efforts to reduce these deleterious interactions have made great progress, with materials being discovered that can last months *in vivo* without eliciting a

FBR[191] and polymer thin films regularly being reported resisting protein and bacterial attachment *in vitro*[12,167]. Limitations still exist for these materials, as the most promising *in vitro* coatings have not translated into the most effective implanted materials[192] and currently commercially applied PEG has now led to some immune responses[193,194]. Further, there is a need for simpler routes to the fabrication of these films, as in real world applications, the complexity of medical devices means that simpler techniques outperform more complex ones[195]. Therefore, the primary objective of this thesis is to derive new, simple, and biocompatible methods to fabricate these coatings, using state of the art monomers.

1.8. Thesis Objectives

The objective of this thesis was to advance the fields of antifouling, bioactive, romantic polymeric coatings for implanted biomaterial and biosensor applications. To this end, we aimed to extend the repertoire of simplified methods available to create polymer thin films to improve the antifouling properties of biomedical devices. This was achieved by establishing new fabrication methods to enhance bimodal graft-from, and graft-to surfaces for applications in label-free sensors and medical devices as outlined in the specific objectives below. The objectives represent significant advancements towards overcoming the important unmet need of translatable romantic surfaces to enable controlled biomaterial interactions. Bimodal polymer architectures have the potential to greatly increase the sensitivity of romantic biosensors, and so simplified and metal free methods are necessary for their production to maximize translatability. Stretchable and responsive plastics and elastomers are common medical materials, so a scalable,

composition agnostic method for producing high density polymer films thereupon is of interest. LSPR active materials are a promising class of biosensor platform as they allow simple optical setups for their use, and so a method for producing romantic LSPR biosensors is important.

With these goals, and the guiding principle of simple and translatable methods underlying the research, three objectives were achieved, as follows:

(1) Establish one-pot, metal-free graft-from RAFT polymerization for antifouling bimodal polymeric surfaces with enhanced bioactivity (Chapter 2),

(2) Create a method for fabricating and improving antifouling surfaces using a scalable grafting-to protocol by applying the grafting-to method to shrinkable substrates (Graft-then-Shrink; Chapter 3 & 4),

(3) Apply these methods to create antifouling, label-free sensors by developing a LSPR biosensor surface, onto which the graft-then-shrink method was used to a produce a functional, antifouling sensor in one step (Chapter 3).

1.9. References

(1) Vaisocherová, H.; Šípová, H.; Víšová, I.; Bocková, M.; Špringer, T.; Laura Ermini, M.; Song, X.; Krejčík, Z.; Chrastinová, L.; Pastva, O.; Pimková, K.; Dostálová Merkerová, M.; Dyr, J. E.; Homola, J. Rapid and Sensitive Detection of Multiple MicroRNAs in Cell Lysate by Low-Fouling Surface Plasmon Resonance Biosensor. *Biosens. Bioelectron.* **2015**, *70*, 226–231. https://doi.org/10.1016/j.bios.2015.03.038.

(2) Vaisocherová-Lísalová, H.; Víšová, I.; Ermini, M. L.; Špringer, T.; Song, X. C.; Mrázek, J.; Lamačová, J.; Scott Lynn, N.; Šedivák, P.; Homola, J. Low-Fouling Surface Plasmon Resonance Biosensor for Multi-Step Detection of Foodborne Bacterial Pathogens in Complex Food Samples. *Biosens. Bioelectron.* **2016**, *80*, 84–90. https://doi.org/10.1016/j.bios.2016.01.040.

(3) Wang, J.; Hui, N. Zwitterionic Poly(Carboxybetaine) Functionalized Conducting Polymer Polyaniline Nanowires for the Electrochemical Detection of Carcinoembryonic Antigen in Undiluted Blood Serum. *Bioelectrochemistry* **2019**, *125*, 90–96. https://doi.org/10.1016/j.bioelechem.2018.09.006.

(4) Liu, N.; Hui, N.; Davis, J. J.; Luo, X. Low Fouling Protein Detection in Complex Biological Media Supported by a Designed Multifunctional Peptide. *ACS Sensors* **2018**, *3*, 1210–1216. https://doi.org/10.1021/acssensors.8b00318.

(5) Baggerman, J.; Smulders, M. M. J.; Zuilhof, H. Romantic Surfaces: A Systematic Overview of Stable, Biospecific, and Antifouling Zwitterionic Surfaces. *Langmuir* **2019**, *35* (5), 1072–1084. https://doi.org/10.1021/acs.langmuir.8b03360.

(6) Sun, F.; Hung, H. C.; Sinclair, A.; Zhang, P.; Bai, T.; Galvan, D. D.; Jain, P.; Li, B.; Jiang, S.; Yu, Q. Hierarchical Zwitterionic Modification of a SERS Substrate Enables Real-Time Drug Monitoring in Blood Plasma. *Nat. Commun.* **2016**, *7*, 1–9. https://doi.org/10.1038/ncomms13437.

(7) Vishwakarma, A.; Bhise, N. S.; Evangelista, M. B.; Rouwkema, J.; Dokmeci, M. R.; Ghaemmaghami, A. M.; Vrana, N. E.; Khademhosseini, A. Engineering Immunomodulatory Biomaterials To Tune the Inflammatory Response. *Trends Biotechnol.* **2016**, *34* (6), 470–482. https://doi.org/10.1016/j.tibtech.2016.03.009.

(8) Zoppe, J. O.; Ataman, N. C.; Mocny, P.; Wang, J.; Moraes, J.; Klok, H. Surface-Initiated Controlled Radical Polymerization: State-of-the-Art, Opportunities, and Challenges in Surface and Interface Engineering with Polymer Brushes. *Chem. Rev.* **2017**, *117* (3), 1105–1318.

(9) Zdyrko, B.; Luzinov, I. Polymer Brushes by the "Grafting to" Method. *Macromol. Rapid Commun.* **2011**, *32* (12), 859–869. https://doi.org/10.1002/marc.201100162.

(10) Michalek, L.; Barner, L.; Barner-Kowollik, C. Polymer on Top: Current Limits and Future Perspectives of Quantitatively Evaluating Surface Grafting. *Adv. Mater.* **2018**, *30* (21), 1–18. https://doi.org/10.1002/adma.201706321.

(11) Krishnamoorthy, M.; Hakobyan, S.; Ramstedt, M.; Gautrot, J. E. Surface-Initiated Polymer Brushes in the Biomedical Field: Applications in Membrane Science, Biosensing, Cell Culture, Regenerative Medicine and Antibacterial Coatings. *Chem. Rev.* **2014**, *114* (21), 10976–11026. https://doi.org/10.1021/cr500252u.

(12) Yang, W.; Xue, H.; Li, W.; And, J. Z.; Jiang, S. Pursuing "Zero" Protein Adsorption of Poly(Carboxybetaine) from Undiluted Blood Serum and Plasma. *Langmuir* **2009**, *25* (19), 11911–11916. https://doi.org/10.1021/la9015788.

(13) Sundaram, H. S.; Han, X.; Nowinski, A. K.; Brault, N. D.; Li, Y.; Ella-Menye, J. R.; Amoaka, K. A.; Cook, K. E.; Marek, P.; Senecal, K.; Jiang, S. Achieving One-Step Surface Coating of Highly Hydrophilic Poly(Carboxybetaine Methacrylate) Polymers on Hydrophobic and Hydrophilic Surfaces. *Adv. Mater. Interfaces* **2014**,

1 (6), 1–8. https://doi.org/10.1002/admi.201400071.

(14) Graham, M.; Cady, N. Nano and Microscale Topographies for the Prevention of Bacterial Surface Fouling. *Coatings* **2014**, *4* (1), 37–59. https://doi.org/10.3390/coatings4010037.

(15) Escorihuela, J.; Marcelis, A. T. M.; Zuilhof, H. Metal-Free Click Chemistry Reactions on Surfaces. *Adv. Mater. Interfaces* **2015**, *2* (13), 1–42. https://doi.org/10.1002/admi.201500135.

(16) Pujari, S. P.; Scheres, L.; Marcelis, A. T. M.; Zuilhof, H. Covalent Surface Modification of Oxide Surfaces. *Angew. Chemie - Int. Ed.* **2014**, *53* (25), 6322–6356. https://doi.org/10.1002/anie.201306709.

(17) Gabriel, M.; Niederer, K.; Becker, M.; Raynaud, C. M.; Vahl, C. F.; Frey, H. Tailoring Novel PTFE Surface Properties: Promoting Cell Adhesion and Antifouling Properties via a Wet Chemical Approach. *Bioconjug. Chem.* **2016**, *27* (5), 1216–1221. https://doi.org/10.1021/acs.bioconjchem.6b00047.

(18) Pop-Georgievski, O.; Zimmermann, R.; Kotelnikov, I.; Proks, V.; Romeis, D.; Kučka, J.; Caspari, A.; Rypáček, F.; Werner, C. Impact of Bioactive Peptide Motifs on Molecular Structure, Charging, and Nonfouling Properties of Poly(Ethylene Oxide) Brushes. *Langmuir* **2018**, *34* (21), 6010–6020. https://doi.org/10.1021/acs.langmuir.8b00441.

(19) Liu, B.; Liu, X.; Shi, S.; Huang, R.; Su, R.; Qi, W.; He, Z. Design and Mechanisms of Antifouling Materials for Surface Plasmon Resonance Sensors. *Acta Biomater.* **2016**, *40*, 100–118. https://doi.org/10.1016/j.actbio.2016.02.035.

(20) Huang, C.; Brault, N. D.; Li, Y.; Yu, Q.; Jiang, S. Controlled Hierarchical Architecture in Surface-Initiated Zwitterionic Polymer Brushes with Structurally Regulated Functionalities. **2012**, 1834–1837.

(21) Brault, N. D.; Sundaram, H. S.; Huang, C. J.; Li, Y.; Yu, Q.; Jiang, S. Two-Layer Architecture Using Atom Transfer Radical Polymerization for Enhanced Sensing and Detection in Complex Media. *Biomacromolecules* **2012**, *13* (12), 4049–4056. https://doi.org/10.1021/bm301335r.

(22) Huang, C. J.; Li, Y.; Jiang, S. Zwitterionic Polymer-Based Platform with Two-Layer Architecture for Ultra Low Fouling and High Protein Loading. *Anal. Chem.* **2012**, *84* (7), 3440–3445. https://doi.org/10.1021/ac3003769.

(23) Mcalvin, J. B.; Karnik, R.; Kohane, D. S.; Mcalvin, J. B.; Wylie, R. G.; Ramchander, K.; Nguyen, M. T.; Lok, C. K.; Shomorony, A.; Vasilyev, N. V.; Armstrong, P.; Yang, J.; Alexander, M.; Okonkwo, O. S.; Karnik, R.; Kohane, D. S. Antibody-Modified Conduits for Highly Selective Cytokine Elimination from Blood Find the Latest Version : Antibody-Modified Conduits for Highly Selective Cytokine Elimination from Blood. *JCI Insight* **2018**, *3* (13), e121133.

https://doi.org/10.1172/jci.insight.121133.

(24) Sumerlin, B. S.; Lowe, A. B.; Stroud, P. A.; Zhang, P.; Urban, M. W.; McCormick, C. L. Modification of Gold Surfaces with Water-Soluble (Co)Polymers Prepared via Aqueous Reversible Addition-Fragmentation Chain Transfer (RAFT) Polymerization. *Langmuir* **2003**, *19* (14), 5559–5562. https://doi.org/10.1021/la034459t.

(25) Gao, C.; Li, G.; Xue, H.; Yang, W.; Zhang, F.; Jiang, S. Functionalizable and Ultra-Low Fouling Zwitterionic Surfaces via Adhesive Mussel Mimetic Linkages. *Biomaterials* **2010**, *31* (7), 1486–1492. https://doi.org/10.1016/j.biomaterials.2009.11.025.

(26) Lowe, A. B. Thiol-Ene "Click" Reactions and Recent Applications in Polymer and Materials Synthesis: A First Update. *Polym. Chem.* **2014**, *5* (17), 4820–4870. https://doi.org/10.1039/c4py00339j.

(27) Lutz, J. F.; Zarafshani, Z. Efficient Construction of Therapeutics, Bioconjugates, Biomaterials and Bioactive Surfaces Using Azide-Alkyne "Click" Chemistry. *Adv. Drug Deliv. Rev.* **2008**, *60* (9), 958–970. https://doi.org/10.1016/j.addr.2008.02.004.

(28) Barbey, R.; Lavanant, L.; Paripovic, D.; Schüwer, N.; Sugnaux, C.; Tugulu, S.; Klok, H. A. Polymer Brushes via Surface-Initiated Controlled Radical Polymerization: Synthesis, Characterization, Properties, and Applications. *Chem. Rev.* **2009**, *109* (11), 5437–5527. https://doi.org/10.1021/cr900045a.

(29) Feder, J. Random Sequential Adsorption. *J. Theor. Biol.* **1980**, *87* (1), 237–254. https://doi.org/10.1103/PhysRevA.40.422.

(30) Schweigerdt, A.; Heinen, S.; Stöbener, D. D.; Weinhart, M. Grafting Density-Dependent Phase Transition Mechanism of Thermoresponsive Poly(Glycidyl Ether) Brushes: A Comprehensive QCM-D Study. *Langmuir* **2021**, *37* (23), 7087–7096. https://doi.org/10.1021/acs.langmuir.1c00695.

(31) Kingshott, P.; Thissen, H.; Griesser, H. J. Effects of Cloud-Point Grafting, Chain Length, and Density of PEG Layers on Competitive Adsorption of Ocular Proteins. *Biomaterials* **2002**, *23* (9), 2043–2056. https://doi.org/10.1016/S0142-9612(01)00334-9.

(32) Schulze, M.; Adigüzel, S.; Nickl, P.; Schmitt, A. C.; Dernedde, J.; Ballauff, M.; Haag, R. A Simple and Robust Method to Prepare Polyelectrolyte Brushes on Polymer Surfaces. *Adv. Mater. Interfaces* **2022**, *9* (5). https://doi.org/10.1002/admi.202102005.

(33) Genzer, J.; Efimenko, K. Creating Long-Lived Superhydrophobic Polymer Surfaces through Mechanically Assembled Monolayers. *Science (80-.).* **2000**, *290* (5499), 2130–2133. https://doi.org/10.1126/science.290.5499.2130.

(34) Jesmer, A. H.; Huynh, V.; Marple, A. S. T.; Ding, X.; Moran-Mirabal, J. M.; Wylie, R. G. Graft-Then-Shrink: Simultaneous Generation of Antifouling Polymeric Interfaces and Localized Surface Plasmon Resonance Biosensors. *ACS Appl. Mater. Interfaces* **2021**, *13* (44), 52362–52373. https://doi.org/10.1021/acsami.1c14930.

(35) Peng, C. H.; Kong, J.; Seeliger, F.; Matyjaszewski, K. Mechanism of Halogen Exchange in ATRP. *Macromolecules* **2011**, *44* (19), 7546–7557. https://doi.org/10.1021/ma201035u.

(36) Matyjaszewski, K.; Hongchen, D.; Jakubowski, W.; Pietrasik, J.; Kusumo, A. Grafting from Surfaces for "Everyone": ARGET ATRP in the Presence of Air. *Langmuir* **2007**, *23* (8), 4528–4531. https://doi.org/10.1021/la063402e.

(37) Wang, M.; Yuan, J.; Huang, X.; Cai, X.; Li, L.; Shen, J. Grafting of Carboxybetaine Brush onto Cellulose Membranes via Surface-Initiated ARGET-ATRP for Improving Blood Compatibility. *Colloids Surfaces B Biointerfaces* **2013**, *103*, 52–58. https://doi.org/10.1016/j.colsurfb.2012.10.025.

(38) Hong, D.; Hung, H. C.; Wu, K.; Lin, X.; Sun, F.; Zhang, P.; Liu, S.; Cook, K. E.; Jiang, S. Achieving Ultralow Fouling under Ambient Conditions via Surface-Initiated ARGET ATRP of Carboxybetaine. *ACS Appl. Mater. Interfaces* **2017**, *9* (11), 9255–9259. https://doi.org/10.1021/acsami.7b01530.

(39) Krause, J. E.; Brault, N. D.; Li, Y.; Xue, H.; Zhou, Y.; Jiang, S. Photoiniferter-Mediated Polymerization of Zwitterionic Carboxybetaine Monomers for Low-Fouling and Functionalizable Surface Coatings. *Macromolecules* **2011**, *44* (23), 9213–9220. https://doi.org/10.1021/ma202007h.

(40) Yilmaz, G.; Yagci, Y. Photoinduced Metal-Free Atom Transfer Radical Polymerizations: State-of-the-Art, Mechanistic Aspects and Applications. *Polym. Chem.* **2018**, *9* (14), 1757–1762. https://doi.org/10.1039/c8py00207j.

(41) Treat, N. J.; Sprafke, H.; Kramer, J. W.; Clark, P. G.; Barton, B. E.; Read De Alaniz, J.; Fors, B. P.; Hawker, C. J. Metal-Free Atom Transfer Radical Polymerization. *J. Am. Chem. Soc.* **2014**, *136* (45), 16096–16101. https://doi.org/10.1021/ja510389m.

(42) Moad, G.; Rizzardo, E.; Thang, S. H. Living Radical Polymerization by the RAFT Process – A Second Update. *Aust. J. Chem.* **2010**, 4–6.

(43) Willcock, H.; Reilly, R. K. O. End Group Removal and Modification of RAFT Polymers. **2010**, No. November 2009, 149–157.

(44) Li, Y.; Zhang, J.; Fang, L.; Jiang, L.; Liu, W.; Wang, T.; Cui, L.; Sun, H.; Yang, B. Polymer Brush Nanopatterns with Controllable Features for Protein Pattern Applications. *J. Mater. Chem.* **2012**, *22* (48), 25116–25122. https://doi.org/10.1039/c2jm35197h.

(45) Kim, M. S.; Khang, G.; Lee, H. B. Gradient Polymer Surfaces for Biomedical Applications. *Prog. Polym. Sci.* **2008**, *33* (1), 138–164. https://doi.org/10.1016/j.progpolymsci.2007.06.001.

(46) Henze, M.; Mädge, D.; Prucker, O.; Rühe, J. "Grafting through": Mechanistic Aspects of Radical Polymerization Reactions with Surface-Attached Monomers. *Macromolecules* **2014**, *47* (9), 2929–2937. https://doi.org/10.1021/ma402607d.

(47) Krishnan, S.; Weinman, C. J.; Ober, C. K. Advances in Polymers for Anti-Biofouling Surfaces. *J. Mater. Chem.* **2008**, *18* (29), 3405–3413. https://doi.org/10.1039/b801491d.

(48) Tang, Y. W.; Santerre, J. P.; Labow, R. S.; Taylor, D. G. Synthesis of Surface-Modifying Macromolecules for Use in Segmented Polyurethanes. *J. Appl. Polym. Sci.* **1996**, *62*, 1133–1145.

(49) Krishnan, S.; Wang, N.; Ober, C. K.; Finlay, J. A.; Callow, M. E.; Callow, J. A.; Hexemer, A.; Sohn, K. E.; Kramer, E. J.; Fischer, D. A. Comparison of the Fouling Release Properties of Hydrophobic Fluorinated and Hydrophilic PEGylated Block Copolymer Surfaces: Attachment Strength of the Diatom Navicula and the Green Alga Ulva. *Biomacromolecules* **2006**, *7* (5), 1449–1462. https://doi.org/10.1021/bm0509826.

(50) Young, G.; Browers, R.; Hall, B.; Port, M. Clinical Comparison of Omafilcon A with Four Control Materials. *CLAO J.* **1997**, *23* (4), 249–258.

(51) Schlenoff, J. B. Zwitteration: Coating Surfaces with Zwitterionic Functionality to Reduce Nonspecific Adsorption. *Langmuir* **2014**, *30* (32), 9625–9636. https://doi.org/10.1021/la500057j.

(52) Chen, S.; Li, L.; Zhao, C.; Zheng, J. Surface Hydration: Principles and Applications toward Low-Fouling/Nonfouling Biomaterials. *Polymer (Guildf).* **2010**, *51* (23), 5283–5293. https://doi.org/10.1016/j.polymer.2010.08.022.

(53) Brault, N. D.; Sundaram, H. S.; Li, Y.; Huang, C. J.; Yu, Q.; Jiang, S. Dry Film Refractive Index as an Important Parameter for Ultra-Low Fouling Surface Coatings. *Biomacromolecules* **2012**, *13* (3), 589–593. https://doi.org/10.1021/bm3001217.

(54) Chapman, R. G.; Ostuni, E.; Takayama, S.; Holmlin, R. E.; Yan, L.; Whitesides, G. M. Surveying for Surfaces That Resist the Adsorption of Proteins [3]. *J. Am. Chem. Soc.* **2000**, *122* (34), 8303–8304. https://doi.org/10.1021/ja000774f.

(55) Ostuni, E.; Chapman, R. G.; Holmlin, R. E.; Takayama, S.; Whitesides, G. M. A Survey of Structure-Property Relationships of Surfaces That Resist the Adsorption of Protein. *Langmuir* **2001**, *17* (18), 5605–5620. https://doi.org/10.1021/la010384m.

(56) Hower, J. C.; He, Y.; Jiang, S. A Molecular Simulation Study of Methylated and Hydroxyl Sugar-Based Self-Assembled Monolayers: Surface Hydration and Resistance to Protein Adsorption. *J. Chem. Phys.* **2008**, *129* (21). https://doi.org/10.1063/1.3012563.

(57) Shao, Q.; He, Y.; White, A. D.; Jiang, S. Difference in Hydration between Carboxybetaine and Sulfobetaine. *J. Phys. Chem. B* **2010**, *114* (49), 16625–16631. https://doi.org/10.1021/jp107272n.

(58) Yang, Q.; Lai, S. K. Anti-PEG Immunity: Emergence, Characteristics, and Unaddressed Questions. *Wiley Interdiscip. Rev. Nanomedicine Nanobiotechnology* **2015**, *7* (5), 655–677. https://doi.org/10.1002/wnan.1339.

(59) Jiang, S.; Cao, Z. Ultralow-Fouling, Functionalizable, and Hydrolyzable Zwitterionic Materials and Their Derivatives for Biological Applications. *Adv. Mater.* **2010**, *22* (9), 920–932. https://doi.org/10.1002/adma.200901407.

(60) Jin, J.; Han, Y.; Zhang, C.; Liu, J.; Jiang, W.; Yin, J.; Liang, H. Effect of Grafted PEG Chain Conformation on Albumin and Lysozyme Adsorption: A Combined Study Using QCM-D and DPI. *Colloids Surfaces B Biointerfaces* **2015**, *136*, 838–844. https://doi.org/10.1016/j.colsurfb.2015.10.025.

(61) Unsworth, L. D.; Sheardown, H.; Brash, J. L. Protein Resistance of Surfaces Prepared by Sorption of End-Thiolated Poly(Ethylene Glycol) to Gold: Effect of Surface Chain Density. *Langmuir* **2005**, *21* (3), 1036–1041. https://doi.org/10.1021/la047672d.

(62) Unsworth, L. D.; Sheardown, H.; Brash, J. L. Protein-Resistant Poly(Ethylene Oxide)-Grafted Surfaces: Chain Density-Dependent Multiple Mechanisms of Action. *Langmuir* **2008**, *24* (5), 1924–1929.

(63) Herold, D. A.; Keil, K.; Bruns, D. E. Oxidation of Polyethylene Glycols by Alcohol Dehydrogenase. *Biochem. Pharmacol.* **1989**, *38* (1), 73–76. https://doi.org/10.1016/0006-2952(89)90151-2.

(64) Leng, C.; Hung, H. C.; Sun, S.; Wang, D.; Li, Y.; Jiang, S.; Chen, Z. Probing the Surface Hydration of Nonfouling Zwitterionic and PEG Materials in Contact with Proteins. *ACS Appl. Mater. Interfaces* **2015**, *7* (30), 16881–16888. https://doi.org/10.1021/acsami.5b05627.

(65) Zhang, Z.; Chao, T.; Chen, S.; Jiang, S. Superlow Fouling Sulfobetaine and Carboxybetaine Polymers on Glass Slides. *Langmuir* **2006**, *22* (24), 10072–10077. https://doi.org/10.1021/la062175d.

(66) Schönemann, E.; Koc, J.; Aldred, N.; Clare, A. S.; Laschewsky, A.; Rosenhahn, A.; Wischerhoff, E. Synthesis of Novel Sulfobetaine Polymers with Differing Dipole Orientations in Their Side Chains, and Their Effects on the Antifouling Properties. *Macromol. Rapid Commun.* **2020**, *41* (1).

https://doi.org/10.1002/marc.201900447.

(67) Rodriguez-emmenegger, C.; Schmidt, B. V. K. J.; Alles, A. B.; Brynda, E.; Sedlakova, Z.; Vladimir, S.; Barner-kowollik, C. Low Temperature Aqueous Living / Controlled (RAFT) Polymerization of Carboxybetaine Methacrylamide up to High Molecular Weights A. **2011**, 958–965.

(68) Cao, B.; Li, L.; Tang, Q.; Cheng, G. The Impact of Structure on Elasticity, Switchability, Stability and Functionality of an All-in-One Carboxybetaine Elastomer. *Biomaterials* **2013**, *34* (31), 7592–7600. https://doi.org/10.1016/j.biomaterials.2013.06.063.

(69) Cao, B.; Tang, Q.; Cheng, G. Recent Advances of Zwitterionic Carboxybetaine Materials and Their Derivatives. *J. Biomater. Sci. Polym. Ed.* **2014**, *25* (14–15), 1502–1513. https://doi.org/10.1080/09205063.2014.927300.

(70) Lange, S. C.; Van Andel, E.; Smulders, M. M. J.; Zuilhof, H. Efficient and Tunable Three-Dimensional Functionalization of Fully Zwitterionic Antifouling Surface Coatings. *Langmuir* **2016**, *32* (40), 10199–10205. https://doi.org/10.1021/acs.langmuir.6b02622.

(71) Hu, G.; Emrick, T. Functional Choline Phosphate Polymers. *J. Am. Chem. Soc.* **2016**, *138* (6), 1828–1831. https://doi.org/10.1021/jacs.5b13156.

(72) Dobrynin, A. V.; Colby, R. H.; Rubinstein, M. Polyampholytes. *J. Polym. Sci. Part B Polym. Phys.* **2004**, *42* (19), 3513–3538. https://doi.org/10.1002/polb.20207.

(73) McCormick, C. L.; Brent Johnson, C. Water-Soluble Polymers. 28. Ampholytic Copolymers of Sodium 2-Acrylamido-2-MethyIpropanesulfonate with (2-Acrylamido-2-Methylpropyl)Dimethylammonium Chloride: Synthesis and Characterization. *Macromolecules* **1988**, *21* (3), 686–693. https://doi.org/10.1021/ma00181a025.

(74) Cheng, G.; Chen, S.; Jiang, S.; Bernards, M. T.; Zhang, Z. Nonfouling Polymer Brushes via Surface-Initiated, Two-Component Atom Transfer Radical Polymerization. *Macromolecules* **2008**, *41* (12), 4216–4219. https://doi.org/10.1021/ma800185y.

(75) Maan, A. M. C.; Hofman, A. H.; de Vos, W. M.; Kamperman, M. Recent Developments and Practical Feasibility of Polymer-Based Antifouling Coatings. *Adv. Funct. Mater.* **2020**, *30* (32), 2000936. https://doi.org/10.1002/adfm.202000936.

(76) Jahangir, A. R.; Mcclung, W. G.; Cornelius, R. M.; Mccloskey, C. B.; Brash, J. L.; Santerre, J. P. Fluorinated Surface-Modifying Macromolecules: Modulating Adhesive Protein and Platelet Interactions on a Polyether-Urethane. **2001**. https://doi.org/10.1002/jbm.10033.

(77) Bandyopadhyay, S.; Jones, A.; McLean, A.; Sterner, M.; Robbins, C.; Cunningham, M.; Walters, M.; Doddapaneni, K.; Keitel, I.; Gallagher, C. Slippery Liquid Infused Fluoropolymer Coating for Central Lines to Reduce Catheter Associated Clotting and Infections. *Sci. Rep.* **2020**, *10*, 14973. https://doi.org/10.1038/s41598-020-71711-6.

(78) Wong, T.; Kang, S. H.; Tang, S. K. Y.; Smythe, E. J.; Hatton, B. D.; Grinthal, A.; Aizenberg, J. Bioinspired Self-Repairing Slippery Surfaces with Pressure-Stable Omniphobicity. *Nature* **2011**, *477* (7365), 443–447. https://doi.org/10.1038/nature10447.

(79) Bonin, C.; Yang, M.; Ernsting, M. J.; Labow, R. S.; Santerre, J. P. Generation of Cell Adhesive Substrates Using Peptide Fluoralkyl Surface Modifiers. **2005**, *26*, 6536–6546. https://doi.org/10.1016/j.biomaterials.2005.04.047.

(80) Yi, L.; Xu, K.; Xia, G.; Li, J.; Li, W.; Cai, Y. New Protein-Resistant Surfaces of Amphiphilic Graft Copolymers Containing Hydrophilic Poly(Ethylene Glycol) and Low Surface Energy Fluorosiloxane. *Appl. Surf. Sci.* **2019**, *480* (February), 923–933. https://doi.org/10.1016/j.apsusc.2019.03.042.

(81) Xu, B.; Liu, Y.; Sun, X.; Hu, J.; Shi, P.; Huang, X. Semi Fluorinated Synergistic Nonfouling/Fouling-Release Surface. *ACS Appl. Mater. Interfaces* **2017**, *9*, 16517–16523. https://doi.org/10.1021/acsami.7b03258.

(82) Kirillova, A.; Marschelke, C.; Friedrichs, J.; Werner, C.; Synytska, A. Hybrid Hairy Janus Particles as Building Blocks for Antibiofouling Surfaces. *ACS Appl. Mater. Interfaces* **2016**, *8*, 32591–32603. https://doi.org/10.1021/acsami.6b10588.

(83) Rahmati, M.; Silva, E. A.; Reseland, J. E.; Heyward, C. A.; Haugen, H. J. Biological Responses to Physicochemical Properties of Biomaterial Surface. *Chem. Soc. Rev.* **2020**, 1–47. https://doi.org/10.1039/d0cs00103a.

(84) Yeung, T.; Georges, P. C.; Flanagan, L. A.; Marg, B.; Ortiz, M.; Funaki, M.; Zahir, N.; Ming, W.; Weaver, V.; Janmey, P. A. Effects of Substrate Stiffness on Cell Morphology , Cytoskeletal Structure , and Adhesion. *Cell Motil. Cytoskeleton* **2005**, *60*, 24–34. https://doi.org/10.1002/cm.20041.

(85) Miller, C. J.; Davidson, L. A. The Interplay between Cell Signalling and Mechanics in Developmental Processes. *Nat. Rev. Genet.* **2013**, *14*, 733–744. https://doi.org/10.1038/nrg3513.

(86) Nguyen, A. T.; Sathe, S. R.; Yim, E. K. F. From Nano to Micro : Topographical Scale and Its Impact on Cell Adhesion , Morphology and Contact Guidance. *J. Phys. Condens. Matter* **2016**, No. 28, 1–16. https://doi.org/10.1088/0953-8984/28/18/183001.

(87) Wu, Y.; Zitelli, J. P.; Tenhuisen, K. S.; Yu, X.; Libera, M. R. Biomaterials Differential Response of Staphylococci and Osteoblasts to Varying Titanium

Surface Roughness. *Biomaterials* **2011**, *32* (4), 951–960. https://doi.org/10.1016/j.biomaterials.2010.10.001.

(88) Anastasaki, A.; Willenbacher, J.; Fleischmann, C.; Gutekunst, W. R.; Hawker, C. J. End Group Modification of Poly(Acrylates) Obtained: Via ATRP: A User Guide. *Polym. Chem.* **2017**, *8* (4), 689–697. https://doi.org/10.1039/c6py01993e.

(89) Grajales, S. Controlled Radical Polymerization Guide. *Aldrich Mater. Sci.* **2012**, 12–14.

(90) Hakobyan, S.; Rzhepishevska, O.; Barbero, D. R.; Ramstedt, M. Functionalization of Zwitterionic Polymer Brushes, Do They Remain Antifouling? *Surf. Interface Anal.* **2018**, No. August 2017, 1–6. https://doi.org/10.1002/sia.6376.

(91) Song, L.; Zhao, J.; Luan, S.; Ma, J.; Liu, J.; Xu, X.; Yin, J. Fabrication of a Detection Platform with Boronic-Acid-Containing Zwitterionic Polymer Brush. *ACS Appl. Mater. Interfaces* **2013**, *5* (24), 13207–13215. https://doi.org/10.1021/am404206v.

(92) Vaisocherová, H.; Yang, W.; Zhang, Z.; Cao, Z.; Cheng, G.; Piliarik, M.; Homola, J.; Jiang, S. Ultralow Fouling and Functionalizable Surface Chemistry Based on a Zwitterionic Polymer Enabling Sensitive and Specific Protein Detection in Undiluted Blood Plasma. *Anal. Chem.* **2008**, *80* (20), 7894–7901. https://doi.org/10.1021/ac8015888.

(93) Gurbuz, N.; Demirci, S.; Yavuz, S.; Caykara, T. Synthesis of Cationic N - [3- (Dimethylamino) Propyl] Methacrylamide Brushes on Silicon Wafer via Surface-Initiated RAFT Polymerization. **2011**, *49*, 423–431. https://doi.org/10.1002/POLA.

(94) Russell, T. X-Ray and Neutron Reflectivity for the Investigation of Polymers. *Mater. Sci. Reports* **1990**, No. June. https://doi.org/10.1016/S0920-2307(05)80002-7.

(95) Akcora, P.; Liu, H.; Kumar, S. K.; Moll, J.; Li, Y.; Benicewicz, B. C.; Schadler, L. S.; Acehan, D.; Panagiotopoulos, A. Z.; Pryamitsyn, V.; Ganesan, V.; Ilavsky, J.; Thiyagarajan, P.; Colby, R. H.; Douglas, J. F. Anisotropic Self-Assembly of Spherical Polymer-Grafted Nanoparticles. *Nat. Mater.* **2009**, *8* (4), 354–359. https://doi.org/10.1038/nmat2404.

(96) Patil, R. R.; Turgman-Cohen, S.; Šrogl, J.; Kiserow, D.; Genzer, J. Direct Measurement of Molecular Weight and Grafting Density by Controlled and Quantitative Degrafting of Surface-Anchored Poly(Methyl Methacrylate). *ACS Macro Lett.* **2015**, *4* (2), 251–254. https://doi.org/10.1021/mz5007188.

(97) Turgman-Cohen, S.; Genzer, J. Simultaneous Bulk- and Surface-Initiated Controlled Radical Polymerization from Planar Substrates. *J. Am. Chem. Soc.* **2011**, *133* (44), 17567–17569. https://doi.org/10.1021/ja2081636.

(98) Coceancigh, H.; Higgins, D. A.; Ito, T. Optical Microscopic Techniques for Synthetic Polymer Characterization. *Anal. Chem.* **2019**, *91*, 405–424. https://doi.org/10.1021/acs.analchem.8b04694.

(99) Walzak, M. J.; Davidson, R.; Biesinger, M. The Use of XPS, FTIR, SEM/EDX, Contact Angle, and AFM in the Characterization of Coatings. *J. Mater. Eng. Perofmrance* **1998**, *7* (3), 317–323.

(100) Stimpson, T. C.; Osorio, D. A.; Cranston, E. D.; Moran-Mirabal, J. M. Direct Comparison of Three Buckling-Based Methods to Measure the Elastic Modulus of Nanobiocomposite Thin Films. *ACS Appl. Mater. Interfaces* **2021**. https://doi.org/10.1021/acsami.1c08056.

(101) Jackson, A. M. S.; Sheiko, S. S.; Ashby, V. S. Grafting Poly(OEGMA) Brushes from a Shape Memory Elastomer and Subsequent Wrinkling Behavior. *Langmuir* **2015**, *31* (19), 5489–5494. https://doi.org/10.1021/la504826w.

(102) Yang, Q.; Jones, S. W.; Parker, C. L.; Zamboni, W. C.; Bear, J. E.; Lai, S. K. Evading Immune Cell Uptake and Clearance Requires PEG Grafting at Densities Substantially Exceeding the Minimum for Brush Conformation. *Mol. Pharm.* **2014**, *11*, 1250–1258.

(103) Mcarthur, S. L. Applications of XPS in Bioengineering. *Surf. Interface Anal.* **2006**, *38*, 1380–1385. https://doi.org/10.1002/sia.

(104) Ton-That, C.; Shard, A. G.; Bradley, R. H. Thickness of Spin-Cast Polymer Thin Films Determined by Angle-Resolved XPS and AFM Tip-Scratch Methods. *Langmuir* **2000**, No. 8, 2281–2284.

(105) Kane, S. R.; Ashby, P. D.; Pruitt, L. A. ATR-FTIR as a Thickness Measurement Technique for Hydrated Polymer-on-Polymer Coatings. *J. Biomed. Mater. Res. Part B Appl. Biomater.* **2009**, *91* (2), 613–620. https://doi.org/10.1002/jbm.b.31436.

(106) Chen, H.; Zhang, Z.; Chen, Y.; Brook, M. A.; Sheardown, H. Protein Repellant Silicone Surfaces by Covalent Immobilization of Poly(Ethylene Oxide). *Biomaterials* **2005**, *26* (15), 2391–2399. https://doi.org/10.1016/j.biomaterials.2004.07.068.

(107) Weinman, C. J.; Gunari, N.; Krishnan, S.; Dong, R.; Paik, M. Y.; Sohn, K. E.; Walker, G. C.; Kramer, E. J.; Fischer, D. A.; Ober, C. K. Protein Adsorption Resistance of Anti-Biofouling Block Copolymers Containing Amphiphilic Side Chains. *Soft Matter* **2010**, *6* (14), 3237–3243. https://doi.org/10.1039/b925114f.

(108) Chen, S.; Ladd, J.; Zhang, Z.; Jiang, S.; Hower, J. C. Zwitterionic Polymers Exhibiting High Resistance to Nonspecific Protein Adsorption from Human Serum and Plasma. *Biomacromolecules* **2008**, *9* (5), 1357–1361. https://doi.org/10.1021/bm701301s.

(109) Visova, I.; Vrabcova, M.; Forinova, M.; Zhigunova, Y.; Mironov, V.; Houska, M.; Dejneka, A.; Bittrich, E.; Eichhorn, K.; Hashim, H.; Schovanek, P.; Vaisocherova-Lisalova, H. Surface Preconditioning Influences the Antifouling Capabilities of Zwitterionic and Nonionic Polymer Brushes. *Langmuir* **2020**. https://doi.org/10.1021/acs.langmuir.0c00996.

(110) Hook, A. L.; Chang, C. Y.; Yang, J.; Luckett, J.; Cockayne, A.; Atkinson, S.; Mei, Y.; Bayston, R.; Irvine, D. J.; Langer, R.; Anderson, D. G.; Williams, P.; Davies, M. C.; Alexander, M. R. Combinatorial Discovery of Polymers Resistant to Bacterial Attachment. *Nat. Biotechnol.* **2012**, *30* (9), 868–875. https://doi.org/10.1038/nbt.2316.

(111) Magennis, E. P.; Hook, A. L.; Davies, M. C.; Alexander, C.; Williams, P.; Alexander, M. R. Engineering Serendipity: High-Throughput Discovery of Materials That Resist Bacterial Attachment. *Acta Biomater.* **2016**, *34*, 84–92. https://doi.org/10.1016/j.actbio.2015.11.008.

(112) Hook, A. L.; Anderson, D. G.; Langer, R.; Williams, P.; Davies, M. C.; Alexander, M. R. High Throughput Methods Applied in Biomaterial Development and Discovery. *Biomaterials* **2010**, *31* (2), 187–198. https://doi.org/10.1016/j.biomaterials.2009.09.037.

(113) Pereira, A. de los S.; Rodriguez-Emmenegger, C.; Surman, F.; Riedel, T.; Alles, A. B.; Brynda, E. Use of Pooled Blood Plasmas in the Assessment of Fouling Resistance. *RSC Adv.* **2014**, *4* (5), 2318–2321. https://doi.org/10.1039/C3RA43093F.

(114) Blaszykowski, C.; Sheikh, S.; Thompson, M. Surface Chemistry to Minimize Fouling from Blood-Based Fluids. *Chem. Soc. Rev.* **2012**, *41*, 5599–5612. https://doi.org/10.1039/c2cs35170f.

(115) Zhang, Z.; Chen, S.; Chang, Y.; Jiang, S. Surface Grafted Sulfobetaine Polymers via Atom Transfer Radical Polymerization as Superlow Fouling Coatings. *J. Phys. Chem. B* **2006**, *110*, 10799–10804. https://doi.org/10.1021/jp057266i.

(116) Edvardsson, M. *Q-Sense E4 Operator Manual*; Q-Sense: Sweden, 2009.

(117) Tonda-turo, C.; Carmagnola, I.; Ciardelli, G. Quartz Crystal Microbalance With Dissipation Monitoring: A Powerful Method to Predict the in Vivo Behavior of Bioengineered Surfaces. *Front. Bioeng. Biotechnol.* **2018**, *6* (158), 1–7. https://doi.org/10.3389/fbioe.2018.00158.

(118) Kushiro, K.; Lee, C.; Takai, M. Simultaneous Characterization of Protein - Material and Cell – Protein Interactions Using Dynamic QCM-D Analysis on SAM Surfaces. *Biomater. Sci.* **2016**, *4*, 989–997. https://doi.org/10.1039/c5bm00613a.

(119) Luan, Y.; Li, D.; Wei, T.; Wang, M.; Tang, Z.; Brash, J. L.; Chen, H. “Hearing

Loss" in QCM Measurement of Protein Adsorption to Protein Resistant Polymer Brush Layers. *Anal. Chem.* **2017**, No. 89, 4184–4191. https://doi.org/10.1021/acs.analchem.7b00198.

(120) Welch, N. G.; Scoble, J. A.; Muir, B. W.; Pigram, P. J. Orientation and Characterization of Immobilized Antibodies for Improved Immunoassays (Review). *Biointerphases* **2017**, *12* (2), 02D301-1. https://doi.org/10.1116/1.4978435.

(121) Hook, F.; Kasemo, B.; Nylander, T.; Fant, C.; Sott, K.; Elwing, H. Variations in Coupled Water, Viscoelastic Properties, and Film Thickness of a Mefp-1 Protein Film during Adsorption and Cross-Linking: A Quartz Crystal Microbalance with Dissipation Monitoring, Ellipsometry, and Surface Plasmon Resonnance Study. *Anal. Chem.* **2001**, *73* (24), 5796–5804. https://doi.org/10.1021/ac0106501.

(122) Kasputis, T.; Pieper, A.; Rodenhausen, K. B.; Schmidt, D.; Sekora, D.; Rice, C.; Schubert, E.; Schubert, M.; Pannier, A. K. Use of Precisely Sculptured Thin Film (STF) Substrates with Generalized Ellipsometry to Determine Spatial Distribution of Adsorbed Fibronectin to Nanostructured Columnar Topographies and Effect on Cell Adhesion. *Acta Biomater.* **2015**, *18*, 88–99. https://doi.org/10.1016/j.actbio.2015.02.016.

(123) Hou, W.; Liu, Y.; Zhang, B.; He, X.; Li, H. Adsorption-Associated Orientational Changes of Immunoglobulin G and Regulated Phagocytosis of Staphylococcus Epidermidis. *J. Biomed. Mater. Res. Part A* **2018**, *106A* (11), 2838–2849. https://doi.org/10.1002/jbm.a.36472.

(124) Pinho, A. C.; Piedade, A. P. Zeta Potential, Contact Angles, and AFM Imaging of Protein Conformation Adsorbed on Hybrid Nanocomposite Surfaces. *ACS Appl. Mater. InterfacesApplied Mater. Interfaces* **2013**, No. 5, 8187–8194. https://doi.org/10.1021/am402302r.

(125) Ju, H.; McCloskey, B. D.; Sagle, A. C.; Kusuma, V. A.; Freeman, B. D. Preparation and Characterization of Crosslinked Poly(Ethylene Glycol) Diacrylate Hydrogels as Fouling-Resistant Membrane Coating Materials. *J. Memb. Sci.* **2009**, *330* (1–2), 180–188. https://doi.org/10.1016/j.memsci.2008.12.054.

(126) Ma, Y.; Bian, X.; He, L.; Cai, M.; Xie, X.; Luo, X. Immobilization of Poly(Acrylamide) Brushes onto Poly(Caprolactone) Surface by Combining ATRP and "Click" Chemistry: Synthesis, Characterization and Evaluation of Protein Adhesion. *Appl. Surf. Sci.* **2015**, *329*, 223–233. https://doi.org/10.1016/j.apsusc.2014.12.149.

(127) Dong, D.; Li, J.; Cui, M.; Wang, J.; Zhou, Y.; Luo, L.; Wei, Y.; Ye, L.; Sun, H.; Yao, F. In Situ "Clickable" Zwitterionic Starch-Based Hydrogel for 3D Cell Encapsulation. *ACS Appl. Mater. Interfaces* **2016**, *8* (7), 4442–4455. https://doi.org/10.1021/acsami.5b12141.

(128) Walker, J. M. *The Protein Protocols Handbook*, 2nd editio.; Humana Press, 1996.

(129) Riedel, T.; Majek, P.; Riedelova-Reicheltola, Z.; Vorobii, M.; Houska, M.; Rodriguez-Emmenegger, C. Total Removal of Intact Blood Plasma Proteins Deposited on Surface-Grafted Polymer Brushes. *Anal. Methods* **2016**, No. 8, 6415–6419. https://doi.org/10.1039/c6ay01833e.

(130) Jesmer, A. H.; Huynh, V.; Wylie, R. G. Fabrication of Low-Fouling, High-Loading Polymeric Surfaces through PH-Controlled RAFT. *RSC Adv.* **2020**, *10*, 20302–20312. https://doi.org/10.1039/d0ra02693j.

(131) Tziampazis, E.; Kohn, J.; Moghe, P. V. PEG-Variant Biomaterials as Selectively Adhesive Protein Templates: Model Surfaces for Controlled Cell Adhesion and Migration. *Biomaterials* **2000**, *21*, 511–520.

(132) Seo, J.; Sakai, K.; Yui, N. Adsorption State of Fibronectin on Poly (Dimethylsiloxane) Surfaces with Varied Stiffness Can Dominate Adhesion Density of Fibroblasts. *Acta Biomater.* **2013**, *9*, 5493–5501. https://doi.org/10.1016/j.actbio.2012.10.015.

(133) Li, B.; Jain, P.; Ma, J.; Smith, J. K.; Yuan, Z.; Hung, H. C.; He, Y.; Lin, X.; Wu, K.; Pfaendtner, J.; Jiang, S. Trimethylamine N-Oxide–Derived Zwitterionic Polymers: A New Class of Ultralow Fouling Bioinspired Materials. *Sci. Adv.* **2019**, *5* (6). https://doi.org/10.1126/sciadv.aaw9562.

(134) Cheng, G.; Li, G.; Xue, H.; Chen, S.; Bryers, J. D.; Jiang, S. Zwitterionic Carboxybetaine Polymer Surfaces and Their Resistance to Long-Term Biofilm Formation. *Biomaterials* **2009**, *30* (28), 5234–5240. https://doi.org/10.1016/j.biomaterials.2009.05.058.

(135) Othman, Z.; Cillero, B.; Rijt, S. Van; Habibovic, P. Biomaterials Understanding Interactions between Biomaterials and Biological Systems Using Proteomics. *Biomaterials* **2018**, *167*, 191–204. https://doi.org/10.1016/j.biomaterials.2018.03.020.

(136) Visalakshan, R. M.; Macgregor, M. N.; Sasidharan, S.; Ghazaryan, A.; Landfester, K.; Mierczynska-vasilev, A. M.; Morsbach, S.; Mailander, V.; Hayball, J. D.; Vasilev, K. Biomaterial Surface Hydrophobicity-Mediated Serum Protein Adsorption and Immune Responses. *ACS Appl. Mater. Interfaces* **2019**, *11*, 27615–27623. https://doi.org/10.1021/acsami.9b09900.

(137) Jansen, L. E.; Amer, L. D.; Chen, E. Y. T.; Nguyen, T. V.; Saleh, L. S.; Emrick, T.; Liu, W. F.; Bryant, S. J.; Peyton, S. R. Zwitterionic PEG-PC Hydrogels Modulate the Foreign Body Response in a Modulus-Dependent Manner. *Biomacromolecules* **2018**, *19* (7), 2880–2888. https://doi.org/10.1021/acs.biomac.8b00444.

(138) Castner, D. G.; Ratner, B. D. Biomedical Surface Science: Foundations to

Frontiers. *Surf. Sci.* **2002**, *500* (1–3), 28–60.

(139) Wagner, M. S.; Mcarthur, S. L.; Shen, M.; Horbett, T. A.; Castner, D. G.; Wagner, M. S.; Mcarthur, S. L.; Shen, M.; Thomas, A. Limits of Detection for Time of Flight Secondary Ion Mass Spectrometry (ToF-SIMS) and X-Ray Photoelectron Spectroscopy (XPS): Detection of Low Amounts of Adsorbed Protein. *J. Biomater. Sci. Polym. Ed.* **2002**, *13* (4), 407–428. https://doi.org/10.1163/156856202320253938.

(140) Foster, R. N.; Harrison, E. T.; Castner, D. G. ToF-SIMS and XPS Characterization of Protein Films Adsorbed onto Bare and Sodium Styrenesulfonate-Grafted Gold Substrates. *Langmuir* **2016**, *32* (13), 3207–3216. https://doi.org/10.1021/acs.langmuir.5b04743.

(141) Menzies, D. J.; Jasieniak, M.; Griesser, H. J.; Forsythe, J. S.; Johnson, G.; Mcfarland, G. A.; Muir, B. W. A ToF-SIMS and XPS Study of Protein Adsorption and Cell Attachment across PEG-like Plasma Polymer Films with Lateral Compositional Gradients. *Surf. Sci.* **2012**, *606* (23–24), 1798–1807. https://doi.org/10.1016/j.susc.2012.07.017.

(142) Marruecos, D. F.; Kastantin, M.; Schwartz, D. K.; Kaar, J. L. Dense Poly(Ethylene Glycol) Brushes Reduce Adsorption and Stabilize the Unfolded Conformation of Fibronectin. **2016**, No. 17, 1017–1025. https://doi.org/10.1021/acs.biomac.5b01657.

(143) Romanowska, J.; Kokh, D. B.; Wade, R. C. When the Label Matters: Adsorption of Labeled and Unlabeled Proteins on Charged Surfaces. *Nano Lett.* **2015**, *15* (11), 7508–7513. https://doi.org/10.1021/acs.nanolett.5b03168.

(144) Hedayati, M.; Marruecos, D. F.; Krapf, D.; Kaar, J. L.; Kipper, M. J. Protein Adsorption Measurements on Low Fouling and Ultralow Fouling Surfaces: A Critical Comparison of Surface Characterization Techniques. *Acta Biomater.* **2020**, *102*, 169–180. https://doi.org/10.1016/j.actbio.2019.11.019.

(145) Bingaman, S.; Huxley, V. H.; Rumbaut, R. E. Fluorescent Dyes Modify Properties of Proteins Used in Microvascular Research. *Microcirculation* **2003**, *10* (2), 221–231. https://doi.org/10.1038/sj.mn.7800186.

(146) Felgueiras, H. P.; Antunes, J. C.; Martins, M. C. L.; Barbosa, M. A. *Fundamentals of Protein and Cell Interactions in Biomaterials*; Elsevier Ltd., 2018. https://doi.org/10.1016/B978-0-08-100803-4.00001-2.

(147) Holmberg, M.; Stibius, K. B.; Ndoni, S.; Larsen, N. B.; Kingshott, P.; Hou, X. L. Protein Aggregation and Degradation during Iodine Labeling and Its Consequences for Protein Adsorption to Biomaterials. *Anal. Biochem.* **2007**, No. 361, 120–125. https://doi.org/10.1016/j.ab.2006.11.016.

(148) Taylor, M.; Urquhart, A. J.; Anderson, D. G.; Williams, P. M.; Langer, R.;

Alexander, M. R.; Davies, M. C. A Methodology for Investigating Protein Adhesion and Adsorption to Microarrayed Combinatorial Polymers. *Macromol. Rapid Commun.* **2008**, *29* (15), 1298–1302. https://doi.org/10.1002/marc.200800171.

(149) González-garcía, C.; Cantini, M.; Ballester-beltrán, J.; Altankov, G.; Salmerón-sánchez, M. Acta Biomaterialia The Strength of the Protein-Material Interaction Determines Cell Fate. *Acta Biomater.* **2018**, *77*, 74–84. https://doi.org/10.1016/j.actbio.2018.07.016.

(150) Mrabet, B.; Nguyen, M. N.; Majbri, A.; Mahouche, S.; Turmine, M.; Bakhrouf, A.; Chehimi, M. M. Anti-Fouling Poly(2-Hydoxyethyl Methacrylate) Surface Coatings with Specific Bacteria Recognition Capabilities. *Surf. Sci.* **2009**, *603* (16), 2422–2429. https://doi.org/10.1016/j.susc.2009.05.020.

(151) Ishihara, K.; Ishikawa, E.; Iwasaki, Y.; Nakabayashi, N. Inhibition of Fibroblast Cell Adhesion on Substrate by Coating with 2-Methacryloyloxyethyl Phosphorylcholine Polymers. *J. Biomater. Sci. Polym. Ed.* **1999**, *10* (10), 1047–1061. https://doi.org/10.1163/156856299X00676.

(152) Katsikogianni, M.; Missirlis, Y. F.; Harris, L.; Douglas, J. Concise Review of Mechanisms of Bacterial Adhesion to Biomaterials and of Techniques Used in Estimating Bacteria-Material Interactions. *Eur. Cells Mater.* **2004**, *8*, 37–57. https://doi.org/10.22203/eCM.v008a05.

(153) Flemming, R. G.; Murphy, C. J.; Abrams, G. A.; Goodman, S. L.; Nealey, P. F. Effects of Synthetic Micro- and Nano-Structured Surfaces on Cell Behavior. *Biomaterials* **1999**, *20* (6), 573–588. https://doi.org/10.1016/S0142-9612(98)00209-9.

(154) Sharifi, F.; Htwe, S. S.; Righi, M.; Liu, H.; Pietralunga, A.; Yesil-celiktas, O.; Maharjan, S.; Cha, B.; Shin, S. R.; Dokmeci, M. R.; Vrana, N. E.; Ghaemmaghami, A. M.; Khademhosseini, A.; Zhang, Y. S. A Foreign Body Response-on-a-Chip Platform. *Adv. Healthc. Mater.* **2019**, *8* (4), 1801425. https://doi.org/10.1002/adhm.201801425.

(155) Luu, T. U.; Gott, S. C.; Woo, B. W. K.; Rao, M. P.; Liu, W. F. Micro- and Nanopatterned Topographical Cues for Regulating Macrophage Cell Shape and Phenotype. *ACS Appl. Mater. Interfaces* **2015**, *7* (51), 28665–28672. https://doi.org/10.1021/acsami.5b10589.

(156) Santoro, F.; Zhao, W.; Joubert, L.; Duan, L.; Schnitker, J.; van de Burgt, Y.; Lou, H.; Liu, B.; Salleo, A.; Cui, L.; Cui, Y.; Cui, B. Revealing the Cell − Material Interface with Nanometer Resolution by Focused Ion Beam/ Scanning Electron Microscopy. *ACS Nano* **2017**, *11* (8), 8320–8328. https://doi.org/10.1021/acsnano.7b03494.

(157) Faulón Marruecos, D.; Saleh, L. S.; Kim, H. H.; Bryant, S. J.; Schwartz, D. K.;

Kaar, J. L. Stabilization of Fibronectin by Random Copolymer Brushes Inhibits Macrophage Activation. *ACS Appl. Bio Mater.* **2019**. https://doi.org/10.1021/acsabm.9b00815.

(158) Pei, J.; Hall, H.; Spencer, N. D. The Role of Plasma Proteins in Cell Adhesion to PEG Surface-Density-Gradient- Modified Titanium Oxide. *Biomaterials* **2011**, *32*, 8968–8978. https://doi.org/10.1016/j.biomaterials.2011.08.034.

(159) Brown, B. N.; Ratner, B. D.; Goodman, S. B.; Amar, S.; Badylak, S. F. Macrophage Polarization: An Opportunity for Improved Outcomes in Biomaterials and Regenerative Medicine. *Biomaterials* **2012**, *33* (15), 3792–3802. https://doi.org/10.1016/j.biomaterials.2012.02.034.

(160) Rostam, H. M.; Fisher, L. E.; Hook, A. L.; Burroughs, L.; Luckett, J. C.; Figueredo, G. P.; Mbadugha, C.; Teo, A. C.; Latif, A.; Kammerling, L.; Day, M.; Lawler, K.; Barrett, D.; Elsheikh, S.; Ilyas, M.; Winkler, D. A.; Alexander, M. R.; Ghaemmaghami, A. M. Immune-Instructive Polymers Control Macrophage Phenotype and Modulate the Foreign Body Response In Vivo. *Matter* **2020**, *2*, 1–18. https://doi.org/10.1016/j.matt.2020.03.018.

(161) Campoccia, D.; Montanaro, L.; Arciola, C. R. A Review of the Biomaterials Technologies for Infection-Resistant Surfaces. *Biomaterials* **2013**, *34* (34), 8533–8554. https://doi.org/10.1016/j.biomaterials.2013.07.089.

(162) Sjollema, J.; Zaat, S. A. J.; Fontaine, V.; Ramstedt, M.; Luginbuehl, R.; Thevissen, K.; Li, J.; Mei, H. C. Van Der; Busscher, H. J. In Vitro Methods for the Evaluation of Antimicrobial Surface Designs. *Acta Biomater.* **2018**, *70*, 12–24. https://doi.org/10.1016/j.actbio.2018.02.001.

(163) Boudarel, H.; Mathias, J.; Blaysat, B.; Grédiac, M. Towards Standardized Mechanical Characterization of Microbial Bio Films: Analysis and Critical Review. *npj Biofilms Microbiomes* **2018**, *4* (1), 1–15. https://doi.org/10.1038/s41522-018-0062-5.

(164) Lagemaat, M. Van De; Grotenhuis, A.; Belt-gritter, B. Van De; Roest, S.; Loontjens, T. J. A.; Busscher, H. J.; van der mei, H. C.; Ren, Y. Comparison of Methods to Evaluate Bacterial Contact-Killing Materials. *Acta Biomater.* **2017**, *59*, 139–147. https://doi.org/10.1016/j.actbio.2017.06.042.

(165) Azeredo, J.; Azevedo, N. F.; Briandet, R.; Cerca, N.; Coenye, T.; Costa, A. R.; Desvaux, M.; Bonaventura, G. Di; Hebraud, M.; Jaglic, Z.; Kačániová, M.; Knøchel, S.; Lourenco, A.; Mergulhão, F.; Meyer, R. L.; Nychas, G.; Simoes, M.; Tresse, O.; Sternberg, C. Critical Reviews in Microbiology Critical Review on Biofilm Methods A. *Crit. Rev. Microbiol.* **2017**, *43* (3), 313–351. https://doi.org/10.1080/1040841X.2016.1208146.

(166) Busscher, H. J.; van der Mei, H. C.; Subbiahdoss, G.; Jutte, P. C.; van den Dungen, J. J. A. M.; Zaat, S. A. J.; Schultz, M. J.; Grainger, D. W. Biomaterial-Associated

Infection: Locating the Finish Line in the Race for the Surface. *Sci. Transl. Med.* **2012**, *4* (153).

(167) Wang, H.; Christiansen, D. E.; Mehraeen, S.; Cheng, G. Winning the Fight against Biofilms: The First Six-Month Study Showing No Biofilm Formation on Zwitterionic Polyurethanes. *Chem. Sci.* **2020**, *11*, 4709–4721. https://doi.org/10.1039/c9sc06155j.

(168) Bakker, D. P.; Plaats, A. Van Der; Verkerke, G. J.; Busscher, H. J.; Mei, H. C. Van Der. Comparison of Velocity Profiles for Different Flow Chamber Designs Used in Studies of Microbial Adhesion to Surfaces. *Appl. Environ. Microbiol.* **2003**, *69* (10), 6280–6287. https://doi.org/10.1128/AEM.69.10.6280.

(169) Dutot, M.; Paillet, H.; Chaumeil, C.; Warnet, J.-M.; Rat, P. Severe Ocular Infections with Contact Lens: Role of Multipurpose Solutions. *Eye* **2009**, *23* (2), 470–476. https://doi.org/10.1038/eye.2008.131.

(170) Dohnt, K.; Sauer, M.; Müller, M.; Atallah, K.; Weidemann, M.; Gronemeyer, P.; Rasch, D.; Tielen, P.; Krull, R. An in Vitro Urinary Tract Catheter System to Investigate Bio Fi Lm Development in Catheter-Associated Urinary Tract Infections. *J. Microbiol. Methods* **2011**, *87* (3), 302–308. https://doi.org/10.1016/j.mimet.2011.09.002.

(171) Azevedo, A. S.; Almeida, C.; Gomes, L. C.; Ferreira, C.; Mergulhão, F. J.; Melo, L. F.; Azevedo, N. F. An in Vitro Model of Catheter-Associated Urinary Tract Infections to Investigate the Role of Uncommon Bacteria on the Escherichia Coli Microbial Consortium. *Biochem. Eng. J.* **2017**, *118*, 64–69. https://doi.org/10.1016/j.bej.2016.11.013.

(172) Li, B.; Webster, T. J. Bacteria Antibiotic Resistance : New Challenges and Opportunities for Implant-Associated Orthopedic Infections. *J. Orthop. Res.* **2017**, *36* (1), 22–32. https://doi.org/10.1002/jor.23656.

(173) Lall, R. R.; Wong, A. P.; Lall, R. R.; Lawton, C. D.; Smith, Z. A.; Dahdaleh, N. S. Evidence-Based Management of Deep Wound Infection after Spinal Instrumentation. *J. Clin. Neurosci.* **2015**, *22* (2), 238–242. https://doi.org/10.1016/j.jocn.2014.07.010.

(174) Vinchon, M.; Dhellemmes, P. Cerebrospinal Fluid Shunt Infection: Risk Factors and Long-Term Follow-Up. *Child's Nerv. Syst.* **2006**, *22* (7), 692–697. https://doi.org/10.1007/s00381-005-0037-8.

(175) Bloomfield, I. G.; Johnston, I. H.; Bilston, L. E. Effects of Proteins, Blood Cells and Glucose on the Viscosity of Cerebrospinal Fluid. *Pediatr. Neurosurg.* **1998**, *28* (5), 246–251.

(176) Casa, L. D. C.; Deaton, D. H.; Ku, D. N. Role of High Shear Rate in Thrombosis. *J. Vasc. Surg.* **2015**, *61* (4), 1068–1080.

(177) Lebeaux, D.; Fernández-hidalgo, N.; Chauhan, A.; Lee, S.; Ghigo, J.; Almirante, B.; Beloin, C. Management of Infections Related to Totally Implantable Venous-Access Ports : Challenges and Perspectives. *Lancet Infect. Dis.* **2014**, *14* (2), 146–159. https://doi.org/10.1016/S1473-3099(13)70266-4.

(178) Saleem, B. R.; Meerwaldt, R.; Tielliu, I. F. J.; Verhoeven, E. L. G.; Dungen, J. J. A. M. Van Den; Zeebregts, C. J. Conservative Treatment of Vascular Prosthetic Graft Infection Is Associated with High Mortality. *Am. J. Surg.* **2010**, *200* (1), 47–52. https://doi.org/10.1016/j.amjsurg.2009.05.018.

(179) Haddadin, Y.; Annamaraju, P.; Regunath, H. Central Line Associated Blood Stream Infections (CLABSI). *StatPearls* **2020**, 1–6.

(180) Richter, R. P.; Brisson, A. R. Following the Formation of Supported Lipid Bilayers on Mica: A Study Combining AFM, QCM-D, and Ellipsometry. *Biophys. J.* **2005**, *88* (5), 3422–3433. https://doi.org/10.1529/biophysj.104.053728.

(181) Madiona, R. M. T.; Welch, N. G.; Scoble, J. A.; Muir, B. W.; Pigram, P. J. Determining the Limit of Detection of Surface Bound Antibody. *Biointerphases* **2017**, *12* (3), 031007. https://doi.org/10.1116/1.4986377.

(182) Pierce Biotechnology. Micro BCA Protein Assay Kit. *Termo Sci.* **2017**, 1–6.

(183) Ngo, B. K. D.; Grunlan, M. A. Protein Resistant Polymeric Biomaterials. *ACS Macro Lett.* **2017**, *6*, 992–1000. https://doi.org/10.1021/acsmacrolett.7b00448.

(184) Rao, W.; Celiz, A. D.; Scurr, D. J.; Alexander, M. R.; Barrett, D. A. Ambient DESI and LESA-MS Analysis of Proteins Adsorbed to a Biometerial Surface Using In-Situ Surface Tryptic Digestion. *J. Am. Soc. Mass Spectrom.* **2013**, *24* (12), 1927–1936. https://doi.org/10.1021/jasms.8b04443.

(185) Maes, K.; Smolders, I.; Michotte, Y.; Eeckhaut, A. Van. Strategies to Reduce Aspecific Adsorption of Peptides and Proteins in Liquid Chromatography – Mass Spectrometry Based Bioanalyses: An Overview. *J. Chromatogr. A* **2014**, *1358*, 1–13. https://doi.org/10.1016/j.chroma.2014.06.072.

(186) Medalsy, I.; Hensen, U.; Muller, D. J. Imaging and Quantifying Chemical and Physical Properties of Native Proteins at Molecular Resolution by Force – Volume AFM. *Angew. Chemie - Int. Ed.* **2011**, *50*, 12103–12108. https://doi.org/10.1002/anie.201103991.

(187) Wei, Q.; Becherer, T.; Angioletti-uberti, S.; Dzubiella, J.; Wischke, C.; Neffe, A. T.; Lendlein, A.; Ballauff, M.; Haag, R. Protein Interactions with Polymer Coatings and Biomaterials. *Angew. Chemie Int. Ed.* **2014**, *53* (31), 8004–8031. https://doi.org/10.1002/anie.201400546.

(188) Ntziachristos, V. Going Deeper than Microscopy: The Optical Imaging Frontier in Biology. *Nat. Publ. Gr.* **2010**, *7* (8), 603–614. https://doi.org/10.1038/nmeth.1483.

(189) Weber, M.; Steinle, H.; Golombek, S.; Hann, L.; Schlensak, C.; Wendel, H. P.; Avci-adali, M. Blood-Contacting Biomaterials : In Vitro Evaluation of the Hemocompatibility. *Front. Bioeng. Biotechnol.* **2018**, *6* (99), 1–11. https://doi.org/10.3389/fbioe.2018.00099.

(190) Murray, P. J.; Allen, J. E.; Biswas, S. K.; Fisher, E. A.; Gilroy, D. W.; Goerdt, S.; Gordon, S.; Hamilton, J. A.; Ivashkiv, L. B.; Lawrence, T.; Locati, M.; Mantovani, Al.; Martinez, F. O.; Mege, J.-L.; Mosser, D. M.; Natoli, G.; Saeij, J. P.; Schultze, J. L.; Shrivey, K. A.; Sica, A.; Suttles, J.; Udalova, I.; van Ginderachter, J. A.; Vogel, S. N.; Wynn, T. A. Macrophage Activation and Polarization: Nomenclature and Experimental Guidelines. *Immunity* **2015**, *41* (1), 14–20. https://doi.org/10.1016/j.immuni.2014.06.008.Macrophage.

(191) Zhang, L.; Cao, Z.; Bai, T.; Carr, L.; Ella-Menye, J.-R.; Irvin, C.; Ratner, B. D.; Jiang, S. Zwitterionic Hydrogels Implanted in Mice Resist the Foreign-Body Reaction. *Nat. Biotechnol.* **2013**, *31* (6), 553–556. https://doi.org/10.1038/nbt.2580.

(192) Xie, X.; Doloff, J. C.; Yesilyurt, V.; Sadraei, A.; Mcgarrigle, J. J.; Omami, M.; Veiseh, O.; Farah, S.; Isa, D.; Ghani, S.; Joshi, I.; Vegas, A.; Li, J.; Wang, W.; Bader, A.; Tam, H. H.; Tao, J.; Chen, H.; Yang, B.; Williamson, K. A.; Oberholzer, J.; Langer, R.; Anderson, D. G. Reduction of Measurement Noise in a Continuous Glucose Monitor by Coating the Sensor with a Zwitterionic Polymer. *Nat. Biomed. Eng.* **2018**, *2*, 894–906. https://doi.org/10.1038/s41551-018-0273-3.

(193) Zhang, P.; Sun, F.; Liu, S.; Jiang, S. Anti-PEG Antibodies in the Clinic: Current Issues and beyond PEGylation. *J. Control. Release* **2016**, *244*, 184–193. https://doi.org/10.1016/j.jconrel.2016.06.040.

(194) Yang, Q.; Jacobs, T. M.; Mccallen, J. D.; Moore, D. T.; Huckaby, J. T.; Edelstein, J. N.; Lai, S. K. Analysis of Pre-Existing IgG and IgM Antibodies against Polyethylene Glycol (PEG) in the General Population. *Anal. Chem.* **2016**, *88*, 11804–11812. https://doi.org/10.1021/acs.analchem.6b03437.

(195) Ukita, R.; Wu, K.; Lin, X.; Carleton, N. M.; Naito, N.; Lai, A.; Do-Nguyen, C. C.; Demarest, C. T.; Jiang, S.; Cook, K. E. Zwitterionic Poly-Carboxybetaine Coating Reduces Artificial Lung Thrombosis in Sheep and Rabbits. *Acta Biomater.* **2019**, *92*, 71–81. https://doi.org/10.1016/j.actbio.2019.05.019.

CHAPTER 2. FABRICATION OF ANTIFOULING, HIGH-LOADING POLYMERIC SURFACES THROUGH PH-CONTROLLED RAFT

Author's Preface:

The following chapter has been reprinted with permission from the Royal Society of Chemistry under a CC-BY license, and was published in *RSC Advances* under the citation:

Jesmer, A.H., Huynh, V. and Wylie, R.G., 2020. Fabrication of low-fouling, high-loading polymeric surfaces through pH-controlled RAFT. RSC advances, 10(34), pp.20302-20312.

A.H. Jesmer planned the study, conducted most of the experiments and wrote the manuscript. V. Huynh assisted with experiments. R.G. Wylie assisted in data interpretation and revised the manuscript.

2.1. ABSTRACT

Antifouling and high-loading surfaces are increasingly important for biosensing and blood purification technologies. Selective and efficient target binding from complex media can be achieved with pCB surfaces that consist of a dense brush layer to resist nonspecific protein adsorption and a sparse "mushroom" upper layer for high-density capture agent immobilization (i.e., high-loading). We developed pH-controlled surface-reversible addition-fragmentation chain-transfer (S-RAFT) polymerization to simplify fabrication of multi-modal, antifouling and high-loading pCB surfaces without the need for quenching or re-initiation steps, toxic transition metals or light irradiation. Multi-modal polymer layers were produced through partial polymer termination by temporarily raising the pH to aminolyse a fraction of dormant chain transfer agents (CTAs); remaining polymer chains with intact CTAs continued uninterrupted extension to create the "mushroom" upper layer. The multi-modal pCB surfaces were antifouling towards proteins (< 6.7 ng cm^{-2}), and macrophages. Compared to mono-modal brush surfaces, multi-modal pCB surfaces were high-loading with 5 times greater capture agent immobilization (e.g., antibody) and 4 times greater target binding (e.g., biotin-fluorescein).

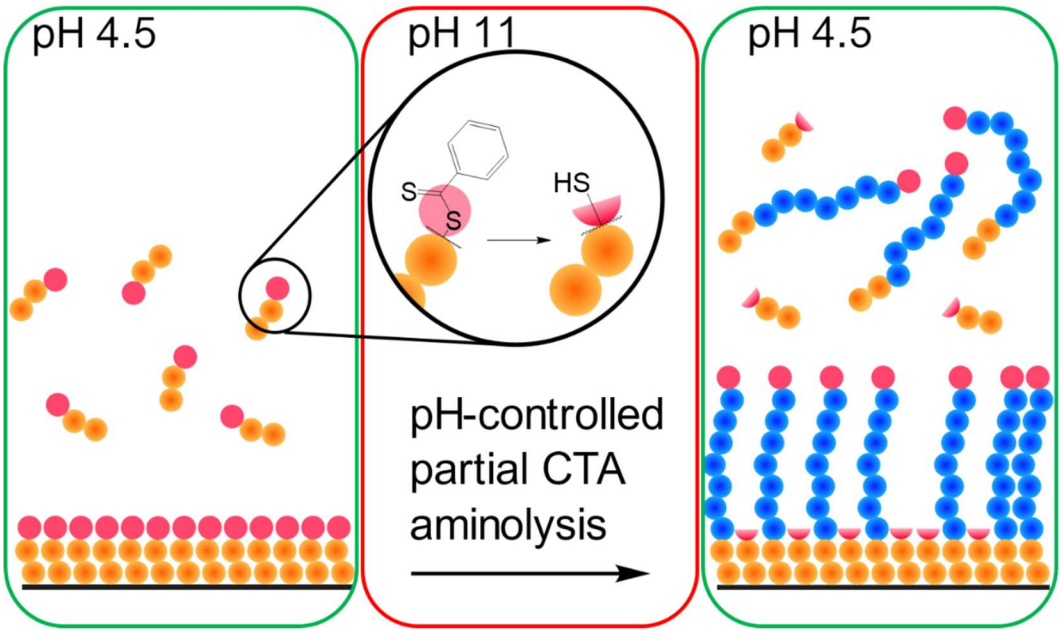

2.2. Introduction

Bioactive polymeric surface coatings for antifouling biointerfaces are being developed for biomolecule sensing in complex fluids and blood purification[1–6]. To date, a variety of polymeric materials have been used to achieve antifouling surfaces such as poly(ethylene glycol) (PEG)[7], fluorinated polymers[8], and zwitterionic polymers[5]. pCB has been identified as a zwitterionic polymer that both resists nonspecific protein adsorption and is readily functionalized with biomolecules that act as capture agents for target molecule binding. Capture agents can be anchored to pCB's carboxylic acid groups while maintaining antifouling properties towards proteins[9]. Furthermore, enzymes and antibodies conjugated to pCB maintain or increase in activity[10] and thermostability by restricting conformational transitions[11], making it optimal for bioactive antifouling surfaces.

Polymer surface coatings are produced by one of two methodologies: (1) "graft-to", where the end group of pre-synthesized polymer are covalently bonded to a surface; or (2) "graft-from", where polymerization is initiated from the surface[12]. Graft-to polymer densities are limited by the polymer chain's R_g leading to low density "pancake" or "mushroom" polymer conformations[13]. Graft-from yields polymer densities that exceed the R_g imposed limit, and extends polymer chains in a brush configuration[13]. While graft-from's high polymer density improves fouling resistance[14], biomolecule immobilization is limited to a monolayer on the brush surface; polymer side-chains are inaccessible due to tight polymer packing [15]. In contrast, graft-to's lower polymer density yields surfaces with greater loading potential but also increases fouling due to lower polymer surface coverage.

Bimodal architectures demonstrate high surface loading while remaining antifouling[9,15,16], combining the advantages of graft-from and graft-to. Bimodal polymer surfaces consist of a short dense polymer layer that resists protein fouling, and a sparse layer for greater biomolecule immobilization. Bimodal architectures have been synthesized previously via surface initiated-atom transfer radical polymerization (SI-ATRP) and surface initiated-photoiniferter mediated polymerization (SI-PIMP)[9,15,16] via two-step procedures that require termination and radical re-initiation steps, copper or surface exposure to light. The methods require two independent sequential radical polymerizations, where the first polymerization is fully quenched before re-initiation of the synthesis of the second polymer layer.

To decrease synthetic complexity and expand accessibility, we developed pH-controlled S-RAFT for multimodal polymer architectures that avoids radical quenching, re-initiation and multiple CTA-immobilization steps (**Figure 2.1**). The procedure terminates a subpopulation of CTAs during polymerization to establish the dense polymer layer, while the remaining chains with active CTAs continue to extend. Polymerization was conducted in the presence of a primary amine, butylamine, that is protonated and unreactive during S-RAFT polymerization at pH 4.5. To establish the first layer, the pH is temporarily raised to 11 with sodium hydroxide (NaOH), which deprotonates butylamine for partial CTA aminolysis. To create the sparse second layer, the pH is returned to 4.5 (by adding 12 M hydrochloric acid (HCl)) before complete CTA aminolysis. The bimodal pCB surfaces resisted nonspecific protein adsorption (< 6.7 ng cm^{-2}) and decreased macrophage adhesion. Compared to brush only layers, the bimodal pCB layers increased antibody, capture agent, loading 5 times and improved the capture of biotin (5-fluorescein) conjugate (biotin-fluorescein) on avidin modified layers by 4 times.

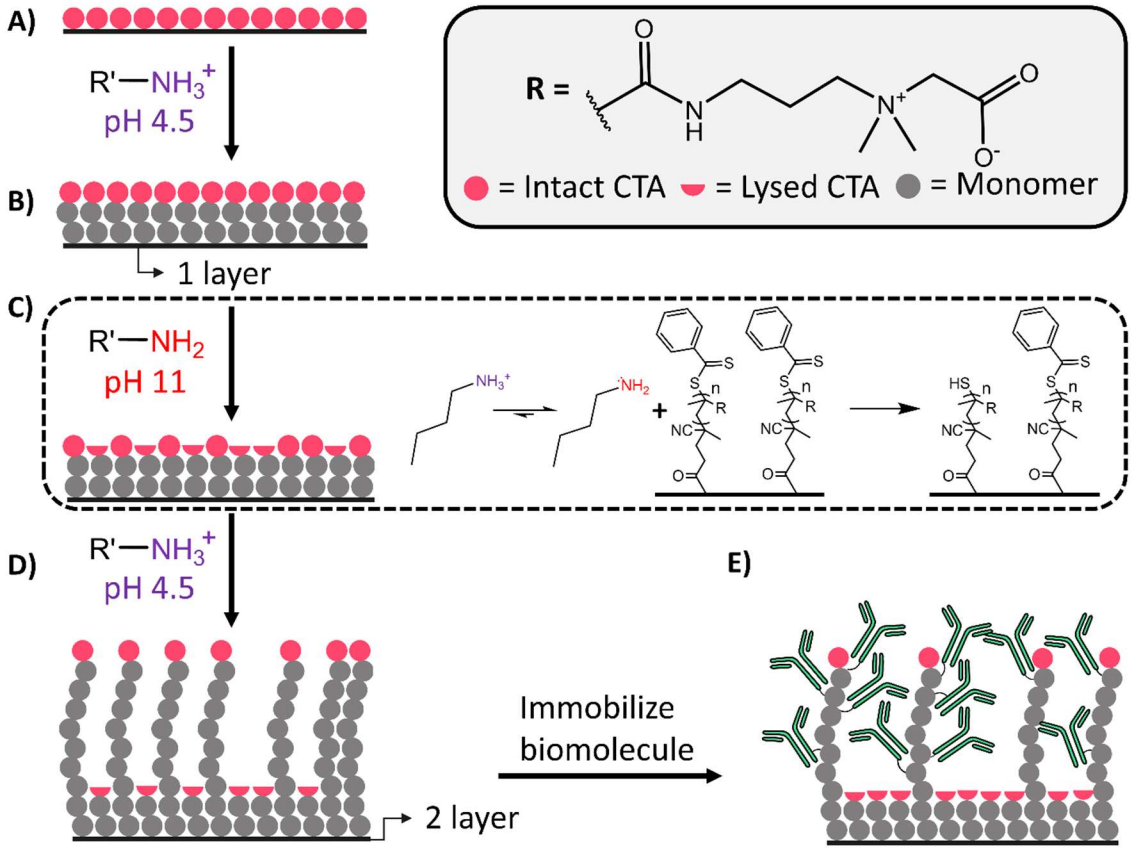

Figure 2.1: Schematic for the synthesis of bimodal pCB layers via pH-controlled S-RAFT for enhanced capture agent immobilization on antifouling surfaces. (A) Surface functionalized with a monolayer of RAFT CTA. (B) Synthesis of the dense pCB layer at pH 4.5 in the presence of a protonated primary amine, butylamine (pKa of 10.5). (C) Temporary increase in pH (4.5 to 11) to deprotonate butylamine for the partial aminolysis of immobilized CTA. (D) pH returned to 4.5 for continued polymerization to yield the lower density, high loading pCB layer; pH 4.5 re-protonates butylamine to prevent further CTA aminolysis. (E) Compared to monomodal architectures, bimodal pCB architectures yield greater surface densities of accessible carboxylic acids for carbodiimide immobilization of capture agents such as antibodies.

2.3. Materials and methods

2.3.1. Materials

N-[3-(dimethylamino)propyl]methacrylamide, tert-butyl bromoacetate, trifluoroacetic acid (TFA), 4-Cyano-4-(phenylcarbonothioylthio)pentanoic acid, 4,4'-azobis(4-cyanovaleric acid), sodium dodecyl sulfate (SDS), (3-

Aminopropyl)triethoxysilane (APTES), N,N′-Diisopropylcarbodiimide (DIC), N-(3-Dimethylaminopropyl)-N′-ethylcarbodiimide hydrochloride (EDC), N-hydroxysuccinimide (NHS), sodium hydroxide (NaOH), QuantiPro™ BCA Assay Kit, sodium acetate, bovine serum albumin (BSA), Biotin (5-fluorescein) conjugate (biotin-fluorescein), TWEEN® 20, were purchased from Sigma Aldrich (Oakville, ON, Canada). Methanol, toluene, dichloromethane (DCM), diethyl ether, 1,4-dioxane, dimethylformamide (DMF), hydrochloric acid (HCl), sulfuric acid, and acetic acid were purchased from Caledon (Georgetown, ON, Canada). Alexa Fluor® 647 NHS ester, calf bovine serum (CBS) and fetal bovine serum (FBS), Calcein AM, HOESCHT stain, trypsin and avidin were obtained from Thermo Fisher Scientific (Burlington, ON, Canada). Dulbecco's modified Eagle medium (DMEM) was purchased from Corning (Tewksbury, MA, USA). Silicon wafers were purchased from University Wafers (Boston, MA, USA). Bevacizumab was provided by Boston Children's Pharmacy (Boston, MA, USA). Phosphate buffered saline (PBS) at pH 7.4 contained 10 mM sodium phosphate and 137 mM NaCl.

Carboxybetaine methacrylamide (CB) monomer was synthesized via a previously published method[17]. Briefly, 23.25 g (136.5 mmol, 1 equiv.) of N-[3-(dimethylamino)propyl]methacrylamide was dissolved in 300 mL of dry acetonitrile under N_2. Tert-butyl bromoacetate (30 g, 153.8 mmol, 1.1 equiv.) was added, and left to react overnight at 50 °C. The reaction was cooled to room temperature and the product was precipitated with 500 mL of ether. The product was left to stand at 4 °C overnight, and decanted. The white powder was collected, washed with 100 mL of ether, decanted,

and dried under a stream of nitrogen, followed by incubation overnight under vacuum. The t-butyl protected intermediate was then deprotected by dissolving in neat TFA and incubating at room temperature for 2 h. The deprotected CB monomer was precipitated in ether, dried under a nitrogen stream, and freeze drying. ^{1}H nuclear magnetic resonance (NMR) (D_2O, 600 MHz) δ: 5.63 (s, 1H), 5.34 (s, 1H), 4.10 (s, 2H), 3.53 (m, 2H), 3.28 (t, J = 6.42, 2H), 3.18 (s, 6H), 1.96 (m, 2H), 1.85 (s, 3H).

Fluorescent bevacizumab (bevacizumab-647) was synthesized by mixing 7.5 µL Alexa fluor-647 NHS DMF solutions (10 mg mL^{-1}; 0.075 mg, 0.06 µmol, 3 equiv.) with 100 µL of a bevacizumab solution (3 mg, 0.02 µmol, 1 equiv.) in PBS (pH 7.4) for 3 h in the dark. Bevacizumab-647 was purified by dialysis (molecular weight cut off (MWCO) 12-14 kDa) against PBS at 4°C in the dark. The final bevacizumab-647 concentration and substitution ratio (dyes per antibody) was calculated from absorbance measurements taken with a Biotek Cytation 5 plate reader equipped with a Take3 micro-volume plate using extinction coefficient for Alexa fluor-647 of 239000 cm^{-1} M^{-1} and a correction factor of 0.03.

2.3.2. Modification of silica surfaces

2.3.2.1. *Modification of silica surfaces and APTES deposition*

Silicon wafers (100 mm, N-type, <100>, 1-10 ohm cm) were soaked in 1:1 HCl:methanol for 30 min, rinsed with milliQ water and dried under nitrogen. The wafers were then soaked in concentrated H_2SO_4 for 30 min, rinsed with milliQ water and dried under a stream of nitrogen. Surfaces were then spin coated with a 0.1% v/v APTES in dry

toluene (dried over 3 Å molecular sieves), sonicated for 1 min in dry toluene, dried under a stream of nitrogen, and incubated for 1 h at 70 °C.

2.3.3. Immobilization of RAFT chain transfer agent

4-Cyano-4-(phenylcarbonothioylthio)pentanoic acid (14 mg, 0.05 mmol, 1 equiv.) was activated with DIC (39 µL, 0.25 mmol, 5 equiv.) and NHS (29 mg, 0.25 mmol, 5 equiv.) in DCM (1 mL; dried over 3 Å molecular sieves) and stirred overnight at room temperature under nitrogen. APTES functionalized silica wafers were then added to the DCM solution, diluted to 5 mL, which was then kept under nitrogen for 60 h with gentle stirring.

2.3.4. Solution and graft-from polymerizations

2.3.4.1. *Synthesis of pDMAPMA*

Bimodal poly(Dimethyl aminopropyl methacrylamide) (pDMAPMA) distributions in solution were synthesized as follows. N-[3-(dimethylamino)propyl]methacrylamide monomer (1.3 mL, 7.8 mmol, 130 equiv.), 4-Cyano-4-(phenylcarbonothioylthio)pentanoic acid (15.4 mg, 0.05 mmol, 1 equiv.), 4,4′-Azobis(4-cyanopentanoic acid) (7.7 mg, 0.27 mmol, 0.5 equiv.) and butylamine (50 µL, 0.5 mmol, 9 equiv.) were dissolved in 5 mL of 2:1 acetate buffer (0.1 M, pH 4.5) and 1,4-dioxane. The pH was adjusted to 4.5 with NaOH (8 M) and degassed via three freeze-pump-thaw cycles with nitrogen backfills and incubated at 70 °C with gentle stirring. Two different bimodal polymerizations were performed: (1) After 2 h at 70 °C, an aliquot of polymerization solution was removed for gel permeation chromatography (GPC)

characterization and degassed NaOH (8 M, 500 μL) was added to the reaction vessel to raise the pH and initiate CTA aminolysis. After 6 min at high pH, HCl (12 M, 335 μL) was added to end aminolysis, and the polymerization was maintained for 22 h. (2) After 4 h at 70 °C, an aliquot of polymerization solution was removed for GPC characterization and degassed NaOH (8 M, 500 μL) was added to the reaction vessel to initiate CTA aminolysis. After 6 min at high pH, HCl (12 M, 335 μL) was then added to end aminolysis and polymerization was maintained for 20 h.

Trimodal pDMAPMA was synthesized similarly to the bimodal pDMAPMA polymerization described in condition 1 above, except degassed NaOH (8 M, 500 μL) was also added after 9 h polymerization, and HCl (12 M, 335 μL) at 9 h and 6 min, with a total polymerization time of 45 h.

2.3.4.2. *Synthesis of bimodal solution and graft-from pCB*

Solution polymerization is simultaneously occurring during graft-from synthesis of pCB layers, we therefore performed the same procedure for solution and graft-from polymerizations. CB monomer (1.5 g, 6.6 mmol, 130 equiv.), 4-Cyano-4-(phenylcarbonothioylthio)pentanoic acid (14.1 mg, 0.05 mmol, 1 equiv.), 4,4′-Azobis(4-cyanopentanoic acid) (7.1 mg, 0.025 mmol, 0.5 equiv.) and butylamine (50 μL, 0.5 mmol, 10 equiv.) were dissolved in 5 mL 2:1 acetate buffer (0.1 M, pH 4.5) and 1,4-dioxane. The pH was adjusted to 4.5 with NaOH (8 M) and a CTA functionalized silicon wafer was submerged in the polymerization solution. The solution was degassed via three freeze-pump-thaw cycles, backfilled with nitrogen and incubated at 70 °C for 1 h with

gentle stirring. After 1 h, an aliquot of polymerization solution was removed for GPC characterization and degassed NaOH (8 M, 500 µL) was added to the reaction vessel to initiate aminolysis. After 5 min at high pH, HCl (12 M, 335 µL) was added to end aminolysis and the solution was reacted for an additional 23 h.

2.3.4.3. GPC characterization of solution polymers

Polymer molecular weights (M_n, M_W) and dispersity (Đ) were determined by GPC using an Agilent 1260 infinity II GPC system equipped with an Agilent 1260 infinity RI detector, and either a Superpose 6 increase 10/300 GL (GE healthcare) column (bimodal pDMAPMA, pCB with and without butylamine), Superose 6 increase 10/300 GL and HiLoad 16/600 Superdex 200 pg (GE healthcare) columns in series (trimodal pDMAPMA), or PL aquagel-OH 30 and PL aquagel-OH 40 (Agilent) columns in series (monomodal pCB) with PBS running buffer at 30°C. Columns were calibrated using polyethylene glycol (PEG) standards (M_n of 3,000 to 60,000 Da).

GPC chromatograms of bimodal pCB were deconvolved with Microsoft Excel assuming two peaks fit as normal Gaussian distributions using the included generalized reduced gradient (GRG) nonlinear algorithm. The ratio of high to low molecular weight polymers in bimodal distributions were calculated as the relative ratio of the area of these Gaussian distributions.

2.3.5. Surface characterization

2.3.5.1. Ellipsometry

Film thickness measurements were obtained using an M-2000UI (J.A. Woolam) variable angle spectroscopic ellipsometer at 55 to 75° in 5° increments with light spectrum from 250 to 1680 nm. All films were modeled as transparent single layer Cauchy films with no surface roughness on Si substrates with the CompleteEase Software package.

2.3.5.2. X-ray Photoelectron Spectroscopy

Modified wafers were analyzed with a PHI Quantera II scanning x-ray photoelectron spectroscopy (XPS) microprobe. A take-off angle of 45° was used for all samples, pass energy and step size were 224 eV and 0.8 eV for survey scans and 55 eV and 0.1 eV for high resolution scans, which were used to determine elemental composition.

2.3.5.3. Water contact angle

Static water contact angle (WCA) measurements and images were acquired with an OCA 20 (Future Digital Scientific) contact angle measurement system and calculated with the SCA 20 software module. 3 µL droplets of milliQ water were deposited on APTES functionalized, CTA functionalized, and 1 and 2 layer pCB surfaces.

2.3.6. Modification of pCB surfaces with capture agents

2.3.6.1. Bevacizumab-647 immobilization

1 and 2 layer pCB wafers were activated for protein immobilization via incubation in 200 µL of a 0.2 M EDC (76.7 mg, 0.4 mmol, 1 equiv.) and 0.05 M NHS

(11.5 mg, 0.1 mmol, 0.25 equiv.) water solution for 7 minutes at 4 °C. The wafers were then rinsed with a sodium acetate buffer (0.1 M, pH 4.5), placed in a 200 µL solution of bevacizumab-647 (500 µg mL^{-1}) in PBS, and incubated for 20 min at 4 °C in the dark. Wafers were then water bath sonicated in fresh PBS 3 times for intervals of 1 min to remove excess protein. Surface fluorescence microscopy imaging was performed with a Biotek Cytation microscope, equipped with a Cy5 filter set. Intensity quantification was performed with the ImageJ Mean Gray Value tool. Surface fluorescence values were converted to ng cm^{-2} by comparison with a calibration curve of dropcast bevacizumab-647 of known total mass onto wafers and imaged under the same conditions as experimental samples to produce a calibration curve.

2.3.6.2. *Avidin immobilization and biotin fluorescein capture*

Avidin was immobilized onto 1 and 2 layer pCB using the same procedure as bevacizumab-647. Following immobilization, surfaces were rinsed 6 times with 0.05% TWEEN 20 in PBS (PBS-T). Avidin functionalized wafers and pCB coated wafers without avidin were incubated in 100 µL of 4 µg mL^{-1} biotin-fluorescein in PBS for 2 h in the dark under agitation (orbital shaker at 100 RPM). The biotin-fluorescein solution was removed, and surfaces were rinsed 6 times with PBS-T. Fluorescence of each well was measured with a Biotek Cytation plate reader and surface fluorescence was imaged by fluorescent microscopy. Surface fluorescence values were converted to ng cm^{-2} by comparison with a calibration curve of dropcast biotin-fluorescein of known total mass onto wafers and imaged under the same conditions as experimental samples.

2.3.7. Characterization of protein and macrophage fouling on pCB coated surfaces

2.3.7.1. *Nonspecific protein fouling*

Total nonspecific protein adsorption was measured by a bicinchoninic acid (BCA) assay of collected protein, as previously reported[18–20]. Pristine silicon, 1 and 2 layer pCB, and pDMAPMA surfaces were incubated with 100% aged CBS at 37 °C for 1 h. Following incubation, the wafers were rinsed with deionized (DI) water and incubated in PBS for 15 min on an orbital shaker table at 100 RPM. The wafers were then removed from the PBS solution and dried under a stream of nitrogen. To extract adsorbed protein from the dry wafers, 120 µL of 8% SDS in DI water was added to cover the surface, the wafers were then incubated in a humidity chamber overnight at 37 °C. The SDS solution was removed from the wafers and incubated for 2 h at 37 °C with BCA assay kit reagents as per manufacturer protocol[21]. Finally, absorbance was read at 562 nm and compared against a BSA calibration curve to determine the total adsorbed protein content. The total amount of protein in the SDS solution was then determined using the BCA protein quantification assay with a calibration curve. The calibration curve was prepared using BSA calibrants in the SDS solution used to remove adsorbed protein from wafers. The lowest detectable concentration in the BSA calibration curve was 0.3 µg/mL. The SDS solutions used for BSA extraction were 120 µL and the wafers were 5.4 cm^2. Therefore, the LOD is equal to:

$$LOD = \frac{Total\ BSA\ adsorbed}{Wafer\ surface\ area}$$

$$= \frac{lowest\ detectable\ [BSA]\ x\ Volume\ of\ SDS\ solution}{Wafer\ surface\ area}$$

$$= \frac{0.3\ \frac{\mu g}{mL} * 0.12\ mL}{5.4\ cm^2} = 6.7\ ng\ cm^{-2}$$

2.3.7.2. Nonspecific macrophage adhesion

pCB coated silicon wafers were placed into a 96 well plate. Wells were soaked in 70% ethanol for 1 h to sterilize the surfaces. The ethanol was removed, and each wafer was rinsed three times with water, and incubated for 24 h with 200 µL of FBS at 37 °C. FBS was removed and 200 µL of RAW 264.7 macrophages (50 000 cells mL^{-1}) in DMEM supplemented with 10% FBS were added to each well and cultured for 2 d at 37 °C and 5% CO_2. Cell media was then removed, and each well was rinsed three times with 37 °C PBS. Cells were stained with Calcein AM and HOESCHT according to manufacturer protocols. Silicon wafers were imaged with a Biotek Cytation fluorescent microscope equipped with DAPI and GFP filter cubes, and cells with colocalized stains were counted.

2.3.8. Statistical methods

All graphed data represents mean ± standard deviation calculated from triplicate measurements of three samples prepared at the same time with one batch of biological material (when applicable), unless otherwise stated. All statistical analysis was performed

using GraphPad Prism 8. $P < 0.05$ is indicated by *, $P < 0.01$ by **, and $P < 0.001$ by ***.

2.4. Results and Discussion

2.4.1. Demonstration of pH-controlled RAFT polymerization in solution: synthesis of multimodal pDMAPMA and pCB

To demonstrate the production of multimodal polymer distributions using pH-controlled RAFT, we first conducted and characterized the solution polymerization of pDMAPMA and pCB, using a thiocarbonylthio containing CTA end group at the polymer's living end. Controlled partial degradation of the thiocarbonylthio group, which prevents further monomer addition, led to bi- or multi-modal polymer M_W distributions. Here, we reacted a fraction of polymer thiocarbonylthio end groups with an amine nucleophile, butylamine, to yield terminal thiols and a thioamide side product (**Scheme 2**).

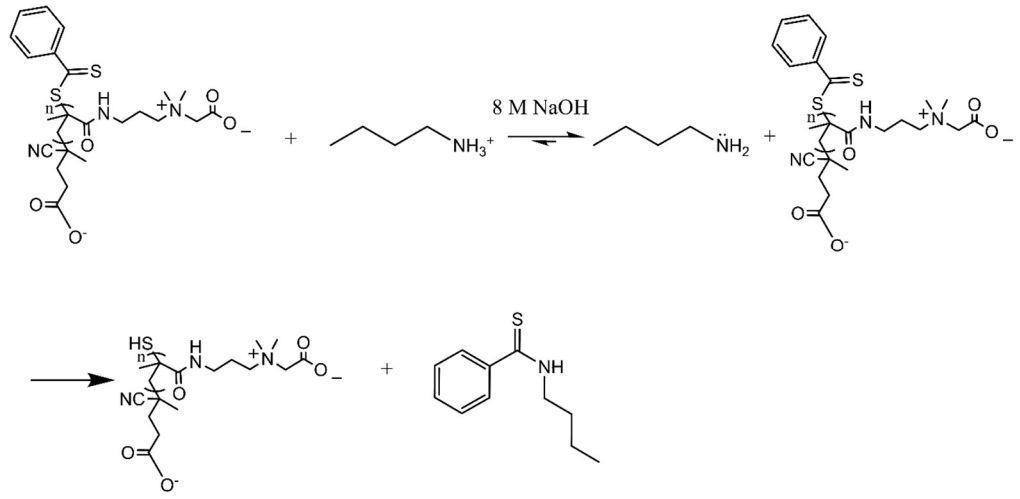

Scheme 2: Mechanism of thiocarbonylthio aminolysis. RAFT chain end modification via pH dependent aminolysis.

Partial termination of CTAs with amino nucleophiles allows for one-pot synthesis of bimodal polymer M_W distributions by temporarily raising the pH; the amine is protonated and unreactive at pH 4.5, and unprotonated and reactive at pH 11. Butylamine was chosen as the nucleophile because it is soluble under pCB's aqueous polymerization conditions and has a pKa of ~10.5[22], which minimizes aminolysis during pH 4.5 RAFT polymerization[23,24]. A 10 times molar excess of butylamine compared to CTA agent during polymerization ensured efficient aminolysis at high pH. The elapsed polymerization time prior to pH raising determined the M_W of the low M_W polymer population.

Two different bimodal pDMAPMAs were synthesized with partial aminolysis at 2 or 4 h after initiation; polymers were characterized by GPC (**Figure 2.2A**) and NMR **(Figure S2.1B).** The low M_W polymer population increased from 8.0 to 9.2 kDa as polymerization time prior to aminolysis increased from 2 to 4 h, minimal differences in Đ were observed (1.03 versus 1.05;

Table 2.1). We also confirmed that pDMAPMA's tertiary amine does not result in CTA aminolysis at pH 4.5 (**Figure S2.2)**. The ability to synthesize multimodal distributions was further tested by synthesizing a trimodal distribution of pDMAPMA with partial aminolysis at 2 and 9 h, and a total polymerization time of 45 h. This resulted in the production of three distinct M_W populations of 7 (Đ = 1.02), 70, and 391 kDa, respectively; the dispersity of the two high M_W populations could not be accurately calculated due to elution near the exclusion limit of the column (**Figure 2.2B**).

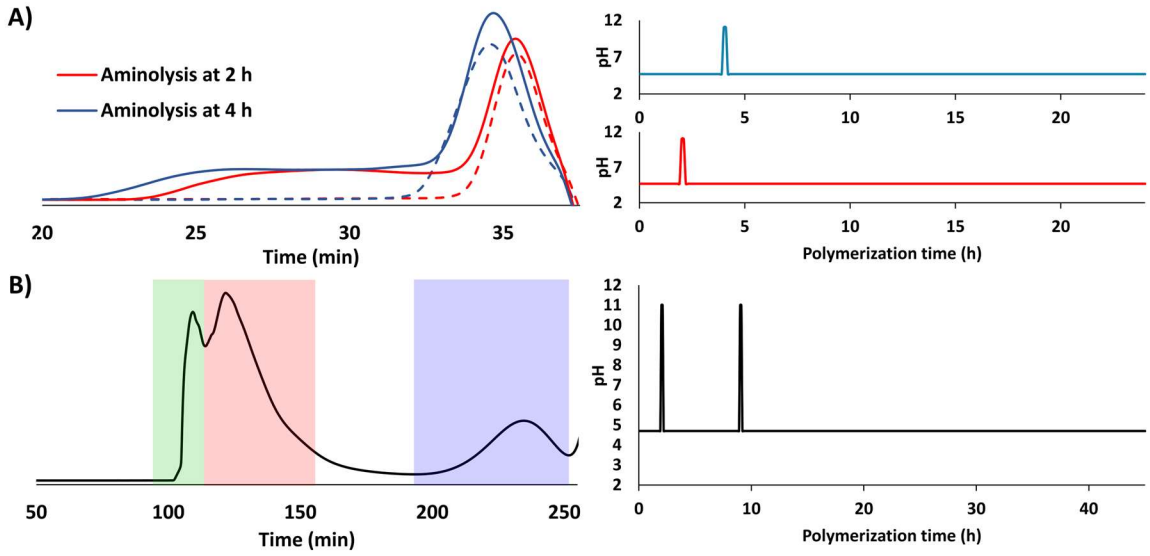

Figure 2.2. GPC analysis of multimodal distributions from solution polymerization of pDMAPMA using pH-controlled RAFT. pH time courses during polymerizations are plotted on the right. (A) GPC analysis of two different pDMAPMA polymerizations with partial CTA aminolysis at 2 (red) or 4 h (blue), respectively, by temporarily raising the pH for 5 min. GPC analysis prior to pH raising (dashed lines) demonstrated that pH raising is required for multimodal distributions. (B) pDMAPMA polymerization with sequential 6 min partial CTA aminolysis at 2 and 9 h resulted in three distinct M_W populations highlighted in blue, red and green.

Table 2.1: Characterization of low and high Mw populations in bimodal solution polymerizations. Mw = weight average molecular weight, M_n = number average molecular weight.

		Low Mw population			High Mw population		
Polymer*	**Aminolysis duration (min)**	**M_w (kDa)**	**M_n (kDa)**	**Đ**	**M_w (kDa)**	**M_n (kDa)**	**Đ**
$pDMAPMA_{2h}$	5	8.0	7.8	1.03	32.5	25.0	1.30
$pDMAPMA_{4h}$	5	9.2	8.8	1.05	43.8	32.4	1.35
pCB_{1h}	5	6.4	6.5	1.02	9.5	10.5	1.11
pCB_{1h}	30	6.4	6.5	1.02	8.8	9.4	1.07
pCB_{1h}	60	6.4	6.7	1.04	10.0	10.8	1.08

*Subscript indicates polymerization time prior to pH raising.

To determine the duration of aminolysis required for pCB bimodal distributions, pCB was synthesized with pH 11 intervals of 5, 30 or 60 mins. The 5 min interval yielded a clear bimodal distribution according to GPC analysis, with two molecular weight populations of 6.5 (Đ = 1.02) and 10.5 kDa (Đ = 1.11) (

Table 2.1, **Figure 2.3A**); the bimodal solution was further characterized by NMR (**Figure S2.1**). The 30 and 60 min intervals most likely resulted in maximum aminolysis of the CTAs and uncontrolled polymerization of propagating chains, which resulted in bimodal distributions dominated by the low M_W population (**Figure 2.3**). To determine the relative distribution of low and high M_W populations, the GPC data was deconvolved assuming Gaussian distribution to yield a 0.43:0.57 ratio of low to high M_w populations for the 5 min pH 11 time interval. Deconvolution of GPC chromatograms of conditions with 30 and 60 mins at pH 11 yielded greater proportions of the low MW population, as expected. To ensure aminolysis is required for bimodal polymerization, the pCB synthesis protocol was repeated in the absence of butylamine; no clear bimodal pCB distributions were observed in the absence of butyl amine (**Figure S2.3**)**.** Therefore, bimodal populations of pCB can be synthesized using pH-controlled RAFT with butylamine and a pH 11 interval of 5 min. Because the monomer must be stable under basic conditions for pH controlled aminolysis, CB with a 1 carbon spacer length (CSL) between charges was chosen; CBs with a CSL of 2 have been reported to undergo elimination reactions under basic conditions[25]. We confirmed that no pCB structure modifications occurred upon exposure to high pH aminolysis conditions by NMR (**Figure S2.1**).

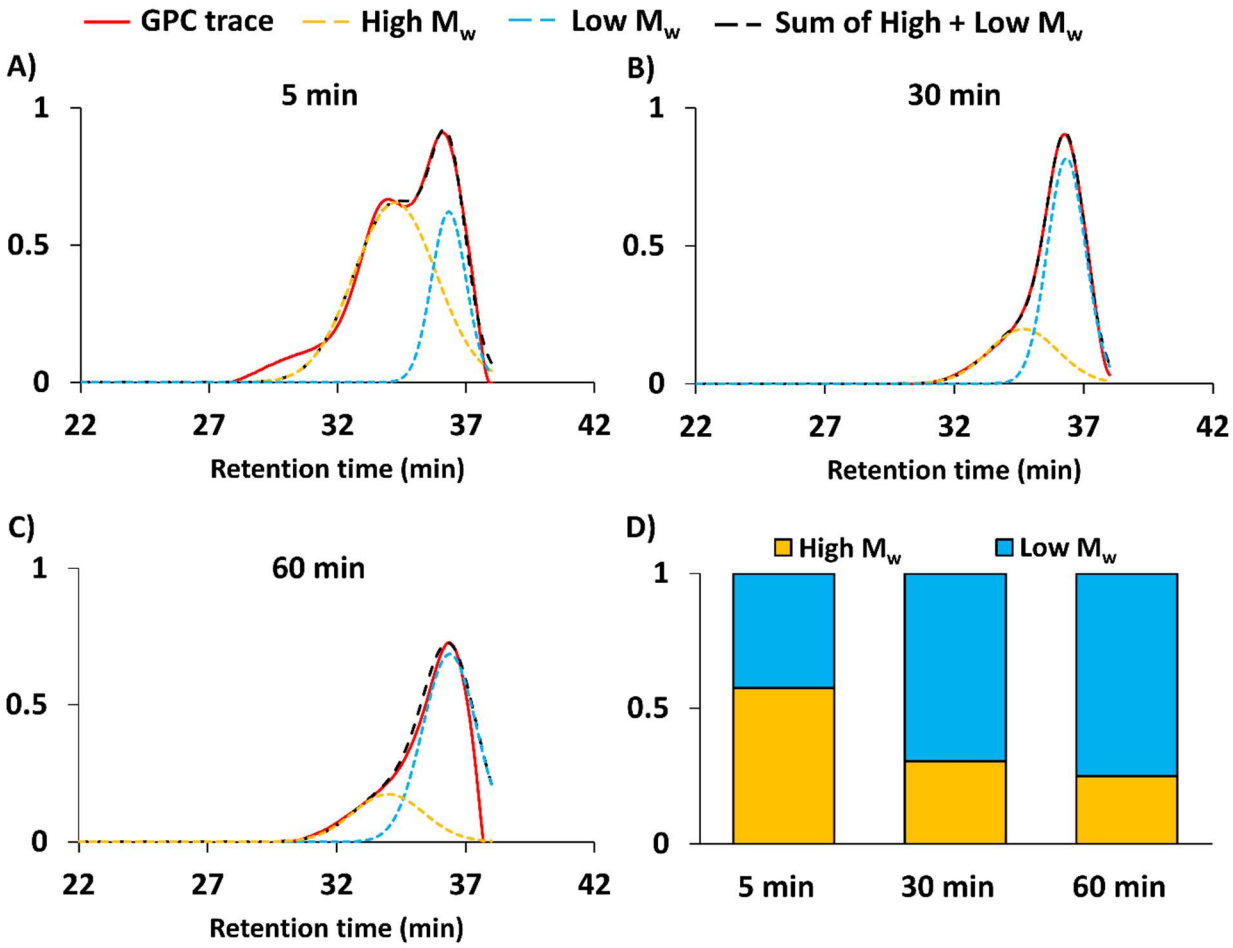

Figure 2.3: Dependence of pH 11 time interval on pCB's bimodal Mw distributions in the presence of butylamine. GPC chromatograms (red line) of bimodal pCB polymerizations conducted as follows: (1) pH was held at 4.5 for 1 h; (2) pH was temporarily raised to 11 for (A) 5, (B) 30 and (C) 60 min, respectively; and, (3) pH was returned to 4.5 for a total polymerization time of 24 h. Dashed lines represent deconvolution of GPC data as gaussian distributions to separate high (yellow) and low (blue) Mw populations; the black dashed line represents the sum of the deconvoluted high and low M_W populations. All y-axes are normalized refractive index intensity. (D) Calculated proportions of high and low M_w polymer populations from deconvolution. Control experiments without butylamine are presented in **Figure S2.3**.

2.4.2. Graft-from pCB synthesis on silicon wafer surfaces was confirmed by XPS

Using XPS, we first confirmed that the silicon wafers were activated with CTA agent and amenable to graft-from polymerization of pCB. Silicon wafers were spin coated with APTES and reacted with CTA's carboxylic acid using DIC to form an unreactive amide bond towards aminolysis. XPS of the wafers confirmed the presence of nitrogen and sulfur after immobilization of APTES and CTA, respectively, which indicates successful surface functionalization. The wafers were then immersed in a pCB polymerization solution that was then heated to initiate concurrent solution and surface pCB polymerization. After polymerization, the pCB modified wafers had greater carbon content compared to CTA modified surfaces according to XPS (**Table 2.2**). Therefore, the CTA modified wafers are amenable to pCB graft-from polymerization.

Table 2.2: XPS derived elemental composition of pristine and modified silicon wafers.

Sample	Atom %				
	C	O	N	S	Si
Pristine	4.4	44.8	–	–	50.8
APTES	13.9	40.9	2.7	–	42.5
CTA	26.9	38.2	5.8	2.2	27
1 Layer pCB	50	23.9	4.3	2.1	19.7

*1 layer pCB had a thickness of 12.6 ± 2.7 nm.

2.4.3. Graft-from synthesis of bimodal pCB through pH-controlled S-RAFT

The synthesis of bimodal pCB surfaces using pH-controlled S-RAFT was confirmed through WCA, spectral ellipsometry, and protein loading. Bimodal pCB layers were successfully polymerized with a 5 min pH 11 interval after 1 h of polymerization, as described in section 3.1. As controls, 1 layer pCB wafers were prepared with a total polymerization time of 1 h at pH 4.5.

To follow each surface modification step, the WCA of the wafers was measured after APTES, CTA, 1 layer pCB and 2 layer pCB synthetic steps. APTES modified surfaces demonstrated a WCA of ~ 40° that is characteristic of an aminosilane monolayer on silicon surfaces[26], where the amines are orientated away from the surface with all three ethoxy groups reacted. CTA functionalized surfaces demonstrated WCAs (~55°) typical of CTA ,4-Cyano-4-(phenylcarbonothioylthio)pentanoic acid, monolayers[27]. The WCA of pCB modified surfaces is dependent on the degree of polymerization[28]; therefore, 2 layer (bimodal) pCB surfaces with a 24 h polymerization time had a lower WCA than 1 layer pCB surfaces with a 1 h polymerization time. The WCA of the bimodal architecture (~10°) is hydrophilic and equivalent to the those previously reported for thick pCB layers[29]. The high variability in WCA for 1 layer pCB modified wafers (standard deviation of 10, **Figure 2.4**) is characteristic of thin coatings due to the sensitivity of WCA measurements to slight film thickness variations[28]. To demonstrate that polymerization time (i.e. degree of polymerization) influences WCA measurements, the WCA of unimodal and bimodal pCB surfaces produced using a 24 h polymerization timed had similar WCAs (**Figure 2.4**, **Figure S2.4**).

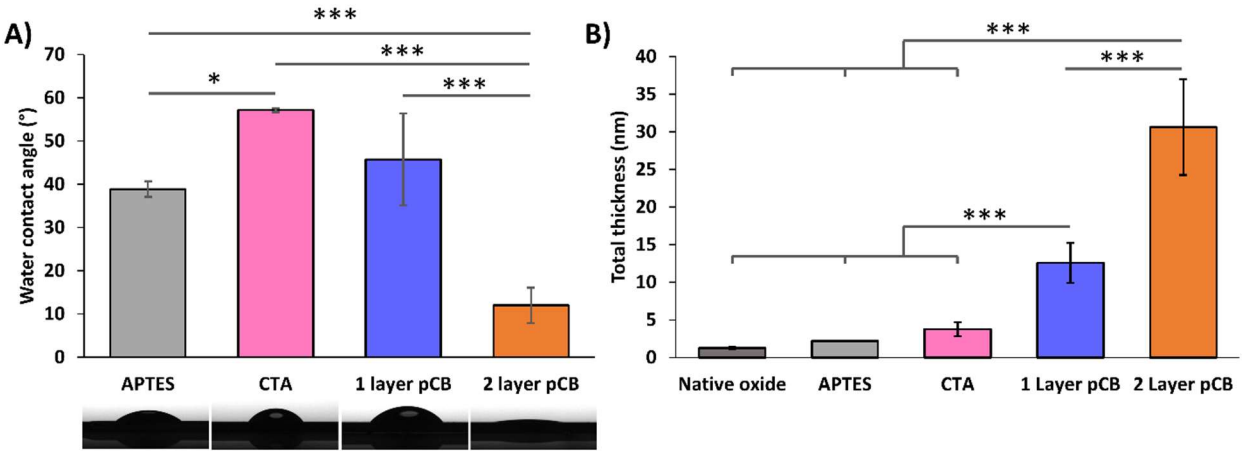

Figure 2.4: Surface characterization of functionalized silicon wafers by WCA and ellipsometry. (A) Static WCA and representative photographs of 3 µL water droplets on wafers functionalized with aminosilane, CTA, and 1 and 2 layer pCB coatings. Hydrophobic CTA increased the WCA contact, whereas increasing pCB content decreased the WCA. The WCA of 1 layer pCB was greater than 2 layer pCB due to differences in layer thickness. (B) Modeled layer thickness of native oxide, APTES, CTA, and 1 and 2 layer pCB coatings from spectral ellipsometric measurements. Statistics performed by one-way analysis of variance (ANOVA) with Bonferroni's multiple comparison test (mean ± standard deviation $p < 0.05$ (*), and $p < 0.001$ by (***)).

The greater thickness of 2 layer pCB architectures compared to 1 layer pCB was confirmed by spectral ellipsometry of dry pCB films. The average thickness of the 2 layer coating was ~2.4 times greater than the 1 layer coating (**Figure 2.4B**), due to the formation of the low-density second layer. The layer thickness increased at each modification step from the native oxide layer on the silicon wafer, APTES, CTA, 1 layer pCB and 2 layer pCB (**Figure 2.4B**), indicating a successful modification procedure.

The 2 layer pCB architecture was also confirmed to have greater antibody loading potential through the immobilization of a fluorescent antibody, bevacizumab modified with Alexa 647 (**Figure 2.5**). Bimodal pCB layers have previously been shown to increase the surface capacity of immobilized antibodies when compared to monomodal

brush pCB layers, where thicker low density layers lead to greater loading levels[16]. High-density monomodal polymer layers demonstrate lower degrees of protein immobilization because high-density of polymer chains prevent biomacromolecule diffusion[30]. Using EDC/NHS chemistry to activate pCB carboxylic acids, Alexa 647 modified bevacizumab was immobilized onto monomodal brush and bimodal pCB surfaces. Wafers were then characterized by surface fluorescence, which indicated ~5 times greater bevacizumab immobilization on bimodal surfaces. Therefore, bimodal pCB surfaces produced through pH controlled S-RAFT retained the advantageous property of greater capture agent immobilization.

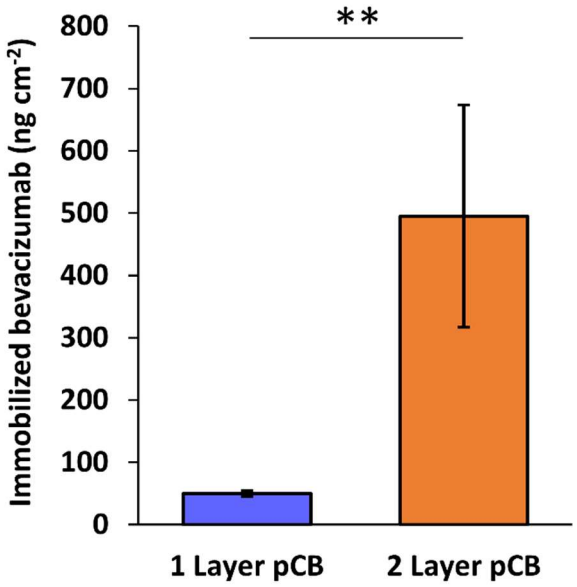

Figure 2.5: Immobilization of bevacizumab confirmed the greater loading capacity of bimodal pCB wafers. Fluorescently labelled bevacizumab was immobilized using EDC/NHS chemistry on 1 (brush) and 2 layer (bimodal) pCB wafers. After quantification by fluorescent microscopy, the 2 layer pCB architecture was confirmed to have a higher loading capacity than 1 layer pCB. $P < 0.01$ (**), by student's t-test, mean ± standard deviation.

2.4.4. Avidin modified bimodal pCB surfaces enhanced biotin capture

Bimodal pCB layers functionalized with avidin captured approximately 4 times more biotin-fluorescein than avidin modified brush pCB surfaces (**Figure 2.6**). The improved capturing capacity is similar to previously reported bimodal polymer surfaces which increased capacity by 1.8 to 3.1 times[9,15]. Avidin was first immobilized on the pCB surfaces using EDC/NHS chemistry. The surfaces were then incubated in biotin-fluorescein solutions for 2 h, then extensively washed to remove unbound biotin. Fluorescence microscopy was performed on biotin-fluorescein exposed 1 and 2 pCB layer surfaces with and without immobilized avidin (**Figure 2.6B**). The bimodal 2 layer pCB surfaces with avidin had greater total fluorescence intensity, which indicates a greater amount of captured biotin-fluorescein compared to 1 layer pCB surfaces. Quantitative surface fluorescence measurements indicated ~4 times increase in biotin-fluorescein capture on bimodal (2 layer) architectures when compared to brush (1 layer) surfaces (**Figure 2.6C**); surfaces without avidin were used as background controls. Therefore, bimodal architectures improved both capture agent immobilization and target molecule binding.

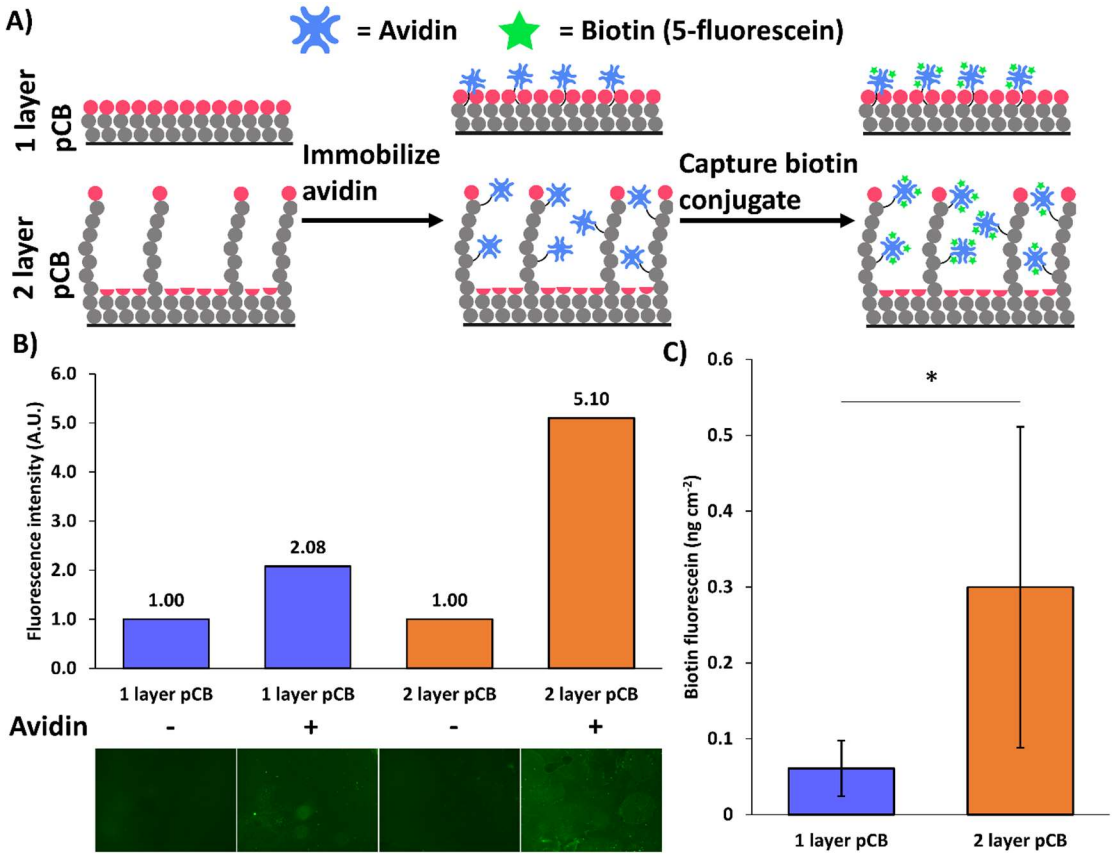

Figure 2.6. Bimodal, two layer, pCB wafers modified with avidin have greater biotin capturing efficiency. (A) Schematic for the modification of pCB surfaces with avidin and subsequent biotin-fluorescein capture. (B) Representative fluorescent micrographs (4x magnification) and micrograph fluorescent intensity from 1 and 2 layer pCB surfaces with and without avidin that were exposed to biotin-fluorescein. (C) Surface fluorescence quantification of biotin-fluorescein bound to avidin modified surfaces (n = 5 for 1 layer pCB, n= 6 for 2 layer pCB, mean ± standard deviation, $p < 0.05$ (*), student's t-test). Background signal was removed by measuring fluorescence of avidin-free surfaces after exposure to biotin-fluorescein.

2.4.5. pCB surfaces prepared by pH-controlled RAFT are antifouling

1 and 2 layer pCB architectures had similar antifouling properties due to the pCB brush architecture present on both surfaces. pCB coatings synthesized by the graft-from method are employed to generate antifouling surfaces towards proteins, which has been

defined as below 5 ng cm^{-2} [31]; whereas, surfaces prepared by graft-to methods exposed to undiluted serum nonspecifically adsorb proteins at 11 ng cm^{-2} [32]. In this study, 1 and 2 layer pCB architectures were exposed to 100% aged CBS to evaluate protein fouling in complex media relevant for biological applications; aged serum has been shown to foul surfaces to a greater degree than fresh serum[33]. pCB surfaces were compared to positive fouling controls of cationic pDMAPMA modified surfaces and anionic plasma cleaned SiO_2 wafers. All surfaces were incubated in CBS for 1 h and washed extensively in PBS prior to adsorbed protein quantification using an SDS extraction method and the BCA protein quantification assay, as previously described[20]. Adsorbed protein on the 1 and 2 layer pCB surfaces was below the assay detection limit of 6.7 ng cm^{-2}, while the pDMAPMA control surface had ~130 ng of adsorbed protein per cm^{-2} (**Figure 2.7A**). The calculated values of adsorbed protein assume complete removal with SDS, which has been shown to not hold for all protein interactions[34], and thus represent lower bounds. Despite the limitations of protein collection with SDS solutions, the relative amounts of protein detected on pCB coated surfaces and control surfaces show that both 1 and 2 layer pCB coatings improve protein fouling resistance. The relative decrease in detected protein here is similar to previously reported relative changes in protein fouling from pCB coatings when compared to uncoated control substrates detected with the same SDS BCA assay (~20x) [35,36]. Therefore, bimodal pCB surfaces synthesized by pH-controlled S-RAFT resist protein fouling to a similar extent as previously reported bimodal architectures synthesized by SI-ATRP and SI-PIMP.

Surface fouling was further characterized by quantifying nonspecific macrophage adhesion to serum exposed surfaces. Both 1 and 2 layer pCB coatings reduced macrophage adhesion by > 90% when compared to tissue culture plastic (TCP) and plasma cleaned wafers (SiO_2; **Figure 2.7B, C**). To ensure maximum macrophage binding, all surfaces were pre-incubated in FBS for 24 h prior to cell seeding (10,000 macrophages per surface). After seeding, surfaces were cultured for an additional 2 d to promote maximum macrophage adhesion to identify potential difference in nonspecific macrophage adhesion. Surfaces were then gently washed with PBS and cells were stained with HOESCHT and calcein AM for counting. Both 1 and 2 layer pCB decreased macrophage adhesion to a similar extent (**Figure 2.7B, C**), indicating both surfaces had similar antifouling properties towards cells, as expected.

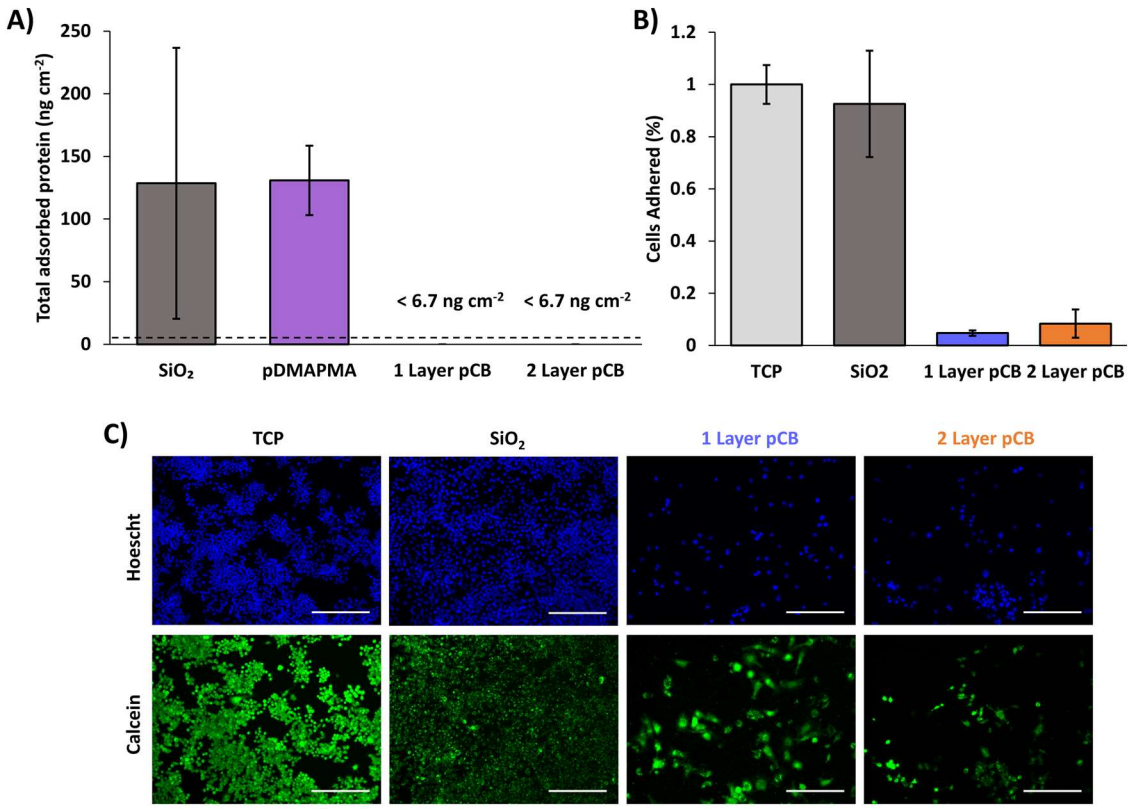

Figure 2.7: One and two layer pCB surfaces were equally antifouling when exposed to serum. (A) Non-specific protein adsorption onto pristine silicon wafers and wafers functionalized with single layers of pDMAPMA and pCB, and bimodal pCB when incubated in CBS for 24 h; cationic pDMAPMA and anionic SiO_2 surfaces were included as a positive fouling control. No adsorbed protein was detected on 1 or 2 layer pCB (detection limit of the assay was 6.7 ng cm^{-2}); protein adsorption was therefore comparable to antifouling surfaces[31]. (B) After 48 h of culturing, relative amounts of adhered macrophages on surfaces pre-exposed to serum for 24 h was quantified. Cell counts were determined from fluorescent micrographs; numbers were normalized to the tissue culture plastic (TCP) control. (C) Representative fluorescent micrographs of adhered macrophages stained with HOESCHT and calcein AM, scale bars = 200 μm.

2.5. Further discussion

pH-controlled bimodal S-RAFT polymerization simplifies the synthesis of bimodal pCB layers and avoids the use of potentially toxic materials (e.g., Cu), increasing the accessibility of bimodal pCB surfaces for incorporation into sensors and medical devices. Bimodal architectures were achieved by the temporal control of pH

(through NaOH and HCl additions) to temporarily deprotonate butylamine for partial CTA aminolysis. The method can be extended to other CTAs due to the standard thiocarbonylthio bond found in many RAFT CTAs[37], enabling polymerization of monomers that may not be compatible with 4-Cyano-4-(phenylcarbonothioylthio)pentanoic acid. This technique can further be extended to other substrate materials such as gold, an important substrate for biosensors, as only the initial amine functionalization chemistry must be adapted; S-RAFT has previously been performed on gold surfaces[38].

The development of high loading, antifouling surfaces is particularly important for biomedical sensors and blood purification devices. The ability to rapidly detect cytokines in blood or tissue extracts is increasingly important due to the development of immune modulating drugs such as cancer immunotherapies, where cytokine levels are carefully tracked[39]. Recently, the development of polymeric surfaces for blood cytokine[40] and lipopolysaccharide[41] (LPS) filtration has shown promise for the treatment of sepsis; cytokine filtration could also have applications in cardio-renal syndromes[42]. Blood filtration with antifouling bioactive surfaces can selectively alter blood biochemistry with temporal control by administering in-line filters to patients[43].

2.6. Conclusions

The development of antifouling surfaces that selectively capture molecules from biological fluids is crucial in the development of biosensors and blood filtration devices. We developed pH-controlled S-RAFT to simplify the synthesis of bimodal pCB layers that increase capturing efficiency while retaining antifouling properties. Compared to

monomodal pCB architectures, bimodal surfaces improved capture agent, antibody, immobilization and target molecule, biotin-fluorescein, capture by 4 to 5 times. pH-controlled S-RAFT only requires a temporary increase in pH for CTA aminolysis during surface preparation, which will help towards increasing the accessibility of bimodal architectures for biomedical applications.

2.7. Supporting information

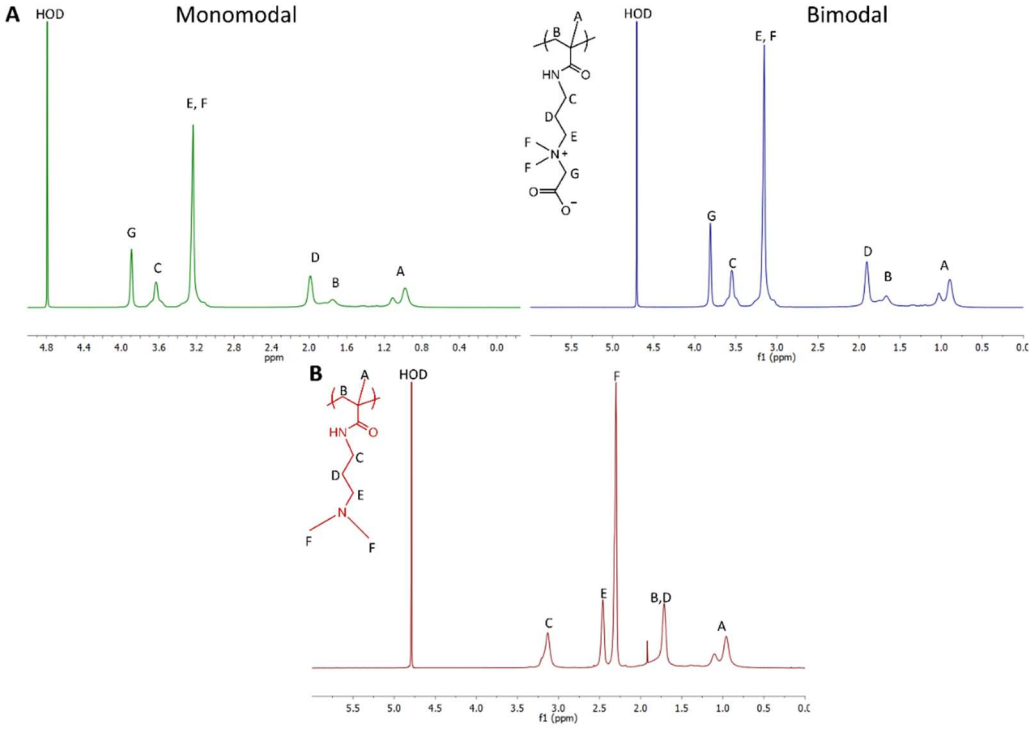

Figure S2.1: ^{1}H NMR (600 MHz) spectra of (A) monomodal and bimodal pCB and (B) pDMAPMA in D_2O.

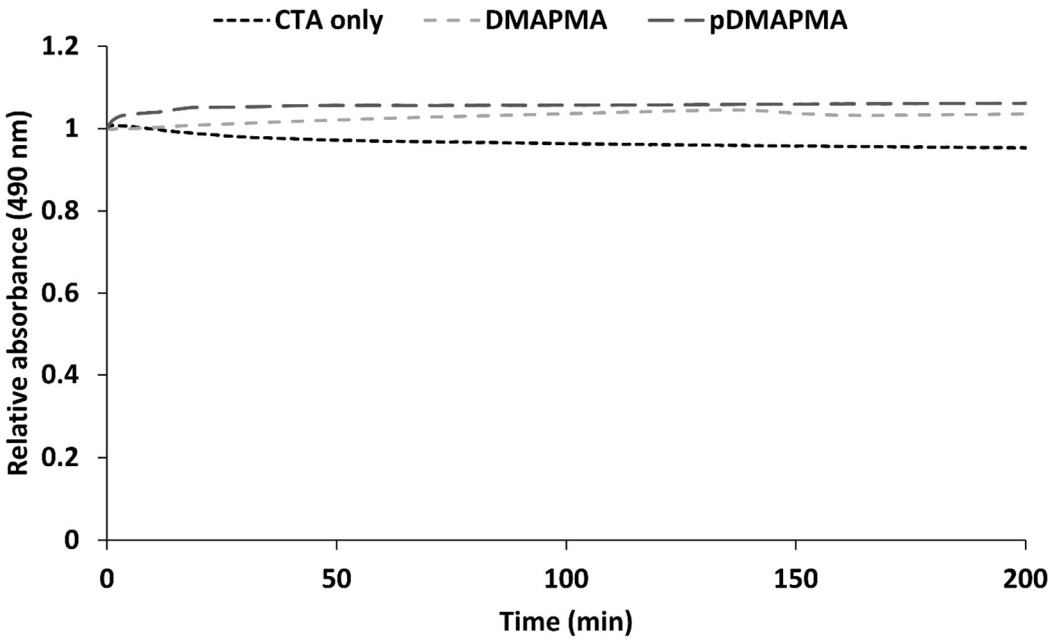

Figure S2.2: Degradation of CTA solutions at pH 4.5. Three solutions of CTA only, CTA + DMAPMA and CTA + pDMAPMA in 2:1 acetate buffer (0.1 M, pH 4.5) and 1,4-dioxane were prepared. The absorbance at 490 nm will decrease upon aminolysis. No decrease in absorbance was observed when CTA was exposed to DMPAMA or pDMAPMA, indicating the tertiary amine of DMPAMA or pDMAPMA does not result in significant CTA aminolysis at pH 4.5.

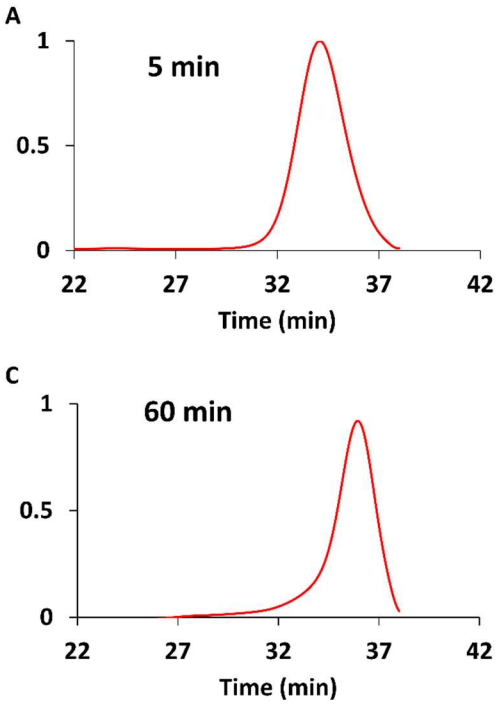

D

Polymer	pH 11 (min)	M_n (kDa)	M_w (kDa)	Đ
pCB_{1h}	5	9.7	10.3	1.06
	30	8.5	8.9	1.05
	60	7.3	7.9	1.07

Figure S2.3: GPC chromatograms of pCB distributions as a function of polymerization time at pH 11 without butylamine. pCB synthesized without butylamine where the pH was raised to 11 at 1 h for A) 5, B) 30 and C) 60 min, respectively, with a total polymerization time of 24 h. All y-axes are normalized refractive index intensity. D) Summary of calculated GPC data for chromatograms A-C. No bimodal distribution was observed in the absence of butylamine.

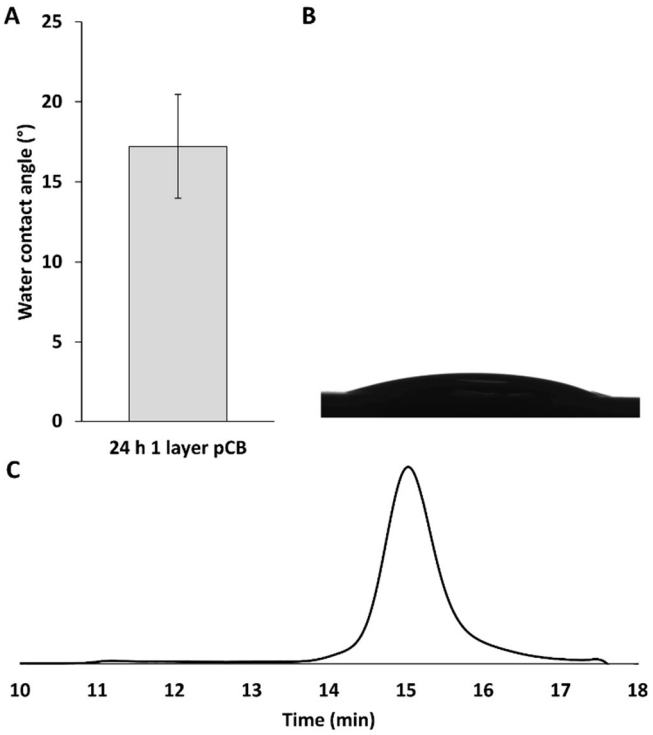

Figure S2.4: Thick 1 layer monomodal pCB surface. A) Static contact angle of 3 µL water droplets on wafers functionalized with 1 layer pCB with a total polymerization time of 24 h. The WCA of the thick layer presented here (17°) was much lower than thin 1 layer pCB surfaces presented in Figure 4A, demonstrating the thickness dependence of WCA measurements. B) Representative photograph of water droplets on pCB functionalized wafer. C) GPC chromatogram of solution monomodal pCB produced during the synthesis of thick 1 layer pCB surfaces (MW = 29 kDa, Đ = 1.1, analyzed on PL aquagel-OH 30 and PL aquagel-OH 40).

2.8. References

(1) Vaisocherová, H.; Šípová, H.; Víšová, I.; Bocková, M.; Špringer, T.; Laura Ermini, M.; Song, X.; Krejčík, Z.; Chrastinová, L.; Pastva, O.; Pimková, K.; Dostálová Merkerová, M.; Dyr, J. E.; Homola, J. Rapid and Sensitive Detection of Multiple MicroRNAs in Cell Lysate by Low-Fouling Surface Plasmon Resonance Biosensor. *Biosens. Bioelectron.* **2015**, *70*, 226–231. https://doi.org/10.1016/j.bios.2015.03.038.

(2) Vaisocherová-Lísalová, H.; Víšová, I.; Ermini, M. L.; Špringer, T.; Song, X. C.; Mrázek, J.; Lamačová, J.; Scott Lynn, N.; Šedivák, P.; Homola, J. Low-Fouling Surface Plasmon Resonance Biosensor for Multi-Step Detection of Foodborne Bacterial Pathogens in Complex Food Samples. *Biosens. Bioelectron.* **2016**, *80*, 84–90. https://doi.org/10.1016/j.bios.2016.01.040.

(3) Wang, J.; Hui, N. Zwitterionic Poly(Carboxybetaine) Functionalized Conducting Polymer Polyaniline Nanowires for the Electrochemical Detection of Carcinoembryonic Antigen in Undiluted Blood Serum. *Bioelectrochemistry* **2019**, *125*, 90–96. https://doi.org/10.1016/j.bioelechem.2018.09.006.

(4) Liu, N.; Hui, N.; Davis, J. J.; Luo, X. Low Fouling Protein Detection in Complex Biological Media Supported by a Designed Multifunctional Peptide. *ACS Sensors* **2018**, *3*, 1210–1216. https://doi.org/10.1021/acssensors.8b00318.

(5) Baggerman, J.; Smulders, M. M. J.; Zuilhof, H. Romantic Surfaces: A Systematic Overview of Stable, Biospecific, and Antifouling Zwitterionic Surfaces. *Langmuir* **2019**, *35* (5), 1072–1084. https://doi.org/10.1021/acs.langmuir.8b03360.

(6) Sun, F.; Hung, H. C.; Sinclair, A.; Zhang, P.; Bai, T.; Galvan, D. D.; Jain, P.; Li, B.; Jiang, S.; Yu, Q. Hierarchical Zwitterionic Modification of a SERS Substrate Enables Real-Time Drug Monitoring in Blood Plasma. *Nat. Commun.* **2016**, *7*, 1–9. https://doi.org/10.1038/ncomms13437.

(7) Prime, K. L.; Whitesides, G. M. Adsorption of Proteins onto Surfaces Containing End-Attached Oligo(Ethylene Oxide): A Model System Using Self-Assembled Monolayers. *J. Am. Chem. Soc.* **1993**, *115* (23), 10714–10721. https://doi.org/10.1021/ja00076a032.

(8) Brady, R. F. Properties Which Influence Marine Fouling Resistance in Polymers Containing Silicon and Fluorine. *Prog. Org. Coatings* **1999**, *35* (1–4), 31–35. https://doi.org/10.1016/S0300-9440(99)00005-3.

(9) Huang, C.; Brault, N. D.; Li, Y.; Yu, Q.; Jiang, S. Controlled Hierarchical Architecture in Surface-Initiated Zwitterionic Polymer Brushes with Structurally Regulated Functionalities. **2012**, 1834–1837.

(10) Keefe, A. J.; Jiang, S. Poly(Zwitterionic)Protein Conjugates Offer Increased Stability without Sacrificing Binding Affinity or Bioactivity. *Nat. Chem.* **2012**, *4* (1), 59–63. https://doi.org/10.1038/nchem.1213.

(11) Zhang, L.; Sun, Y. Poly(Carboxybetaine Methacrylate)-Grafted Silica Nanoparticle: A Novel Carrier for Enzyme Immobilization. *Biochem. Eng. J.* **2018**, *132*, 122–129. https://doi.org/10.1016/j.bej.2018.01.013.

(12) Zoppe, J. O.; Ataman, N. C.; Mocny, P.; Wang, J.; Moraes, J.; Klok, H. Surface-Initiated Controlled Radical Polymerization: State-of-the-Art, Opportunities, and Challenges in Surface and Interface Engineering with Polymer Brushes. *Chem. Rev.* **2017**, *117* (3), 1105–1318.

(13) Michalek, L.; Barner, L.; Barner-Kowollik, C. Polymer on Top: Current Limits and Future Perspectives of Quantitatively Evaluating Surface Grafting. *Adv. Mater.* **2018**, *30* (21), 1–18. https://doi.org/10.1002/adma.201706321.

(14) Norde, W.; Gags, D. Interaction of Bovine Serum Albumin and Human Blood Plasma with PEO-Tethered Surfaces: Influence of PEO Chain Length, Grafting Density, and Temperature. *Langmuir* **2004**, *20* (10), 4162–4167. https://doi.org/10.1021/la030417t.

(15) Huang, C. J.; Li, Y.; Jiang, S. Zwitterionic Polymer-Based Platform with Two-Layer Architecture for Ultra Low Fouling and High Protein Loading. *Anal. Chem.* **2012**, *84* (7), 3440–3445. https://doi.org/10.1021/ac3003769.

(16) Brault, N. D.; Sundaram, H. S.; Huang, C. J.; Li, Y.; Yu, Q.; Jiang, S. Two-Layer Architecture Using Atom Transfer Radical Polymerization for Enhanced Sensing and Detection in Complex Media. *Biomacromolecules* **2012**, *13* (12), 4049–4056. https://doi.org/10.1021/bm301335r.

(17) Cao, Z.; Yu, Q.; Xue, H.; Cheng, G.; Jiang, S. Nanoparticles for Drug Delivery Prepared from Amphiphilic PLGA Zwitterionic Block Copolymers with Sharp Contrast in Polarity between Two Blocks. *Angew. Chemie - Int. Ed.* **2010**, *49* (22), 3771–3776. https://doi.org/10.1002/anie.200907079.

(18) Ma, Y.; Bian, X.; He, L.; Cai, M.; Xie, X.; Luo, X. Immobilization of Poly(Acrylamide) Brushes onto Poly(Caprolactone) Surface by Combining ATRP and "Click" Chemistry: Synthesis, Characterization and Evaluation of Protein Adhesion. *Appl. Surf. Sci.* **2015**, *329*, 223–233. https://doi.org/10.1016/j.apsusc.2014.12.149.

(19) Ju, H.; McCloskey, B. D.; Sagle, A. C.; Kusuma, V. A.; Freeman, B. D. Preparation and Characterization of Crosslinked Poly(Ethylene Glycol) Diacrylate Hydrogels as Fouling-Resistant Membrane Coating Materials. *J. Memb. Sci.* **2009**, *330* (1–2), 180–188. https://doi.org/10.1016/j.memsci.2008.12.054.

(20) Dong, D.; Li, J.; Cui, M.; Wang, J.; Zhou, Y.; Luo, L.; Wei, Y.; Ye, L.; Sun, H.; Yao, F. In Situ "Clickable" Zwitterionic Starch-Based Hydrogel for 3D Cell Encapsulation. *ACS Appl. Mater. Interfaces* **2016**, *8* (7), 4442–4455. https://doi.org/10.1021/acsami.5b12141.

(21) Thermo Scientific. Pierce BCA Protein Assay Kit, 1296.9. *Pierce Biotechnol.* **2011**, *0747* (23225, 23227), 1–7. https://doi.org/10.1016/j.ijproman.2010.02.012.

(22) Ayediran, D.; Bamkole, T.; Hirst, J.; Onyido, I. Kinetics of the Reactions of Piperidine, n-Butylamine, Morpholine, and Benzylamine with 2,4-Dinitrophenyl Phenyl Ether. *Tetrahedron* **1974**, No. 1670, 1970–1975.

(23) Thomas, D. B.; Convertine, A. J.; Hester, R. D.; Lowe, A. B.; Mccormick, C. L. Hydrolytic Susceptibility of Dithioester Chain Transfer Agents and Implications in Aqueous RAFT Polymerizations. **2004**, 1735–1741.

(24) McCormick, C. L.; Lowe, A. B. Aqueous RAFT Polymerization: Recent Developments in Synthesis of Functional Water-Soluble (Co)Polymers with

Controlled Structures. *Acc. Chem. Res.* **2004**, *37* (5), 312–325. https://doi.org/10.1021/ar0302484.

(25) Cao, B.; Li, L.; Tang, Q.; Cheng, G. The Impact of Structure on Elasticity, Switchability, Stability and Functionality of an All-in-One Carboxybetaine Elastomer. *Biomaterials* **2013**, *34* (31), 7592–7600. https://doi.org/10.1016/j.biomaterials.2013.06.063.

(26) Kyaw, H. H.; Al-Harthi, S. H.; Sellai, A.; Dutta, J. Self-Organization of Gold Nanoparticles on Silanated Surfaces. *Beilstein J. Nanotechnol.* **2015**, *6* (1), 2345–2353. https://doi.org/10.3762/bjnano.6.242.

(27) Gurbuz, N.; Demirci, S.; Yavuz, S.; Caykara, T. Synthesis of Cationic N - [3- (Dimethylamino) Propyl] Methacrylamide Brushes on Silicon Wafer via Surface-Initiated RAFT Polymerization. **2011**, *49*, 423–431. https://doi.org/10.1002/POLA.

(28) Wang, M.; Yuan, J.; Huang, X.; Cai, X.; Li, L.; Shen, J. Grafting of Carboxybetaine Brush onto Cellulose Membranes via Surface-Initiated ARGET-ATRP for Improving Blood Compatibility. *Colloids Surfaces B Biointerfaces* **2013**, *103*, 52–58. https://doi.org/10.1016/j.colsurfb.2012.10.025.

(29) Aldred, N.; Li, G.; Gao, Y.; Clare, A. S.; Jiang, S. Modulation of Barnacle (Balanus Amphitrite Darwin) Cyprid Settlement Behavior by Sulfobetaine and Carboxybetaine Methacrylate Polymer Coatings. *Biofouling* **2010**, *26* (6), 673–683. https://doi.org/10.1080/08927014.2010.506677.

(30) Ma, H.; He, J.; Liu, X.; Gan, J.; Jin, G.; Zhou, J. Surface Initiated Polymerization from Substrates of Low Initiator Density and Its Applications in Biosensors. *ACS Appl. Mater. Interfaces* **2010**, *2* (11), 3223–3230. https://doi.org/10.1021/am1006832.

(31) Brault, N. D.; Sundaram, H. S.; Li, Y.; Huang, C. J.; Yu, Q.; Jiang, S. Dry Film Refractive Index as an Important Parameter for Ultra-Low Fouling Surface Coatings. *Biomacromolecules* **2012**, *13* (3), 589–593. https://doi.org/10.1021/bm3001217.

(32) Brault, N. D.; Gao, C.; Xue, H.; Piliarik, M.; Homola, J.; Jiang, S.; Yu, Q. Ultra-Low Fouling and Functionalizable Zwitterionic Coatings Grafted onto SiO2via a Biomimetic Adhesive Group for Sensing and Detection in Complex Media. *Biosens. Bioelectron.* **2010**, *25* (10), 2276–2282. https://doi.org/10.1016/j.bios.2010.03.012.

(33) Yang, W.; Xue, H.; Li, W.; And, J. Z.; Jiang, S. Pursuing "Zero" Protein Adsorption of Poly(Carboxybetaine) from Undiluted Blood Serum and Plasma. *Langmuir* **2009**, *25* (19), 11911–11916. https://doi.org/10.1021/la9015788.

(34) Riedel, T.; Majek, P.; Riedelova-Reicheltola, Z.; Vorobii, M.; Houska, M.; Rodriguez-Emmenegger, C. Total Removal of Intact Blood Plasma Proteins

Deposited on Surface-Grafted Polymer Brushes. *Anal. Methods* **2016**, No. 8, 6415–6419. https://doi.org/10.1039/c6ay01833e.

(35) Zhang, Z.; Chao, T.; Chen, S.; Jiang, S. Superlow Fouling Sulfobetaine and Carboxybetaine Polymers on Glass Slides. *Langmuir* **2006**, *22* (24), 10072–10077. https://doi.org/10.1021/la062175d.

(36) Lin, X.; Kelly, M. O.; Wu, K.; Jain, P.; Liu, E. J.; Hsieh, Y.; Zhou, Q.; Li, B.; Hung, H.; Jiang, S. Zwitterionic Carboxybetaine Polymers Extend the Shelf-Life of Human Platelets. *Acta Biomater.* **2020**, No. xxxx. https://doi.org/10.1016/j.actbio.2020.03.032.

(37) Chong, B. Y. K.; Le, T. P. T.; Moad, G.; Rizzardo, E.; Thang, S. H. More Versatile Route to Block Copolymers and Other Polymers of Complex Architecture by Living Radical Polymerization: The RAFT Process. *Macromolecules* **1999**, *32* (6), 2071–2074. https://doi.org/10.1021/ma981472p.

(38) Raula, J.; Shan, J.; Nuopponen, M.; Niskanen, A.; Jiang, H.; Kauppinen, E. I.; Tenhu, H. Synthesis of Gold Nanoparticles Grafted with a Thermoresponsive Polymer by Surface-Induced Reversible-Addition-Fragmentation Chain-Transfer Polymerization. *Langmuir* **2003**, *19* (8), 3499–3504. https://doi.org/10.1021/la026872r.

(39) Hegde, P. S.; Karanikas, V.; Evers, S. The Where , the When and the How of Immune Monitoring for Cancer Immunotherapies. *Clin. Cancer Res.* **2016**, No. 9, 1865–1875.

(40) Mcalvin, J. B.; Karnik, R.; Kohane, D. S.; Mcalvin, J. B.; Wylie, R. G.; Ramchander, K.; Nguyen, M. T.; Lok, C. K.; Shomorony, A.; Vasilyev, N. V.; Armstrong, P.; Yang, J.; Alexander, M.; Okonkwo, O. S.; Karnik, R.; Kohane, D. S. Antibody-Modified Conduits for Highly Selective Cytokine Elimination from Blood Find the Latest Version : Antibody-Modified Conduits for Highly Selective Cytokine Elimination from Blood. *JCI Insight* **2018**, *3* (13), e121133. https://doi.org/10.1172/jci.insight.121133.

(41) Kostina, N. Y.; Singh, S.; Vorobii, M.; Horak, D.; Grottke, O.; Grama, S.; Rahimi, K.; Söder, D.; Pop-Georgievski, O.; Sturcova, A.; Rodriguez-Emmenegger, C. Antifouling Microparticles To Scavenge Lipopolysaccharide from Human Blood Plasma. *Biomacromolecules* **2019**.

(42) Di Lullo, L.; Bellasi, A.; Barbera, V.; Russo, D.; Russo, L.; Di Iorio, B.; Cozzolino, M.; Ronco, C. Pathophysiology of the Cardio-Renal Syndromes Types 1–5: An Uptodate. *Indian Heart J.* **2017**, *69* (2), 255–265. https://doi.org/10.1016/j.ihj.2017.01.005.

(43) Monard, C.; Rimmelé, T.; Ronco, C. Extracorporeal Blood Purification Therapies for Sepsis. *Blood Purif.* **2019**, *47* (Suppl3), 2–15. https://doi.org/10.1159/000499520.

CHAPTER 3. GRAFT-THEN-SHRINK: SIMULTANEOUS GENERATION OF ANTIFOULING POLYMERIC SURFACES AND LSPR BIOSENSORS

Author's Preface:

The following chapter has been reprinted with permission from ACS Appl. Mater. Interfaces 2021, 13, 44, 52362–52373. Copyright 2021 American Chemical Society., and was published in *ACS Applied Materials & Interfaces* under the citation:

Jesmer, A.H., Huynh, V., Marple, A.S., Ding, X., Moran-Mirabal, J.M. and Wylie, R.G., 2021. Graft-Then-Shrink: Simultaneous Generation of Antifouling Polymeric Interfaces and Localized Surface Plasmon Resonance Biosensors. ACS Applied Materials & Interfaces, 13(44), pp.52362-52373.

A.H. Jesmer planned the study, conducted most of the experiments and wrote the manuscript. V. Huynh assisted with protein fouling experiments, A.S. Marple assisted with sensing experiments, and X. Ding performed SEM. J.M. Moran-Mirabal provided supervision, assisted in experimental design, and revised the manuscript. R.G. Wylie assisted in experimental design and data interpretation and revised the manuscript.

3.1. Abstract

Antifouling polymer coatings that are simple to manufacture are crucial for the performance of medical devices such as biosensors. “Grafting-to”, a simple technique where pre-synthesized polymers are immobilized onto surfaces, is commonly employed but suffers from non-ideal polymer packing leading to increased biofouling. Herein, we present a material prepared via the grafting-to method with improved antifouling surface properties and intrinsic localized surface plasmon resonance (LSPR) sensor capabilities. A new substrate shrinking fabrication method, Graft-then-Shrink, improved antifouling properties of polymer coated Au surfaces by altering graft-to polymer packing while simultaneously generating wrinkled Au structures for LSPR biosensing. Thiol-terminated, antifouling, hydrophilic polymers were grafted to Au coated pre-stressed polystyrene (PS) followed by shrinking upon heating above PS’s glass transition temperature. Interestingly, polymer molecular weight and hydration influenced Au wrinkling patterns. Compared to Shrink-then-Graft controls, where polymers are immobilized post shrinking, Graft-then-Shrink increased polymer content by 76% in defined footprints and improved antifouling properties as demonstrated by 84% and 72% reduction in macrophage adhesion and protein (BSA) adsorption, respectively. Wrinkled Au LSPR sensors had sensitivities of ~200-1000 $\Delta\lambda/\Delta$RIU, comparing favorably to commercial LSPR sensors, and detected biotin-avidin and desthiobiotin-avidin complexation in a concentration dependent manner using a standard plate reader and 96-well format.

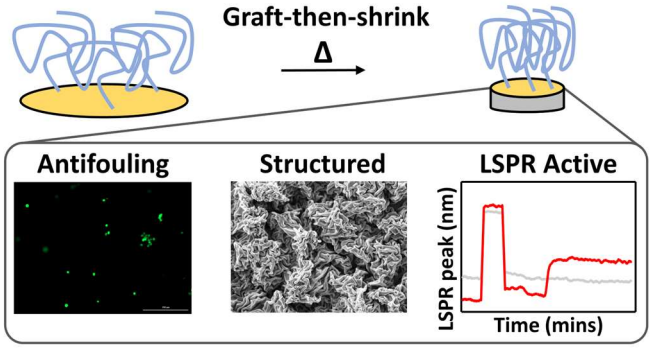

3.2. Introduction

Antifouling polymeric coatings are commonly created by grafting pre-synthesized polymers onto device surfaces,[1,2] a method referred to as "graft-to", to minimize nonspecific interactions and foreign body responses initiated by medical devices[3] as well as to improve the performance of water contacting and marine materials by preventing biofilm formation. There is therefore a great need to improve the performance of antifouling polymer coatings for many applications. Optimizing antifouling polymer coatings on biointerfaces remains an active area of research that is particularly important for biosensors where detectable signals are limited by background noise from nonspecific binding and bulk shifts.[4,5] To improve antifouling properties of graft-to polymer coated surfaces, previous work has primarily focused on the discovery of new antifouling polymers and anchoring mechanisms,[6] or through grafting of structures such as microgels.[7] Opportunities to improve polymer surface coverage from graft-to fabrication methods remain underexplored and represent new avenues to decrease nonspecific interactions. Herein, for the first time, we describe a new technique that simultaneously improves surface coverage of antifouling polymers and generates localized surface

plasmon resonance (LSPR) sensors without the need for complex synthetic techniques or the discovery of new materials.

To improve the fouling properties of graft-to functionalized surfaces, we developed "Graft-then-Shrink", where polymers are first grafted onto shrinkable materials followed by device shrinking to increase the polymer content per geometrical area. Because antifouling properties of hydrophilic polymer coated surfaces improve with greater polymer surface coverage,[8] we can enhance antifouling properties of biointerfaces by combining graft-to polymer coating methods and shrinkable devices. Many medical materials currently in use are shrinkable (e.g., heat shrinkable PTFE[9]), or expandable (e.g., balloon catheters[10]). Sensor applications have also leveraged shrinkable substrates to produce flexible wearable electronics,[11] stretchable surgical robotics[12] and simplified microfluidics.[13,14] Shrinking materials to improve fidelity for 3D printing of bioactive nanostructures have also recently drawn attention.[15] Grafting low molecular weight (MW) semifluorinated trichlorosilanes onto mechanically stretched elastomeric substrates has been shown to increase packing density and improve self-assembled monolayer quality for the production of superhydrophobic surfaces.[16]

The shrinking process can simultaneously produce LSPR sensors by first depositing a thin film of Au or other plasmonic material onto the shrinkable substrate. Upon shrinking, the Au layer forms LSPR active micro- and nano-wrinkles[17] that are exploited here to detect protein interactions by tracking changes in visible light absorbance using a standard plate reader. This represents the first descriptions of substrate shrinking to improve the fouling properties of polymer coatings as well as of Au

wrinkled LSPR sensors for the detection of protein interactions. Graft-then-Shrink has the potential to improve antifouling properties for shrinkable or expandable surfaces and simplify the production of antifouling LSPR biosensors.

Polymeric surface layers are created by either graft-to or graft-from methodologies. Graft-from polymerization occurs from the device surface to achieve high polymer density but requires complex device manufacturing processes.[18] Graft-to involves a simple fabrication process by immobilizing pre-synthesized polymers on the device surface but results in lower polymer packing densities.[19] Due to manufacturing constraints and complexity of many lab-scale processes, graft-to is the preferred technique and antifouling properties are often sacrificed in produced surfaces.[6] Therefore, the combination of graft-to and shrinkable materials that do not require surface pre-treatments or complex grafting steps may improve the antifouling properties of manufacturable devices.

Antifouling polymeric coatings are ideal for LSPR biosensors because direct analyte-surface interactions are not required, and the polymer functional groups act as grafting sites for the immobilization of biorecognition and capture agents. LSPR sensors are typically constructed by immobilizing a capture agent directly to Au nanoparticles or a polymeric coating on the nanoparticle surface; capture agent – analyte complexation results in an absorbance peak shift that is measured using specialized optics and light sources.[20] Because LSPR's sensing volume extends from the sensor surface (decay length ~5 – 15 nm[21]), the analyte only needs to interact with immobilized capture agents on the Au surface or within the polymeric layer. Therefore, improving antifouling properties by

increasing polymer content within a defined footprint through methods such as Graft-then-Shrink will not interfere with the sensitivity of LSPR biosensors.

Graft-then-Shrink simultaneously improves fouling properties of polymeric coatings and generates LSPR active surfaces for biosensing using a simple fabrication process by combining graft-to polymer immobilization with shrinking substrates. First, a thin Au layer (<10 nm) was sputtered onto prestressed polystyrene (PS) discs followed by grafting antifouling polymers (thiol-terminated poly(carboxybetaine)[22] (pCB) or poly(carboxybetaine-*co*-*N*-(3-aminopropyl)methacrylamide) (pCB-*co*-APMA)) onto the flat Au layer using the graft-to method. Heating above the glass transition temperature of PS shrinks the devices footprint and wrinkles the Au layer,[23] which simultaneously improved polymer packing for enhanced antifouling properties and generated LSPR active surfaces with sensitivities of 200-1000 $\Delta\lambda/\Delta$RIU, similar to or greater than current commercial sensors composed of Au nanoparticles (nanoparticle sensitivity 50 – 100 $\Delta\lambda/\Delta$RIU[24]). This represents the first demonstration of shrinking substrates to improve antifouling polymeric coatings on surfaces and the generation of LSPR sensors from wrinkled Au.

3.3. Results and discussion

We first investigated pCB coatings on thermally shrunken PS-Au surfaces, where the discs shrunk to ~16% of their original footprint from 1.39 to 0.23 cm^2 (**Figure 3.1**) and the Au layer formed micro- and nano-wrinkles (**Figure 3.1C, D**). This level of shrinking is consistent with previous reports using this commercially available PS used for gold sensor applications, and was therefore used for all subsequent experiments[23]. The

influence of the shrinking/grafting order (Shrink-then-Graft versus Graft-then-Shrink; **Figure 3.1B**) and pCB MW was investigated on the following PS-Au surface properties: (1) pCB content within a defined footprint; (2) Au wrinkling patterns; and (3) macrophage adhesion. Interestingly, Graft-then-Shrink not only improved antifouling properties but also altered the Au film wrinkling patterns compared to Shrink-then-Graft. LSPR sensitivity of the newly formed surfaces was also quantified for potential applications in biosensing by measuring avidin interactions with biotin and desthiobiotin using a 96-well plate and a standard plate reader to track absorbance between 700 to 870 nm over time (**Figure 3.1F**).

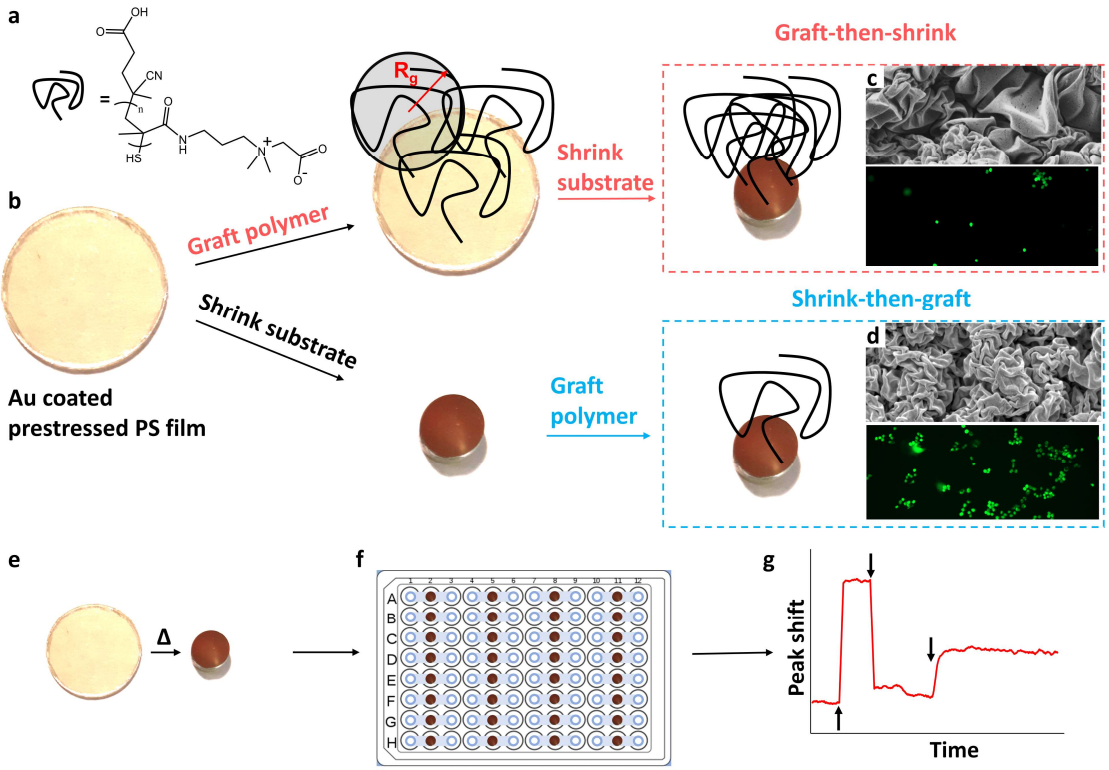

Figure 3.1: Graft-then-shrink: Simultaneous improvement of polymer surface coverage for improved antifouling properties and generation of LSPR active Au surfaces. a) Structure of thiol terminated pCB for grafting to the Au layer. b) Prestressed, PS discs were sputter coated with thin Au layers (< 10 nm) and functionalized with pre-made thiol-terminated polymers. The density of the polymers was limited by the polymer's radius of gyration (Rg). The PS-Au-pCB surfaces were then heated to 130 ºC to shrink the PS discs and wrinkle the Au layer, which simultaneously improves polymer surface coverage to enhance antifouling properties and generates LSPR active wrinkled Au surfaces, producing Graft-then-Shrink surfaces. Control surfaces of Shrink-then-Graft where PS discs coated in thin Au layers were shrunk prior to pCB grafting. SEM of surfaces and fluorescence micrograph of adhered cells to c) Graft-then-Shrink and d) Shrink-then-Graft surfaces depicting polymer-induced wrinkle size differences and resistance to nonspecific cell adhesion on Graft-then-Shrink surfaces. e) Photograph of Au coated PS before and after shrinking with heat. f) Schematic of plate layout of fluidic sensor devices in a 96 well plate. g) Representative sensorgram produced by Graft-then-Shrink sensors depicting functionalization of the surface with a capture agent, rinsing, and binding of a corresponding biomolecule to the immobilized capture agent.

3.3.1. Graft-then-Shrink increases pCB content within a defined footprint

The degree of shrinking is determined by the stress present in the PS discs; Shrink-then-Graft and Graft-then-Shrink samples therefore have the same final footprint. pCB content on PS-Au shrunken discs was quantified using a colorimetric detection assay for amide bonds and X-ray photoelectron spectroscopy (XPS) to compare the signal due to nitrogen, which are both unique to pCB.

The amount of pCB immobilized on PS-Au discs was quantified by the colorimetric bicinchoninic acid (BCA) assay, which quantitively detects amide bonds (**Figure 3.1A**) in polymers and protein through the reduction of Cu^{2+} in alkaline solutions. To validate the assay, we first confirmed that absorbance changes within the BCA assay were linearly dependent on pCB concentration in solution (**Figure S3.1**). Graft-then-Shrink dry surfaces with 60 kDa pCB resulted in an absorbance signal 2.9× greater than flat (unwrinkled) surfaces (**Figure 3.2A**) with the same footprint, and 1.76× greater than Shrink-then-Graft surfaces indicating an increased polymer content on Graft-then-Shrink surfaces. Shrink-then-Graft surfaces showed increased absorbance compared to flat, but the difference was not statistically significant (adjusted p value 0.28). Performing shrinking of Graft-then-Shrink surfaces in both dry and wet conditions produced similar BCA signals, indicating little influence of humidity on pCB-S-Au bond stability. Polymers immobilized to Au surfaces by S-Au have previously been shown to withstand autoclaving[25] but under vacuum conditions S-Au bound polymer stability was found to be side chain dependent at temperatures similar to those used here[26].

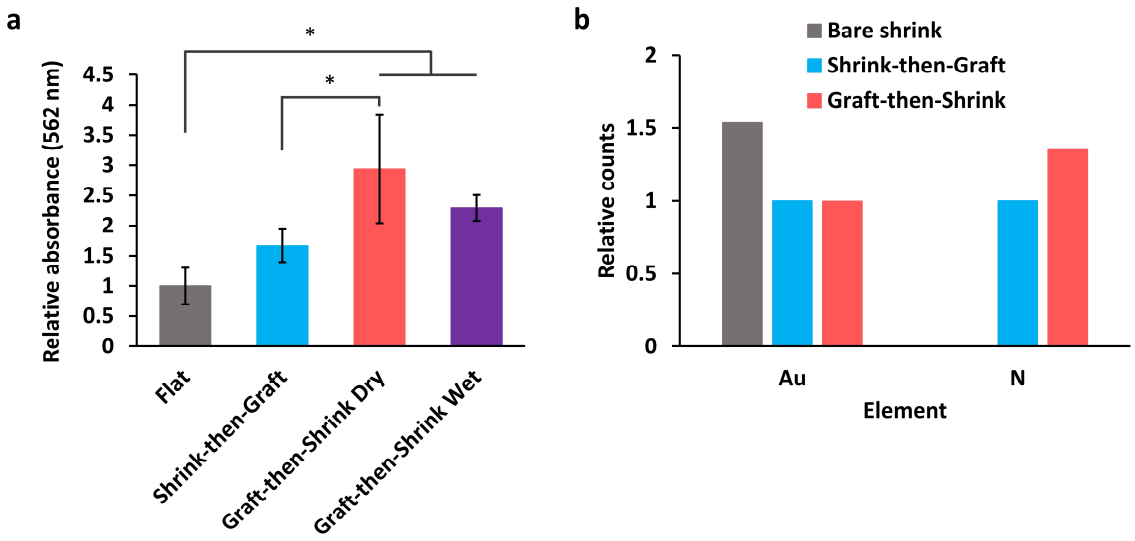

Figure 3.2: pCB content is greater on Graft-then-Shrink Au surfaces. a) Relative absorbance upon pCB quantification using the BCA assay for the detection of pCB's amide bonds on surfaces with the same footprint. Comparison of the amount of 60 kDa pCB on flat (unwrinkled), Shrink-then-Graft, Graft-then-Shrink under dry conditions, and Graft-then-Shrink under wet conditions (mean ± SD, n = 3). Flat Au surfaces were prepared by first shrinking PS prior to Au sputtering. b) XPS of 60 kDa pCB coatings on Shrink-then-Graft and Graft-then-Shrink dry surfaces compared to bare (no pCB) wrinkled surfaces (bare shrink) of equal surface area. Graft-then-Shrink dry had a greater N signal than Shrink-then-Graft and bare shrink, indicating greater pCB content in a defined footprint. Au signals were greatest on bare shrink surfaces due to the lack of pCB overlayer.

XPS was used to characterize the elemental composition of 60 kDa pCB layers on flat and wrinkled surfaces. XPS showed decreased Au content on pCB coated surfaces compared to bare Au as the pCB layer limited the penetration depth for XPS detection. To directly compare pCB content, we measured the relative nitrogen signal because the atom is unique to pCB in the PS-Au discs. Graft-then-Shrink surfaces had ~1.36× the nitrogen content of Shrink-then-Graft surfaces (**Figure 3.2B, Figure S3.2**), in agreement with the BCA results discussed above. Because the XPS spot size was equal for all

conditions, the greater pCB content represents an increased density within the surface volume of the Graft-then-Shrink surfaces.

Compared to Shrink-then-Graft, Graft-then-Shrink can increase immobilized polymer content within a footprint by improving accessibility of the reactive surface (e.g., Au) due to surface topography, steric hindrance between polymer chains, and polymer coating rearrangements. Polymer density from the Shrink-then-Graft method will be limited by the polymer's radius of gyration, as the procedure is akin to grafting-to methods.[19] Whereas Graft-then-Shrink increases Au and thereby polymer content per footprint compared to flat surfaces. Our results demonstrate that grafting pCB on flat Au surfaces followed by wrinkling enhances polymer content within a defined footprint by ~75% compared to pCB immobilization on pre-wrinkled substrates and ~200-300% compared to flat (unwrinkled) surfaces according to the BCA assay. To directly compare apparent chain density between Graft-then-Shrink and Shrink-then-Graft surfaces, grafted fluorescently labelled 60 kDa pCB-*co*-APMA was quantified to yield 0.02 ± 0.01 chains per nm^2 for Shrink -then-Graft and 0.11 ± 0.03 chains per nm^2 for Graft-then-Shrink surfaces (**Figure S3.3**). Although Graft-then-Shrink improves polymer content within a footprint, it does not result in brush regimes similar to graft-from upon surface wrinkling. In comparison, Michalek et al. has reported greater grafting densities of 0.17 – 0.32 chains nm^{-2} for poly(2-(methacryloyloxy)ethyl phosphorylcholine) (PMPC, a zwitterionic polymer of similar side chain length and MW to pCB-*co*-APMA) films prepared via surface initiated ATRP.

3.3.2. Influence of grafted polymers and shrinking conditions on Au wrinkled structures

Interestingly, the presence, MW, and hydration of grafted pCB influenced Au wrinkling patterns with the formation of large, unwrinkled regions apparent in SEM micrographs of Graft-then-Shrink dry surfaces. As expected, samples wrinkled in the absence of grafted pCB, i.e., PS-Au discs without pCB and Shrink-then-Graft discs, had similar Au wrinkle patterns as shown by SEM and wrinkle length calculations (**Figure 3.3A-C, J, Figure S3.4**). Conversely, SEM characterization of Graft-then-Shrink dry surfaces with 25 and 60 kDa pCB showed increased heterogeneity in Au layer wrinkled pattern sizes with islands of large micron-scale wrinkles surrounded by nano-scale wrinkling (**Figure 3.3E, F**). These unique wrinkled Au structures may indicate increased film stiffness, as the modulus of the rigid skin material determines the wrinkle size,[27,28] which may be due to interchain polymer interactions during the shrinking process. No change in Au wrinkling was observed on the 10 kDa pCB Graft-then-Shrink discs, indicating a reduced impact from polymer interchain interactions on stiffness due to the polymer's smaller MW. The observed morphology differences in wrinkle length and generation of large flat regions in Graft-then-Shrink samples is in agreement with the increased polymer content found by BCA and XPS (**Figure 3.2**) and suggests polymer-polymer interactions on the surfaces during shrinking.

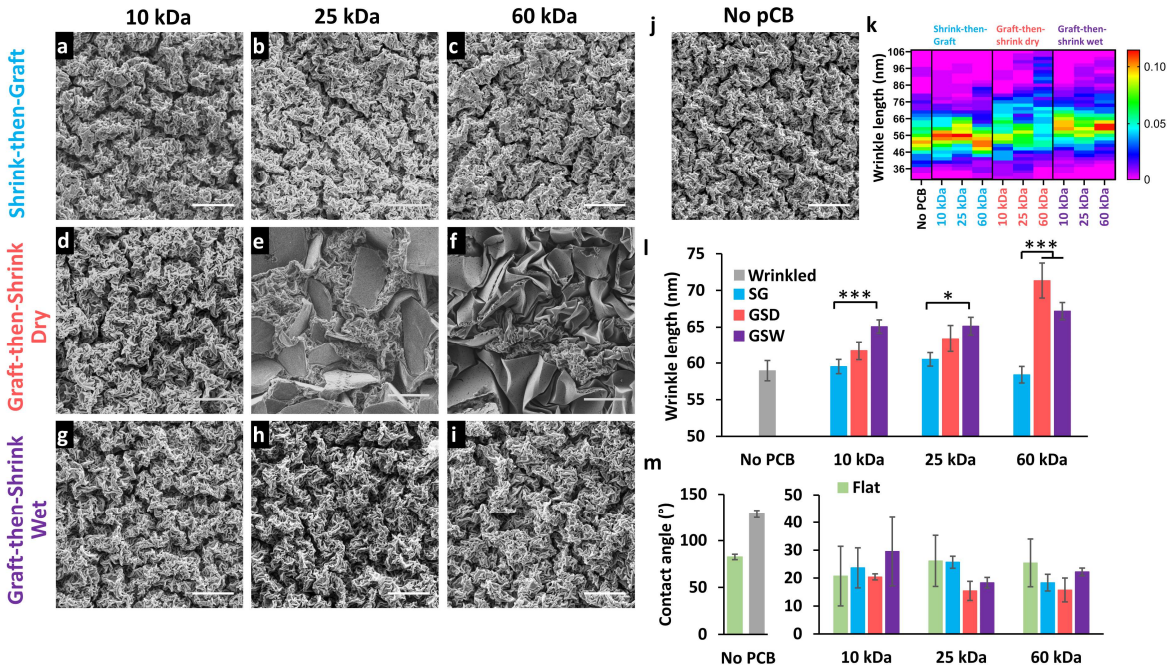

Figure 3.3: SEM micrographs of wrinkled Au surfaces from Shrink-then-Graft and Graft-then-Shrink (dry and wet) with immobilized pCB of various MWs. Shrink-then-Graft surfaces with immobilized a) 10 kDa, b) 25 kDa, and c) 60 kDa polymers. Graft-then-Shrink dry surfaces with d) 10 kDa, e) 25 kDa, and f) 60 kDa pCB polymers. Graft-then-Shrink wet surfaces with g) 10 kDa, h) 25 kDa, and i) 60 kDa pCB polymers. j) Wrinkled Au surface without pCB. Scale bar = 1 µm. K) Heat map of wrinkle length distributions of structured surfaces. l) Characteristic wrinkle lengths of structured surfaces (mean ± SE, n = 60 to 100 wrinkles), large flat (unwrinkled) regions were not included in measurements. m) WCAs of 3 µL MilliQ water drops on bare and pCB coated flat (unwrinkled) and wrinkled surfaces (mean ± SD, n = 3).

The influence of the polymer film on sub-micron wrinkles was dependent on a combination of fabrication order, polymer MW and hydration. Micron-scale features did not appear when Graft-then-Shrink surfaces were shrunk with a hydrated polymer layer using an autoclave (Graft-then-Shrink wet), suggesting a decreased polymer film stiffness due to polymer hydration (**Figure 3.3H, I**). Therefore, Graft-then-Shrink wet will produce Au wrinkling patterns with greater uniformity than Graft-then-Shrink dry. Bare wrinkled 5 nm Au produced wrinkle wavelengths 9% smaller than those predicted by

theory (eq. S1) (actual = 59, predicted = 64)[29], suggesting the sputtered Au films were slightly thinner than expected (4.6 nm vs 5 nm). Outside of the large flat microstructures observed in Graft-then-Shrink dry, all Graft-then-Shrink surfaces had larger wrinkle sizes (dry: 61 ± 1 nm to 71 ± 2 nm, wet: 65 ± 1 nm to 67 ± 1 nm) compared to bare (59 ± 1 nm) and Shrink-then-Graft surfaces (58 ± 1 nm to 61 ± 1 nm), further demonstrating the influence of the polymer film on wrinkle size (**Figure 3.3K, L**). The heterogeneous structures which arise on the Graft-then-Shrink dry surfaces could be due to the increased interactions between pCB polymers in the dry state where overlapping zwitterionic moieties could exhibit strong electrostatic associations, as previously reported in hydrogels, increasing stiffness locally[30]. Polymer MW had an increased influence on wrinkle patterns for Graft-then-Shrink dry than for wet, which is expected as hydration would decrease the mechanical strength of the polymer film.[31] Moreover, higher MW polymers would be expected to increase the mechanical strength of polymer films in the dry state and therefore alter wrinkling patterns. The relative uniformity of the increased wrinkle lengths in the Graft-then-Shrink wet conditions suggest that immobilized polymers evenly coat the surface.

All surfaces modified had low water contact angles (WCAs) irrespective of MW due to the pCB's hydrophilicity (**Figure 3.3M, Figure S3.5**). For 10 and 60 kDa pCB, no differences were observed between Graft-then-Shrink, Shrink-then-Graft or unwrinkled Au controls. Surfaces with 25 kDa pCB demonstrated lower WCAs with Graft-then-Shrink (15° ± 3) than Shrink-then-Graft (25° ± 2) or unwrinkled Au (26° ± 9). All pCB coated wrinkled surfaces maintained the hydrophilic nature of the flat coated surfaces, or

improved upon it, in contrast to the dramatic increase in hydrophobicity of uncoated wrinkled Au (WCA = 129° ± 4, **Figure 3.3M**). The Graft-then-Shrink method only showed a small decrease in WCA for the 60 kDa pCB polymer when compared to the Shrink-then-Graft but both approached the lower limit of 15° for most pCB surfaces, indicating good surface coverage or increased film thickness due to the polymer's high MW. For 10 kDa pCB surfaces, no decrease in WCA was observed for either shrinking method when compared to non-shrunken surfaces. The polymer was most likely too small for a meaningful increase in apparent polymer density even upon shrinking. All pCB coated surfaces had WCAs between 15.4 and 29.5°, none of which were significantly different from previously reported WCAs of pCB with a carbon spacer length of 1, of 17° ± 3[32] ($p = 0.22$, One-way ANOVA with Bonferroni post-hoc test comparing all pairs of columns), making it difficult to compare WCAs due to high variance of flat and 10 kDa pCB coated surfaces. Flat pCB coated surfaces, and surfaces coated with 10 kDa pCB, had much higher variance than all wrinkled surfaces coated with pCB of 25 or 60 kDa (**Figure S3.5**), indicating improved consistency in coverage with higher molecular weights and on roughened surfaces, which are known to intensify hydrophilic contact angles[33]."

3.3.3. Graft-then-Shrink enhances pCB coated surface resistance to macrophage adhesion

Graft-then-Shrink surfaces had lower nonspecific macrophage adhesion compared to pCB coated flat or Shrink-then-Graft surfaces. Because pCB coated surfaces made from traditional graft-to procedures are already antifouling, we used high fouling

experimental conditions to differentiate the fouling rates. To this end, the surfaces were soaked in 100% aged bovine serum for 48 hours for maximum nonspecific protein adsorption, followed by macrophage exposure for 24 hours. Graft-then-Shrink with 25 and 60 kDa pCB improved resistance to macrophage adhesion, whereas 10 kDa pCB did not (**Figure 3.4**). Therefore, smaller polymers (e.g., 10 kDa pCB) are likely too small to sufficiently enhance surface coverage upon shrinking of the PS discs and Au wrinkling, while larger polymers (e.g., 60 kDa pCB) can increase polymeric surface coverage to aid in the resistance of macrophage adhesion. Although a lower cell fouling trend was observed for 25 kDa pCB when comparing Shrink-then-Graft to Graft-then-Shrink, the

differences were not statistically significant.

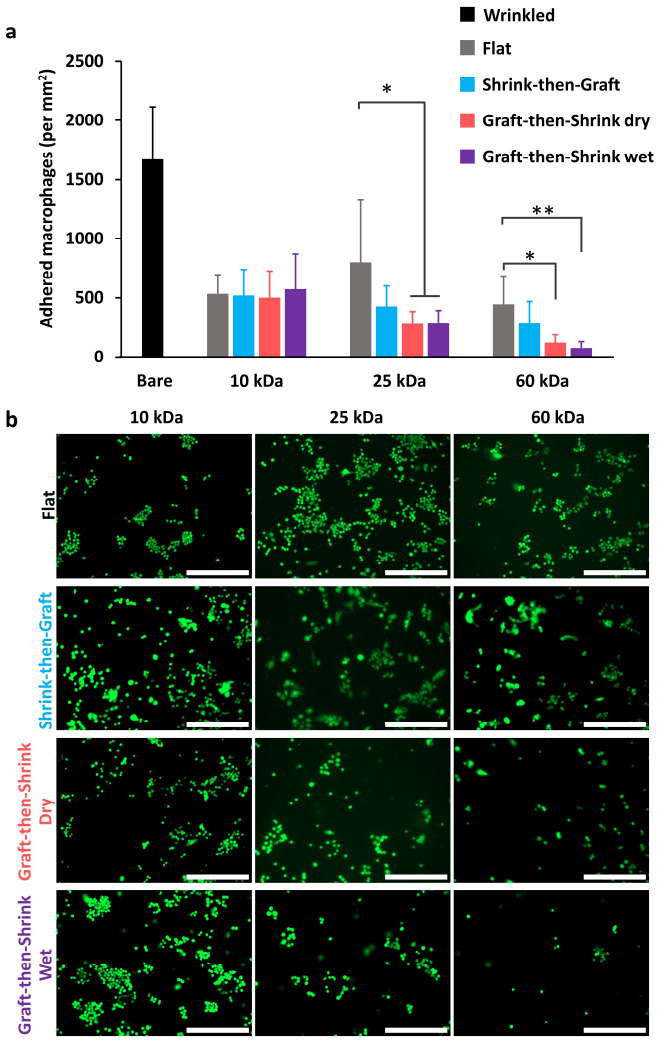

Figure 3.4: Graft-then-Shrink improved resistance to nonspecific macrophage adhesion. Macrophage adhesion to 5 nm Au surfaces modified with pCB of three different MWs under high fouling experimental conditions. Surfaces were soaked in 100% aged bovine serum for 48 hours for maximum nonspecific protein adsorption, followed by macrophage exposure for 24 hours. a) Average number of adhered macrophages per mm^2 for each surface type (mean ± SD, n = 6). b) Representative fluorescent micrographs of Calcein AM stained RAW 264.7 macrophages. Scale bar = 250 µm.

Au wrinkling is not responsible for the improvement of fouling properties, though structured surfaces can reduce and direct cell adhesion.[34] Compared to flat (non-shrunk,

non-wrinkled) Au surfaces for both 25 and 60 kDa pCB, only Graft-then-Shrink, and not Shrink-then-Graft, surfaces were significantly different. Furthermore, no significant difference in macrophage adhesion was observed between Graft-then-Shrink dry and wet, which indicates that differences in wrinkle length and topography (**Figure 3.3K**) did not significantly influence adhesion here. Therefore, the lower fouling properties of Graft-then-Shrink are mainly due to the increased pCB content per footprint over Shrink-then-Graft surfaces.

Improvement in macrophage adhesion resistance from Graft-then-Shrink is dependent on pCB MW and WCA, which correspond to pCB content. The lowest macrophage adhesion condition was Graft-then-Shrink with 60 kDa pCB in either the dry or wet condition (120 cells ± 70 per mm^2 and 70 cells ± 60 per mm^2), where shrinking occurs with a dry or hydrated pCB layer, respectively. 60 kDa pCB will result in greater surface coverage and polymer layer thickness, as demonstrated by greater polymer content within a defined footprint; polymer layer thickness alone may not significantly improve fouling as demonstrated by comparing 10 and 60 kDa on flat surfaces. 25 kDa and 60 kDa pCB with Graft-then-Shrink led to a 65% and 84% reduction in total cells compared to flat surfaces coated with the same polymers, while the same polymers on Shrink-then-Graft surfaces produced only a 47% and 37% reduction in cells compared to flat surfaces. Therefore, Graft-then-Shrink can improve fouling properties of polymer layers with sufficiently high MWs.

Resistance to bacterial adhesion and bovine serum albumin (BSA) adsorption followed similar trends as macrophage adhesion (**Figure S3.6** and **Figure S3.7**). For 10

kDa pCB, nonspecific adhesion of *P. aeruginosa* was lower in Graft-then-Shrink dry and wet conditions with 26.2 and 71.0 % reductions compared to Shrink-then-Graft. Larger polymers (e.g., 60 kDa pCB) showed little bacterial adhesion under any conditions (91 to 96 % reduction compared to 10 kDa Shrink-then-Graft), making comparisons difficult. Wrinkled Au films with no polymer coating are antifouling towards bacteria due to their extremely hydrophobic surface, which is observed here as well.[35] Nonspecific adsorption of fluorescently tagged BSA was also tested and although the Shrink-then-Graft conditions demonstrated high variability, Graft-then-Shrink surfaces trended to lower BSA adsorption for 25 and 60 kDa pCB with a decrease of 71.5 and 72.3 %, respectively (**Figure S3.7**). Therefore, Graft-then-Shrink can improve resistance to bacterial adhesion and nonspecific protein binding.

3.3.4. Characterization and sensitivity of Graft-then-Shrink LSPR sensors

Graft-then-Shrink offers a simple method to create sensitive LSPR sensors from wrinkled Au surfaces. LSPR active surfaces require curvature of SPR active metals to locally confine surface plasmons, which is traditionally achieved by depositing nanoparticles smaller in size than the plasmon excitation wavelength. More complex and manufacturing intensive LSPR active surfaces can be produced by creating nanostructured arrays using patterning techniques.[36] The Au wrinkles on Graft-then-Shrink surfaces confine the surface plasmons for LSPR sensing without the need for nanoparticles, complex deposition techniques, or patterned arrays.

The Au nano- and micro-wrinkles formed upon thermal shrinking of the Au-PS discs produce LSPR activity that is dependent on the refractive index of the sensing

volume. To first characterize the sensitivity of bare (no pCB) wrinkled Au surfaces, absorbance measurements of discs with varying initial Au thicknesses in alcoholic and aqueous environments were performed. Sensitivity was determined by the shift in maximum absorbance wavelength (δλ) over the change in the bulk refractive index units of the solution or solvent being measured (δRIU). Ethanol (EtOH), isopropyl alcohol (IPA) and butanol (BuOH) were chosen as solvents because of their defined refractive indices, ability to wet the hydrophobic uncoated wrinkled Au, and their compatibility with the PS disc, allowing for full sensor immersion. The maximum absorbance wavelength increased linearly with refractive index of the solvent (**Figure 3.5A, B**). Au thickness, which determines wrinkle length,[37] influenced both the sensor's sensitivity (**Figure 3.5C**) and wavelength of peak absorbance (**Figure 3.5B**). Thicker Au layers shifted the peak absorbance range to longer wavelengths, shifting the range from 548-569 nm to 789-834 nm for Au thicknesses of 2.5 and 3.7 nm, respectively, in the solvents tested. Sensitivity of uncoated wrinkled surfaces was greatest for 5 nm Au coatings at over 600 δλ/δRIU in alcoholic solvents; the sensitivity dropped by ~2× in aqueous glucose solutions (**Figure 3.5C**) most likely due to lower wetting of the uncoated hydrophobic surface.

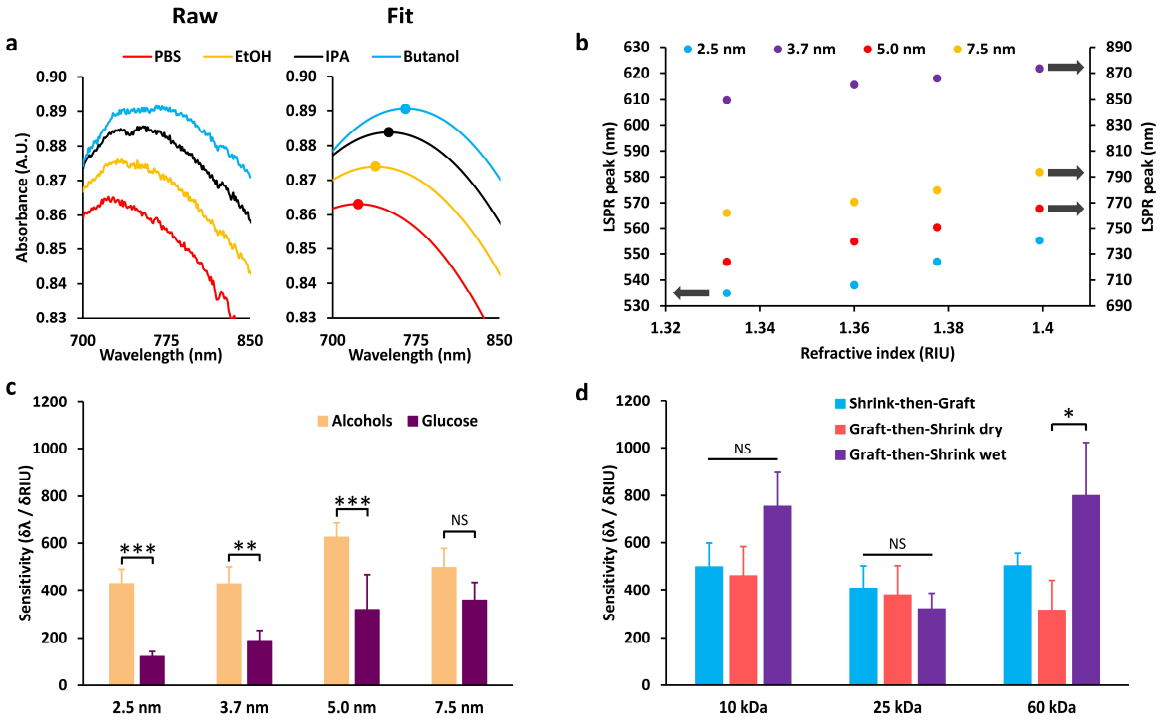

Figure 3.5: Sensitivity characterization of bare (no pCB) and pCB coated wrinkled Au LSPR sensors. a) Representative raw and fit absorbance spectra of bare 5 nm Au in PBS and alcohol solvents. Circles denote peak location (maximum absorbance) on fitted data. b) Peak absorbance locations of 2.5, 3.7, 5 and 7.5 nm Au in MeOH, EtOH, IPA and BuOH. c) Compiled sensitivities of bare Au sensors in alcohol and aqueous glucose solutions (mean ± SD, n = 3). d) Compiled sensitivities of hydrophilic pCB coated 5 nm Au sensors in aqueous glucose solutions (mean ± SD, n = 3).

Sensors coated with hydrophilic pCB have greater sensitivity than bare sensors in aqueous solutions. The sensitivity of pCB coated Au surfaces in glucose solutions of varying concentration and refractive indexes showed sensitivities similar or greater than bare sensors exposed to alcohols (**Figure 3.5D**). The Graft-then-Shrink fabrication method with pCB produces sensors that operate in aqueous environments with sensitivities of 320 ± 120 to 800 ± 200 δλ/δRIU, depending on grafted polymer MW and hydration state, which is similar to sensitivity of many types of LSPR sensors.[36] All methods that produce Au wrinkling (Graft-then-Shrink wet/dry and Shrink-then-Graft)

will yield LSPR sensors, with no clear obvious bulk sensitivity benefit for any method. No improvement in sensitivity from glucose bulk shifts would be expected from an increase in polymer content.

3.3.5. Capture ligand immobilization and analyte sensing with Graft-then-Shrink sensors

Using the Graft-then-Shrink fabrication method, polymer coated sensors were developed for the immobilization of biotin or desthiobiotin as the capture ligand and detection (sensing) of avidin binding using similar procedures to commercial LSPR sensors where capture ligands are covalently immobilized to polymer coatings, followed by exposure to the corresponding analyte. This is the first demonstration of a wrinkled Au surface as an LSPR sensor for the detection of biomolecules; previous LSPR sensors have been made from nano sized particles, rods, stars, cubes and triangles or nano/micro arrays, which suffer from lower sensitivities or require more complex processing methods.[36]

To demonstrate that Graft-then-Shrink (dry) LSPR sensors detect the covalent immobilization of biomolecules, avidin was first immobilized to 10, 25 and 60 kDa pCB coatings using EDC/NHS chemistry. After avidin immobilization, all three MW pCBs showed similar responses with peak shifts of ~ 2.5 nm. Poly(oligo(ethylene glycol)methyl ether methacrylate) (POEGMA) coated surfaces had a much smaller shift of ~ 0.3 nm post avidin immobilization because each polymer chain only contains one terminal carboxylic acid for conjugation (**Figure 3.6A**). Similar responses from all three pCB MWs suggests that the protein is primarily immobilized on the surface of the

polymer layer, with limited penetration. Therefore, the Graft-then-Shrink sensors can detect macromolecules binding to their polymeric coatings like commercial sensors. To improve the efficiency of sensing volume usage, multiple sizes of polymer could be grafted prior to shrinking to produce hierarchical surfaces similar to those previously created by surface-initiated methods.[32,38,39]

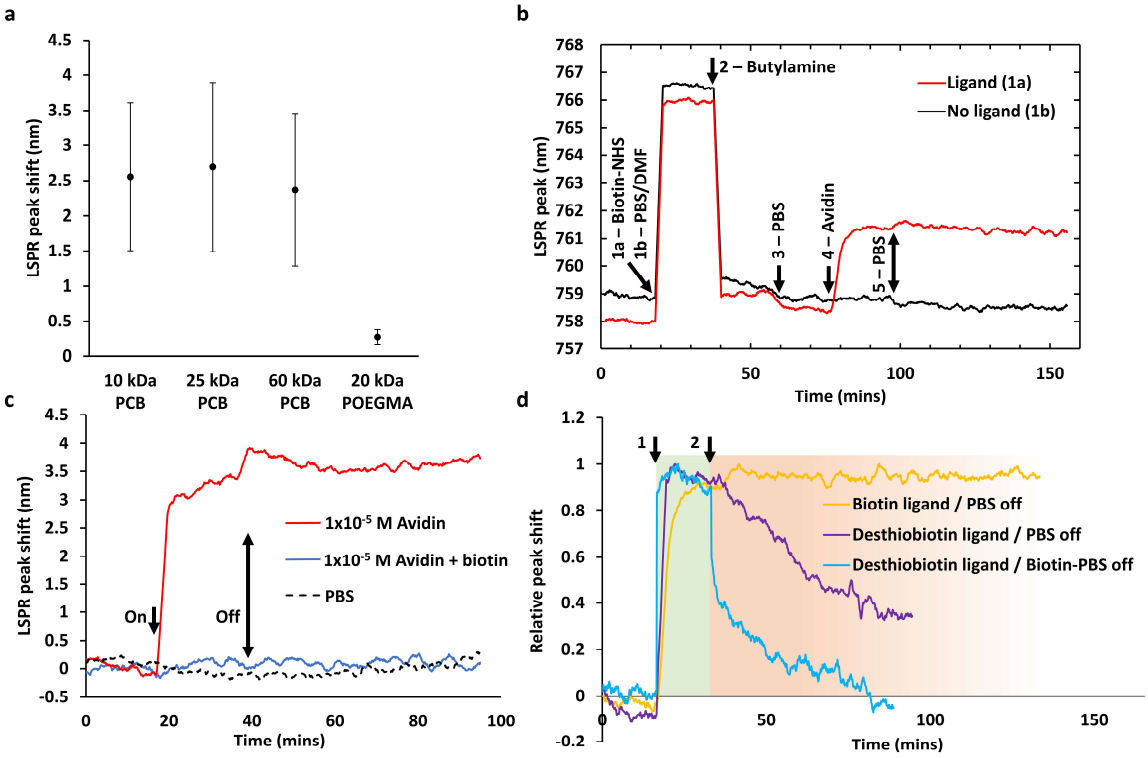

Figure 3.6: Sensing avidin binding/unbinding with polymer coated LSPR sensors. a) LSPR peak shift of Graft-then-Shrink dry surfaces from avidin immobilization via EDC/NHS onto pCB and POEGMA surfaces (mean ± SD, n = 2 or 3). b) A sensorgram of peak absorbance shifts over time of a 5 nm Au film fabricated using Graft-then-Shrink with 10 kDa pCB-*co*-APMA (30% APMA content). The "No Ligand" control shows no response to avidin; pCB-*co*-APMA was not modified with biotin or desthiobiotin. The "Ligand" condition includes a ~ 3 nm increase in peak absorbance wavelength following exposure of the biotinylated surface to avidin (10^{-5} M) in PBS. The injection sequence for both sensors was: (1a) Biotin-NHS in 4:1 PBS:DMF, (1b) 4:1 PBS:DMF without Biotin-NHS, (2) 0.1 M butylamine, (3) PBS, (4) avidin (10^{-5} M) in PBS, (5) PBS. c) Overlaid sensorgrams of PBS, avidin pre-saturated with biotin, and free

avidin using a sensor modified with biotin, demonstrating minimal nonspecific binding of pre-saturated avidin. d) Overlaid sensorgrams of Graft-then-Shrink sensors with 10 kDa pCB-*co*-APMA (30% APMA) functionalized with either NHS-biotin or NHS-desthiobiotin: (1) association of avidin (10^{-5} M) and (2) dissociation of avidin in either PBS or a biotin solution (10^{-3} M). Maximum peak absorbance shifts are normalized to illustrate the different dissociation rates from different ligands and dissociation buffers.

Graft-then-Shrink LSPR sensors successfully detected biotin-avidin interactions as shown by sensorgrams obtained using a standard plate reader. Because the LSPR signal is proportional to the analyte's MW, Au surfaces were modified with a primary amine containing pCB copolymer, pCB-*co*-APMA (10 kDa, Đ = 1.06). The surfaces were then shrunk to produce amine functionalized Graft-then-Shrink sensors for immobilization of NHS-Biotin, the capture ligand (step 1a, red line in **Figure 3.6B**); a large peak shift was observed due to the refractive index of NHS-Biotin's DMF/PBS solution. The activity of pCB-*co*-APMA conjugated biotin was confirmed using the HABA displacement assay (**Figure S3.8**). Sensors were then washed with butylamine to inactivate unreacted NHS-Biotin or residual EDC molecules (step 2), followed by PBS (step 3); the peak shift between step 3 and before step 1a is due to the immobilization of biotin. The sensor was then exposed to an avidin solution in PBS (step 4), and a clear peak shift of ~3 nm was registered, similar to the covalent avidin immobilization obtained in **Figure 3.6B** (~2.5 nm). The avidin solution was then removed from the sensor and replaced with PBS (step 5). No decrease in signal was observed because of the long half-life of the biotin-avidin interaction (~200 d).[40] A control experiment (black line in **Figure 3.6B**) where the sensor was exposed to a DMF/PBS mixture without NHS-Biotin was conducted to detect nonspecific binding of avidin. After avidin exposure (black line step 4), no peak shift was observed, indicating little to no avidin binding.

Graft-then-Shrink sensors can therefore detect the immobilization of biotin and the capture of avidin and are applicable for the detection of specific protein-ligand interactions.

Sensorgrams with avidin and biotin-saturated avidin were then constructed to demonstrate that the biotin-avidin interaction is responsible for the detection signal. Graft-then-Shrink sensors with pCB-*co*-APMA modified with NHS-biotin were exposed to: 1) 10^{-5} M avidin pre-saturated with biotin; 2) 10^{-5} M avidin; and, 3) PBS only. Only the avidin condition produced a significant signal from the complexation of avidin with pCB-*co*-APMA immobilized biotin (**Figure 6C**). Because avidin pre-saturated with biotin cannot bind biotin modified sensor surfaces, the sensorgram signal increase of ~0.25 nm compared to the PBS only control is due to bulk shifts and nonspecific binding, which is similar to the signal from the bulk shift in RI produced by non-binding protein solutions of BSA at comparable concentrations (**Figure S3.9**). The sensors therefore have minimal nonspecific binding, and the signal is due to the specific binding of avidin to surface biotin.

Graft-then-Shrink sensors can also detect dissociation events after the association phase. Graft-then-Shrink sensors with biotin or desthiobiotin immobilized to pCB-*co*-APMA were fabricated and exposed to avidin solutions. Because of avidin's long half-life with biotin (dissociation rate constant of 7.5×10^{-8} s^{-1}[141]), no peak shift was observed during the dissociation phase of the biotin modified sensor (yellow line in **Figure 3.6D**); the dissociation phase occurs once the avidin solution is removed from the sensor and replaced with PBS buffer. The weaker desthiobiotin-avidin interaction (d-desthiobiotin at

pH 7, K_D $5x10^{-13}$ M vs $1.3x10^{-15}$ M)[40] and greater dissociation rate constant compared to biotin ($3.6x10^{-5}$ s^{-1} vs $7.5x10^{-8}$ s^{-1}; unmodified desthiobiotin and biotin) allows for avidin dissociation from desthiobiotin modified sensors and acquisition of the dissociation phase once the sensor is in the PBS solution (purple line in **Figure 3.6D**). Modification of desthiobiotin's carboxylic acid, such as in the immobilization technique used here, has been shown to increase its dissociation rate from avidin.[40] The sensors were placed in a biotin solution to prevent re-association of avidin with surface desthiobiotin during the dissociation phase[42] (blue line in **Figure 3.6D**), yielding the true dissociation rate of avidin from the sensor surface. Therefore, Graft-then-Shrink sensors can detect both the association and dissociation phase of sensorgrams.

Graft-then-Shrink sensors functionalized with ligand detect analytes in a concentration dependent manner. A biotin modified sensor was sequentially exposed to solutions of increasing avidin concentrations in HEPES (**Figure 3.7**). It should be noted that biotin immobilized to a polymer coating will have a greater K_D than free biotin for avidin. A small shift in LSPR peak position was observed at the lowest concentration of avidin ($1x10^{-7}$ M) when compared to buffer only. More appreciable shifts from 740 to 745 nm at higher concentrations were then observed, with peak positions remaining after avidin removal and exposure to buffer due to the near irreversible nature of the biotin-avidin interaction (**Figure 3.7A**, buffer line without avidin). Concentrations between $2x10^{-7}$ and $1x10^{-5}$ M produced a sigmoidal response (**Figure 3.7B**), which is similar dynamic concentrations ranges reported in previous reports of LSPR sensors with biotin ligands.[43] The sensing dynamic range occurs over 2 orders of magnitude, similar to

streptavidin binding to immobilized biotin on an LSPR sensor and follows the typical dynamic range of protein-ligand binding curves.[43]

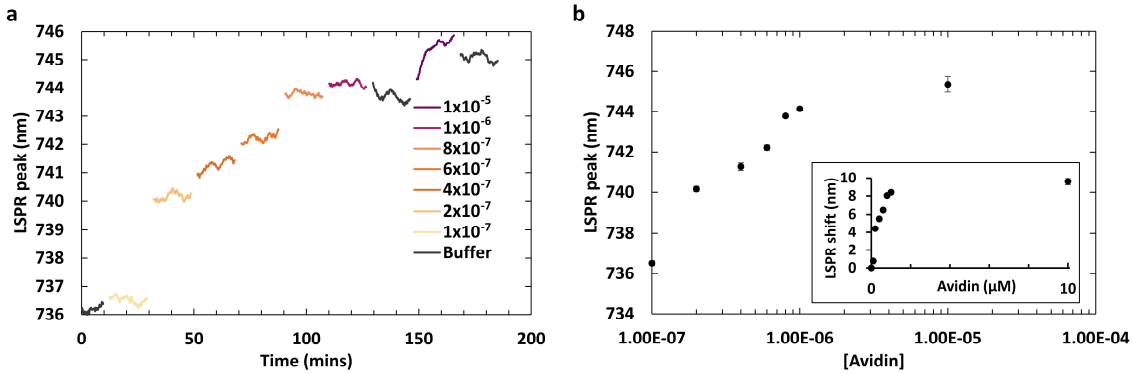

Figure 3.7: Graft-then-Shrink LSPR sensors are concentration sensitive. a) Sensorgram of 10 kDa pCB-*co*-APMA (30 mol% APMA) covalently functionalized with biotin-NHS and exposed to solutions of increasing avidin concentrations in 10 mM HEPES buffer supplemented with 1% BSA. b) Average (± SD, SD is variation in signal from a single sensor) LSPR peak location from the sensorgrams in a); inset of dose response curve composed of peak shift on linear axes (average ± SD, SD is variation in signal from a single sensor).

3.4. Conclusion

Enhancing antifouling properties of surfaces remains an active area of research for application in medicine, biosensing and materials exposed to natural elements such as coatings for marine equipment. Graft-then-Shrink is a new method that improves the antifouling properties of polymer coated surfaces over traditional graft-to methods. The method can be extended to other shrinkable, expandable or stretchable substrates, with higher shrinking ratios such as polyolefin,[44] or elastomeric substrates to produce similarly high-performing surfaces through simple "graft-to" functionalization. For example, Graft-then-Shrink may be applied to many elastomeric implantable biomaterials (e.g., silicone) or marine coatings. Graft-then-Shrink could also be combined with other "graft-

to" methods, such as cloud point grafting,[45] to maximize polymer density. Furthermore, the Graft-then-Shrink method, when applied to thin Au layers with functionalizable polymers, yields highly sensitive biosensors with limited bulk shift and nonspecific binding. This method has been applied for the benchtop production of LSPR biosensors from commonly available and affordable materials, yielding a platform which can be used in a 96 well format within ubiquitously available plate readers, eliminating the need for specialized SPR or LSPR equipment. Graft-then-Shrink sensors may lead to the development of cost-effective, antifouling sensors using simple fabrication techniques for both in vitro and in vivo applications.

3.5. Experimental Section/Methods

3.5.1. Materials

N-[3-(dimethylamino)propyl]methacrylamide, tert-butyl bromoacetate, 2,4,6 trinitrobenzene sulfonic acid, trifluoroacetic acid (TFA), 4-Cyano-4-(phenylcarbonothioylthio)pentanoic acid, 4,4'-azobis(4-cyanovaleric acid), N-(3-Dimethylaminopropyl)-N′-ethylcarbodiimide hydrochloride (EDC), N-hydroxysuccinimide (NHS), sodium hydroxide, QuantiPro™ BCA Assay Kit, 2-(N-morpholino)ethanesulfonic acid sodium salt (MES), fluorescein sodium salt, n-butanol, isopropyl alcohol, ethanol, sodium acetate, D-(+)-glucose, Poly(ethylene glycol) methyl ether methacrylate (M_n 500), and bovine serum albumin (BSA) were purchased from Sigma Aldrich (Oakville, ON, Canada). Avidin, fetal bovine serum (FBS), and calf bovine serum (CBS) were obtained from Thermo Fisher Scientific (Burlington, ON, Canada). Methanol from Caledon Laboratories (Georgetown, ON, Canada). Pre-stressed

polystyrene from Graphix (Maple Heights, OH, USA). Au (99.999%) from LTS Chemical (Chestnut Ridge, NY, USA). Phosphate buffered saline (PBS) at pH 7.4 contained 10 mM sodium phosphate and 137 mM NaCl.

3.5.2. Substrate preparation

Prestressed PS shrink film was cleaned by sequential submersion in 2-propanol, ethanol, and DI water for 5 min each with orbital shaking at 100 RPM and dried under nitrogen stream between each step. The PS film was then cut into 1.4 cm diameter discs, which were then sputter coated with Au at 0.3 Å s^{-1} to final thicknesses of 2.5, 3.7, 5 or 7.5 nm. Following sputter coating, Au coated PS discs (PS-Au) were stored at room temperature.

3.5.3. Carboxybetaine methacrylamide monomer synthesis

Carboxybetaine methacrylamide (CB) monomer was synthesized via a previously published method.[46] Briefly, 23.25 g of N-[3-(dimethylamino)propyl]methacrylamide was dissolved in 300 mL of dry acetonitrile under nitrogen. Tert-butyl bromoacetate (30 g) was added, and left to react overnight at 50 °C. The reaction was cooled to room temperature and the product was precipitated with 500 mL of ether. The product was left to stand at 4 °C overnight, and then decanted. The white powder was collected, washed with 100 mL of ether, decanted, and dried under a stream of nitrogen followed by overnight under vacuum. ^{1}H NMR (D_2O, 600 MHz) δ: 5.63 (s, 1H), 5.34 (s, 1H), 4.10 (s, 2H), 3.53 (m, 2H), 3.28 (t, J = 6.42, 2H), 3.18 (s, 6H), 1.96 (m, 2H), 1.85 (s, 3H).

3.5.4. Synthesis of thiol terminated polycarboxybetaine methacrylamide

Polycarboxybetaine methacrylamide (pCB) polymers at three different molecular weights (10 , 25 and 60 kDa) were synthesized. CB monomer (750 mg) was dissolved in 4.2 mL of 2:1 acetate buffer (0.1 M, pH 4.5):1,4-dioxane. This solution was split into 3 equal parts in 50 mL round bottom flasks and to each 4-Cyano-4-(phenylcarbonothioylthio)pentanoic acid was added (21.56 mg for 10 kDa pCB, 8.48 mg for 25 kDa pCB, 3.51 mg for 60 kDa pCB), following this, 4,4′-Azobis(4-cyanopentanoic acid) was added to each flask (10.81 mg for 10 kDa pCB, 4.25 mg for 25 kDa pCB, 1.76 mg for 60 kDa pCB). Each flask was then degassed by 3 subsequent freeze pump thaw cycles, backfilled with nitrogen gas and left to react at 70 °C for 24 h. The polymerizations were quenched by exposure to air and freezing, and 50 μL of butylamine was added to each flask, pH adjusted to 10 with 8 M NaOH and stirred for 2 h at room temperature to produce thiol-terminated pCB (pCB-SH). Each aminolysed pCB solution was then dialyzed against water for 2 d before the addition of 15 mg of TCEP. Finally, pCB solutions were dialyzed at pH 4 for 3 d and lyophilized to yield a white powder (300 – 400 mg).

3.5.5. Synthesis of thiol terminated polycarboxybetaine methacrylamide – co – N-(3-aminopropyl)methacrylamide

pCB-*co*-APMA copolymer containing 30% mole fraction APMA was synthesized as follows: CB monomer (0.7 g), APMA-HCl (0.24 g), and 2,2'-Azobis[2-(2-imidazolin-2-yl)propane]dihydrochloride (3.4 mg) were dissolved in 0.1 M acetate buffer (pH 4.9). Next, 4-Cyano-4-(phenylcarbonothioylthio)pentanoic acid (13.2 mg) was

dissolved in 2:1 acetate buffer:1,4-dioxane and added to the monomer mixture. The pH was adjusted to 4.5 and transferred into a Schlenk flask. The solution underwent three freeze-pump-thaw cycles, followed by five minutes of nitrogen flow, and was immersed into a 40°C oil bath overnight with gentle stirring. The solution was dialyzed against water adjusted to pH 5 with HCl for 3 d and lyophilized yielding a pink powder. The lyophilized polymer was then aminolysed by dissolving in water adjusted to pH 10 with 8 M NaOH and 50 μL of butylamine and stirred for 2 h at room temperature. The resulting clear solution was dialyzed for 2 d before the addition of 15 mg of TCEP. This solution was then dialyzed for 3 d at pH 5 and lyophilized, yielding a white powder.

3.5.6. Synthesis of thiol terminated poly (oligo ethylene glycol) methyl ether methacrylate

Poly(ethylene glycol) methyl ether methacrylate monomer (1 g) was dissolved in 1.1 mL of 1,4-dioxane. 14.1 mg of 4-Cyano-4-(phenylcarbonothioylthio)pentanoic acid was added, following this, 7.1 mg of 4,4′-Azobis(4-cyanopentanoic acid) was added. The flask was then degassed by 3 subsequent freeze pump thaw cycles, backfilled with nitrogen gas and left to react at 70 °C for 24 h. The polymerization was quenched by exposure to air and freezing, and 50 μL of butylamine was added, pH adjusted to 10 with 8 M NaOH and stirred for 2 h at room temperature to produce thiol-terminated POEGMA (POEGMA-SH). Aminolysed POEGMA was then dialyzed against water for 2 d before the addition of 15 mg of TCEP. Finally, POEGMA-SH was dialyzed at pH 4 for 3 d and lyophilized yielding a clear viscous liquid.

3.5.7. Preparation of Graft-then-Shrink PS-Au-pCB

Thiol terminal pCB (5 mg) was dissolved in 5 mL pH 6.5 MES buffer (10 mM) and incubated with PS-Au discs for 4 d under nitrogen atmosphere, producing "No Shrink" PS-Au-pCB. The surfaces were rinsed with DI water and subsequently, "No Shrink" PS-Au-pCB discs were incubated at 130 °C for 15 min to shrink the PS substrate, producing "Graft-then-Shrink dry" surfaces, or autoclaved in PBS at 121 °C for 15 min producing "Graft-then-Shrink wet" surfaces. Graft-then-Shrink wet surfaces were subsequently rinsed with DI water, dried under a stream of nitrogen, and finally incubated in a 130 °C oven for 15 min to remove cloudiness in PS base from the autoclave procedure (**Figure S3.10**).

3.5.8. Preparation of Shrink-then-Graft PS-Au-pCB

PS-Au discs were incubated at 130 °C for 15 min to shrink the PS substrate. These shrunk surfaces were then incubated with thiol terminal pCB-SH (5 mg) in 5 mL pH 6.5 MES buffer (10 mM) and incubated for 4 d under nitrogen atmosphere. Substrates were removed and rinsed with DI water, yielding "Shrink-then-Graft" surfaces.

3.5.9. Polymer characterization by GPC

Polymer molecular weight (M_n, M_w) and dispersity (Đ) was determined by gel permeation chromatography using an Agilent 1260 infinity II GPC system equipped with an Agilent 1260 infinity RI detector, and either PL aquagel-OH 30 and PL aquagel-OH 40 (Agilent) columns in series or a Superose 6 10/300 GL (GE) column, with PBS running buffer at 30 °C. The column was calibrated using polyethylene glycol (PEG) standards (Mn of 3,000 to 60,000; **Figure S3.11**).

3.5.10. Characterization of surface hydrophilicity

Static water contact angle measurements were performed with an OCA 20 (future digital scientific) contact angle measurement system and calculated with the SCA 20 software module. 3 μL droplets of MilliQ water (>18.2 MΩ cm resistivity) were deposited on PS-Au and PS-Au-pCB surfaces and photographed. Three droplets were placed at different locations on non-shrunk surfaces and single droplets were placed on shrunk surfaces due to the small size following the shrinking procedure. Three surfaces for each condition were measured.

3.5.11. Scanning electron microscopy

SEM images were acquired with a JSM-7000S SEM (JEOL USA Inc., Peabody, MA, USA). All images were collected with a working distance of (10 mm), accelerating voltage of (3.0 kV) and a probe current setting of "small". PS-Au discs were attached to the SEM stub via graphite tape and nickel paint was used to connect the Au surfaces to the SEM stub. Length of wrinkles was measured using 100 peak to peak measurements in ImageJ.

3.5.12. Determination of relative polymer content

Graft-then-Shrink and Shrink-then-Graft PS-Au-pCB discs were incubated in a 1:1 solution of DI water and BCA solution prepared according to manufacturer protocols. The discs were incubated for 2 h at 37 °C in a 96 well plate, the discs were then removed from the solution and solution absorbance at 562 nm measured with a Biotek Cytation 5 plate reader.

3.5.13. XPS

Surface elemental composition of PS-Au-pCB_{60} discs were analyzed with a PHI Quantera II scanning x-ray photoelectron spectroscopy (XPS) microprobe. A 45° take-off angle was used for all samples, pass energy and step size were 55 eV and 0.1 eV for high resolution scans, which were used to determine elemental composition.

3.5.14. Determination of grafting density by fluorescent polymer microscopy

Fluorescein-NHS was synthesized by combining 82.5 mg of fluorescein sodium salt, 21 mg of EDC and 12.6 mg of NHS in 1 mL of PBS at 4˚C and incubating for 1 h. 60 kDa pCB-*co*-APMA with 5% APMA content was fluorescently labeled with fluorescein-NHS by addition of 50 mg of polymer to previous solution, followed by incubation overnight at 4˚C. The fluorescent polymer solution was then centrifuged at 5000 RPM for 5 mins, and the supernatant dialyzed for 3 d against DI water, and freeze dried yielding 40 mg of orange powder. Known masses of pCB-*co*-APMA labeled with fluorescein were drop cast onto Au discs and shrunk. Shrink-then-Graft and Graft-then-Shrink surfaces were prepared by immersion of the surfaces in 1 mg mL^{-1} solutions of fluorescent pCB-*co*-APMA for 4 d. These surfaces were then imaged and surface fluorescence of known mass calibrants were used to determine the mass of polymers on Shrink-then-Graft and Graft-then-Shrink surfaces. The known area of the surfaces and molecular weight of the polymers determined by gel permeation chromatography were used to calculate chains per nm^2.

3.5.15. Macrophage adhesion

PS-Au-pCB discs were bonded to PS plates with 40 µL of silicone (Sylgard™ 184) and cured at 60 °C for 1 h, then sterilized by incubation with 70% ethanol for 1 h and exposed to UV light for 1 h. Surfaces were then incubated with 100% CBS for 48 h to allow for nonspecific protein adhesion to surfaces. Finally, serum was removed, and wells were seeded with 200 µL per 96 well and 1 mL per 24 well, of 50 000 cells mL^{-1} Raw 264.7 macrophages. Following a 24 h incubation at 37 °C at 5% CO_2, cells were stained with Calcein AM according to manufacturer instructions and imaged with a Biotek Cytation 5 plate reader equipped with a GFP filter cube.

3.5.16. Pseudomonas aeruginosa adhesion

PS-Au-pCB surfaces were immobilized onto glass slides with droplets of silicone (Sylgard 184) and cured at 60 °C for 1 h. All slides were then sterilized via autoclave in sterilization pouches, and then heated at 130 °C for 15 min to remove haze from the PS bases. *Pseudomonas aeruginosa* (PA01) were incubated in LB at 37 °C until and OD_{600} of 0.1 was reached. Samples were then incubated for 20 h with *P. aeruginosa* at 37 °C in LB media. The glass slides were then removed from the bacterial suspension and rinsed gently 3 times with room temperature sterile PBS. Bacteria on each surface were then stained with a BacLight kit according to the manufacturer's instructions. A cover slip was taped over the PS-Au surfaces and fluorescence microscopy was performed with a Nikon Eclipse Ti inverted microscope.

3.5.17. LSPR sensitivity measurements

Non-coated PS-Au and coated PS-Au-pCB surfaces were immobilized into a 96 well plate with 40 μL of silicone (Sylgard 184) and cured at 60 °C for 1 h. Each non-coated surface (2.5, 3.7, 5, and 7.5 nm Au thickness) was then exposed to various aqueous solutions of D-(+)-glucose and alcohols (MeOH, EtOH, IPA and n-BuOH), coated pCB-Au-pCB (5 nm Au thickness) surfaces were exposed to D-(+)-glucose solutions only. Absorbance spectra from 300 to 999 nm (1 nm step size) were acquired of each sensor with a Biotek Cytation 5 plate reader. Peaks were then fit to data between 750 and 870 nm with GraphPad Prism 5.

3.5.18. Protein sensing with LSPR surfaces

Avidin detection was performed by immobilizing protein covalently to pCB homopolymer surfaces and through non-covalent avidin-desthiobiotin and avidin-biotin interactions with desthiobiotinylated and biotinylated pCB-*co*-APMA sensor surfaces. Absorbance was measured in 1 nm intervals from 700 to 870 nm every 9 s with a Biotek Cytation 5 plate reader for the duration of each reading period.

3.5.19. Covalent protein immobilization

For covalent avidin detection, sensors with pCB coatings were sequentially exposed to PBS (5 mL), EDC (0.1 M) and NHS (0.1 M) in water (1 mL), Avidin (1 μM; 200 μL) in PBS and PBS buffer for 23 minutes each. Sensors were rinsed with sodium acetate buffer (10 mM, pH 4.5) after EDC/NHS step. The immobilization process was tracked by maximum absorbance peak position.

3.5.20. Fluidic device fabrication

Wells were removed from a polystyrene 96 well plate with pliers, and 2 mL of Sylgard 184 PDMS was cured in the well free area to create a flat surface. A 0.54 cm diameter sensor was placed in the location of a well in the 96 well plate and was held in place by curing 2 mL of Sylgard 184 PDMS around the sensor. A slab of PDMS was cured with a 0.6 cm wide channel, an inlet, and an outlet, and adhered over the embedded sensor with a thin layer of PDMS to allow solutions to flow over the sensor surface (**Figure S3.12**).

3.5.21. Non-covalent protein sensing

Non-covalent avidin detection was performed similarly to covalent sensing with maximum absorption peak position tracked for 21 minutes for each exposed solution. Sensors with pCB-*co*-APMA coatings were functionalized with biotin or desthiobiotin prior to exposure to avidin solutions; sensors were exposed to biotin-NHS or desthiobiotin-NHS at 2 mg mL^{-1} in 4:1 PBS:DMF (1 mL) for 21 minutes, then rinsed with 0.1 M butylamine in PBS (1 mL) to passivate unreacted EDC/NHS. Finally, sensors were flushed with 20 mL of PBS before exposure to analytes.

3.5.22. Statistical analysis

All statistical analyses were performed using GraphPad Prism 8. Significant differences were determined by one-way ANOVA with Bonferroni post hoc test. Significant p-values are indicated on graphs as follows $p < 0.05$ is indicated by *,and $p < 0.01$ by **. Replicates were performed on multiple samples prepared and analyzed at the same time, in a single experiment.

3.6. Supporting information

Additional experimental figures, photographs and equations including BCA assay, High-resolution XPS, Fluorescent microscopy, Low magnification SEM, WCA, P. aeruginosa fouling, Confocal microscopy of BSA-Cy5, HABA – Avidin displacement assay, Calibration curve of BSA on sensor, Removal of haze from PS, Gel permeation chromatographs, Construction of fluidic channel

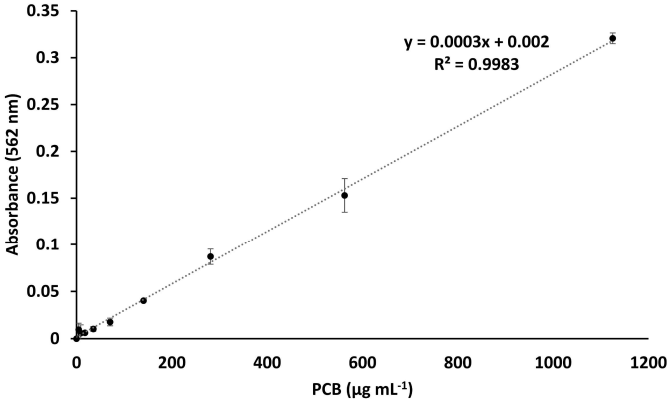

Figure S3.1: BCA activity with pCB. Calibration curve for the BCA assay with 10 kDa pCB solutions (mean ± SD, n = 3).

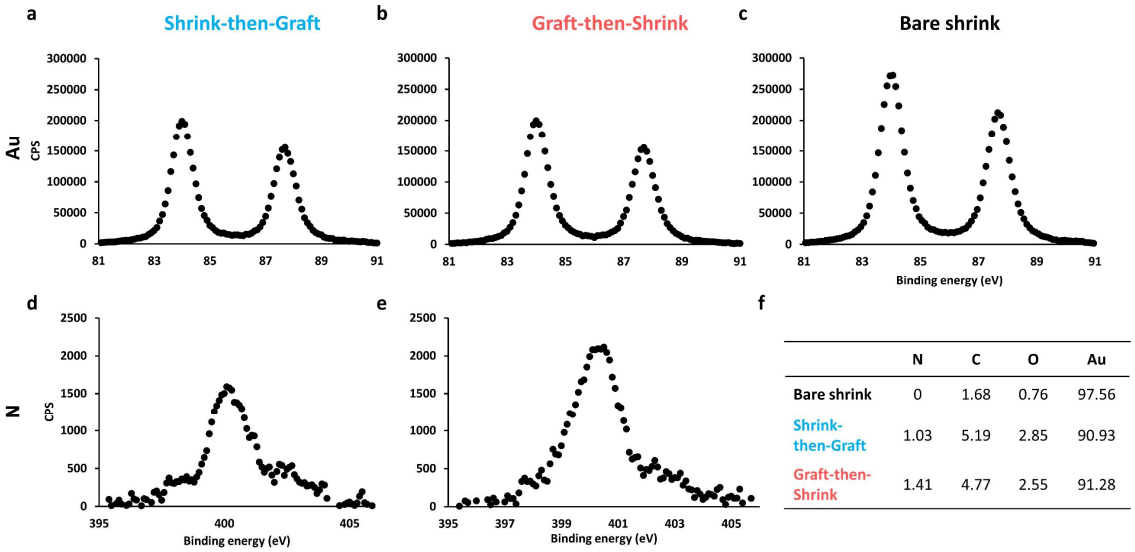

	N	C	O	Au
Bare shrink	0	1.68	0.76	97.56
Shrink-then-Graft	1.03	5.19	2.85	90.93
Graft-then-Shrink	1.41	4.77	2.55	91.28

Figure S3.2: High-resolution XPS of wrinkled Au surfaces. XPS of binding energy in Au region for a) Shrink-then-Graft, b) Graft-then-Shrink, and c) bare wrinkled Au surfaces. XPS of binding energy in N region for d) Shrink-then-Graft and e) Graft-then-Shrink surfaces. 60 kDa pCB was used for all surfaces. f) Table of elemental concentrations of bare and pCB modified surfaces.

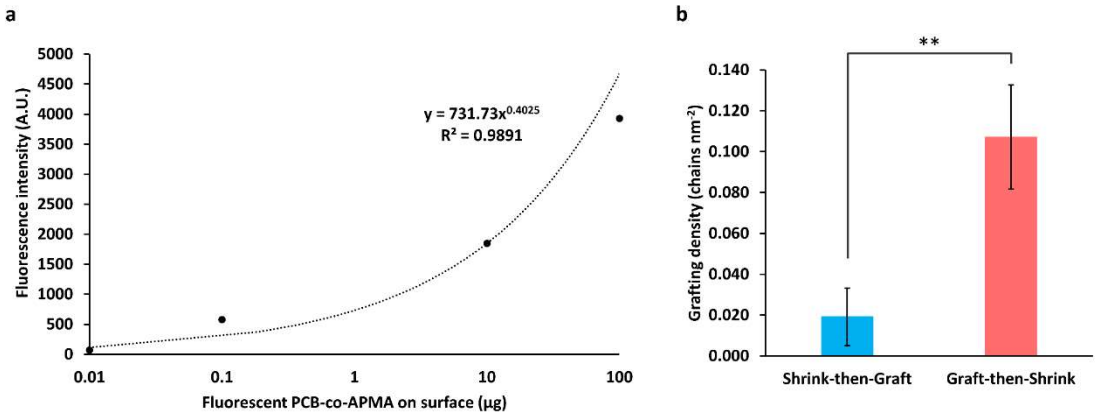

Figure S3.3: Determination of chain density of fluorescently labeled pCB-*co*-APMA. a) Quantification of fluorescent micrographs of dropcast known masses of fluorescent pCB-*co*-APMA and b) calculated chain densities of fluorescent pCB-*co*-APMA surfaces prepared via either Shrink-then-Graft or Graft-then-Shrink techniques. (mean ± SD, n = 3).

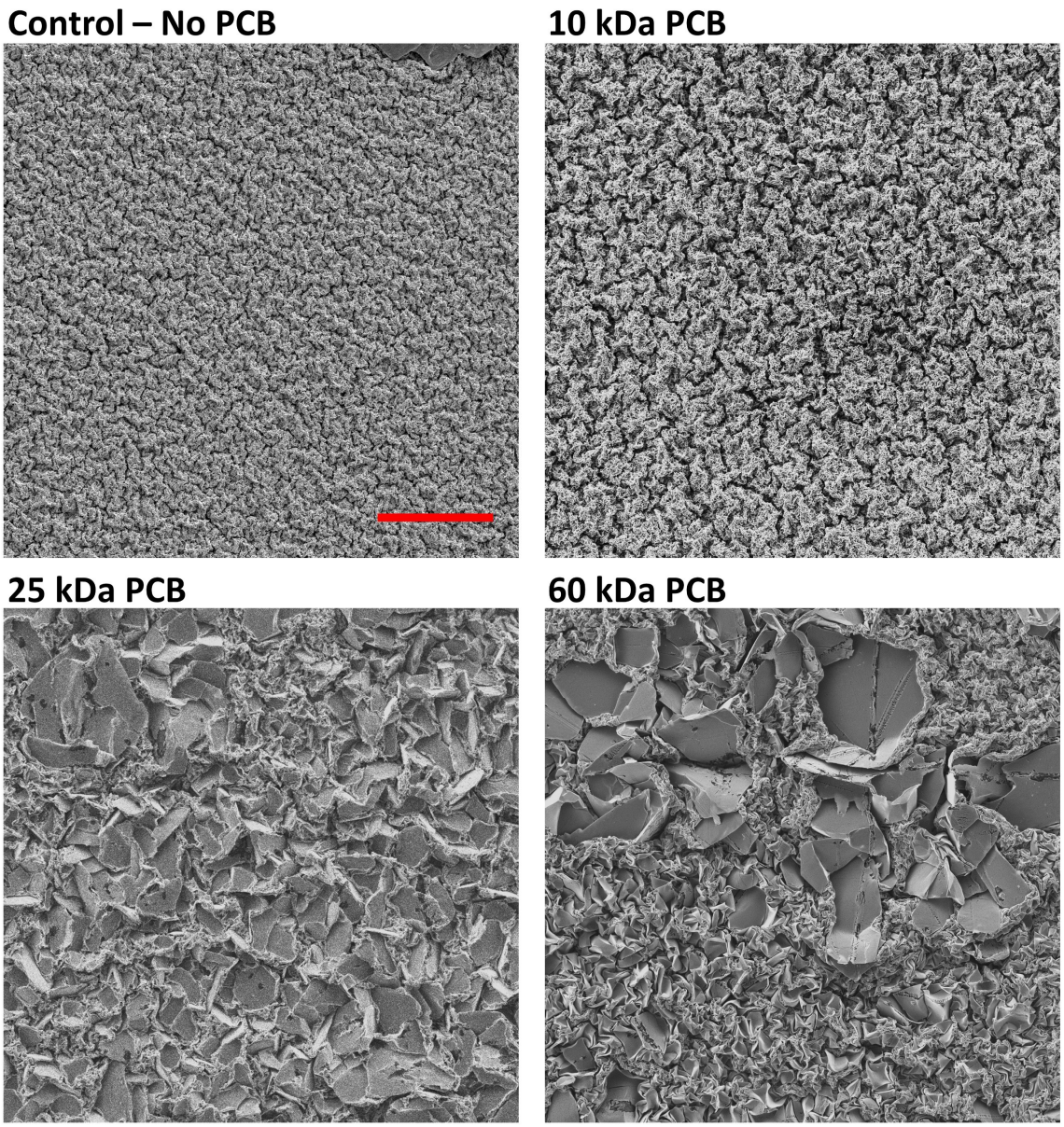

Figure S3.4: Low magnification SEM of surfaces. SEM of control 5 nm gold surface with no polymer coating and pCB coated Graft-then-Shrink dry surfaces showing large scale heterogeneity in 25 and 60 kDa samples. Scale bar = 10 μm.

$$\lambda = 2\pi h\left(\frac{E_s}{E_b}\right)^{\frac{1}{3}} \qquad (S1)$$

Where λ is the wrinkle length, h is the thickness of the film, E_s is the modulus of the skin, 78 GPa in the case of Au, and E_b is the modulus of the base material, 3 GPa in the case of polystyrene.

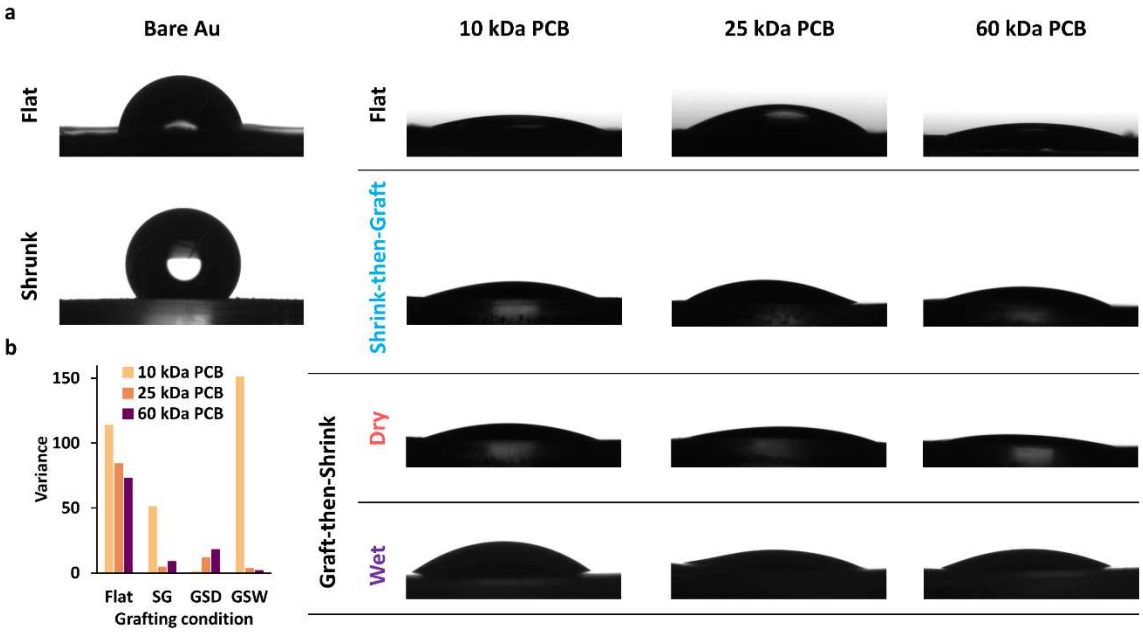

Figure S3.5: Hydrophilicity of pCB coated surfaces. a) Micrographs of 3 µL MilliQ water droplets on bare and pCB coated flat and shrunk (wrinkled) 5 nm gold surfaces. b) Variance of WCAs of coated surfaces from a) (mean ± SD, n = 3). WCAs for polymer coated surfaces are shown in **Figure** 3.3.

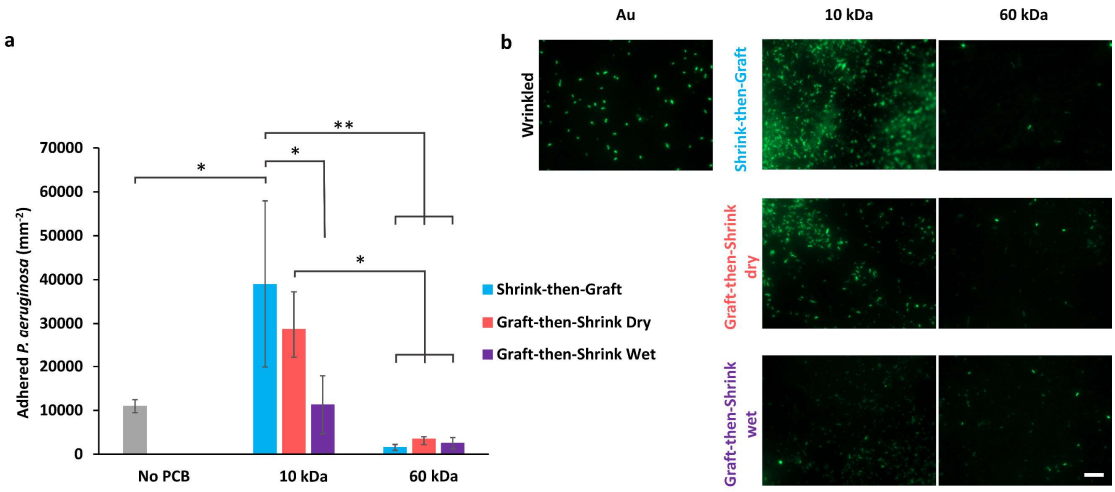

Figure S3.6: Nonspecific adhesion of *P. aeruginosa* to bare and pCB coated wrinkled gold. a) Quantification of adhered cells in each field of view (mean ± SD, n = 3). b) Fluorescence micrographs of stained *P. aeruginosa*. Scale bar = 10 μm.

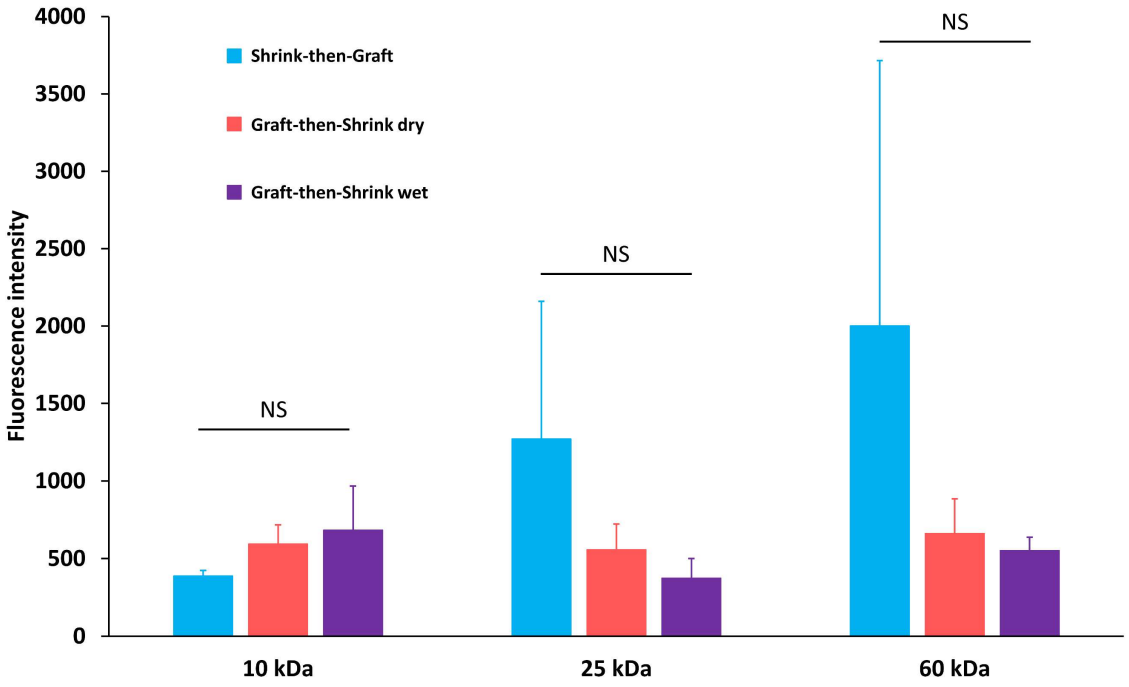

Figure S3.7: Confocal microscopy for quantification of nonspecific BSA-Cy5 adsorption to wrinkled pCB-Au surfaces. pCB-Au surfaces with 3 molecular weights of pCB were exposed to BSA-Cy5 solutions, rinsed, and imaged via confocal microscopy (mean ± SD, n = 3). Graft-then-Shrink conditions for 25 and 60 kDa pCB trended to lower BSA adsorption, although samples were not statistically significant due to large variability in Shrink-then-Graft controls. Similar trends in nonspecific adsorption were seen in macrophage fouling experiments.

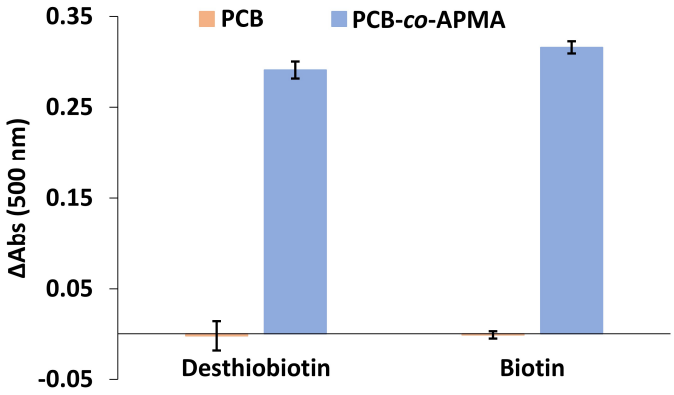

Figure S3.8: HABA – Avidin displacement assay of pCB-*co*-APMA modified with biotin and desthiobiotin. To determine if pCB conjugated desthiobiotin and biotin remains bioactive, the HABA displacement assay was used to observe desthiobiotin and biotin binding events. Both pCB-*co*-APMA modified with desthiobiotin and biotin resulted in absorbance changes due to displacement of HABA from avidin binding pocket, demonstrating their bioactivity. Unmodified pCB (without desthiobiotin or biotin) did not displace HABA, as expected. The HABA-avidin assay was performed according to the manufacturer's protocol. First, absorbance at 500 nm was quantified for 180 µL of HABA-avidin solutions. 20 µL of 1 mg mL^{-1} polymer solutions in water were then added to each corresponding well. After a 20 minute incubation at room temperature with shaking, absorbance at 500 nm was measured and the change in absorbance was calculated. (mean ± SD, n = 3).

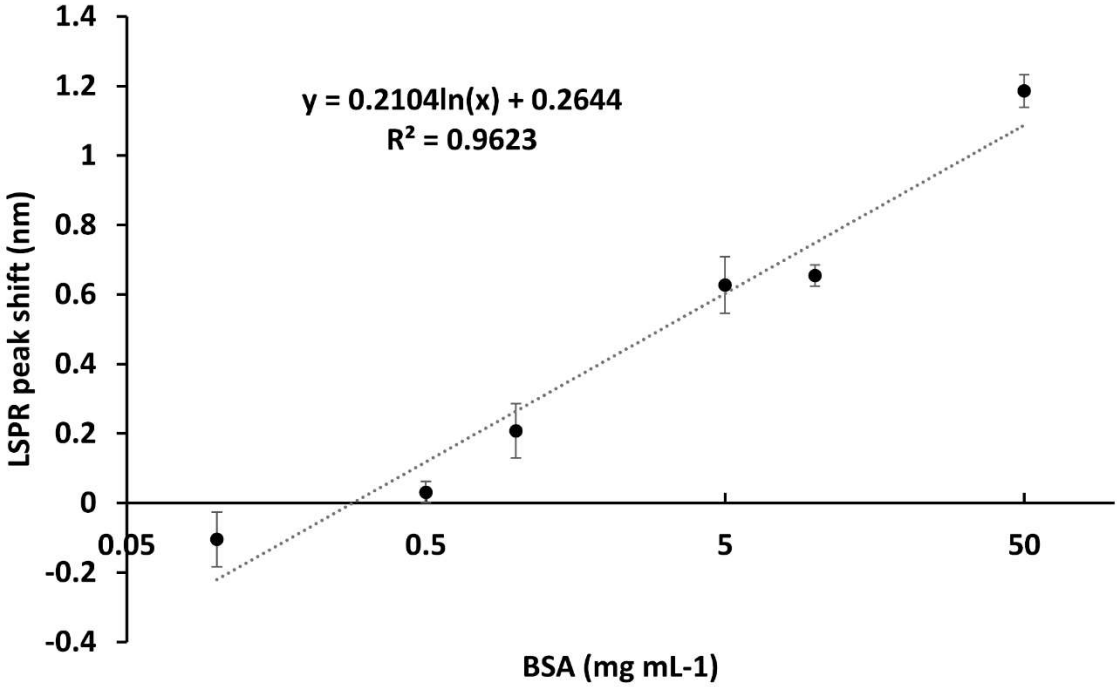

Figure S3.9: LSPR response of biotin modified pCB-*co*-APMA sensor exposed to BSA in HEPES buffer. To determine bulk shift response due to nonspecific protein signal in solution and adsorbed to the sensor surface, a biotin modified LSPR sensor similar to that used for avidin detection was exposed to various concentrations of BSA in HEPES.

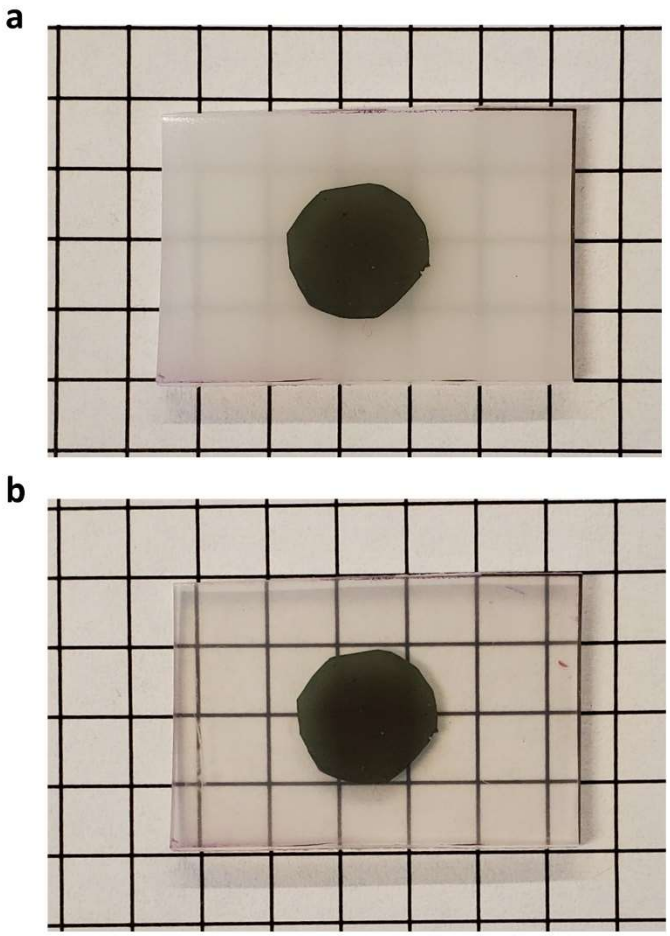

Figure S3.10: Removal of haze from PS following Graft-then-Shrink wet. After the shrinking process in Graft-then-Shrink wet, the PS is cloudy. To remove the cloudiness and return the PS to transparent, the devices were heated for 15 minutes at 130 °C. a) Circular 5 nm Au layer on polystyrene base following shrinking in an autoclave to produce Graft-then-Shrink wet surface. b) Sample from a) after 15 min incubation at 130 °C to remove cloudiness.

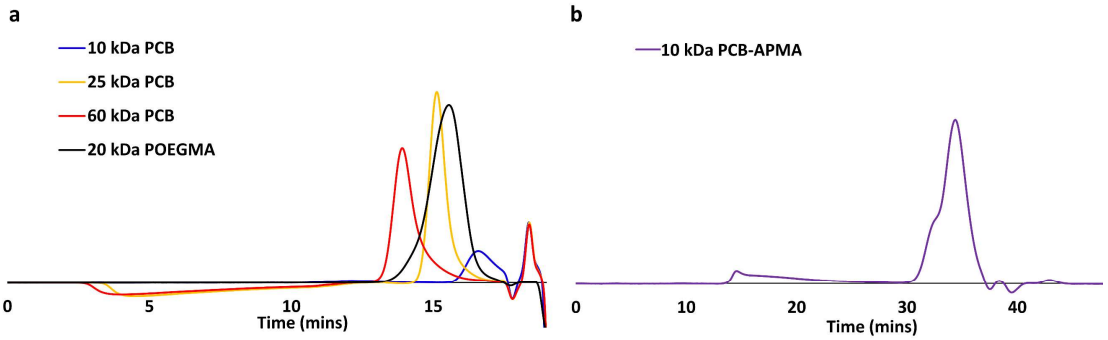

c

Polymer	M_n	M_w	M_p	Đ
PCB_{10}	9.9	10.6	10.8	1.07
PCB_{25}	25.3	27.0	28.4	1.07
PCB_{60}	46.9	56.2	62.9	1.20
PCB-$APMA_{10}$	9.9	10.6	9.6	1.06
$POEGMA_{20}$	21.8	25.5	21.4	1.17

Figure S3.11: Gel permeation chromatographs of polymers used. a) homopolymer pCB and POEGMA using Agilent PL aquagel-OH 30 and Agilent PL aquagel-OH 40 columns in series (y-axes represent normalized refractive index intensity) and b) pCB-APMA copolymer using a Superose 6 Increase 10/300 GL column. c) Calculated MWs and dispersities of polymers in a) and b).

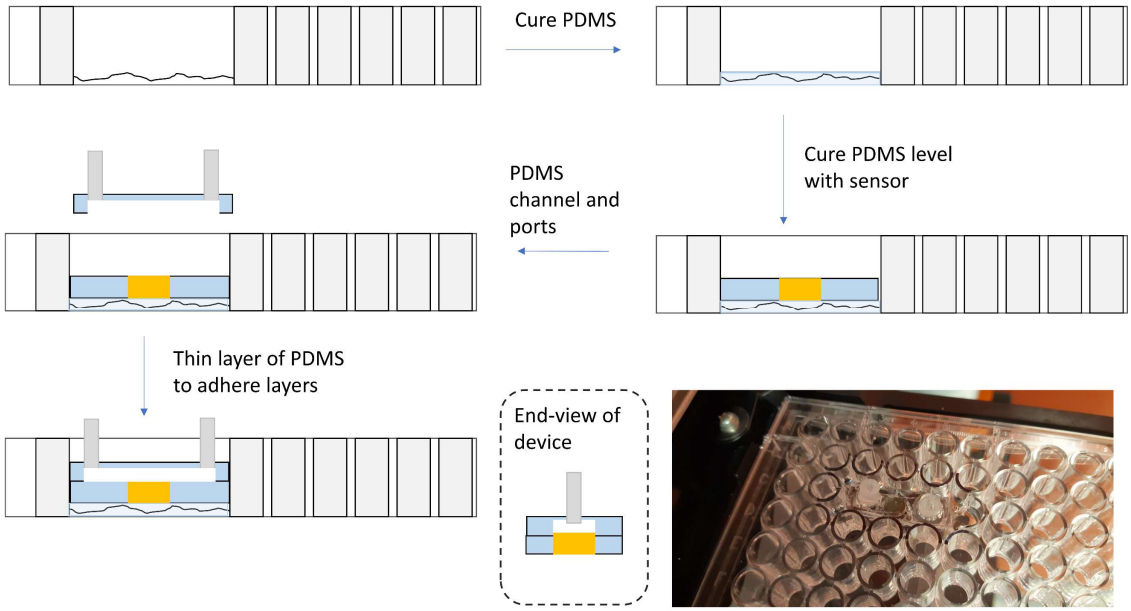

Figure S3.12: Construction of fluidic channel in a 96 well plate for placement of a Graft-then-Shrink sensor. Wells are first removed from a section of the plate, leaving a rough surface, PDMS is the cured to create a flat surface, and a sensor is placed onto a region of the plate that corresponds to a well location. The sensor is held in place by the layer of PDMS. A simple channel is the placed over the sensor for the flow of solutions over the sensor surface; the device is held in place with a thin layer of PDMS.

3.7. References

(1) Sundaram, H. S.; Han, X.; Nowinski, A. K.; Brault, N. D.; Li, Y.; Ella-Menye, J. R.; Amoaka, K. A.; Cook, K. E.; Marek, P.; Senecal, K.; Jiang, S. Achieving One-Step Surface Coating of Highly Hydrophilic Poly(Carboxybetaine Methacrylate) Polymers on Hydrophobic and Hydrophilic Surfaces. *Adv. Mater. Interfaces* **2014**, *1* (6), 1–8. https://doi.org/10.1002/admi.201400071.

(2) Sundaram, H. S.; Han, X.; Nowinski, A. K.; Ella-Menye, J. R.; Wimbish, C.; Marek, P.; Senecal, K.; Jiang, S. One-Step Dip Coating of Zwitterionic Sulfobetaine Polymers on Hydrophobic and Hydrophilic Surfaces. *ACS Appl.*

Mater. Interfaces **2014**, *6* (9), 6664–6671. https://doi.org/10.1021/am500362k.

(3) Ukita, R.; Wu, K.; Lin, X.; Carleton, N. M.; Naito, N.; Lai, A.; Do-Nguyen, C. C.; Demarest, C. T.; Jiang, S.; Cook, K. E. Zwitterionic Poly-Carboxybetaine Coating Reduces Artificial Lung Thrombosis in Sheep and Rabbits. *Acta Biomater.* **2019**, *92*, 71–81. https://doi.org/10.1016/j.actbio.2019.05.019.

(4) Vaisocherová, H.; Brynda, E.; Homola, J. Functionalizable Low-Fouling Coatings for Label-Free Biosensing in Complex Biological Media: Advances and Applications. *Anal. Bioanal. Chem.* **2015**, *407* (14), 3927–3953. https://doi.org/10.1007/s00216-015-8606-5.

(5) Zhang, S.; Geryak, R.; Geldmeier, J.; Kim, S.; Tsukruk, V. V. Synthesis, Assembly, and Applications of Hybrid Nanostructures for Biosensing. *Chem. Rev.* **2017**, *117* (20), 12942–13038. https://doi.org/10.1021/acs.chemrev.7b00088.

(6) Maan, A. M. C.; Hofman, A. H.; de Vos, W. M.; Kamperman, M. Recent Developments and Practical Feasibility of Polymer-Based Antifouling Coatings. *Adv. Funct. Mater.* **2020**, *30* (32), 2000936. https://doi.org/10.1002/adfm.202000936.

(7) Scott, E. A.; Nichols, M. D.; Cordova, L. H.; George, B. J.; Jun, Y. S.; Elbert, D. L. Protein Adsorption and Cell Adhesion on Nanoscale Bioactive Coatings Formed from Poly(Ethylene Glycol) and Albumin Microgels. *Biomaterials* **2008**, *29* (34), 4481–4493. https://doi.org/10.1016/j.biomaterials.2008.08.003.

(8) Banerjee, I.; Pangule, R. C.; Kane, R. S. Antifouling Coatings: Recent Developments in the Design of Surfaces That Prevent Fouling by Proteins, Bacteria, and Marine Organisms. *Adv. Mater.* **2011**, *23* (6), 690–718. https://doi.org/10.1002/adma.201001215.

(9) Bandyopadhyay, S.; Jones, A.; McLean, A.; Sterner, M.; Robbins, C.; Cunningham, M.; Walters, M.; Doddapaneni, K.; Keitel, I.; Gallagher, C. Slippery Liquid Infused Fluoropolymer Coating for Central Lines to Reduce Catheter Associated Clotting and Infections. *Sci. Rep.* **2020**, *10*, 14973. https://doi.org/10.1038/s41598-020-71711-6.

(10) Kim, D.-H.; Lu, N.; Ghaffari, R.; Kim, Y.-S.; Lee, S. P.; Xu, L.; Wu, J.; Kim, R.-H.; Song, J.; Liu, Z.; Viventi, J.; De Graff, B.; Elolampi, B.; Mansour, M.; Slepian, M. J.; Hwang, S.; Moss, J. D.; Won, S.-M.; Huang, Y.; Litt, B.; Rogers, J. A. Materials for Multifunctional Balloon Catheters with Capabilities in Cardiac Electrophysiological Mapping and Ablation Therapy. *Nat. Mater.* **2011**, *10* (4), 316–323. https://doi.org/10.1038/nmat2971.

(11) Park, S. J.; Kim, J.; Chu, M.; Khine, M. Highly Flexible Wrinkled Carbon Nanotube Thin Film Strain Sensor to Monitor Human Movement. *Adv. Mater. Technol.* **2016**, *1* (5), 1–8. https://doi.org/10.1002/admt.201600053.

(12) Chang, T.-H.; Tian, Y.; Li, C.; Gu, X.; Li, K.; Yang, H.; Sanghani, P.; Lim, C. M.; Ren, H.; Chen, P.-Y. Stretchable Graphene Pressure Sensors with Shar-Pei-like Hierarchical Wrinkles for Collision-Aware Surgical Robotics. *ACS Appl. Mater.*

Interfaces **2019**, *11* (10), 10226–10236. https://doi.org/10.1021/acsami.9b00166.

(13) Grimes, A.; Breslauer, D. N.; Long, M.; Pegan, J.; Lee, L. P.; Khine, M. Shrinky-Dink Microfluidics: Rapid Generation of Deep and Rounded Patterns. *Lab Chip* **2007**, *8* (1), 170–172. https://doi.org/10.1039/b711622e.

(14) Chen, C. S.; Breslauer, D. N.; Luna, J. I.; Grimes, A.; Chin, W. C.; Lee, L. P.; Khine, M. Shrinky-Dink Microfluidics: 3D Polystyrene Chips. *Lab Chip* **2008**, *8* (4), 622–624. https://doi.org/10.1039/b719029h.

(15) Oran, D.; Rodrigques, S. G.; Gao, R.; Asano, S.; Skylar-scott, M. A.; Chen, F.; Tillberg, P. W.; Marblestone, A. H.; Boyden, E. S. 3D Nanofabrication by Volumetric Deposition and Controlled Shrinkage of Patterned Scaffolds. *Science (80-.).* **2018**, *362* (6420), 1281–1285.

(16) Genzer, J.; Efimenko, K. Creating Long-Lived Superhydrophobic Polymer Surfaces through Mechanically Assembled Monolayers. *Science (80-.).* **2000**, *290* (5499), 2130–2133. https://doi.org/10.1126/science.290.5499.2130.

(17) Mousavi M, S. S.; Bicket, I. C.; Bellido, E. P.; Soleymani, L.; Botton, G. A. Electron Energy-Loss Spectroscopy of Surface Plasmon Activity in Wrinkled Gold Structures. *J. Chem. Phys.* **2020**, *153* (22), 224703. https://doi.org/10.1063/5.0031469.

(18) Zoppe, J. O.; Ataman, N. C.; Mocny, P.; Wang, J.; Moraes, J.; Klok, H. Surface-Initiated Controlled Radical Polymerization: State-of-the-Art, Opportunities, and

Challenges in Surface and Interface Engineering with Polymer Brushes. *Chem. Rev.* **2017**, *117* (3), 1105–1318.

(19) Michalek, L.; Barner, L.; Barner-Kowollik, C. Polymer on Top: Current Limits and Future Perspectives of Quantitatively Evaluating Surface Grafting. *Adv. Mater.* **2018**, *30* (21), 1–18. https://doi.org/10.1002/adma.201706321.

(20) Chen, Y.; Liu, J.; Yang, Z.; Wilkinson, J. S.; Zhou, X. Optical Biosensors Based on Refractometric Sensing Schemes: A Review. *Biosens. Bioelectron.* **2019**, *144*, 111693. https://doi.org/10.1016/j.bios.2019.111693.

(21) Haes, A. J.; Zou, S.; Schatz, G. C.; Van Duyne, R. P. Nanoscale Optical Biosensor: Short Range Distance Dependence of the Localized Surface Plasmon Resonance of Noble Metal Nanoparticles. *J. Phys. Chem. B* **2004**, *108* (22), 6961–6968. https://doi.org/10.1021/jp036261n.

(22) Zhang, Z.; Chen, S.; Jiang, S. Dual-Functional Biomimetic Materials: Nonfouling Poly(Carboxybetaine) with Active Functional Groups for Protein Immobilization. *Biomacromolecules* **2006**, *7* (12), 3311–3315. https://doi.org/10.1021/BM060750M.

(23) Gabardo, C. M.; Zhu, Y.; Soleymani, L.; Moran-Mirabal, J. M. Bench-Top Fabrication of Hierarchically Structured High-Surface-Area Electrodes. *Adv. Funct. Mater.* **2013**, *23* (24), 3030–3039. https://doi.org/10.1002/adfm.201203220.

(24) Jatschka, J.; Dathe, A.; Csáki, A.; Fritzsche, W.; Stranik, O. Propagating and

Localized Surface Plasmon Resonance Sensing - A Critical Comparison Based on Measurements and Theory. *Sens. Bio-Sensing Res.* **2016**, *7*, 62–70. https://doi.org/10.1016/j.sbsr.2016.01.003.

(25) França, Á.; Pelaz, B.; Moros, M.; Sánchez-Espinel, C.; Hernández, A.; Fernández-López, C.; Grazú, V.; De La Fuente, J. M.; Pastoriza-Santos, I.; Liz-Marzán, L. M.; González-Fernández, Á. Sterilization Matters: Consequences of Different Sterilization Techniques on Gold Nanoparticles. *Small* **2010**, *6* (1), 89–95. https://doi.org/10.1002/smll.200901006.

(26) Chandekar, A.; Sengupta, S. K.; Whitten, J. E. Thermal Stability of Thiol and Silane Monolayers: A Comparative Study. *Appl. Surf. Sci.* **2010**, *256* (9), 2742–2749. https://doi.org/10.1016/j.apsusc.2009.11.020.

(27) Genzer, J.; Groenewold, J. Soft Matter with Hard Skin: From Skin Wrinkles to Templating and Material Characterization. *Soft Matter* **2006**, *2* (4), 310–323. https://doi.org/10.1039/b516741h.

(28) Stimpson, T. C.; Osorio, D. A.; Cranston, E. D.; Moran-Mirabal, J. M. Direct Comparison of Three Buckling-Based Methods to Measure the Elastic Modulus of Nanobiocomposite Thin Films. *ACS Appl. Mater. Interfaces* **2021**. https://doi.org/10.1021/acsami.1c08056.

(29) Chapman, C. T.; Paci, J. T.; Lee, W. K.; Engel, C. J.; Odom, T. W.; Schatz, G. C. Interfacial Effects on Nanoscale Wrinkling in Gold-Covered Polystyrene. *ACS Appl. Mater. Interfaces* **2016**, *8* (37), 24339–24344.

https://doi.org/10.1021/acsami.6b08554.

(30) Huynh, V.; Jesmer, A. H.; Shoaib, M. M.; Wylie, R. G. Influence of Hydrophobic Cross-Linkers on Carboxybetaine Copolymer Stimuli Response and Hydrogel Biological Properties. *Langmuir* **2019**, *35* (5), 1631–1641. https://doi.org/10.1021/acs.langmuir.8b03908.

(31) Gill, U.; Sutherland, T.; Himbert, S.; Zhu, Y.; Rheinstädter, M. C.; Cranston, E. D.; Moran-Mirabal, J. M. Beyond Buckling: Humidity-Independent Measurement of the Mechanical Properties of Green Nanobiocomposite Films. *Nanoscale* **2017**, *9* (23), 7781–7790. https://doi.org/10.1039/c7nr00251c.

(32) Jesmer, A. H.; Huynh, V.; Wylie, R. G. Fabrication of Low-Fouling, High-Loading Polymeric Surfaces through PH-Controlled RAFT. *RSC Adv.* **2020**, *10*, 20302–20312. https://doi.org/10.1039/d0ra02693j.

(33) Zhang, L.; Zhao, N.; Xu, J. Fabrication and Application of Superhydrophilic Surfaces: A Review. *J. Adhes. Sci. Technol.* **2014**, *28* (8–9), 769–790. https://doi.org/10.1080/01694243.2012.697714.

(34) Nguyen, D. H. K.; Bazaka, O.; Bazaka, K.; Crawford, R. J.; Ivanova, E. P. Three-Dimensional Hierarchical Wrinkles on Polymer Films: From Chaotic to Ordered Antimicrobial Topographies. *Trends Biotechnol.* **2020**, *38* (5), 558–571. https://doi.org/10.1016/j.tibtech.2019.12.004.

(35) Nguyen, D. H. K.; Pham, V. T. H.; Truong, V. K.; Sbarski, I.; Wang, J.; Balčytis,

A.; Juodkazis, S.; Mainwaring, D. E.; Crawford, R. J.; Ivanova, E. P. Role of Topological Scale in the Differential Fouling of: Pseudomonas Aeruginosa and Staphylococcus Aureus Bacterial Cells on Wrinkled Gold-Coated Polystyrene Surfaces. *Nanoscale* **2018**, *10* (11), 5089–5096. https://doi.org/10.1039/c7nr08178b.

(36) Mayer, K. M.; Hafner, J. H. Localized Surface Plasmon Resonance Sensors. *Chem. Rev.* **2011**, *111* (6), 3828–3857. https://doi.org/10.1021/cr100313v.

(37) Fu, C. C.; Grimes, A.; Long, M.; Ferri, C. G. L.; Rich, B. D.; Ghosh, S.; Ghosh, S.; Lee, L. P.; Gopinathan, A.; Khine, M. Tunable Nanowrinkles on Shape Memory Polymer Sheets. *Adv. Mater.* **2009**, *21* (44), 4472–4476. https://doi.org/10.1002/adma.200902294.

(38) Brault, N. D.; Sundaram, H. S.; Huang, C. J.; Li, Y.; Yu, Q.; Jiang, S. Two-Layer Architecture Using Atom Transfer Radical Polymerization for Enhanced Sensing and Detection in Complex Media. *Biomacromolecules* **2012**, *13* (12), 4049–4056. https://doi.org/10.1021/bm301335r.

(39) Huang, C. J.; Li, Y.; Jiang, S. Zwitterionic Polymer-Based Platform with Two-Layer Architecture for Ultra Low Fouling and High Protein Loading. *Anal. Chem.* **2012**, *84* (7), 3440–3445. https://doi.org/10.1021/ac3003769.

(40) Green, M. N. Avidin. *Adv. Protein Chem.* **1975**, *29*, 85–133. https://doi.org/10.1007/978-3-540-37885-3_11.

(41) Piran, U.; Riordan, W. J. Dissociation Rate Constant of the Biotin-Streptavidin Complex. *J. Immunol. Methods* **1990**, *133* (1), 141–143. https://doi.org/10.1016/0022-1759(90)90328-S.

(42) Hirsch, J. D.; Eslamizar, L.; Filanoski, B. J.; Malekzadeh, N.; Haugland, R. P.; Beechem, J. M.; Haugland, R. P. Easily Reversible Desthiobiotin Binding to Streptavidin, Avidin, and Other Biotin-Binding Proteins: Uses for Protein Labeling, Detection, and Isolation. *Anal. Biochem.* **2002**, *308* (2), 343–357. https://doi.org/10.1016/S0003-2697(02)00201-4.

(43) Aćimovic, S. S.; Ortega, M. a; Sanz, V.; Berthelot, J.; Garcia-Cordero, J. L.; Renger, J.; Maerkl, S. J.; Kreuzer, M. P.; Quidant, R. LSPR Chip for Parallel, Rapid, and Sensitive Detection of Cancer Markers in SerumMarkers in Serum. *Nano Lett.* **2014**, *14* (5), 2636–2641.

(44) Nguyen, D.; Taylor, D.; Qian, K.; Norouzi, N.; Rasmussen, J.; Botzet, S.; Lehmann, M.; Halverson, K.; Khine, M. Better Shrinkage than Shrinky-Dinks. *Lab Chip* **2010**, *10* (12), 1623–1626. https://doi.org/10.1039/c001082k.

(45) Kingshott, P.; Thissen, H.; Griesser, H. J. Effects of Cloud-Point Grafting, Chain Length, and Density of PEG Layers on Competitive Adsorption of Ocular Proteins. *Biomaterials* **2002**, *23* (9), 2043–2056. https://doi.org/10.1016/S0142-9612(01)00334-9.

(46) Cao, Z.; Yu, Q.; Xue, H.; Cheng, G.; Jiang, S. Nanoparticles for Drug Delivery Prepared from Amphiphilic PLGA Zwitterionic Block Copolymers with Sharp

Contrast in Polarity between Two Blocks. *Angew. Chemie - Int. Ed.* **2010**, *49* (22), 3771–3776. https://doi.org/10.1002/anie.200907079.

CHAPTER 4. GRAFTING POLYMERS TO SOLVENT SWELLED PDMS ELASTOMERS INCREASES THIN FILM DENSITY AND ANTIFOULING PERFORMANCE

Author's Preface:

The following chapter has been submitted for publication under the citation:

Jesmer, A.H., Marple, A.S.T., Wylie, R.G. Grafting polymers to solvent swelled PDMS elastomers increases thin film density and antifouling performance.

A.H. Jesmer planned the study, conducted most of the experiments and wrote the manuscript. A.S.T. Marple assisted with conducting fouling experiments and material preparation and revised the manuscript. R.G. Wylie assisted in experimental design and data interpretation and revised the manuscript.

4.1. Abstract:

Elastomers, such as PDMS, are clinically important materials for implanted medical devices such as those used in urinary and venous catheters, cosmetic and reconstructive surgeries, and sensor platforms. These materials continue to suffer from nonspecific interactions with cells and proteins, leading to failure modes. To reduce these deleterious interactions, antifouling polymer coatings are routinely grafted on to the device surface. Even though graft-from techniques result in higher polymer densities and lower fouling in controlled settings, graft-to methods often show improved results due to real world fabrication complexities. Herein, we demonstrate enhanced efficiency of graft-to procedures for poly(oligo(ethylene glycol) methyl ether methacrylate) (pOEGMA) with pre-swollen PDMS, referred to as Graft-then-Shrink. Polymer grafting occurs via Click conjugations onto pre-swollen PDMS substrate that are subsequently deswelled to yield improved antifouling coatings. By using this method, total grafted polymer content of pOEGMA was increased by 44.9× over non swollen controls. By optimizing solvent swelling conditions with toluene to ethyl acetate, which both swells PDMS and solubilizes pOEGMA, polymer content increased by another 5× compared toluene swollen PDMS. These increases in polymer density led to bacterial and mammalian cell adhesion reductions of 75% and 91% respectively, compared to Shrink-then-Graft pOEGMA coated PDMS. The Graft-then-Shrink method did improve immobilization content of a zwitterionic polymer, poly(carboxybetaine), by 9.4× but did not consistently improve antifouling activity compared to controls. Interestingly, grafting pCB in the presence of a specific guanidinium concentration onto swollen PDMS further improved

grafting by over an order of magnitude. The Graft-then-Shrink method using swollen elastomers allows for 3D coated materials and provides a simple method for the improvement of antifouling pOEGMA coatings on common medical devices.

4.2. Introduction

Nonspecific interactions and immune responses between medical implants or implantable biomaterials and host cells and proteins continues to result in negative outcomes for current and new devices. Capsular contractions (i.e., breast implants[1] and the foreign body response (FBR)) often lead to issues in patient comfort and compromised performance. More recently, devices for the *in vivo* monitoring of biomolecules, such as glucose sensors for diabetes[2], are proving difficult for clinical translation because of nonspecific interactions. To overcome these limitations, we can introduce immunomodulatory agents to reduce the FBR or incorporate antifouling coatings to minimize nonspecific interactions, which is particularly important for temporary implants (e.g., catheters) and *in vivo* sensors to improve device performance and patient comfort[3].

Polydimethylsiloxane (PDMS) remains a widely used elastomeric material for implanted biomaterials[4]. PDMS is used in many applications including catheters, cosmetic and reconstructive implants, and implanted sensors. Nonspecific interactions of device surfaces with bacterial and mammalian cells remains an undesirable occurrence leading to hospital acquired infections[5,6], degradation of device performance[2], pain[3], and implant removal[7]. For example, urinary catheters result in two infections per 1000 days of use, making them the most common source of hospital acquired infection[8]. Methods to improve device performance towards decreasing the rate of hospital-acquired infection is therefore needed.

To control or eliminate these undesirable nonspecific interactions, the effects of surface topography[9–12], material stiffness[13], and the inclusion of antifouling materials have been widely explored[14]. Because polymer coatings can be applied to materials without changing the underlying properties, they provide a path to device optimization by minimizing alterations of existing materials. Among potential polymers, thin coatings of zwitterionic polymers (such as poly(2-methacryloiloxyethyl phosphorylcholine)[15,16], poly(sulfobetaine methacrylate)[17] (pSBMA) and poly(carboxybetaine methacrylamide)[18] (pCB)) and non-charged hydrophilic polyethylene glycol (PEG)[19] and poly(oligo(ethylene glycol)) methyl ether methacrylate (pOEGMA)[20] based polymers have shown promise. PDMS has been functionalized with polymers either by grafting-from (i.e., surface initiated polymerization)[21–23], or grafting-to,[24,25] where pre-synthesized polymers are immobilized onto the surface. Even though graft-from can result in higher polymer densities and thus better anti-fouling properties in simple material conditions[26], the coating of complex materials (e.g., medical devices) is practically difficult using graft-from surface-initiated procedures.[27] Indeed, simpler graft-to coatings exceed the *in vivo* performance of graft-from for complex polymeric devices with the use of end functionalized polymer groups[28]. Efforts to improve graft-to techniques therefore represent a viable strategy to improve antifouling polymer coatings.

Polymer coatings tethered to elastomeric substrates respond to the mechanical stimulus applied through stretching and relaxation as the interchain distance is effectively modified, leading to changes in surface properties. For example, immobilizing initiators to mechanically stretched PDMS, provides access to tailored polymer density via the

graft-from technique[29,30]. Also, thermoresponsive poly(N-isopropylacrylamide) (pIPAAM) was grafted from PDMS, and then mechanical stretching and temperature variation produced a dual stimuli responsive thin film, as stretching was able to effectively reduce the thickness of the grafted pIPAAM and influence cell adhesion[31]. Similarly, pSBMA was grafted from poly(vinylmethylsiloxane) (PVMS) and, following biofilm formation, stretching the elastomer showed release of the film[32]. Mechanical stimuli can therefore influence the fouling properties of polymer coated materials.

Recently, a method dubbed "Graft-then-Shrink" was developed on thermoplastic shrinkable substrates to improve the antifouling performance of graft-to pCB films on gold coatings. Therein, a thiol terminated polymer layer was grafted onto a gold coated thermoplastic substrate, and then thermally shrunk, producing a microstructured surface with greater grafted polymer content within a defined footprint[33]. Here, we extended the Graft-then-Shrink method beyond thermoplastic shrinking substrates and two dimensional surfaces to PDMS and the ability to increase pOEGMA and pCB content on all solvent swollen surfaces (**Figure 4.1**). pOEGMA and pCB were directly compared to evaluate antifouling properties of uncharged versus zwitterionic polymer coatings for PDMS.

Applying the graft-to method in concert with the previously developed Graft-then-Shrink approach led to increased grafted polymer content on elastomers. PDMS elastomers were functionalized with maleimide click handles, and a library of 15 thiol terminated pOEGMA (all pOEGMA polymers used have a side chain length of 8-9 OEG units, unless otherwise stated as 2mer or 4mer) and pCB polymers, synthesized via

reversible addition-fragmentation chain-transfer polymerization (RAFT), were immobilized to swelled elastomer substrates. The degree of swelling of the elastomer substrate, controlled by combinations of crosslinker density and swelling solvent, was shown to tune total grafted polymer content, with increased swelling yielding greater amounts of grafted polymer. Using the adapted Graft-then-Shrink protocol on elastomers improved the antifouling properties of grafted pOEGMA towards mammalian macrophages and bacterial *E. coli* by 95% and 75% respectively compared to PDMS modified with the same polymer using the control Shrink-then-Graft procedures, where polymers are immobilized to deswelled PDMS. Interestingly, even though pCB content was improved by Graft-then-Shrink, no benefit to antifouling properties was observed. Therefore, Graft-then-Shrink can further improve the already promising graft-to, as compared to graft-from, procedures for the modification of PDMS devices with uncharged hydrophilic polymers.

4.3. Results and discussion

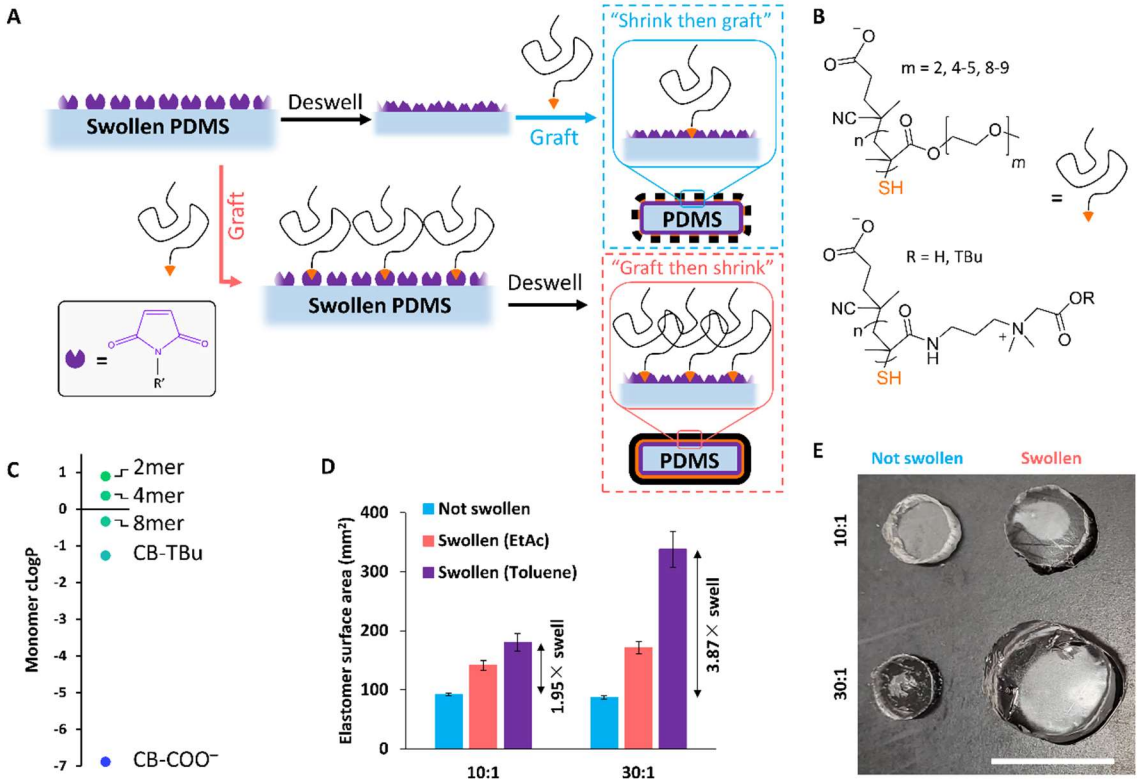

Figure 4.1. Graft-then-Shrink via thiol maleimide click chemistry for increasing grafted polymer content on PDMS. (A) Overview schematic of the Graft-then-Shrink method using swelled elastomers, where swollen PDMS is functionalized with succinimidyl-4-(N-maleimidomethyl)cyclohexane-1-carboxylate (SMCC), then either deswelled before grafting thiol terminated polymers ("Shrink-then-Graft" control) or deswelled after grafting thiol terminated polymers ("Graft-then-Shrink"). (B) Structures of RAFT synthesized thiol terminated pOEGMA 2mer, 4mer and 8mer, and pCB-TBu/COOH polymers. (C) Calculated LogP values of monomers corresponding to pOEGMA and pCB. (D) Swelling ratio with toluene of Sylgard™ 184 PDMS with 10:1 (1.94×) and 30:1 (3.87×) base:crosslinker ratio (mean ± SD, n = 3) by calculation of total surface area using calibrated photographs of top area and thickness, measured in ImageJ. (E) Photographs of PDMS in non-swollen and toluene swollen states. Scale bar = 10 mm.

4.3.1. Graft-then-Shrink with substrate swelling increases polymer content on PDMS

Using fluorescent copolymers ($pOEGMA_f$, $pCB\text{-}Tbu_f$, $pCB\text{-}COOH_f$) and microscopy characterization, it was found that Graft-then-Shrink improved grafting efficiency by up to 44.9× and 9.4× for $pOEGMA_f$ and $pCB\text{-}COOH_f$, respectively, which resulted in enhanced polymer mediated properties such as limited fouling rates for pOEGMA base polymers, compared to Shrink-then-Graft modified surfaces. For appropriate characterizations and comparisons, samples where polymers were grafted onto swollen PDMS (referred to as "Graft-then-Shrink," GtS in figures) were compared to control samples where polymers were grafted onto deswelled PDMS (referred to as "Shrink-then-Graft," StG in figures); all PDMS materials were thoroughly washed before any experiments to extract free PDMS chains. By using PDMS unreactive to polymers (no maleimide modification), it was determined that polymers did not significantly entangle into the top layer of the PDMS in the swelled state; surfaces with maleimides were required for a significant fluorescent signal (**Figure 4.2A, Figure S4.1**). As expected, maleimide content on the PDMS surfaces decreased following the polymer immobilization (**Figure S4.2**), though some maleimide content remained, which was hydrolyzed with pH 8.5 borate buffer before conducting nonspecific adhesions assays to avoid covalent maleimide-protein bonding. Therefore, Graft-then-Shrink utilizing swollen PDMS modified with maleimide can enhance thiol-terminated polymer immobilization.

Controlling the PDMS base:crosslinker ratio can control the swelling degree and thus polymer immobilization amount. Swelling increased the grafted $pOEGMA_f$ polymer content by 7.5× on the 10:1 PDMS and 13.8× on the 30:1 PDMS compared to respective Shrink-then-Graft controls. When comparing 30:1 to 10:1, 30:1 resulted in 44.9× more polymer content, thus greater swelling (30:1 PDMS) provides increased grafted polymer content over less swelling (10:1 PDMS), though even in the deswelled state, 30:1 PDMS has greater surface fluorescence than 10:1 PDMS. Confocal microscopy z-stacks showed that all grafted polymer fluorescence was located within the first 200 μm of all PDMS materials studied, with Graft-then-Shrink PDMS having broader grafted polymer distributions (full width at half maximum (FWHM) = 60 – 140 μm) than Shrink-then-Graft (FWHM = 30 – 50 μm) (**Figure 4.2B, C**), likely because of polymer penetration into the swollen PDMS. Increased swelling leads to greater polymer modification of PDMS and a deeper polymer penetration into the first ~200 μm from the surface.

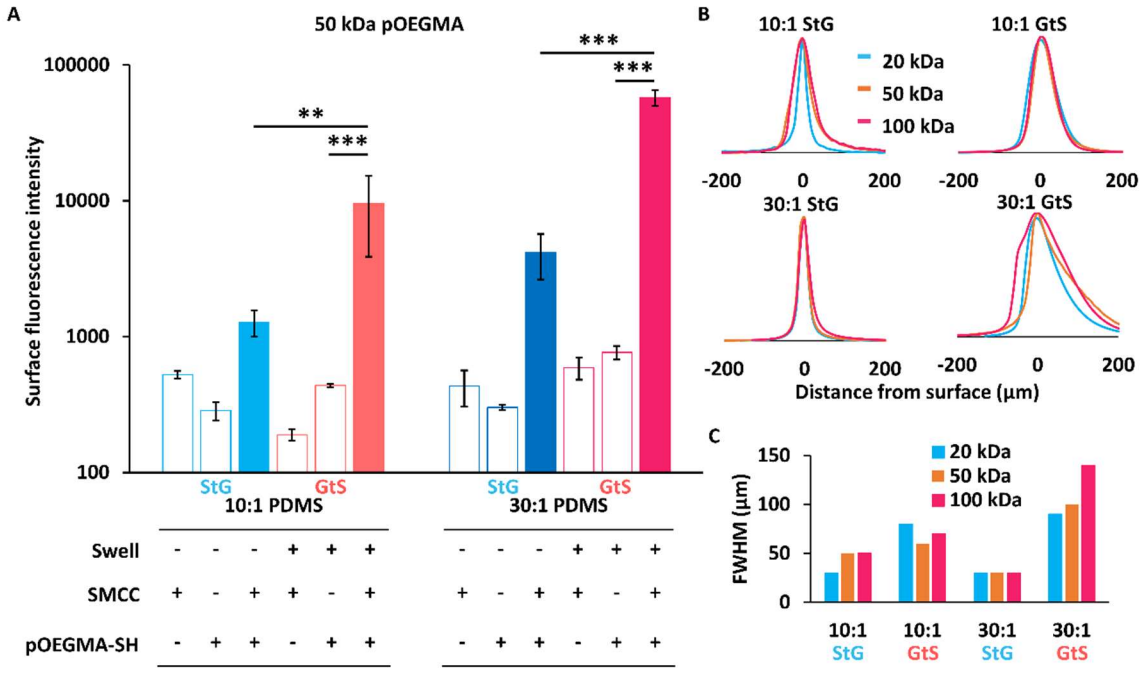

Figure 4.2. Grafting polymers onto swelled PDMS increases graft polymer content. (A) Fluorescence intensity by microscopy of 50 kDa fluorescein methacrylate pOEGMA (8mer) copolymers grafted onto PDMS (mean ± SD, n = 3). (B) Confocal microscopy of depth distribution of fluorescently labeled polymer. (C) Calculated FWHM of the polymer distributions in (B).

Besides base polymer content and crosslinking density, grafted polymer content can also be tuned by choice of swelling solvent, as increased solvent mediated swelling of PDMS increased polymer grafting (**Figure 4.3A, B**). The solvents for swelling PDMS were chosen to have different swelling ratios (S) for PDMS but similar solubility parameters (δ) to best isolate swelling ratio alone (toluene: $S = 1.31$, $\delta = 8.9$ cal$^{1/2}$ cm$^{-3/2}$ and ethyl acetate (EtAc): $S = 1.18$, $\delta = 9.0$ cal$^{1/2}$ cm$^{-3/2}$)[34]. The surface fluorescence intensity of the pCB-COOH$_f$ and pCB-TBu$_f$ modified elastomers was strongly correlated to swelling ratio as mediated by solvent choice (**Figure 4.3A, B**), providing a route to tailor grafted polymer content independent of crosslinker density so that elastomer

properties such as stiffness can be partially tailored outside of swelling degree. For example, 10:1 PDMS swelled with toluene and 30:1 PDMS swelled with EtAc have similar swelling ratios (1.95 and 1.96 respectively) but the 30:1 elastomer had 76% more surface fluorescence upon grafting fluorescent pCB-Tbu $_f$. Therefore, PDMS swelling for Graft-then-Shrink applications can be controlled by solvent swelling, crosslinker density or a combination thereof.

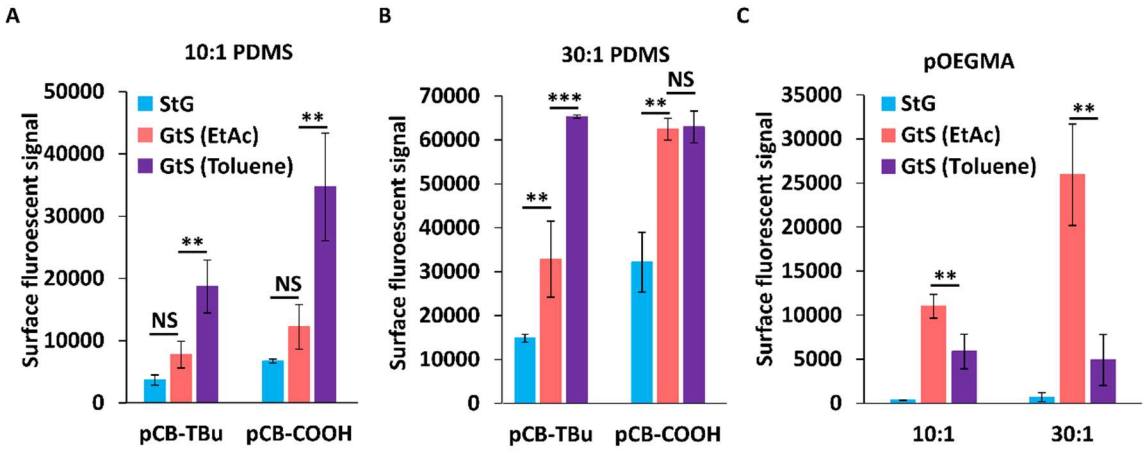

Figure 4.3: PDMS swelling solvent modulates polymer grafting content. Fluorescence intensity of (A) 10:1 and (B) 30:1 PDMS swelled in EtAc or toluene functionalized with pCB-COOH and pCB-TBu fluorescent copolymers and (B) 8mer pOEGMA fluorescence copolymers (mean ± SD, n = 3).

The solubility of the graft polymer in the elastomer swelling solvent was investigated with swollen PDMS exposed to pOEGMA$_f$ in aqueous MES buffer solutions. EtAc is a good solvent for both PDMS and pOEGMA$_f$, which lead to increased grafted polymer content, compared to toluene which is not able to solubilize the pOEGMA$_f$. Conversely to CB based polymers, 50 kDa 8mer pOEGMA$_f$ (50 kDa 8mer) had greater fluorescence intensities on EtAc swelled PDMS than on toluene swelled PDMS. Despite the similar δ of the two solvents, their LogP values differ by almost 2,

denoting a near 100× difference in partition (toluene LogP = 2.60, EtAc LogP = 0.65[35]) between water and octanol. Previously it has been shown that pOEGMA based materials can partition between water and EtAc solvent systems, but not between water and toluene systems, partly explaining improved functionalization with EtAc[36]. Oppositely to pOEGMA, pCB polymers showed greater grafted content when conducted with toluene. This difference in solvent swelling effect between the two polymer types is likely due to the insolubility of pCB polymers in both swelling solvents (EtAc and toluene), and solubility of pOEGMA in the EtAc but not toluene. Solubility of the grafting polymers and PDMS swelling degree must therefore be considered when conducting Graft-then-Shrink PDMS with polymers like pOEGMAs.[35,36]

To further illustrate that factors beyond swelling degree and solubility must be considered, we compared the grafting of zwitterionic pCB-$COOH_f$ and the positively charged pCB-Tbu_f, where, in most conditions, pCB-Tbu resulted in less grafting. Hydrophobicity and total charge influenced polymer immobilization with TBu protected CB based polymers (which are both more hydrophobic and positively charged) producing less surface fluorescent signal than deprotected free carboxylic pCB-$COOH_f$, potentially due to electrostatic repulsion between the polycations (**Figure 4.3**). It should be noted that the pCB-TBu_f and pCB-$COOH_f$ fluorescent content was identical as both polymers were sourced from the same batch; pCB-$COOH_f$ was produced by deprotecting pCB-TBu_f under acid conditions (**Figure S4.3**). As most graft-to procedures, polymer-polymer interactions within the coating can influence grafting density.

The effect of buffer composition and concentration on grafting density were further investigated using zwitterionic pCB-$COOH_f$ given the effects salts exhibit on zwitterion hydration from the antipolyelectrolyte effect[37]. Two grafting buffer compositions were compared, MES and guanidine HCl (GHCl). MES has been previously used in similar applications, and GHCl is a strong chaotrope and guanidine salts have been shown to interact with amide bonds present in the methacrylamide backbone of the pCB-$COOH_f$[38]. Interestingly, the incorporation of specific GHCl concentrations enhanced the grafting of pCB-$COOH_f$, with 10 mM GHCl resulting in the greatest grafting degree (**Figure 4.4**, **Figure S4.4**). Absorbance of PDMS and the loss of fluorescence from the grafting solution was used to quantify the grafting degree of the pCB-$COOH_f$ copolymer; the high grafting density on the PDMS resulted in fluorescence quenching[39,40] (**Figure S4.4**). Absorbance values at 502 nm were used to quantify polymer content in lieu of fluorescence, where 10 mM GHCl values were the highest overall, with intense absorbance due to fluorescein methacrylate content observed.

To explore the influence of GHCl on pCB-COOH, we conducted gel permeation chromatography (GPC) studies in buffers containing GHCl. GPC analysis of pCB-COOH in varying GHCl buffer strengths between 1 and 100 mM (pH 6.5) showed decreasing apparent M_ws and hydrodynamic radii with increasing buffer concentration, while PEG standards eluted at nearly identical times, with no change in apparent M_w, in all three GHCl buffer strengths tested (**Figure S4.5**). Differences in grafting efficiency may be the result of improved polymer packing at 10 mM over 1 mM and improved thiol accessibility and reactivity at 10 mM over 100 mM due to the more extended polymer conformation at

10 mM. Guanidine has previously shown effects on amphiphilic block copolymer grafting density[41], and has also been shown to control the collapsed and uncollapsed state of elastin like peptides in solution through interactions with amide bonds[38], which are also present in pCB-COOH. Therefore, GHCl is most likely influencing the hydrodynamic radii of pCB-COOH, indicating that buffer conditions beyond solubility can also influence grafting density for zwitterionic polymers.

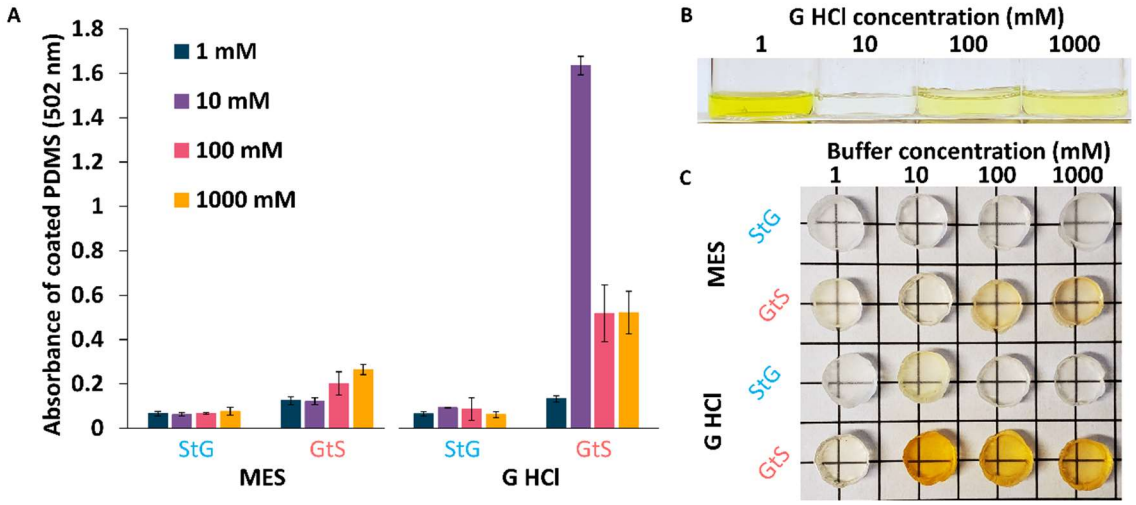

Figure 4.4. Grafting salt choice and concentration modifies grafted pCB-COOH content. (A) Absorbance of elastomers at 502 nm modified with fluorescent pCB-COOH copolymers (mean ± SD, n = 3). Concentrations refer to MES or GHCl (B, C) Photographs of grafting solution after polymer grafting procedure and 10:1 Graft-then-Shrink elastomers grafted with fluorescent pCB-COOH$_f$ copolymers in various buffers.

4.3.2. Characterization of biological fouling properties

For medical devices to be implanted, the binding of macrophages is an important parameter and metric for relative FBRs. The nonspecific adhesion of RAW 264.7 macrophages to functionalized PDMS was therefore characterized by fluorescence

microscopy. Interestingly, Graft-then-Shrink improved the antifouling properties of pOEGMA towards macrophages but not pCB (see section **4.3.4** for further discussion). In all pOEGMA conditions Graft-then-Shrink was equally or more antifouling than Shrink-then-Graft, with 100 kDa pOEGMA on 10:1 PDMS reducing adhesion by 98% compared to hydrolyzed SMCC controls and 91% compared to the Shrink-then-Graft condition, with similar improvements on the 30:1 PDMS. Therefore, Graft-then-Shrink is suited for the functionalization of PDMS using pOEGMA polymers, and can improve fouling resistance towards macrophages by up to 98%.

Fouling resistance was found to be M_w dependent, with pOEGMA being most antifouling at the highest studied M_ws in the Graft-then-Shrink condition (in agreement with bacterial resistance on pOEGMA presented below). The highest M_w pCB-COOH on 10:1 PDMS was also the best performing zwitterion condition, reducing macrophage adhesion by 97% (8 ± 5 cells) compared to hydrolyzed SMCC control, potentially due to a thicker layer being produced at higher M_ws, which provides improved antifouling[42,43]. We have previously seen resistance towards macrophage adhesion to be dependent on polymer molecular weight (M_w) for wrinkled gold Graft-then-Shrink surfaces, but no correlation on flat or Shrink-then-Graft was seen[33]. Here, pOEGMA based polymers on both 10:1 and 30:1 PDMS show similar M_w dependence on Graft-then-Shrink conditions and not on Shrink-then-Graft surfaces, as expected from previous studies.

As expected, applying the Graft-then-Shrink procedure to pOEGMAs with shorter 2 and 4 repeat unit OEG side chains (i.e., more hydrophobic) enhanced their cell adhesive properties. On the highly swelling 30:1 PDMS, effects of 2mer and 4mer pOEGMA are

maximized in Graft-then-Shrink conditions, cell adhesive 2mer and 4-5mer polymers (m = 2 or 4-5 in **Figure 4.1**) increased cell adhesion by 359 and 403% respectively, compared to Shrink-then-Graft (**Figure S4.6**). 10:1 PDMS produced insignificant differences on 2mer and 4mer surfaces between Graft-then-Shrink and Shrink-then-Graft, indicating insufficient polymer differences to influence fouling. Graft-then-Shrink can therefore modulate cell adhesive properties in either direction depending on the properties of the polymer to be grafted.

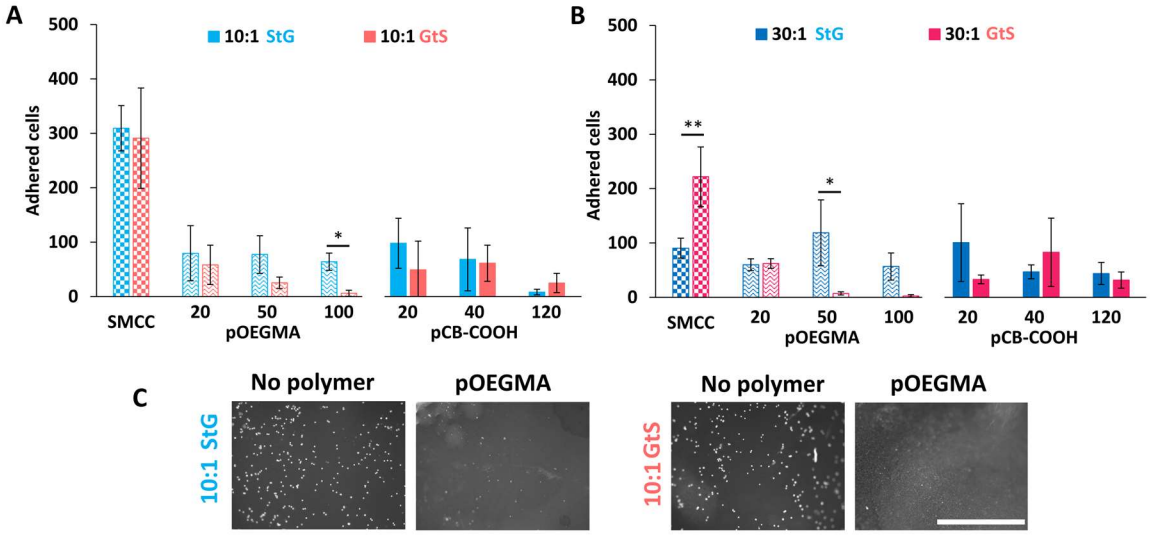

Figure 4.5. Graft the shrink with high M_w pOEGMA onto swelled elastomers improves antifouling properties. (A, B) Cell adhesion of Raw 264.7 macrophages on 10:1 and 30:1 PDMS modified with pOEGMA and pCB-COOH polymers (mean ± SD, n = 3). (C) Representative images of cell adhesion on 10:1 PDMS modified with 100 kDa pOEGMA. Scale bar = 1000 µm. Representative micrographs of all other conditions are shown in **Figure S4.7**.

4.3.2.1. Nonspecific bacterial adhesion

Similar to nonspecific macrophage adhesion, the Graft-then-Shrink protocol consistently for the nonspecific adhesion of *E.coli* to pOEGMA coatings but not pCB.

Because the polymer materials used are not antibacterial but are cell repellant, we measured adhesion resistance by live bacterial transfer. To detect small degrees of bacterial binding, PDMS devices were exposed to bacteria under orbital shaking, then dipped into three sequential sterile LB broth wash containers to remove unbound bacteria and exposed to sterile LB growth media to detect bacteria by optical density at 600 nm (OD600) following overnight incubation. 100 kDa pOEGMA Graft-then-Shrink on 10:1 PDMS (OD600 = 0.04 ± 0.03) showed the best improvement at resisting live bacteria transfer compared to the corresponding Shrink-then-Graft condition (OD600 = 0.16 ± 0.1; **Figure 4.6**). For bacterial adhesion, no consistent trend was observed between 10:1 and 30:1 PDMS, with increasing pOEGMA M_w improving antifouling properties for 10:1 PDMS but not 30:1 (**Figure 4.6B**). Therefore, the Graft-then-Shrink procedure using solvent swelled PDMS is dependent on the grafted polymer type and M_w with the antifouling properties of uncharged polymers being improved.

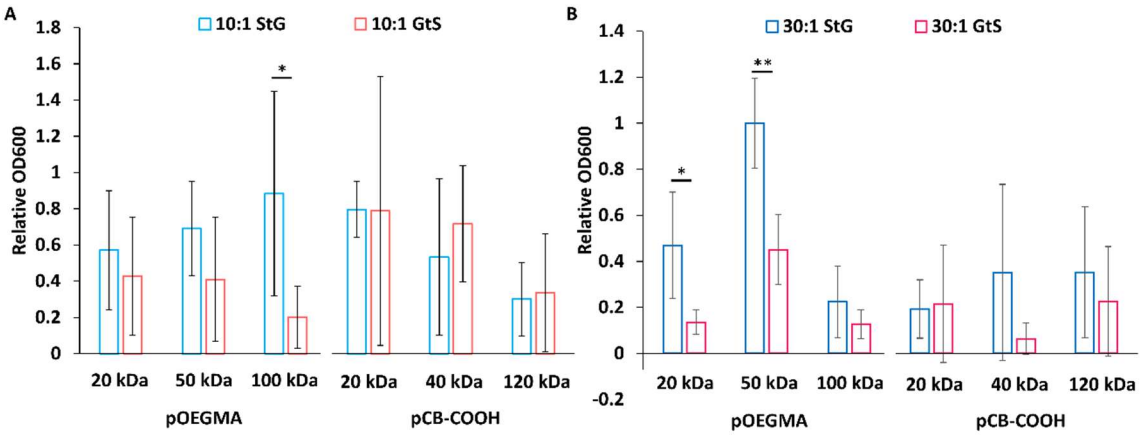

Figure 4.6. Resistance of pOEGMA and pCB-COOH modified elastomers towards *E. coli* bacterial attachment.
Live bacterial adhesion was characterized by culturing the elastomers in *E. coli* suspensions overnight and then gently rinsing the elastomers with sterile LB broth and

incubating them in fresh LB broth overnight, allowing adhered bacteria to proliferate. OD600 values of the LB broth following overnight incubation with bacteria exposed (A)10:1 and (B) 30:1 elastomers modified with pOEGMA and pCB-COOH was then measured (mean ± SD, n = 4).

4.3.3. Physical characterization of modified elastomers

Because water contact angle is often used to predict antifouling properties of surfaces by comparing hydrophilicity, we compared pOEGMA of varying OEG side chain length (2mer, 4mer, and 8mer) and pCB-COOH grafted before and after deswelling. For nearly all polymer compositions, M_ws and base ratios, Shrink-then-Graft and Graft-then-Shrink surfaces had statistically similar hydrophilicities. In the water contact angle comparisons, 2mer modified elastomers were the lone exception with Graft-then-Shrink elastomers displaying increased hydrophilicity compared to Shrink-then-Graft. Interestingly, the traditionally more hydrophobic 2mer modified PDMS also showed the lowest absolute water contact angle at 67° (**Figure 4.7**, **Figure S4.8**), despite being the most hydrophobic monomer (cLogP = 0.89). Water contact angles of graft-from pOEGMA on PDMS have been reported between 54° and 71° depending on layer thickness, appreciably lower than most of the values for pOEGMAs reported here, indicating polymer grafting was either not as dense or as thick as traditional graft-from procedures[44], even though Graft-then-Shrink enhanced antifouling properties towards macrophages and bacteria for the 8mer pOEGMA.

The change in WCA between the two conditions is influenced by two variables, the amount of grafted hydrophilic polymer, and the accelerated hydrophobic recovery of the PDMS surface due to the extended solvent swelling in the Graft-then-Shrink state. In

the Graft-then-Shrink procedure PDMS was swollen during the 4 d polymer grafting where Shrink-then-Graft was not, which can lead differences in PDMS hydrophobic recovery. To validate if the difference in swelling procedure influences the WCA, we prepared SMCC modified PDMS by Graft-then-Shrink and Shrink-then-Graft without grafting polymers (i.e., exposed swollen and non-swollen SMCC modified elastomers to MES buffer for 4 d). The SMCC modified Shrink-then-Graft surface had lower WCAs (10:1 = 80° ± 10, 30:1 = 105° ± 3) than SMCC modified Graft-then-Shrink surfaces (10:1 = 96° ± 4, 30:1 = 107° ± 1), demonstrating that both lower crosslink density and swelling increases hydrophobic recovery. Even though Graft-then-Shrink results in greater polymer immobilization (**Figure 4.3**), Graft the shrink results in higher WCAs for hydrophilic polymers because of accelerated hydrophobic PDMS recovery from solvent swelling. For hydrophobic polymers (i.e., pOEGMA 2mer), Graft-then-Shrink decreased WCAs which may be due to hydrophobic POEGMA-POEGMA interactions (lower critical solution temperature of 26°C for 2mer) limiting rearrangement at the surface.

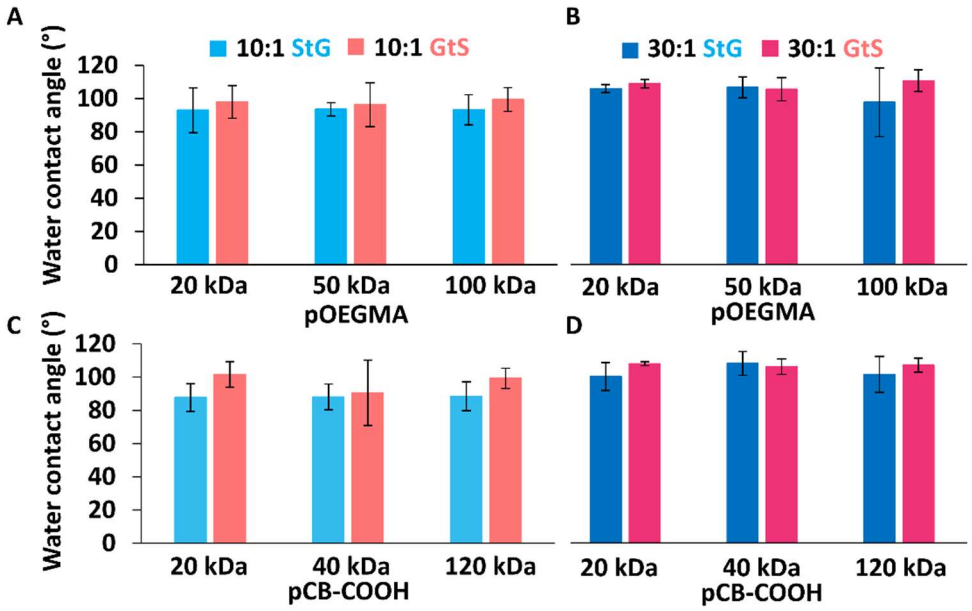

Figure 4.7. Graft-then-Shrink on elastomers does not modify hydrophilicity. (A)Water contact angles of 3 µL droplets of Milli-Q water on pOEGMA modified (A) 10:1 and (B) 30:1 PDMS and pCB-COOH modified (C) 10:1 and (D) 30:1 PDMS elastomers. Mean ± SD, n = 4.

4.3.4. Further Discussion

The efficiency of the Graft-then-Shrink method is maximized when the properties of the graft polymer – swollen elastomer system are chosen to achieve a solvated reaction environment and a high degree of swelling. The total grafted polymer content was highest when using neutral high M_w pOEGMAs, coupled with a low crosslink density elastomer, which maximizes swelling, that is swollen with a solvent that also solubilizes the graft polymer. In this case, considering two different measures of hydrophobicity, δ and LogP, allowed the solvent to be matched to the elastomer (δ) for swelling purposes and LogP solvent selection maximized the graft polymer partitioning onto the swollen surface.

The two polymer types investigated here represent two separate classes of hydrophilic antifouling polymer, uncharged, and neutral charged (i.e., zwitterionic). Both polymers prevent protein adsorption via strong interactions with a water shell, but the branched pOEGMA also repels protein through steric repulsion due to the long (M_n = 500 Da) OEG side chains. These differences in antifouling mechanisms, and the difference in cLogP between the constituent monomers (8-9mer OEGMA = -0.34, CB = -6.88) may make OEGMA based polymers more amenable to the Graft-then-Shrink method on hydrophobic PDMS and other medically relevant elastomers. Moreover, because Graft-then-Shrink distributed the polymer within the first ~200 μm, the larger and branched pOEGMAs may improve antifouling activity at the surface through steric repulsion mechanisms.

The Graft-then-Shrink method for swellable elastomeric substrates could be extended to other commonly used medical polymers such as polyurethane or polyvinylchloride[45].The wide range of relevant swellable materials, growing number of ways to fabricate antifouling polymer films via graft-to, and recent indications that the graft-to method can perform better than graft-from in medical applications means that the Graft-then-shrink method represents a path to improve the already leading technique. The method could also be used on PDMS with higher swelling ratios such as 60:1 Sylgard™ 184[46], or on highly stretchable PDMS via mechanical stretching[47] rather than solvent swelling. Grafting of polymers onto swelled elastomers could also be performed using physicochemical methods such as 3,4-dihydroxyphenylalanine (DOPA) anchoring rather than click reactions to expand potential materials for coating[48]. Though click reactions,

especially thiol ene reactions, are well suited for Graft-then-Shrink and have been previously explored for the modification of biomaterial surfaces[49], due to the simple production of thiol terminated polymers and the catalyst free mild reaction conditions[50]. Finally, the growing array of click reactions allow for the method to be extended to allow for multiple types of polymers to be patterned at once, before shrinking the material to improve final fidelity. Therefore, Graft-then-Shrink has the potential to be widely applied to medical devices and implants.

4.4. Conclusions

The Graft-then-Shrink technique was applied to two formulations of commercially available PDMS with multiple antifouling homo and copolymers of various compositions. The degree of swelling of the elastomeric substrate can tune total polymer grafting, either through crosslink density or through swelling solvent choice. Graft-then-Shrink on stiffer 10:1 material with higher M_w pOEGMA (100 kDa) had the best overall results, reducing macrophage adhesion by 98% compared to hydrolyzed SMCC controls and 91% compared to 10:1 PDMS coated using Shrink-then-Graft, potentially due to the grafted pOEGMA penetrating less deeply into the elastomer compared to the 30:1 PDMS, leading to a higher concentration near the surface of the material. Although, Graft-then-Shrink did not improve the antifouling properties for pCB even though polymer content was increased, indicating that polymer and swelling procedures must be carefully chosen. With appropriate swelling solvent and polymer choice, Graft-then-Shrink offers a method to both increase polymer coating content and improve antifouling properties for graft-to procedures on PDMS.

4.5. Materials and methods

4.5.1. Materials

N-[3-(dimethylamino)propyl]methacrylamide, tert-butyl bromoacetate, trifluoroacetic acid (TFA), 4-Cyano-4-(phenylcarbonothioylthio)pentanoic acid, 4,4'-azobis(4-cyanovaleric acid), sodium hydroxide, 2-(N-morpholino)ethanesulfonic acid sodium salt (MES), ethanol, sodium acetate, and Poly(ethylene glycol) methyl ether methacrylate (M_n = 186, 300, and 500), fluorescein methacrylate, fluorescein maleimide assay kit, guanidine hydrochloride, (3-aminopropyl)triethoxy silane (APTES), acetonitrile, and ethyl acetate were purchased from Sigma Aldrich (Oakville, ON, Canada). Fetal bovine serum (FBS), Calcein AM, Hoescht, Sylgard 184 elastomer kit, was obtained from Thermo Fisher Scientific (Burlington, ON, Canada). LB broth was purchased from Bioshop Canada (Burlington, ON, Canada). SMCC was donated by Todd Hoare from McMaster University (Hamilton, ON, Canada). Phosphate buffered saline (PBS) at pH 7.4 contained 10 mM sodium phosphate and 137 mM NaCl.

4.5.2. PDMS elastomer preparation and swelling

PDMS was prepared using a Sylgard™ 184 elastomer kit, with ratios of 10:1 and 30:1 base to crosslinker. Elastomers were mixed, degassed, and then cured for 30 min at 80°C. Discs of 3 mm thickness and 6 mm diameter were punched out using a leather punch. Discs were then extracted with toluene 4 times to remove uncured free PDMS. Finally, discs were deswelled and stored at room temperature until use.

4.5.3. *Tert*-butyl protected Carboxybetaine methacrylamide monomer synthesis

Adapted from previously published procedure[51], N-[3(dimethylamino)propyl]methacrylamide (25 g, 147 mmol, 1 equiv.) was dissolved in 200 mL of dry acetonitrile under nitrogen. *Tert*-butyl bromoacetate (34 g, 176 mmol, 1.2 equiv.) was added, and left to react overnight at 50 °C. The reaction was cooled to room temperature and the white product was precipitated with 500 mL of ether, decanted, washed with 100 mL of ether 3 times and dried under a stream of nitrogen. 1H NMR (D2O, 600 MHz) δ: 5.7 (s, 1H), 5.5 (s, 1H), 4.3 (s, 2H), 3.6 (m, 2H), 3.4 (t, 2H), 3.3 (m, 6H), 2.1 (tt, 2H), 1.9 (s, 3H), 1.5 (s, 9H) (**Figure S4.9**).

4.5.4. General polymerization protocol

Reaction mixtures for pDMAPMA and pOEGMA homopolymers and pOEGMA-fluorescein and pCB-fluorescein copolymers were prepared for reactions using a RAFT polymerization technique with appropriate amounts of monomer, 4-Cyano-4-(phenylcarbonothioylthio)pentanoic acid chain transfer agent (CTA), 4,4'-azobis(4-cyanopentanoic acid) initiator and solvent as detailed in **Table S4.1**. Reaction mixtures were then degassed by 3 rounds of the freeze pump thaw method, and incubated, with stirring, at 70°C overnight. The crude polymer mixtures were then aminolysed by incubation with butylamine (10x CTA mol amount) for 2 h, at pH 10, and finally dialyzed for 3 d against pH 5 water, and lyophilized. Synthesized pDMAPMA was then reacted with *tert*-butyl bromo acetate at a 3:1 molar excess of TBu to DMAPMA monomer content, in acetonitrile for 3 d, and dialyzed against methanol for 3 d to

produce pCB-TBu. pCB-TBu was then deprotected by incubation at 50°C for 6 hours in pH 1.3 HCl, and dialyzed for 3 d against pH 5 water to yield pCB-COOH. Protection and deprotection steps were quantified by H NMR (**Figure S4.10**).

4.5.5. Polymer characterization by GPC

Characteristic molecular weights (M_n and M_w) and dispersities (Đ) were measured by an Agilent 1260 infinity II GPC system equipped with an Agilent 1260 infinity RI detector at 30°C, a Superose 6 Increase 10/300 GL column, and with PBS running buffer supplemented with 0.05% sodium azide at room temperature. The column was calibrated using polyethylene glycol (PEG) standards (Mn of 3,000 to 60,000). Degree of polymerization (*N*) was calculated using monomer molecular weight and reported measured M_n by GPC (**Table S4.2**).

4.5.6. Polymer grafting procedure

PDMS discs were plasma oxidized for 45 s on "high" setting, then immediately placed into 1% (v/v) APTES in dry toluene and shaken for 1 h. The APTES solution was then removed, and the discs were rinsed 3 times with dry toluene. A solution of 2 mg mL^{-1} SMCC in PBS was added to the discs and shaken for 2 h. The SMCC solution was then removed, then discs were dried and either deswelled prior to polymer grafting, reswollen with EtAc or kept swollen in toluene. The discs were then incubated with the appropriate thiol terminated polymer at 2 mg mL^{-1} in either MES or GHCl buffer at pH 6.5 for 4 d with shaking. Materials that had polymer grafting in the swollen state were then deswelled overnight. Finally, discs were incubated overnight with shaking in pH 9.3 borate buffer to hydrolyze remaining maleimides on the material surface.

4.5.7. Excess maleimide assay

Maleimides on the surface of the PDMS discs were quantified using a modified fluorescence detection assay kit. Fluorescent maleimide reactive probes were prepared according to the manufacturer guidelines and 100 μL of fluorescent probe in supplied Assay Buffer was added to a well containing a PDMS disc to be assayed and incubated at room temperature overnight, with shaking. Each disc was then rinsed 3 times with DI water, dried with a laboratory wipe, and surface fluorescence was quantified by fluorescence microscopy using a Biotek Cytation5 plate reader equipped with a GFP channel filter cube.

4.5.8. Fluorescent polymer content characterization

Fluorescent polymer distribution into modified elastomers was characterized by confocal laser scanning microscopy depth profiles Z-stacks corresponding of the fluorescein tagged copolymers were acquired at a step size of 10 μm.

4.5.9. Characterization of surface hydrophilicity

Material hydrophilicity was characterized by static water contact angle measurements (OCA 20 contact angle goniometer, with SCA 20 software). Droplets of MilliQ water (2 μL, resistivity > 18.2 MΩ cm) were placed onto modified PDMS discs and photographed. One measurement per disc was made, replicates represent three separate discs.

4.5.10. Bacterial adhesion assay

A culture of *E. coli* BL21 was inoculated in LB broth and incubated overnight at room temperate with shaking. The following day, the culture was subcultured and grown to an OD of 0.5 and then 200 µL of this suspension was added to functionalized PDMS discs in a 96 well plate and incubated at room temperature overnight with shaking. The PDMS discs were then removed from the bacterial suspension, rinsed 3 times with sterile LB broth and placed into fresh LB broth to grown overnight. Following overnight incubation, the OD of the LB broth was measured.

4.5.11. Macrophage adhesion

PDMS discs were immobilized into a 96 well plate with PDMS (Sylgard™ 184) and cured at 80 °C for 30 mins, then sterilized by incubation with 70% ethanol for 1 h, and rinsed with sterile DI water 3 times. Sterilized materials were then incubated with 100% aged FBS overnight at 37°C at 5% CO_2 then the serum was removed and the materials were incubated with RAW 264.7 macrophages (10 000 cells per well) for 48 hours 37°C at 5% CO_2. Following incubation, the cell containing media was removed from the wells, surfaces were gently rinsed a single time with PBS to remove non-adhered cells from the well, and the materials were stained with Calcein AM and Hoescht according to the manufacturer protocol prior to imaging with a Biotek Cytation5 microscope.

4.5.12. Statistical analysis

All statistical analyses were performed using GraphPad Prism 8. Significant differences were determined by multiple comparisons corrected multiple t-tests, using the Holm-Sidak method. Significant p-values are indicated on graphs as follows $p < 0.05$ is indicated by *, $p < 0.01$ by **, and $p < 0.001$ by ***. All replicates were multiple samples prepared at the same time under the same conditions, and tested within a single experiment with biological material derived from a single lot, inoculation, or cell passage, where applicable.

4.6. Supporting information

Additional supporting figures and tables related to maleimide content of elastomers, GPC characterization of pCB-COOH molecular weights in guanidine, *tert*-butyl ester deprotection and NMR characterization, water contact angle measurements, micrographs of cell adhesion, NMR characterization of synthesized monomers, and GPC analysis of polymers

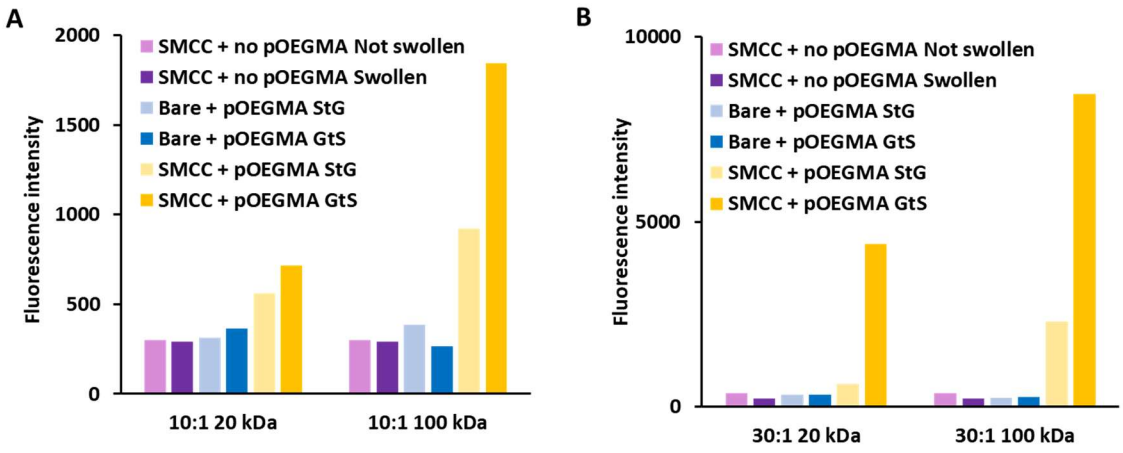

Figure S4.1. Surface fluorescence of pOEGMA on PDMS.

Grafting of fluorescent (A) 20 and (B) 100 kDa 8mer pOEGMA to PDMS with and without maleimide functionalization.

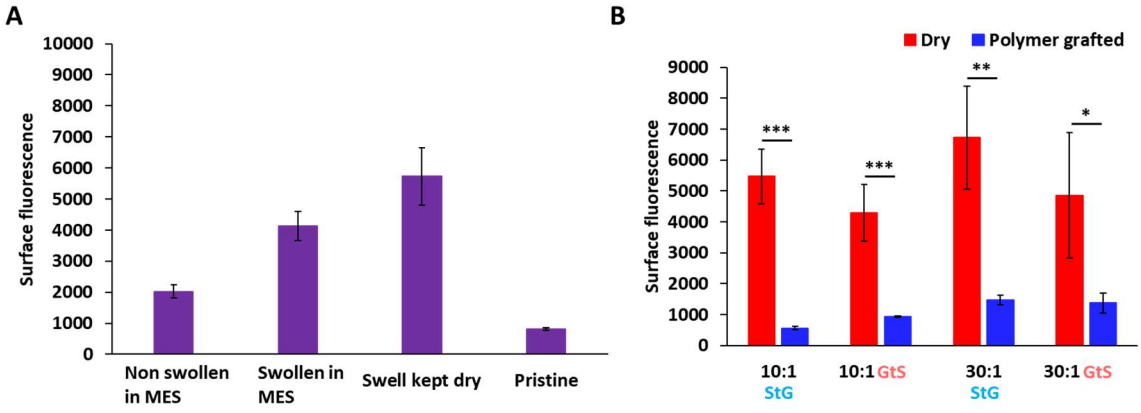

Figure S4.2. Maleimide content of elastomers after polymer grafting. (A) Surface fluorescence of SMCC modified elastomers after reaction with a thiol-fluorescein tracer. (B) Maleimide content of elastomers before and after polymer grafting. Means ± SD, n = 3.

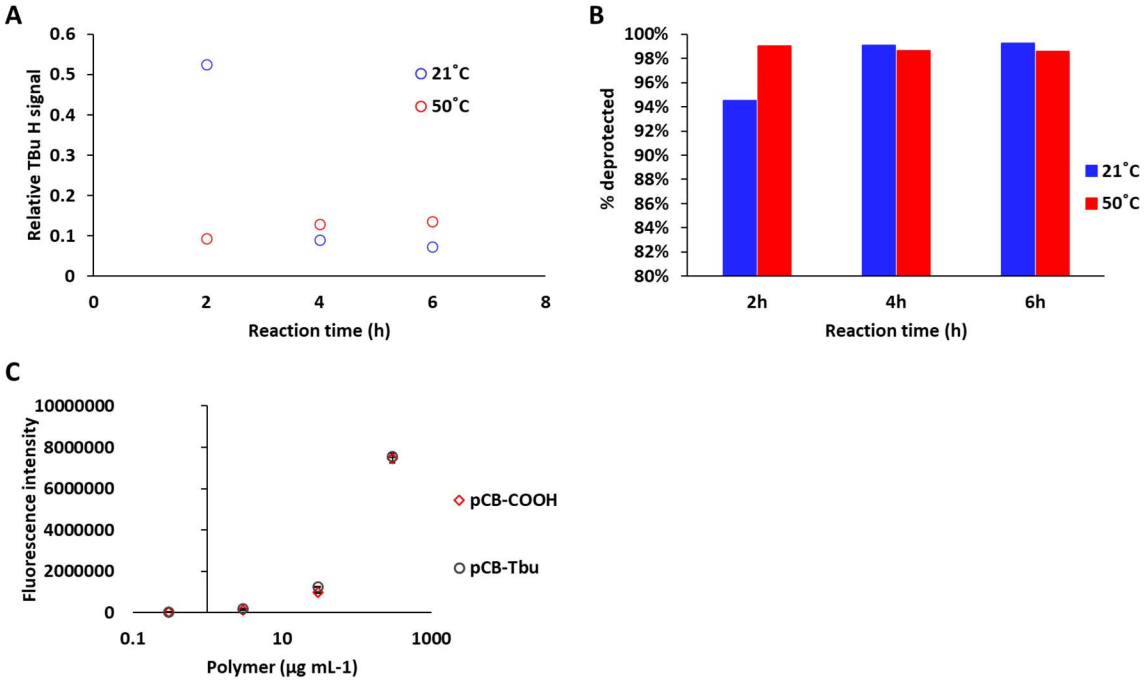

Figure S4.3. pCB-TBu ester deprotection in pH 1.3 HCl. (A) Relative *tert*-butyl group signal by NMR after exposure to HCl at pH 1.3 for between 2 and 6 hours at room temperature and 50°C. (B) Calculated percent of ester deprotection based on relative signal from NMR of pCB-TBu. (C) Solution fluorescence intensity of pCB-TBu and pCB-COOH fluorescein methacrylate copolymers. Mean ± SD, n = 3.

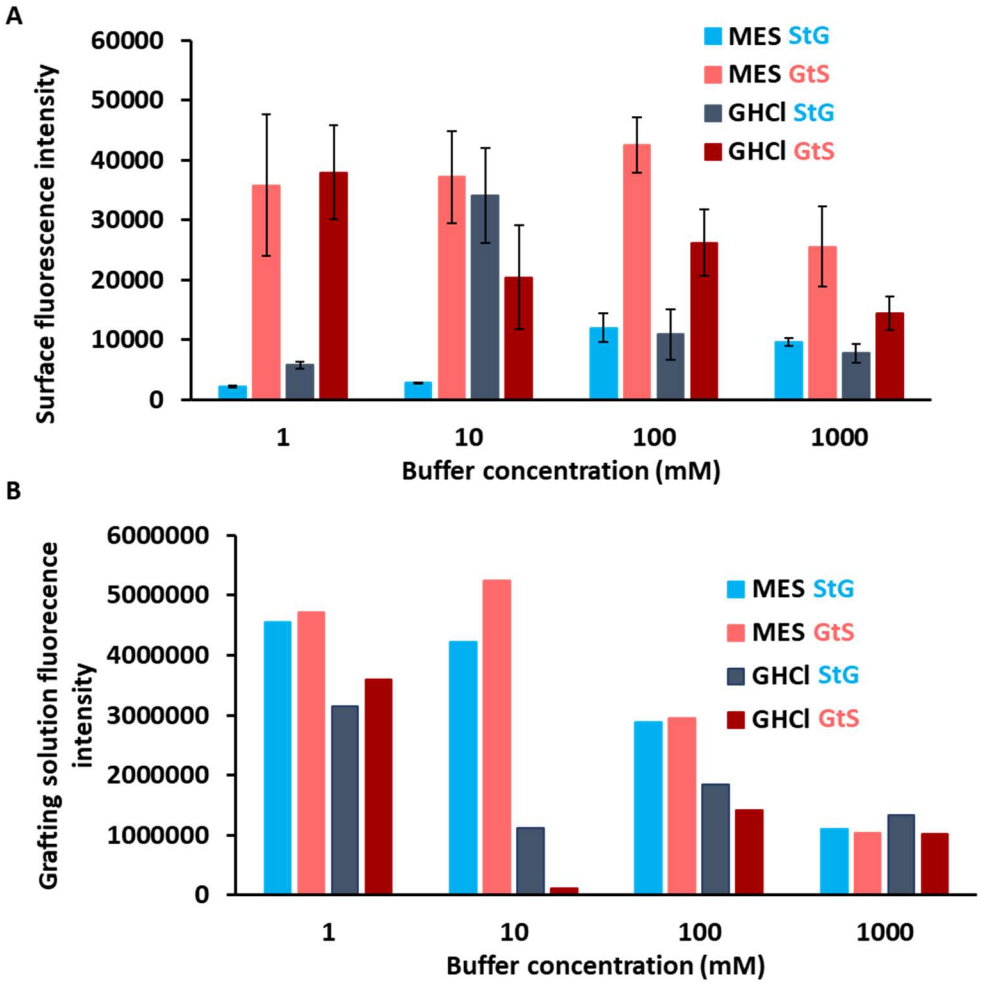

Figure S4.4. Quantification of fluorescence of pCB copolymers grafted in MES and GHCl on PDMS.

(A) Surface fluorescence of 10:1 PDMS elastomers modified with fluorescent pCB-COOH in MES and GHCl grafting buffers between 1 and 1000 mM. (B) Grafting solution fluorescence of 10:1 PDMS elastomers modified with fluorescent pCB in MES and GHCl grafting buffers between 1 and 1000 mM.

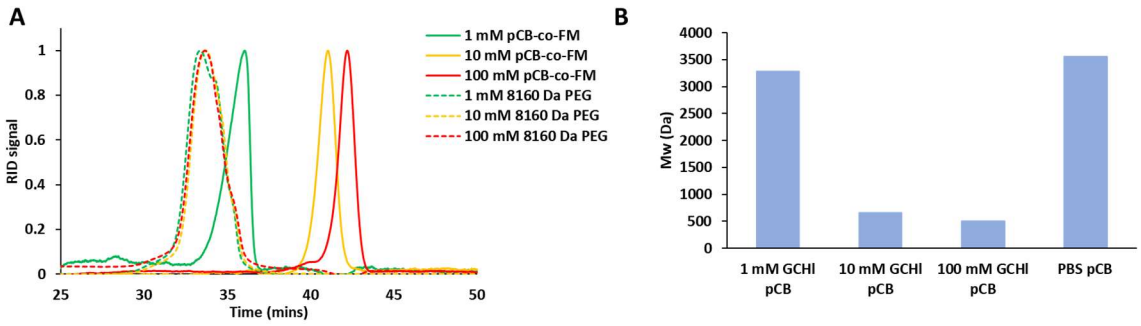

Figure S4.5. Apparent molecular weight of pCB changes with GHCl concentration. (A) GPC of PEG standards and pCB-*co*-methacrylate in three GHCl buffer concentrations. (B) Plotted apparent molecular weight of pCB calculated by GPC calibrated with PEG standards in PBS.

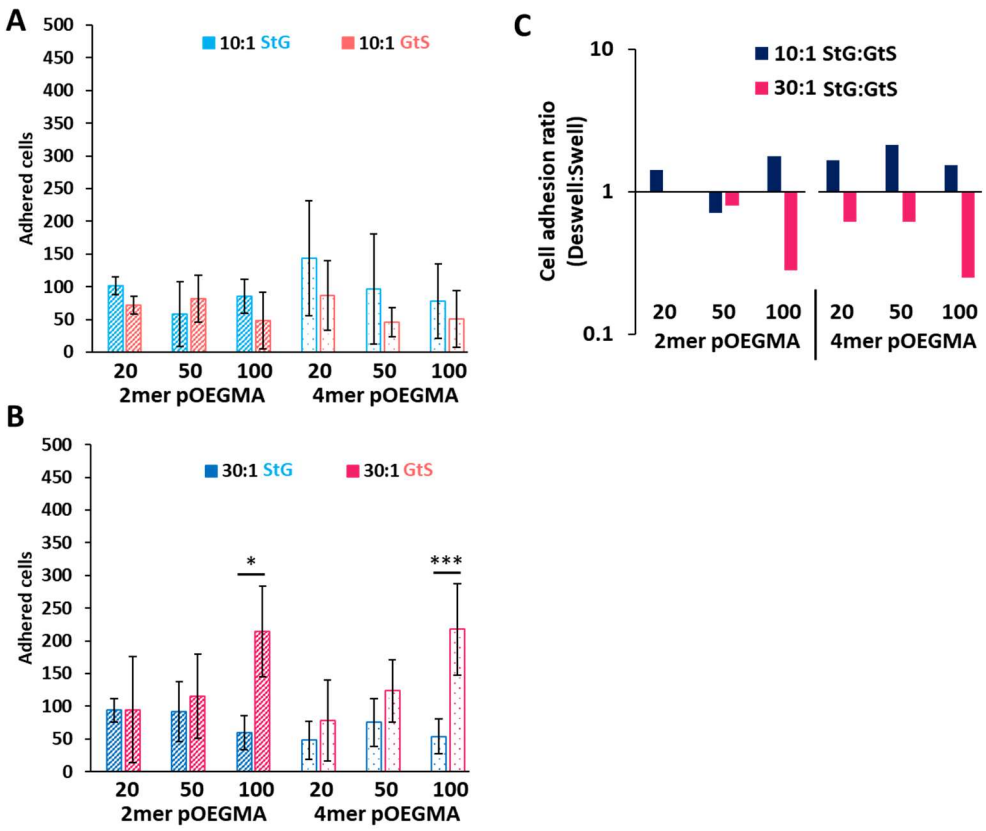

Figure S4.6. Macrophage adhesion to PDMS modified with non-antifouling polymers. (A) Cell adhesion of Raw 264.7 macrophages on 10:1 and 30:1 PDMS modified with 2mer and 4mer pOEGMA (mean ± SD, n = 3). (C) Ratio of cells adhered between Graft-then-Shrink and Shrink-then-Graft materials modified with 2mer and 4mer pOEGMA.

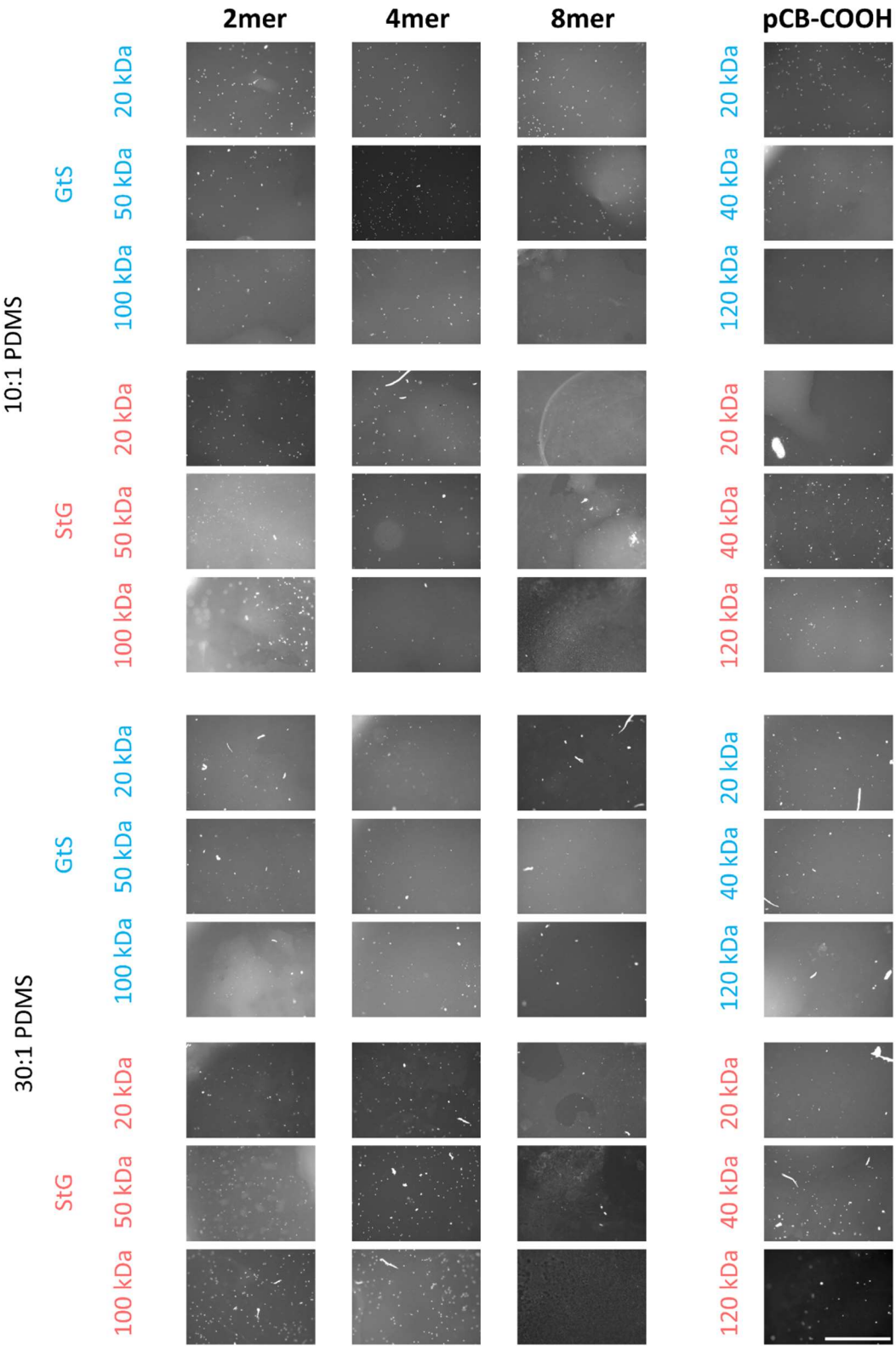
2mer
4mer
8mer
pCB-COOH
10:1 PDMS
30:1 PDMS
GtS
StG
20 kDa
50 kDa
100 kDa
40 kDa
120 kDa

Figure S4.7. Representative fluorescence micrographs of RAW 264.7 macrophage adhesion on polymer modified PDMS.

Scale bar = 1000 μm.

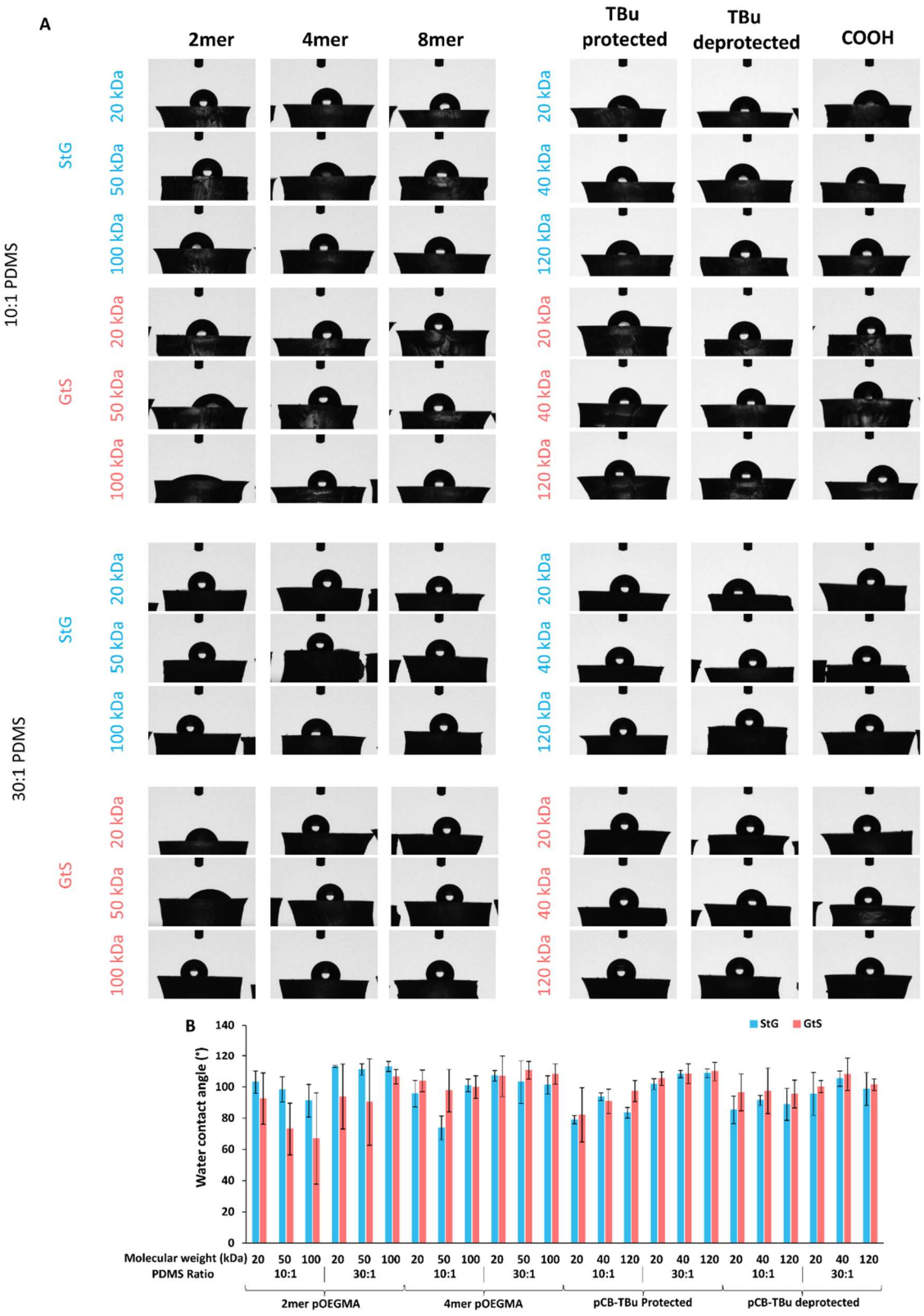
A
2mer
4mer
8mer
TBu protected
TBu deprotected
COOH
10:1 PDMS
30:1 PDMS
StG
GtS
20 kDa
50 kDa
100 kDa
40 kDa
120 kDa
B
StG
GtS
Water contact angle (°)
Molecular weight (kDa)
PDMS Ratio
2mer pOEGMA
4mer pOEGMA
pCB-TBu Protected
pCB-TBu deprotected

Figure S4.8. Water contact angle measurements of polymer modified PDMS. (A) Representative images of 3 µL droplets of MilliQ water on PDMS samples. (B) Average water contact angle of PDMS samples. Mean ± SD, n = 4.

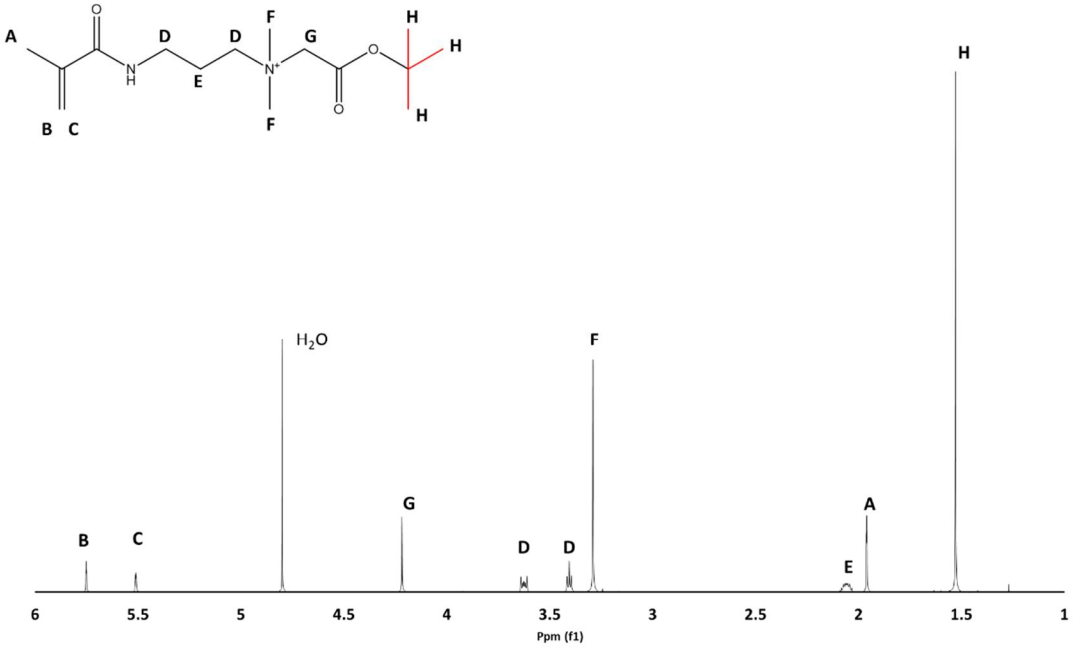

Figure S4.9. H NMR spectroscopy of CB-TBu monomer.

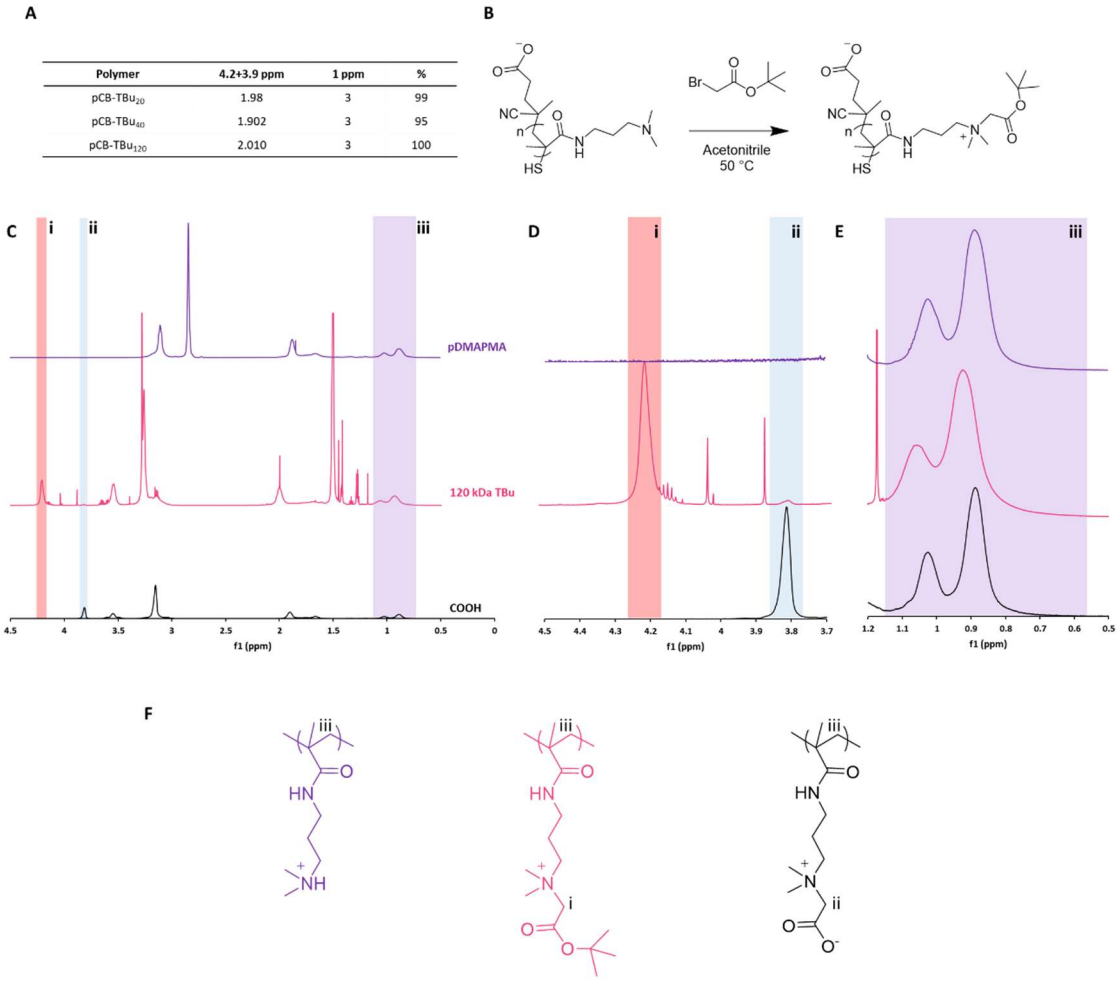

Figure S4.10. NMR spectroscopic characterization of pCB-TBu synthesis from pDMAPMA. (A) Quantification of monomer percent modification by NMR. (B) Reaction scheme of pCB-TBu preparation. (C-E) H NMR of precursor pDMAPMA, protected pCB-TBu and deprotected pCB-COOH. (F) Structures and assignments of H NMR.

Table S4.1: Polymerization conditions used for the preparation of RAFT polymer library.

Monomer	Molecular weight (kDa)	Monomer (g)	CTA (mg)	Initiator (mg)	Solvent (mL)	Solvent type
2mer	20	2	28.3	14.2	8.7	Dioxane
	50	2	11.2	5.6	8.7	Dioxane
	100	2	5.6	2.8	8.7	Dioxane
4mer	20	2	28.3	14.2	7.6	Dioxane
	50	2	11.2	5.6	4.7	Dioxane
	100	2	5.6	2.8	7.6	Dioxane
8mer	20	2	28.3	14.2	3.9	Dioxane
	50	2	11.2	5.6	3.9	Dioxane
	100	2	5.6	2.8	3.9	Dioxane
pOEGMA$_{8,9}$-fluo	20	0.5 / 0.004	7.1	3.6	0.98	Dioxane
	50	0.5 / 0.004	2.6	1.4	0.98	Dioxane
	100	0.5 / 0.004	1.4	0.7	0.98	Dioxane
pDMAPMA	20	2	27.9	18.7	11	2:1 Buffer*:Dioxane
	40	2	14.0	9.3	11	2:1 Buffer*:Dioxane
	120	2	4.7	3.1	11	2:1 Buffer*:Dioxane

*Sodium acetate buffer (pH 5, 1 M)

Table S4.2: Calculated molecular weights, dispersities and degrees of polymerization of polymers used.

Name		Monomer MW	M_n	M_w	Đ	*N*
20 kDa	2mer	186	5.7	7.8	1.36	31
	4mer	300	7.9	9.7	1.21	26
	8mer	500	7.8	11.1	1.41	16
50 kDa	2mer	186	10.4	14.5	1.40	56
	4mer	300	16.2	27.2	1.67	54
	8mer	500	16.9	34.5	2.04	34
100 kDa	2mer	186	15.9	30.2	1.90	85
	4mer	300	44.8	112.3	2.50	149
	8mer	500	51.3	157.8	3.07	103
pOEGMA$_{8}$ $_{9}$- fluo	20 kDa	499	13.1	14.4	1.10	26
	50 kDa	499	24.4	34.3	1.41	49
	100 kDa	499	41.1	84.5	2.06	82
pCB-TBu	20 kDa	285	16.0	23.5	1.46	56
	40 kDa	285	33.1	83.9	2.53	116
	120 kDa	285	122.1	409.1	3.34	428

4.7. References

(1) Mempin, M.; Hu, H.; Chowdhury, D.; Deva, A.; Vickery, K. The A, B and C's of Silicone Breast Implants: Anaplastic Large Cell Lymphoma, Biofilm and Capsular Contracture. *Materials (Basel).* **2018**, *11* (12). https://doi.org/10.3390/ma11122393.

(2) Xie, X.; Doloff, J. C.; Yesilyurt, V.; Sadraei, A.; Mcgarrigle, J. J.; Omami, M.; Veiseh, O.; Farah, S.; Isa, D.; Ghani, S.; Joshi, I.; Vegas, A.; Li, J.; Wang, W.;

Bader, A.; Tam, H. H.; Tao, J.; Chen, H.; Yang, B.; Williamson, K. A.; Oberholzer, J.; Langer, R.; Anderson, D. G. Reduction of Measurement Noise in a Continuous Glucose Monitor by Coating the Sensor with a Zwitterionic Polymer. *Nat. Biomed. Eng.* **2018**, *2*, 894–906. https://doi.org/10.1038/s41551-018-0273-3.

(3) Zhang, D.; Chen, Q.; Shi, C.; Chen, M.; Ma, K.; Wan, J.; Liu, R. Dealing with the Foreign-Body Response to Implanted Biomaterials: Strategies and Applications of New Materials. *Adv. Funct. Mater.* **2021**, *31* (6), 2007226. https://doi.org/10.1002/adfm.202007226.

(4) Teo, A. J. T.; Mishra, A.; Park, I.; Kim, Y.-J.; Park, W.-T.; Yoon, Y.-J. Polymeric Biomaterials for Medical Implants and Devices. *ACS Biomater. Sci. Eng.* **2016**, *2* (4), 454–472. https://doi.org/10.1021/acsbiomaterials.5b00429.

(5) Busscher, H. J.; van der Mei, H. C.; Subbiahdoss, G.; Jutte, P. C.; van den Dungen, J. J. A. M.; Zaat, S. A. J.; Schultz, M. J.; Grainger, D. W. Biomaterial-Associated Infection: Locating the Finish Line in the Race for the Surface. *Sci. Transl. Med.* **2012**, *4* (153).

(6) Arciola, C. R.; Campoccia, D.; Montanaro, L. Implant Infections: Adhesion, Biofilm Formation and Immune Evasion. *Nat. Rev. Microbiol.* **2018**, *16* (7), 397–409. https://doi.org/10.1038/s41579-018-0019-y.

(7) Rieger, U. M.; Mesina, J.; Kalbermatten, D. F.; Haug, M.; Frey, H. P.; Pico, R.; Frei, R.; Pierer, G.; Lüscher, N. J.; Trampuz, A. Bacterial Biofilms and Capsular Contracture in Patients with Breast Implants. *Br. J. Surg.* **2013**, *100* (6), 768–774.

https://doi.org/10.1002/bjs.9084.

(8) Saint, S.; Greene, T.; Krein, S.; Rogers, M.; Ratz, D.; Fowler, K.; Edson, B.; Watson, S.; Meyer-Lucas, B.; Masuga, M.; Faulkner, K.; Gould, C.; Battles, J.; Fakih, M. A Program to Prevent Catheter-Associated Urinary Tract Infection in Acute Care. *N. Engl. J. Med.* **2016**, *374* (22), 2111–2119. https://doi.org/10.1056/NEJMoa1504906.

(9) Majd, H.; Scherer, S. S.; Boo, S.; Ramondetti, S.; Cambridge, E.; Raffoul, W.; Friedrich, M.; Pittet, B.; Pioletti, D.; Hinz, B.; Pietramaggiori, G. Novel Micropatterns Mechanically Control Fibrotic Reactions at the Surface of Silicone Implants. *Biomaterials* **2015**, *54*, 136–147. https://doi.org/10.1016/j.biomaterials.2015.03.027.

(10) Malheiro, V.; Lehner, F.; Dinca, V.; Hoffmann, P.; Maniura-Weber, K. Convex and Concave Micro-Structured Silicone Controls the Shape, but Not the Polarization State of Human Macrophages. *Biomater. Sci.* **2016**, *4* (11), 1562–1573. https://doi.org/10.1039/c6bm00425c.

(11) Robotti, F.; Bottan, S.; Fraschetti, F.; Mallone, A.; Pellegrini, G.; Lindenblatt, N.; Starck, C.; Falk, V.; Poulikakos, D.; Ferrari, A. A Micron-Scale Surface Topography Design Reducing Cell Adhesion to Implanted Materials. *Sci. Rep.* **2018**, *8* (1), 1–13. https://doi.org/10.1038/s41598-018-29167-2.

(12) Doloff, J. C.; Veiseh, O.; de Mezerville, R.; Sforza, M.; Perry, T. A.; Haupt, J.; Jamiel, M.; Chambers, C.; Nash, A.; Aghlara-Fotovat, S.; Stelzel, J. L.; Bauer, S.

J.; Neshat, S. Y.; Hancock, J.; Romero, N. A.; Hidalgo, Y. E.; Leiva, I. M.; Munhoz, A. M.; Bayat, A.; Kinney, B. M.; Hodges, H. C.; Miranda, R. N.; Clemens, M. W.; Langer, R. The Surface Topography of Silicone Breast Implants Mediates the Foreign Body Response in Mice, Rabbits and Humans. *Nat. Biomed. Eng.* **2021**, *5* (10), 1115–1130. https://doi.org/10.1038/s41551-021-00739-4.

(13) Noskovicova, N.; Schuster, R.; van Putten, S.; Ezzo, M.; Koehler, A.; Boo, S.; Coelho, N. M.; Griggs, D.; Ruminski, P.; McCulloch, C. A.; Hinz, B. Suppression of the Fibrotic Encapsulation of Silicone Implants by Inhibiting the Mechanical Activation of Pro-Fibrotic TGF-β. *Nat. Biomed. Eng.* **2021**, *5* (12), 1437–1456. https://doi.org/10.1038/s41551-021-00722-z.

(14) Maan, A. M. C.; Hofman, A. H.; de Vos, W. M.; Kamperman, M. Recent Developments and Practical Feasibility of Polymer-Based Antifouling Coatings. *Adv. Funct. Mater.* **2020**, *30* (32), 2000936. https://doi.org/10.1002/adfm.202000936.

(15) Ishihara, K.; Ziats, N. P.; Tierney, B. P.; Nakabayashi, N.; Anderson, J. M. Protein Adsorption from Human Plasma Is Reduced on Phospholipid Polymers. *J. Biomed. Mater. Res.* **1991**, *25* (11), 1397–1407. https://doi.org/10.1002/jbm.820251107.

(16) Ueda, T.; Oshida, H.; Kurita, K.; Ishihara, K.; Nakabayashi, N. Preparation of 2-Methacryloyloxyethyl Phosphorylcholine Copolymers with Alkyl Methacrylates and Their Blood Compatibility. *Polym. J.* **1992**, *24* (11), 1259–1269. https://doi.org/10.1295/polymj.24.1259.

(17) Zhang, Z.; Chen, S.; Chang, Y.; Jiang, S. Surface Grafted Sulfobetaine Polymers via Atom Transfer Radical Polymerization as Superlow Fouling Coatings. *J. Phys. Chem. B* **2006**, *110*, 10799–10804. https://doi.org/10.1021/jp057266i.

(18) Zhang, Z.; Chen, S.; Jiang, S. Dual-Functional Biomimetic Materials: Nonfouling Poly(Carboxybetaine) with Active Functional Groups for Protein Immobilization. *Biomacromolecules* **2006**, *7* (12), 3311–3315. https://doi.org/10.1021/BM060750M.

(19) Lowe, S.; O'Brien-Simpson, N. M.; Connal, L. A. Antibiofouling Polymer Interfaces: Poly(Ethylene Glycol) and Other Promising Candidates. *Polym. Chem.* **2015**, *6* (2), 198–212. https://doi.org/10.1039/c4py01356e.

(20) Ma, H.; Hyun, J.; Stiller, P.; Chilkoti, A. "Non-Fouling" Oligo(Ethylene Glycol)-Functionalized Polymer Brushes Synthesized by Surface-Initiated Atom Transfer Radical Polymerization. *Adv. Mater.* **2004**, *16* (4), 338–341. https://doi.org/10.1002/adma.200305830.

(21) Diaz Blanco, C.; Ortner, A.; Dimitrov, R.; Navarro, A.; Mendoza, E.; Tzanov, T. Building an Antifouling Zwitterionic Coating on Urinary Catheters Using an Enzymatically Triggered Bottom-up Approach. *ACS Appl. Mater. Interfaces* **2014**, *6* (14), 11385–11393. https://doi.org/10.1021/am501961b.

(22) Leigh, B. L.; Cheng, E.; Xu, L.; Derk, A.; Hansen, M. R.; Guymon, C. A. Antifouling Photograftable Zwitterionic Coatings on PDMS Substrates. *Langmuir* **2019**, *35* (5), 1100–1110. https://doi.org/10.1021/acs.langmuir.8b00838.

(23) Keefe, A. J.; Brault, N. D.; Jiang, S. Suppressing Surface Reconstruction of Superhydrophobic PDMS Using a Superhydrophilic Zwitterionic Polymer. *Biomacromolecules* **2012**, *13* (1), 1683–1687. https://doi.org/10.1021/bm300399s.

(24) Hu, P.; Zeng, H.; Zhou, H.; Zhang, C.; Xie, Q.; Ma, C.; Zhang, G. Silicone Elastomer with Self-Generating Zwitterions for Antifouling Coatings. *Langmuir* **2021**, *37* (27), 8253–8260. https://doi.org/10.1021/acs.langmuir.1c00984.

(25) Dundua, A.; Franzka, S.; Ulbricht, M. Improved Antifouling Properties of Polydimethylsiloxane Films via Formation of Polysiloxane/Polyzwitterion Interpenetrating Networks. *Macromol. Rapid Commun.* **2016**, *37* (24), 2030–2036. https://doi.org/10.1002/marc.201600473.

(26) Hong, D.; Hung, H. C.; Wu, K.; Lin, X.; Sun, F.; Zhang, P.; Liu, S.; Cook, K. E.; Jiang, S. Achieving Ultralow Fouling under Ambient Conditions via Surface-Initiated ARGET ATRP of Carboxybetaine. *ACS Appl. Mater. Interfaces* **2017**, *9* (11), 9255–9259. https://doi.org/10.1021/acsami.7b01530.

(27) Bose, S.; Volpatti, L. R.; Thiono, D.; Yesilyurt, V.; McGladrigan, C.; Tang, Y.; Facklam, A.; Wang, A.; Jhunjhunwala, S.; Veiseh, O.; Hollister-Lock, J.; Bhattacharya, C.; Weir, G. C.; Greiner, D. L.; Langer, R.; Anderson, D. G. A Retrievable Implant for the Long-Term Encapsulation and Survival of Therapeutic Xenogeneic Cells. *Nat. Biomed. Eng.* **2020**, *4* (8), 814–826. https://doi.org/10.1038/s41551-020-0538-5.

(28) Ukita, R.; Wu, K.; Lin, X.; Carleton, N. M.; Naito, N.; Lai, A.; Do-Nguyen, C. C.;

Demarest, C. T.; Jiang, S.; Cook, K. E. Zwitterionic Poly-Carboxybetaine Coating Reduces Artificial Lung Thrombosis in Sheep and Rabbits. *Acta Biomater.* **2019**, *92*, 71–81. https://doi.org/10.1016/j.actbio.2019.05.019.

(29) Genzer, J.; Efimenko, K. Creating Long-Lived Superhydrophobic Polymer Surfaces through Mechanically Assembled Monolayers. *Science (80-.).* **2000**, *290* (5499), 2130–2133. https://doi.org/10.1126/science.290.5499.2130.

(30) Wu, T.; Efimenko, K.; Genzer, J. Preparing High-Density Polymer Brushes by Mechanically Assisted Polymer Assembly. *Macromolecules* **2001**, *34* (4), 684–686. https://doi.org/10.1021/ma001750w.

(31) Akiyama, Y.; Matsuyama, M.; Yamato, M.; Takeda, N.; Okano, T. Poly(N-Isopropylacrylamide)-Grafted Polydimethylsiloxane Substrate for Controlling Cell Adhesion and Detachment by Dual Stimulation of Temperature and Mechanical Stress. *Biomacromolecules* **2018**, *19* (10), 4014–4022. https://doi.org/10.1021/acs.biomac.8b00992.

(32) Shivapooja, P.; Yu, Q.; Orihuela, B.; Mays, R.; Rittschof, D.; Genzer, J.; López, G. P. Modification of Silicone Elastomer Surfaces with Zwitterionic Polymers: Short-Term Fouling Resistance and Triggered Biofouling Release. *ACS Appl. Mater. Interfaces* **2015**, *7* (46), 25586–25591. https://doi.org/10.1021/acsami.5b09199.

(33) Jesmer, A. H.; Huynh, V.; Marple, A. S. T.; Ding, X.; Moran-Mirabal, J. M.; Wylie, R. G. Graft-Then-Shrink: Simultaneous Generation of Antifouling

Polymeric Interfaces and Localized Surface Plasmon Resonance Biosensors. *ACS Appl. Mater. Interfaces* **2021**, *13* (44), 52362–52373. https://doi.org/10.1021/acsami.1c14930.

(34) Lee, J. N.; Park, C.; Whitesides, G. M. Solvent Compatibility of Poly(Dimethylsiloxane)-Based Microfluidic Devices. *Anal. Chem.* **2003**, *75* (23), 6544–6554. https://doi.org/10.1021/ac0346712.

(35) Reslow, M.; Adlercreutz, P.; Mattiasson, B. *Organic Solvents for Bioorganic Synthesis 1. Optimization of Parameters for a Chymotrypsin Catalyzed Process*; 1987; Vol. 26.

(36) Li, D.; Zhao, B. Temperature-Induced Transport of Thermosensitive Hairy Hybrid Nanoparticles between Aqueous and Organic Phases. *Langmuir* **2007**, *23* (4), 2208–2217. https://doi.org/10.1021/la0628165.

(37) Xiao, S.; Ren, B.; Huang, L.; Shen, M.; Zhang, Y.; Zhong, M.; Yang, J.; Zheng, J. Salt-Responsive Zwitterionic Polymer Brushes with Anti-Polyelectrolyte Property. *Curr. Opin. Chem. Eng.* **2018**, *19*, 86–93. https://doi.org/10.1016/j.coche.2017.12.008.

(38) Heyda, J.; Okur, H. I.; Hladílková, J.; Rembert, K. B.; Hunn, W.; Yang, T.; Dzubiella, J.; Jungwirth, P.; Cremer, P. S. Guanidinium Can Both Cause and Prevent the Hydrophobic Collapse of Biomacromolecules. *J. Am. Chem. Soc.* **2017**, *139* (2), 863–870. https://doi.org/10.1021/Jacs.6b11082.

(39) Bae, W.; Yoon, T. Y.; Jeong, C. Direct Evaluation of Self-Quenching Behavior of Fluorophores at High Concentrations Using an Evanescent Field. *PLoS One* **2021**, *16* (2 February 2021). https://doi.org/10.1371/journal.pone.0247326.

(40) Besford, Q. A.; Merlitz, H.; Schubotz, S.; Yong, H.; Chae, S.; Schnepf, M. J.; Weiss, A. C. G.; Auernhammer, G. K.; Sommer, J. U.; Uhlmann, P.; Fery, A. Mechanofluorescent Polymer Brush Surfaces That Spatially Resolve Surface Solvation. *ACS Nano* **2022**, *16* (2), 3383–3393. https://doi.org/10.1021/acsnano.2c00277.

(41) Schulze, M.; Adigüzel, S.; Nickl, P.; Schmitt, A. C.; Dernedde, J.; Ballauff, M.; Haag, R. A Simple and Robust Method to Prepare Polyelectrolyte Brushes on Polymer Surfaces. *Adv. Mater. Interfaces* **2022**, *9* (5). https://doi.org/10.1002/admi.202102005.

(42) Yang, W.; Xue, H.; Li, W.; And, J. Z.; Jiang, S. Pursuing "Zero" Protein Adsorption of Poly(Carboxybetaine) from Undiluted Blood Serum and Plasma. *Langmuir* **2009**, *25* (19), 11911–11916. https://doi.org/10.1021/la9015788.

(43) Zhao, C.; Li, L.; Wang, Q.; Yu, Q.; Zheng, J. Effect of Film Thickness on the Antifouling Performance of Poly(Hydroxy-Functional Methacrylates) Grafted Surfaces. *Langmuir* **2011**, *27* (8), 4906–4913. https://doi.org/10.1021/la200061h.

(44) Mousavi, M.; Ghaleh, H.; Jalili, K.; Abbasi, F. Multi-Layer PDMS Films Having Antifouling Property for Biomedical Applications. *J. Biomater. Sci. Polym. Ed.* **2020**, *32* (5), 678–693. https://doi.org/10.1080/09205063.2020.1856300.

(45) Maitz, M. F. Applications of Synthetic Polymers in Clinical Medicine. *Biosurface and Biotribology* **2015**, *1* (3), 161–176. https://doi.org/10.1016/j.bsbt.2015.08.002.

(46) Glover, J. D.; Mclaughlin, C. E.; Mcfarland, M. K.; Pham, J. T. Extracting Uncrosslinked Material from Low Modulus Sylgard 184 and the Effect on Mechanical Properties. *J. Polym. Sci.* **2020**, *58* (2), 343–351. https://doi.org/10.1002/pola.29558.

(47) Zhou, L. Y.; Gao, Q.; Fu, J. Z.; Chen, Q. Y.; Zhu, J. P.; Sun, Y.; He, Y. Multimaterial 3D Printing of Highly Stretchable Silicone Elastomers. *ACS Appl. Mater. Interfaces* **2019**, *11* (26), 23573–23583. https://doi.org/10.1021/acsami.9b04873.

(48) Sundaram, H. S.; Han, X.; Nowinski, A. K.; Brault, N. D.; Li, Y.; Ella-Menye, J. R.; Amoaka, K. A.; Cook, K. E.; Marek, P.; Senecal, K.; Jiang, S. Achieving One-Step Surface Coating of Highly Hydrophilic Poly(Carboxybetaine Methacrylate) Polymers on Hydrophobic and Hydrophilic Surfaces. *Adv. Mater. Interfaces* **2014**, *1* (6), 1–8. https://doi.org/10.1002/admi.201400071.

(49) Donahoe, C. D.; Cohen, T. L.; Li, W.; Nguyen, P. K.; Fortner, J. D.; Mitra, R. D.; Elbert, D. L. Ultralow Protein Adsorbing Coatings from Clickable PEG Nanogel Solutions: Benefits of Attachment under Salt-Induced Phase Separation Conditions and Comparison with PEG/Albumin Nanogel Coatings. *Langmuir* **2013**, *29* (12), 4128–4139. https://doi.org/10.1021/la3051115.

(50) Kakwere, H.; Perrier, S. Orthogonal “Relay” Reactions for Designing

Functionalized Soft Nanoparticles. *J. Am. Chem. Soc.* **2009**, *131* (5), 1889–1895. https://doi.org/10.1021/ja8075499.

(51) Keefe, A. J.; Jiang, S. Poly(Zwitterionic)Protein Conjugates Offer Increased Stability without Sacrificing Binding Affinity or Bioactivity. *Nat. Chem.* **2012**, *4* (1), 59–63. https://doi.org/10.1038/nchem.1213.

CHAPTER 5. CONCLUSIONS

The number of implantable devices is increasing, with physicians and patients expecting increased performance with respect to infection and foreign body response prevention and improvements to outcomes such as implant longevity, pain, and implant associated diseases. Further, the increased interdisciplinary nature of research related to protein therapeutics and biomaterials require label free biosensor technology that is both accessible and high performance.

5.1. Major Contributions

Simple methods for romantic polymer coatings for biosensor applications were found, providing new routes to these important materials. The novel use of wrinkled gold films as LSPR biosensors was also investigated, and coupled with Graft-then-Shrink coating methods, widens access to romantic biosensors. Accomplishments supporting these contributions include:

1. **pH controlled RAFT for hierarchical surfaces.**
2. **Novel continuous wrinkled gold LSPR sensor material.**
3. **Graft-then-Shrink method for increasing polymer content for thermoplastic and elastomeric substrates.**

The work in this thesis demonstrates that the performance of RAFT synthesized polymer coatings is strongly dependent on polymer density, and through controlling this parameter, simple routes to romantic materials can be found. These methods, and their extensions, will improve access to high performance biosensors.

5.2. Limitations

The coatings produced throughout this thesis were characterized as platform technologies, without specific application environments. Because of the general nature of the platforms, the biological characterization is limited with respect to activation states of the environment. In specific, macrophage adhesion experiments were designed to determine and compare nonspecific cell adhesion characteristics exclusively, and so activation signals of human derived macrophages should be explored for specific in vivo applications. Other unexplored aspects of biological characterization include the blood compatibility of the materials, and the resistance to a variety of bacterial types and flow environments, specific to individual applications.

In Chapter 2, pH controlled partial aminolysis and Graft from techniques were successfully used to produce high-loading, low-fouling surfaces. Nevertheless, these employed techniques are limited in complexity of the modified surfaces, and limited specifically in the use of pH labile monomers. Open questions remain generally around the layer densities of bimodal surfaces, and molecular weight distributions within the layers. Layer density differences could be probed in situ by QCM-D as silicon sensor chips are amenable to the methods used in the synthesis. Further interrogation of the molecular weights could be undertaken by removing and collecting the grafted polymers for analysis. Initial attempts at this via surface etching and GPC analysis were unsuccessful due likely to the limited surface area of the modifications producing less than 100 μg of total polymer for analysis.

Chapter 3 explored two phenomena, the first being the introduction of an extension to the grafting to polymer layer synthesis technique, and the second being a novel LSPR biosensor application exploiting the resulting wrinkled gold, biofunctional coating. The Graft-then-Shrink technique produced polymer densities of ~ 0.11 chains nm^{-2}, this value is a 5.5 times increase in apparent density compared to Shrink-then-Graft but represents an apparent increase derived from a fluorescent polymer grafting. More thorough interrogation of the actual polymer densities on the surfaces, and their comparison against the same polymers produced via grafting from would provide useful insight into the limits of performance of the new method. This improved probing of the polymer densities, coupled with shrinking substrates of different shrink ratios would allow for better design of high quality antifouling and sensing surfaces. Finally, sensing in complex environments with non-target proteins present would be a useful next step towards understanding the performance of the platform.

Chapter 4 extends the methods developed in the previous chapter to three dimensional elastomers, using a two-part silicone as the model material, a suite of neutral hydrophilic and zwitterionic polymers, and a click chemistry immobilization scheme. Towards the goal of reduced synthetic complexity of these antifouling elastomers, the multistep elastomer modification process should be eliminated. Initial attempts at employing vinyl containing PDMS, and immobilizing the thiol terminated graft polymers directly to the elastomer via radically initiated thiol – ene reaction were not successful, so a different approach such as maleimide containing PDMS copolymers to imbue the elastomer with a click functionality could be explored.

The stability of the modified antifouling elastomers should also be explored, particularly in the relevant biologic environments. The surface reconstruction of PDMS can move the modifying polymers away from the surface, so a longer term antifouling experiment should be conducted to understand the impact of this phenomenon. Finally, the propensity of silicone materials to absorb lipids in vivo should be investigated, and compared against other elastomeric substrates to inform material choices for specific applications past these initial platform demonstrations.

5.3. Concluding Remarks

Here it was demonstrated that strong effects of polymer density on material function can be leveraged to modify the performance of polymer films without changing the polymer composition. By grafting polymers onto a metallic surface, and shrinking, it was also shown that even without decreasing the distance between grafting sites, the effective polymer density above a structured surface can be increased, and this increase can translate into improved performance. Further, these methods were simple to implement, and can be applied to a wide range of material substrates, given the array of deformable materials and simple grafting methods via click chemistry and dopa grafting.

There remain a variety of open avenues of research for both the Graft-then-Shrink methods and the LSPR wrinkled biosensors described in this thesis. For example, the variety of grafting strategies (e.g., click handles, dopa grafting, physisorption etc.) as well as the variety of underlying substrates with controllable levels shrinkage and expansion provide a ripe opportunity for novel architectures and grafted polymer patterns to be explored. Further, effects of grafted polymer patterns and compositions in conjunction

with wrinkled material structure should be investigated. The physics of the polymer compression during shrinkage, in the dry and hydrated state, as well as state of thermoresponsive polymers during shrinkage also requires investigation.

Production of antifouling materials has been an area of growing research intensity for decades, with polymer coatings to this end receiving a high level of interest. The implementation of these kinds of coatings still suffers from the complexity of the problem hand, namely that all protein and cell interactions must be resisted, despite the enormous variety of these interactions, and length of time for which they must be resisted, requiring either exceptionally durable coatings, or self-healing or self-rejuvenating degradable properties, as even small defects can lead to failure over time. The field might focus on developing a series of standardized conditions for testing the relevant long term performance of newly discovered surfaces to work towards translation of the enormous body of research to overcome the associated important challenges of nonspecific interactions, as has been suggested by a number of groups recently[1–3].

5.4. References

(1) Faria, M.; Björnmalm, M.; Thurecht, K. J.; Kent, S. J.; Parton, R. G.; Kavallaris, M.; Johnston, A. P. R.; Gooding, J. J.; Corrie, S. R.; Boyd, B. J.; Thordarson, P.; Whittaker, A. K.; Stevens, M. M.; Prestidge, C. A.; Porter, C. J. H.; Parak, W. J.; Davis, T. P.; Crampin, E. J.; Caruso, F. Minimum Information Reporting in Bio-Nano Experimental Literature. *Nat. Nanotechnol.* **2018**, *13* (9), 777–785. https://doi.org/10.1038/s41565-018-0246-4.

(2) Jesmer, A. H.; Wylie, R. G. Controlling Experimental Parameters to Improve Characterization of Biomaterial Fouling. *Front. Chem.* **2020**, *8* (December). https://doi.org/10.3389/fchem.2020.604236.

(3) Le, T. C.; Penna, M.; Winkler, D. A.; Yarovsky, I. Quantitative Design Rules for Protein-Resistant Surface Coatings Using Machine Learning. *Sci. Rep.* **2019**, *9* (1), 1–12. https://doi.org/10.1038/s41598-018-36597-5.